



**HAL**  
open science

# Contribution to fault detection of PV modules using I-V curves

Vorachack Kongphet

► **To cite this version:**

Vorachack Kongphet. Contribution to fault detection of PV modules using I-V curves. Electric power. Université Paris-Saclay, 2022. English. NNT : 2022UPAST149 . tel-03903993

**HAL Id: tel-03903993**

**<https://theses.hal.science/tel-03903993>**

Submitted on 16 Dec 2022

**HAL** is a multi-disciplinary open access archive for the deposit and dissemination of scientific research documents, whether they are published or not. The documents may come from teaching and research institutions in France or abroad, or from public or private research centers.

L'archive ouverte pluridisciplinaire **HAL**, est destinée au dépôt et à la diffusion de documents scientifiques de niveau recherche, publiés ou non, émanant des établissements d'enseignement et de recherche français ou étrangers, des laboratoires publics ou privés.

# Contribution to fault detection of PV modules using I-V curves

*Contribution à la détection de défauts dans les modules PV en utilisant  
les courbes I-V*

## Thèse de doctorat de l'université Paris-Saclay

École doctorale n°575, Electrical, Optical, Bio-Physics and Engineering (EOBE)  
Spécialité de doctorat : Génie électrique  
Graduate School : Sciences de l'ingénierie et des systèmes. Référent : CentraleSupélec

Thèse préparée dans les unités de recherche Laboratoire de Génie Electrique et Electronique de Paris (Université Paris-Saclay, CentralesSupélec) et Laboratoire des signaux et systèmes (Université Paris-Saclay, CNRS, CentralesSupélec), sous la direction de **Demba DIALLO**, professeur des universités (Université Paris-Saclay), le co-encadrement d'**Anne MIGAN-DUBOIS**, professeure des universités (Université Paris-Saclay) et le co-encadrement de **Claude DELPHA**, Maître de Conférence – HDR (Université Paris-Saclay).

Thèse soutenue à Paris-Saclay, le 25 Novembre 2022, par

**Vorachack KONGPHET**

## Composition du Jury

Membres du jury avec voix délibérative

<b>Eric LABOURE</b> Professeur des Universités, Université Paris-Saclay, GeePs	Président du jury
<b>Yassine AMIRAT</b> Enseignant-Chercheur – HDR, YNCREA-ISEN	Rapporteur & Examineur
<b>Yvan BONNASSIEUX</b> Professeur des Universités, Ecole Polytechnique	Rapporteur & Examineur
<b>Corinne ALONSO</b> Professeure des Universités, Université Paul Sabatier, LAAS-CNRS,	Examinatrice
<b>Pierre-Olivier LOGERAI</b> Maître de Conférences – HDR, UPEC, CERTES	Examineur
<b>Zhixue ZHENG</b> Maître de Conférences, Université de Lorraine, LMOPS	Examinatrice

# Table of contents

Acknowledgement .....	i
Résumé .....	ii
General introduction.....	vii
<i>Background and motivation</i> .....	vii
<i>Solar Energy</i> .....	viii
<i>Thesis outline</i> .....	ix
Chapter I: Development of the experimental test bench .....	3
I.1. Introduction .....	3
I.2. I-V tracer: state-of-the-art.....	3
I.2.1. Variable load resistance .....	3
I.2.2. Electronic load technique .....	4
I.2.3. Capacitive load technique .....	5
I.2.4. Four-quadrant power supply.....	6
I.2.5. DC-DC converter .....	7
I.3. Experimental Test Bench .....	9
I.3.1. Low-cost I-V tracer .....	10
I.3.2. Measurement of the PV module temperature and Irradiance .....	14
I.3.3. Emulation of $R_s$ and $R_{sh}$ degradation .....	15
I.3.4. Data acquisition system.....	16
I.4. The distribution of the points on the PV module's I-V curve .....	18
I.4.1. Qualitative analysis of the sensitivity of the five parameters of the single diode model to the number of points on the I-V curve .....	20
I.4.2. Results and Analysis .....	22
I.4.3. Summary of the sensitivity analysis .....	26
I.4.4. Implementation of the LDP in the I-V tracer.....	26
I.5. Calibration and validation of the I-V tracer .....	29
I.5.1. I-V tracer calibration .....	32
I.5.2. I-V tracer validation .....	34
I.5.3. Summary of the validation.....	37
I.6. Elimination of abnormal I-V curves due to over-illumination .....	37
I.6.1. Observation of abnormal curves .....	37
I.6.2. Partial shading detection methods using the I-V curve.....	38
I.7. Conclusion.....	43
References of chapter I.....	55
List of figures of chapter I.....	59
List of tables of chapter I.....	61
Chapter II: Modeling, extraction, and validation of Electrical PV model in healthy cases .....	64

II.1.	Introduction .....	64
II.2.	State of the art on electrical PV model .....	64
II.2.1.	<i>Ideal model</i> .....	67
II.2.2.	<i>Single diode model with series resistance (four parameters)</i> .....	67
II.2.4.	<i>Two diode model (seven parameters)</i> .....	69
II.2.5.	<i>Three diode model (nine parameters)</i> .....	70
II.2.6.	<i>Bishop model</i> .....	70
II.2.6.	<i>Summary of PV model</i> .....	71
II.3.	Description of the SDM five parameters and their variation with environmental operating conditions .....	73
II.3.1.	<i>The photo-generated current (<math>I_{ph}</math>)</i> .....	73
II.3.2.	<i>The diode saturation current (<math>I_0</math>)</i> .....	74
II.3.3.	<i>The series resistance (<math>R_s</math>)</i> .....	75
II.3.4.	<i>Shunt resistance (<math>R_{sh}</math>)</i> .....	75
II.3.5.	<i>The diode ideality factor (<math>n</math>)</i> .....	76
II.3.6.	<i>Summary of parameter model variation with environmental conditions</i> .....	76
II.4.	Parameters extraction methods.....	77
II.4.1.	<i>Analytical approach</i> .....	77
II.4.2.	<i>Numerical approach</i> .....	77
II.4.3.	<i>Metaheuristic approach</i> .....	78
II.4.4.	<i>Hybrid approach</i> .....	78
II.4.5.	<i>Summary of extraction methods</i> .....	78
II.5.	Levenberg-Marquardt optimization algorithm description .....	79
II.5.1.	<i>Implementation in MATLAB</i> .....	79
II.6.	Description and validation of the analytical models .....	82
II.6.1.	<i>The training stage</i> .....	84
II.6.2.	<i>The validation stage</i> .....	95
II.7.	Description and validation of the hybrid PV model.....	97
II.7.1.	<i>Resampling I-V curves of simulation</i> .....	98
II.7.2.	<i>Hybrid PV model validation</i> .....	100
II.8.	Analysis of sensitivity to errors due to variations of PV module temperature ( $T_{pv}$ ) .....	103
II.9.	Conclusion.....	108
	References of chapter II .....	110
	List of figures of chapter II.....	117
	List of tables of chapter II .....	119
	Chapter III: PV panel fault detection and diagnosis.....	122
III.1.	Introduction .....	122
III.2.	Faults in Photovoltaic systems .....	122

III.2.1.	<i>Faults in PV module</i> .....	124
III.2.2.	<i>Classification of defects according to their frequency of occurrence</i> .....	128
III.2.3.	<i>Impact of the defect in terms of power losses</i> .....	130
III.3.	Fault Detection and diagnosis of PV panel .....	132
III.3.1.	<i>Introduction</i> .....	132
III.3.2.	<i>Visual inspection</i> .....	132
III.3.3.	<i>Automatic analysis method based on features analysis</i> .....	133
III.3.4.	<i>Fault detection and diagnosis proposal</i> .....	135
III.4.	Results of fault detection and diagnosis with methods M1 and M2.....	136
III.4.1.	<i>Rs degradation</i> .....	136
III.4.2.	<i>Rsh degradation</i> .....	145
III.4.3.	<i>Partial shading</i> .....	153
III.5.	Conclusion.....	157
	Reference of chapter III.....	159
	List of figures of chapter III .....	162
	List of tables of chapter III .....	164
	General Conclusion .....	165
	Perspectives .....	166
	<i>Appendix: Hybrid PV model based on the single diode with Rs and Rsh model</i> .....	168

## Acknowledgement

Forty-eight months have passed. It is the duration during which I stayed in the Group of Electrical Engineering of Paris (GeePs) and the Laboratory of Signals and Systems (L2S) to carry out my research work, which was both enriching and pleasant, but sometimes stressful. This duration is short or long, depending on the moment we live. I would not have succeeded in crossing this path without the people, and I will try to mention them all on this page. And believe me, this is not "copy and paste," but it comes from the heart.

First of all, I would like to express my deepest appreciation to my Ph.D. supervisors, Prof. Demba DIALLO, Prof. Claude DELPHA, Prof Anne MIGAN-DUBOIS, Prof. Jean Yves LECHENADEC for the trust they have given me by accepting to supervise me for this thesis. I thank them warmly for their support, guidance, and encouragement during my thesis.

Secondly, I would also like to express my sincere gratitude to all the members of my jury, Prof. Eric LABOURE, Prof. Yassine AMIRAT, Prof. Yvan BONNASSIEUX, Prof. Corinne ALONSO, Prof. Pierre-Olivier LOGERAIS, Prof. Zhixue ZHENG for my Ph.D. defense and their constructive comments on my thesis.

I thank the director of the IUT de Cachan, Prof. Francisco De Oliveira Alves, who allowed me to make the experimental test bench and install it at his institution.

Finally, thank you to all the family members who have supported me during these years. Especially, I would like to thank my wife (Chansamone LIEMKEO), who decided to stay in France with me during my Ph.D. work.

## Résumé

Depuis plus de dix ans, une coopération s'est établie entre l'Université Paris-Saclay et la Faculté d'Ingénierie de l'Université Nationale du Laos (FE-NUOL) dans le domaine des énergies renouvelables afin de fournir des systèmes de travaux pratiques aux enseignants et étudiants laotiens dans le domaine du génie électrique. Cette collaboration a pour objectif de développer une pédagogie de l'expérimentation en ingénierie et de faciliter l'électrification des zones isolées à partir de ressources renouvelables (énergie solaire photovoltaïque et hydroélectricité). Au Laos, le taux d'électrification des habitations a progressivement et régulièrement augmenté depuis la fin des années 90. En effet, il a été multiplié par environ cinq sur les 20 dernières années, passant de 15 % en 1995 à environ 73 % en 2010. Entre autres, l'électrification hors réseau utilisant les ressources énergétiques renouvelables locales, c'est-à-dire les rivières et l'énergie solaire, s'est concentrée sur les zones rurales et isolées. C'est pour cette raison que le gouvernement laotien s'est fixé l'objectif ambitieux de fournir de l'électricité à 90 % de la population d'ici 2030 [1].

L'énergie hydroélectrique est utilisée depuis de très longues années au Laos, et le pays dispose de structures de formation (cours d'hydroélectricité en génie électrique à FE-NUOL), ce qui n'est pas le cas pour le photovoltaïque. La création d'un site photovoltaïque pour la formation d'ingénieurs et de techniciens, ainsi que la mise en œuvre d'activités de recherche est donc une priorité pour FE-NUOL. Sa mise en œuvre se fera grâce à la collaboration avec des chercheurs et ingénieurs français.

FE-NUOL et l'Université Paris-Saclay ont signé un accord pour créer le premier laboratoire de recherche au Laos, dans le domaine du génie électrique, afin de soutenir les enseignants laotiens dans leurs activités d'enseignement et de recherche.

La mise en place d'un laboratoire est un objectif ambitieux qui doit être envisagé à long terme et réalisé étape par étape. Le thème principal du laboratoire est l'optimisation des réseaux intelligents. Un réseau intelligent est un réseau énergétique autonome et intelligent composé de plusieurs sources d'énergies renouvelables, de dispositifs de stockage d'énergie, de dispositifs de contrôle et de communication pour la gestion et le suivi de l'énergie.

Dans ce cadre, cette thèse de doctorat est consacrée au développement de deux systèmes photovoltaïques isolés identiques, l'un en France et l'autre au Laos. Le sujet principal de la thèse est d'évaluer la fiabilité et l'efficacité des modules photovoltaïques à l'aide d'un système de

surveillance de l'état de santé peu coûteux mais efficace. Le travail a commencé en France pour bénéficier de l'expertise locale avant le transfert de compétences.

Après une baisse en 2020, la demande d'électricité devrait augmenter de plus de 1000 térawattheures (TWh) en 2021, bien au-delà des niveaux pré-pandémiques. En 2020, la croissance sans précédent des énergies renouvelables a permis de réduire la consommation d'énergie, ce qui s'est traduit par une augmentation significative de 28 % de la production d'énergie renouvelable et une pression sur la production non renouvelable. En conséquence, les émissions mondiales du secteur de l'électricité ont diminué d'environ 3 %, soit la plus forte baisse jamais enregistrée. En 2021, une nouvelle augmentation était attendue, mais elle sera bien inférieure à l'augmentation de la demande, comme le montre la figure 1 [2].

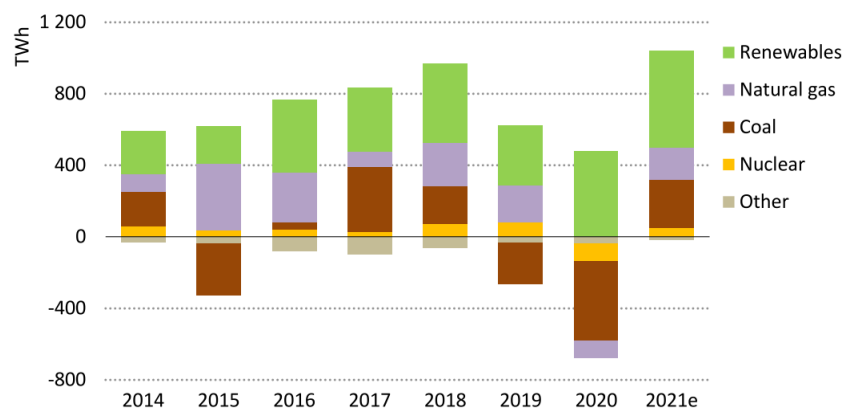


Fig. 1 : Évolution de la production mondiale d'électricité, 2014-2021

Afin de satisfaire les besoins énergétiques futurs et de réduire l'impact environnemental, l'utilisation d'énergies propres et renouvelables a récemment été reconsidérée, en particulier l'énergie solaire. Le solaire photovoltaïque a connu une nouvelle année record, avec de nouvelles installations atteignant 139 GW, ce qui porte le total mondial à 760 GW, y compris la capacité en réseaux et en sites isolés, comme le montre la figure 2 [3].

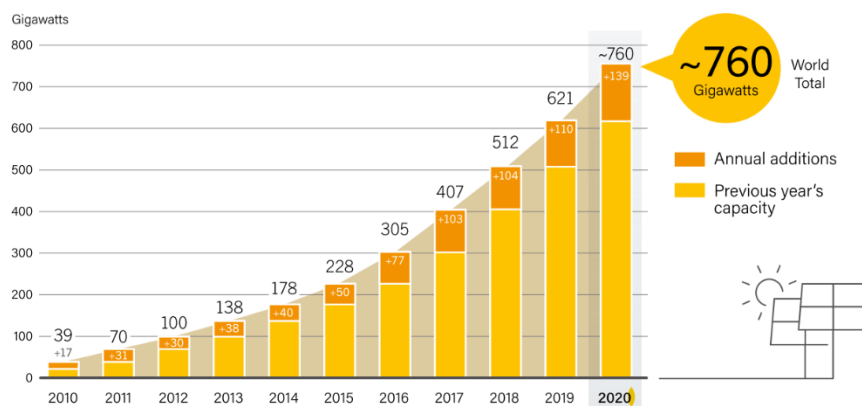


Fig.2 : Capacité mondiale et augmentation annuelle du solaire PV



Grâce aux différents facteurs stimulants (réduction des coûts de production et politiques de soutien), le retour sur investissement des installations photovoltaïques s'est amélioré. Cependant, comme tout autre processus industriel, une installation photovoltaïque peut être sujette à divers défauts et anomalies, qui dégradent les performances du système ou, pire, arrêtent la production. Par conséquent, la productivité peut être considérablement affectée en réduisant la rentabilité en raison de coûts de maintenance plus élevés.

Dans les centrales solaires, les panneaux photovoltaïques sont les éléments clés. Ils sont sujets à des défauts intrinsèques (jaunissement, points chauds, par exemple) ou extrinsèques (ombrage, encrassement, rupture de cellules) qui doivent être diagnostiqués à leur stade le plus précoce pour atténuer les pertes de production et prévenir les dommages irréversibles. Les méthodes de détection et de diagnostic des défauts (FDD) sont nécessaires pour surveiller en permanence le système étudié. Les approches FDD peuvent être décomposées en quatre étapes : modélisation, prétraitement, choix et analyse des caractéristiques. La modélisation (construction de la connaissance) est basée sur des modèles physiques ou/et des données. Plusieurs techniques peuvent être utilisées pour le prétraitement dont l'objectif est de préparer l'extraction des caractéristiques les plus sensibles aux défauts, qui seront analysées pour détecter et classer les défauts.

La thèse a pour objectif de développer un système de surveillance de l'état de santé basé sur l'analyse des courbes I-V et sur le modèle analytique des modules PV. En effet, les courbes I-V contiennent des informations utiles sur l'état de santé des modules PV. La solution doit être efficace mais pas chère pour faciliter le déploiement dans les zones à faibles revenus.

Le manuscrit est structuré en trois chapitres.

Le chapitre 1 est consacré au développement de la plateforme expérimentale. Elle comprend les capteurs (irradiance, courant, tension, température), les systèmes d'acquisition de données et de communication, l'émulateur de défauts, et le traceur I-V. Les principaux sujets abordés dans ce chapitre sont : la structure et le fonctionnement du traceur I-V à faible coût, l'optimisation du nombre et de la distribution des points mesurés sur la courbe I-V. Le chapitre décrit également la méthodologie pour calibrer et valider le traceur I-V. Le chapitre se termine par la description du prétraitement indispensable des courbes I-V mesurées pour éliminer les courbes anormales dues aux effets de sur-illumination sur le panneau PV.

Dans le chapitre 2, nous présentons le modèle analytique du module PV. Sur la base de la synthèse de la littérature, nous avons retenu le modèle à une diode caractérisé par ses cinq paramètres. Nous avons implémenté l'algorithme de Levenberg-Marquardt pour extraire les

paramètres du modèle à partir de la courbe I-V. Les modèles analytiques des paramètres ont été validés avec des données expérimentales mesurées sur des modules PV sains à travers une méthodologie en quatre étapes : les deux premières étapes sont consacrées à l'apprentissage, tandis que les deux dernières sont destinées à la validation. Ces modèles analytiques sont combinés avec le modèle numérique dans Matlab-Simulink pour construire le modèle hybride qui sera utilisé comme référence pour générer des courbes I-V saines.

Le chapitre 3 est consacré au développement de deux méthodes de détection et diagnostic des défauts basées sur les caractéristiques de la courbe courant-tension (I-V). Dans un premier temps, une revue de la littérature est réalisée sur les différents défauts d'un système PV. La deuxième partie du chapitre présente les méthodes de détection de défauts, leur mise en œuvre, ainsi que les résultats de simulation et expérimentaux pour les trois cas de défauts que nous avons étudiés : dégradation de la résistance série, dégradation de la résistance shunt, et ombrage partiel.

Une conclusion et des perspectives clôturent le manuscrit.

### Contribution

Dans notre étude, un traceur embarqué à faible coût est développé et optimisé pour mesurer les vingt-six points de la courbe I-V en moins de 0,2 s afin de minimiser la durée de l'interruption de la production électrique. Le traceur proposé est validé avec un analyseur du commerce. Les données expérimentales sont utilisées pour valider le modèle analytique du module PV. Ce modèle s'appuie sur les cinq paramètres ( $I_{ph}$ ,  $R_s$ ,  $R_{sh}$ ,  $I_0$  and  $n$ ) du circuit électrique à une diode. Il est combiné au modèle numérique de Matlab-Simulink pour mettre en place le modèle hybride qui sera utilisé comme référence pour le diagnostic. Ce modèle est validé avec une erreur relative inférieure à 3% pour plusieurs conditions environnementales (éclairage et température). Les données mesurées sont utilisées pour extraire les cinq paramètres du modèle électrique équivalent ainsi que les principales caractéristiques de la courbe I-V (courant ( $I_{pv}$ ), tension ( $V_{pv}$ ), tension de circuit ouvert ( $V_{oc}$ ), courant de court-circuit ( $I_{sc}$ ) et puissance maximale ( $P_{mpp}$ )).

Les courbes I-V mesurées sont aussi utilisées pour évaluer les deux méthodes de diagnostic des défauts notées M1 et M2. M1 s'appuie sur le modèle analytique des cinq paramètres ( $I_{ph}$ ,  $R_s$ ,  $R_{sh}$ ,  $I_0$ ,  $n$ ) alors que M2 utilise les cinq caractéristiques ( $I_{pv}$ ,  $V_{pv}$ ,  $P_{mpp}$ ,  $V_{oc}$ ,  $I_{sc}$ ) et le modèle hybride pour générer les courbes I-V de référence. Les résidus sont calculés entre les indicateurs des défauts extraits des mesures expérimentales et ceux issus des courbes de

référence. Trois cas de défaut ont été étudiés : dégradation de la résistance série  $R_s$ , dégradation de la résistance shunt  $R_{sh}$  et l'ombrage partiel. Les résultats basés sur des données expérimentales obtenues pour différentes températures et éclairagements ont montré que la dégradation des résistances série et shunt et l'ombrage partiel étaient mieux détectés par les caractéristiques qu'avec les paramètres.

- 
- [1] “Annual Reports – EDL-GENERATION PUBLIC COMPANY.” [Online]. Available: <https://edlgen.com.la/annual-reports/?lang=en>. [Accessed: 25-July-2022].
- [2] IEA, “World Energy Outlook 2021,” Technical Report, 2021. [Online]. Available: <https://www.iea.org/reports/world-energy-outlook-2021> [Accessed: 25-July-2022]
- [3] REN21, “Renewables 2021 Global Status Report”, Technical report of the Renewable Energy Policy Network for the 21st century, Paris, 2021

## General introduction

### *Background and motivation*

For more than ten years, cooperation has been established between Université Paris-Saclay and the Faculty of Engineering of the National University of Laos (FE-NUOL) in renewable energies to provide practical work systems to Laotian teachers and students in the field of electrical engineering. This alliance aims to promote a pedagogy of experimentation for Laotian engineering students and facilitate the electrification of isolated areas using solar and hydroelectric energy. In Laos, the household electrification rate gradually and steadily increased by the end of the 90s. Indeed, it rose nearly fivefold during the last 20 years, from 15 % in 1995 to around 73 % in 2010. Among others, off-grid electrification using local renewable energy resources, i.e., rivers and solar power, has been focused on rural, isolated areas. Therefore, the Government of Laos has set an ambitious goal of providing electricity to 90% of the population by 2030[1]. Hydroelectric energy has been used for many years in Laos, and the country has training facilities (hydroelectric course in Electrical Engineering at FE-NUOL), which is not the case for photovoltaics. Creating a photovoltaic site for the training of engineers and technicians, as well as the implementation of research activities is, therefore, a priority for FE-NUOL. Its implementation will be done with the support of French researchers and engineers.

FE-NUOL and the Université Paris-Saclay have signed an agreement to create the first research laboratory in Laos, which is focused on Electrical Engineering to support the Laotian teachers in their teaching and research activities.

A laboratory setting is an ambitious objective that should be envisaged in the long term and done step by step. The main topic of the laboratory is the optimization of smart grids. A smart grid is an autonomous and intelligent energy network composed of several renewable energy sources, energy storage devices, control and communication devices for energy management and monitoring.

In this framework, this Ph.D. thesis is devoted to develop two identical isolated photovoltaic-based smart grids, one in France and one in Laos. The Ph.D.'s main topic is to assess the PV modules' reliability and efficiency with low-cost but effective health monitoring. The work started in France to benefit from the local expertise before the transfer of competence.

*Solar Energy*

Following a decline in 2020, power demand is predicted to rise by over 1000 terawatt-hours (TWh) in 2021, well beyond pre-pandemic levels. In 2020, unprecedented growth in renewables coincided with a drop in energy consumption, resulting in a significant increase of 28% in renewable energy generation and a strain on non-renewable output. Consequently, worldwide power sector emissions fell by roughly 3%, the highest decrease on record. In 2021, another record increase in renewable energy was expected, but it will fall well short of the increase in demand, as seen in *Fig.1* [2].

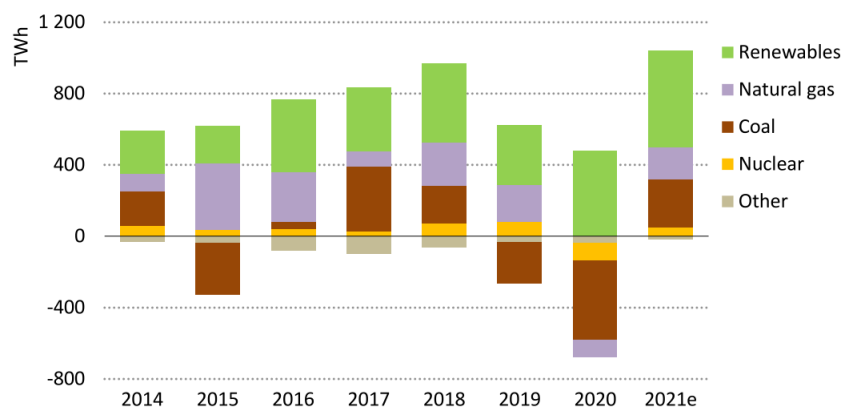


*Fig.1 : Changing in global electricity generation, 2014-2021*

In order to satisfy future energy needs, and reduce environmental impact, the use of clean, renewable energy has recently been reconsidered, particularly solar energy. Solar PV experienced another record-breaking year, with new installations reaching as high as 139 GW, bringing the worldwide total to 760 GW, including both on-grid and off-grid capacity. These early worldwide figures are unreliable, and the amount of uncertainty grows year after year, as seen in *Fig.2* [3].

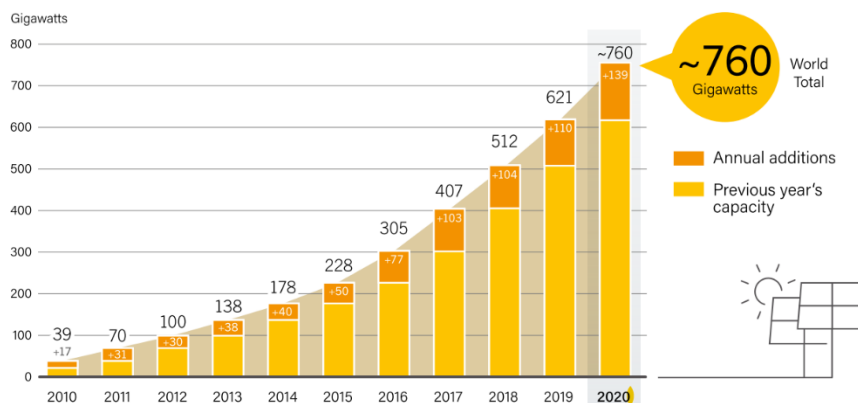


*Fig.2 : Solar PV Global capacity and annual addition, 2010-2020*

Thanks to the different stimulating factors: reduction of production costs and support policies. These stimulating factors make the return on investment of photovoltaic installations more and more enjoyable. However, like all other industrial processes, a photovoltaic system can be subject to various defects and anomalies, which degrade the system performance or, worse, stop production. Consequently, productivity can be significantly affected by reducing profitability due to higher maintenance costs.

In solar power plants, the PV panels are the key components. They are prone to intrinsic defects (yellowing, hotspots, for example) or extrinsic (shading, soiling, cell breakage) that should be diagnosed at their earliest stage to mitigate production losses, and prevent irreversible damages. Fault detection and diagnosis (FDD) methods are required to monitor continuously the system under study. FDD approaches can be decomposed in four steps; modelling, preprocessing, features selection, and features analysis. The modelling (knowledge building) is based on physical models or/and data. Several techniques can be used for the preprocessing whose target is to prepare the extraction of the most sensitive features, which will be analyzed to detect and classify the faults.

I-V curves embed useful information on the health status of PV modules. This thesis aims to develop a health monitoring based on the analysis of I-V curves, and the analytical model of PV modules. The solution should be efficient but not expensive to ease the deployment in low income areas.

### *Thesis outline*

The manuscript is structured in three chapters.

Chapter 1 is devoted to the development of the experimental platform. It includes the sensors (irradiance, current, voltage, temperature), the data acquisition and communication systems, the faults emulator, and the I-V tracer. for emulating faults in PV installation. The main topics in this chapter are: the structure and the setting of the low-cost I-V tracer, the optimization of the number and distribution of the points on the I-V curve. The chapter also describes the methodology to calibrate and validate the I-V tracer. The chapter is closed with the description of the mandatory preprocessing of the measured I-V curves to eliminate abnormal curves due to over-illumination effects on the PV panel.

In chapter 2, we present the analytical model of the PV module. Based on the literature review, we have retained the single diode model characterized by its five parameters. We have implemented the Levenberg-Marquardt algorithm to extract the model parameters from the I-V curve. The analytical models of the parameters have been validated with experimental data

measured on healthy PV modules through a four-step methodology: the first two steps are devoted to the training, while the last two are for validation. These analytical models are combined with the numerical model in Matlab-Simulink to build the hybrid model that will be used as a reference to generate healthy I-V curves.

Chapter 3 is dedicated to the development of two fault detection and diagnosis methods based on the characteristics of the current-voltage (I-V) curve. First, a literature review is conducted on the various faults in a PV system. The second part of the chapter will present the fault detection methods, their implementation, and the simulation and experimental results for the three fault cases we have studied: series resistance degradation, shunt resistance degradation, and partial shading.

A conclusion and future works close the manuscript.

### *Contribution*

In our study, two FDD methodologies have been evaluated. The first one uses the parameters of the single diode model (SDM) as fault features. The second one uses the current and voltage of the PV module, and the extracted characteristics; PV current ( $I_{pv}$ ), PV voltage ( $V_{pv}$ ) maximum power ( $P_{mpp}$ ), Short circuit current ( $I_{sc}$ ) and open circuit voltage ( $V_{oc}$ ) as fault features.

The main contributions are:

- Design and implementation of a low-cost embedded I-V tracer with a logarithmic distribution of the points (LDP) on the I-V curve to reduce the measurement time,
- Proposal of a four-step methodology to validate the PV model: the first two steps for training and the last two for validation,
- Experimental validation of the analytical equations used to calculate the parameters of the SDM,
- Evaluation of series or shunt resistance degradation and partial shading using either SDM parameters or characteristic points of I-V curves as fault features under a wide variety of environmental conditions.

---

[1] “Annual Reports – EDL-GENERATION PUBLIC COMPANY.” [Online]. Available: <https://edlgen.com.la/annual-reports/?lang=en>. [Accessed: 25-July-2022].

[2] IEA, “World Energy Outlook 2021,” Technical Report, 2021. [Online]. Available: <https://www.iea.org/reports/world-energy-outlook-2021> [Accessed: 25-July-2022]

[3] REN21, “Renewables 2021 Global Status Report”, Technical report, “of the Renewable Energy Policy Network for the 21st century, Paris, 2021

# Chapter I

## Development of the experimental test bench

### Table of Contents

Chapter I: Development of the experimental test bench .....	3
I.1. Introduction .....	3
I.2. I-V tracer: state-of-the-art.....	3
I.2.1. Variable load resistance .....	3
I.2.2. Electronic load technique .....	4
I.2.3. Capacitive load technique .....	5
I.2.4. Four-quadrant power supply.....	6
I.2.5. DC-DC converter .....	7
I.3. Experimental Test Bench .....	9
I.3.1. Low-cost I-V tracer .....	10
I.3.2. Measurement of the PV module temperature and Irradiance .....	14
I.3.3. Emulation of $R_s$ and $R_{sh}$ degradation .....	15
I.3.4. Data acquisition system.....	16
I.4. The distribution of the points on the PV module's I-V curve .....	18
I.4.1. Qualitative analysis of the sensitivity of the five parameters of the single diode model to the number of points on the I-V curve .....	20
I.4.2. Results and Analysis .....	22
I.4.3. Summary of the sensitivity analysis .....	26
I.4.4. Implementation of the LDP in the I-V tracer.....	26
I.5. Calibration and validation of the I-V tracer .....	29
I.5.1. I-V tracer calibration .....	32
I.5.2. I-V tracer validation .....	34
I.5.3. Summary of the validation.....	37
I.6. Elimination of abnormal I-V curves due to over-illumination .....	37
I.6.1. Observation of abnormal curves .....	37
I.6.2. Partial shading detection methods using the I-V curve.....	38
I.7. Conclusion.....	43
References of chapter I.....	55



Chapter I: Development of the experimental test bench

---

List of figures of chapter I..... 59  
List of tables of chapter I..... 61

## Chapter I: Development of the experimental test bench

### I.1. Introduction

Monitoring PV plants is critical to guarantee high output power availability and reliability and minimize maintenance costs. The I-V curve is recognized as one of the most used information to retrieve the health status of PV modules. The I-V curve is measured with an I-V tracer. Besides the current and the voltage, the I-V tracer also measures environmental data. The most popular is the irradiance, and the temperature of the PV module. There are several commercial products already available in the market.

Although they have proven effective in monitoring PV modules, I-V tracers are not widely used mainly because of their cost and because their operation requires a momentary interruption in production. Therefore, if we want to promote the deployment of I-V tracers at the module level in a PV plant, we need to offer a solution that is low cost and minimizes the measurement time.

The objective of this chapter is to present the experimental test bench developed for the health monitoring of a PV module. Section I.2 reviews the state-of-art of I-V tracers. Section I.3 presents the low-cost I-V tracer, the electrical circuit to emulate the degradation of series and shunt resistances, and the data acquisition system. The distribution of points on the I-V curve is presented in Section I.4. Section I.5 is devoted to calibrate and validate the I-V tracer. Section I.6 presents the preprocessing of the I-V curve to eliminate the over-illumination issue. Finally, Section I.7 closes the chapter.

### I.2. I-V tracer: state-of-the-art

The operating point of the PV module must be varied between short-circuit and open-circuit operation to measure the I-V curve. The most common method is to use a variable load, either a resistor, a controllable electronic load, a capacitive load, a four-quadrant power supply or a DC-DC converter [1][2].

#### *I.2.1. Variable load resistance*

The variable load resistance technique is illustrated in [Fig.I.1](#) [3]. The value of  $R$  is adjusted manually from zero to infinity while the current and voltage are measured with a multimeter [4]. Although the method is simple, it is best suited to low-power modules to

minimize Joule losses. Moreover, the short-circuit current ( $I_{sc}$ ) can not be reached, and the reverse bias characteristics cannot be identified [2].

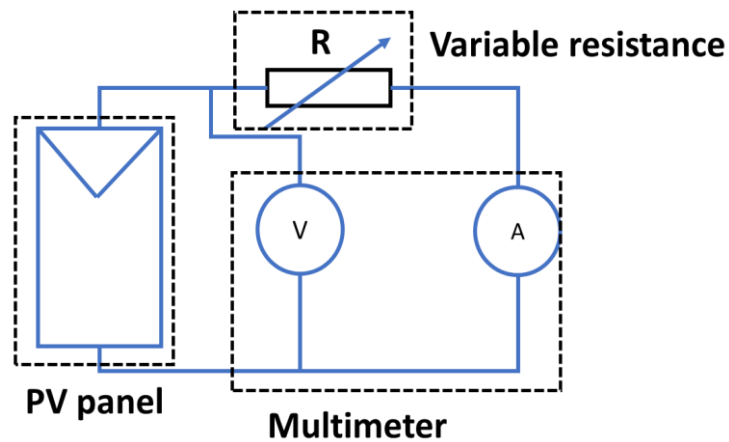


Fig.I.1: Variable load resistance technique

### I.2.2. Electronic load technique

The schematic circuit of the I-V tracer with a power switch (e.g., a MOSFET) used as the load is shown in Fig.I.2. The operating point of the PV panel moves along the I-V characteristic curve as shown in Fig.I.3 thanks to the variation of the gate voltage ( $v_{GS}$ ) with a PWM control signal. It is shown that this technique employed to measure the I-V characteristics of PV panels under real operation conditions is reasonable. The result obtained shows the capacity for monitoring the degradation of the PV characteristics accurately, at low cost, and with flexibility [5]. Nevertheless, if the array's voltage is greater than 1000 V, the power switches need to be connected in series, which requires an equalizing circuit [6].

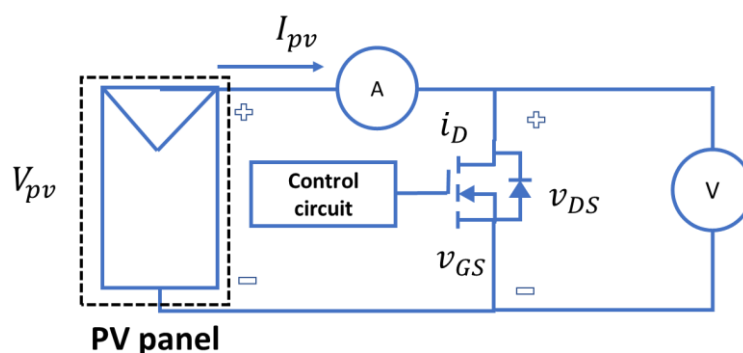


Fig.I.2: Electronic load technique for the I-V tracer

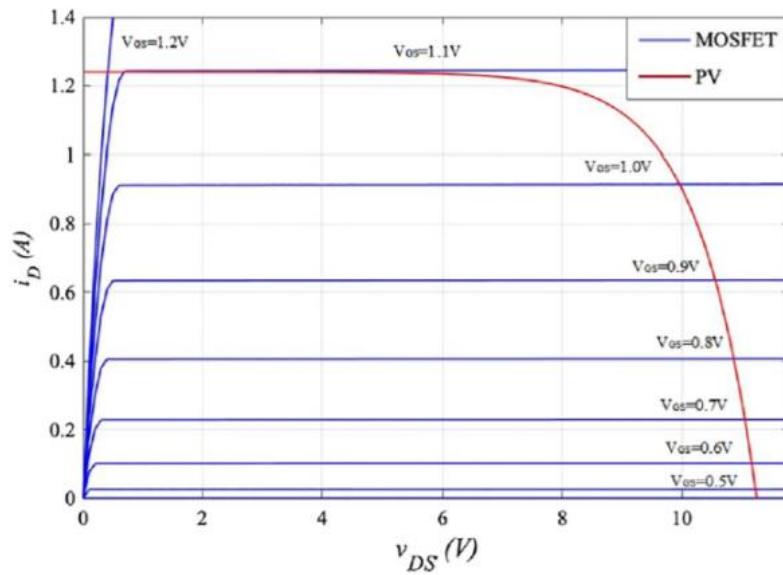


Fig.I.3: The I-V curve and the MOSFET characteristics [2]

The disadvantage of this technique is that a heatsink is required to dissipate the heat from the transistor. Then, the size and weight of the tracer are increased. To conclude, this method is more suitable for low-power applications.

### I.2.3. Capacitive load technique

Fig.I.4 shows the schematic circuit with the capacitive load and the discharge resistance. When S2 is turned OFF and S1 is turned ON, the voltage across the capacitor rises progressively, and the current reduces as the capacitor charge increases. When the charge is fully completed, the current delivered by the PV module drops to zero, and the device works under the open circuit status.

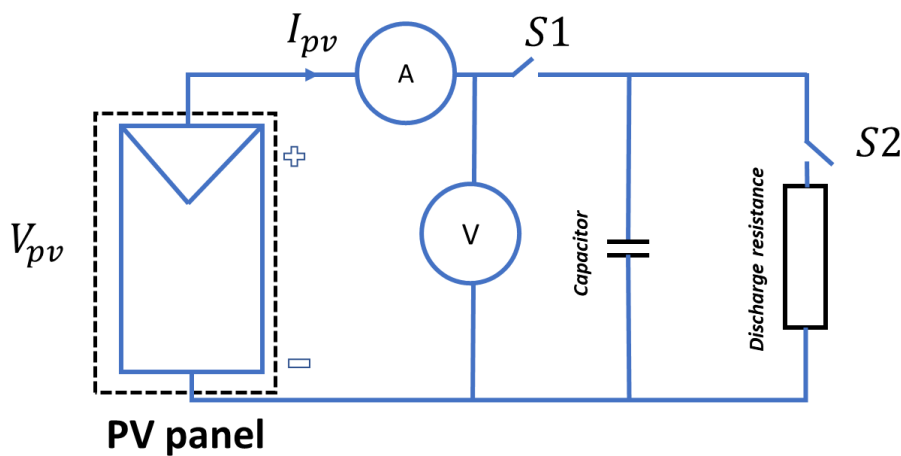
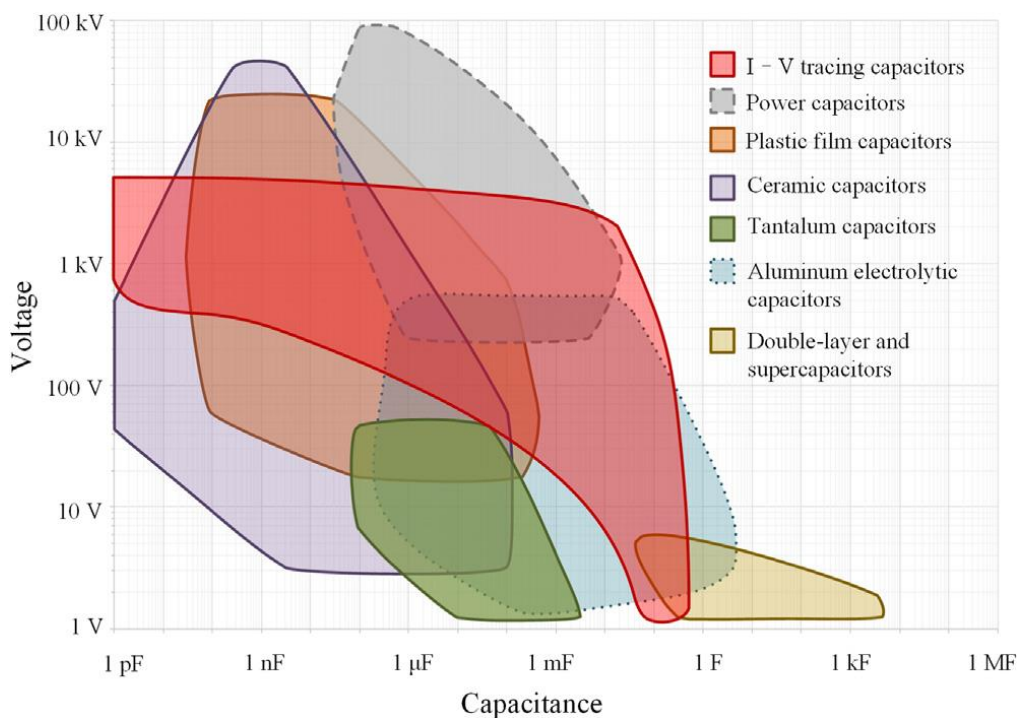


Fig.I.4: Capacitor load technique for I-V tracer

High-quality capacitors (with low Equivalent Series Resistance) are preferable. The capacitor bank may be sized to fit the measurement's duration and resolution's requirements [7]. According to the literature, the capacitive load technique is suitable for PV arrays with an open-circuit voltage of up to 500 V and a maximum short-circuit current of 20 A [8]. It is also used to determine the global MPP [9]. However, the capacitor bank's size and cost will increase for high-power applications. Furthermore, the duration of the measurement strongly depends on the PV parameters and the charging behavior of the capacitors. *Fig.1.5* shows the different technologies and voltage ranges of several major PV panel manufacturers (e.g., LG Energy, SunPower, REC, Winaico, and Q-Cells).



*Fig.1.5: I-V capacitor: technologies and voltage ranges [2]*

#### 1.2.4. Four-quadrant power supply

A four-quadrant power supply can provide and absorb power; it is bidirectional in current and voltage. It can operate as a variable load. The system can be operated in the four quadrants, as shown in *Fig.1.6*. Even if the PV panel operates in the first quadrant, the points in the second and fourth quadrants might be a useful diagnostic tool for detecting mismatching, such as one or more partly shaded cells when connected in series [10].

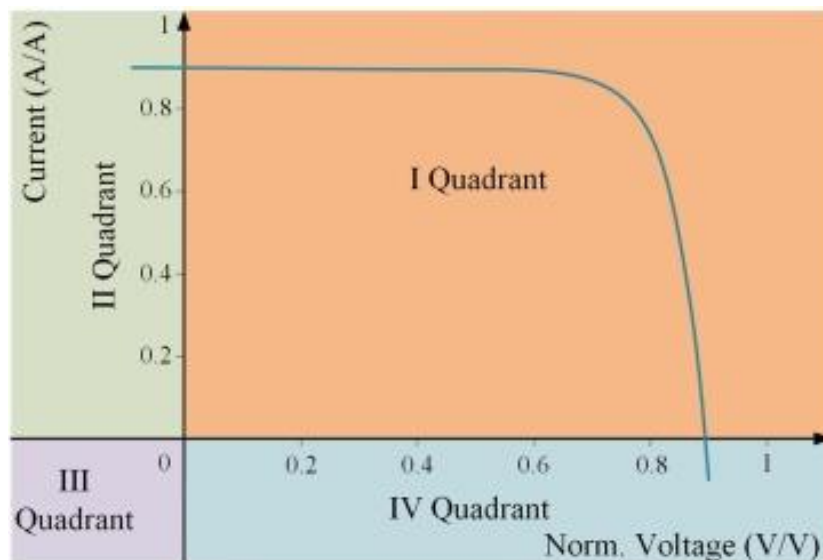


Fig.I.6: I-V curve and four-quadrant power supply

The output of a four-quadrant power supply can be varied by a reference input signal or controlled to sweep a range of values, as seen in Fig.I.7.

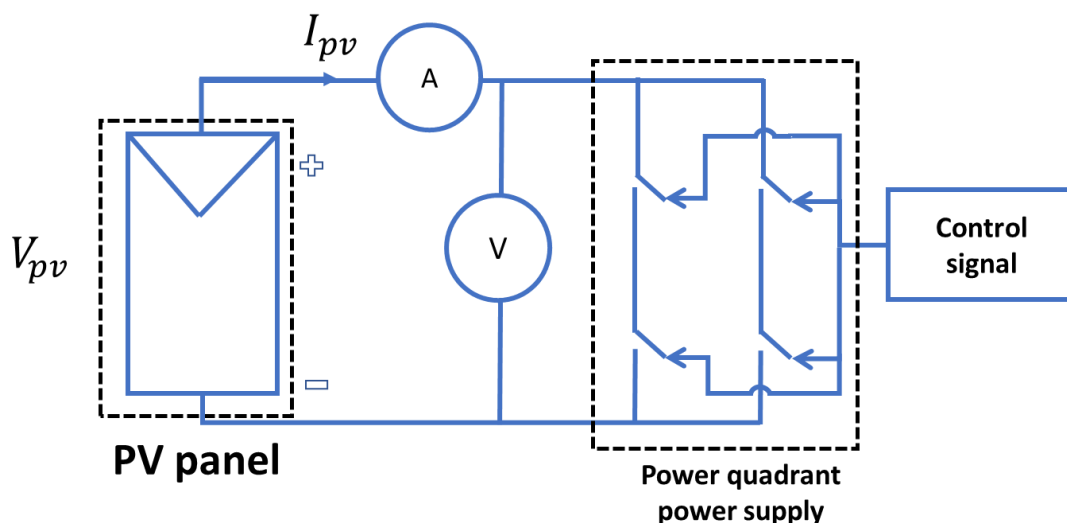


Fig.I.7: Basic circuit for an I-V tracer using the four-quadrant power supply technique

Different methods have been developed to regulate the voltage of the four-quadrant power supply [6, 13, 14]. This technique is limited to very low-power applications (< 1 kW) mainly because of its cost and size. Therefore, it is mostly used for laboratory tests.

### 1.2.5. DC-DC converter

In several applications, the capability of DC-DC converters to simulate a variable resistor was investigated and evaluated. The DC-DC converter connected to the load resistance  $R_L$ , is controlled with a variable duty cycle. As a consequence, the operating point moves along

the I-V curve of the PV module. The circuit is displayed in *Fig.I.8*. One disadvantage of the DC-DC converter technique is the generation of voltage and current ripples.

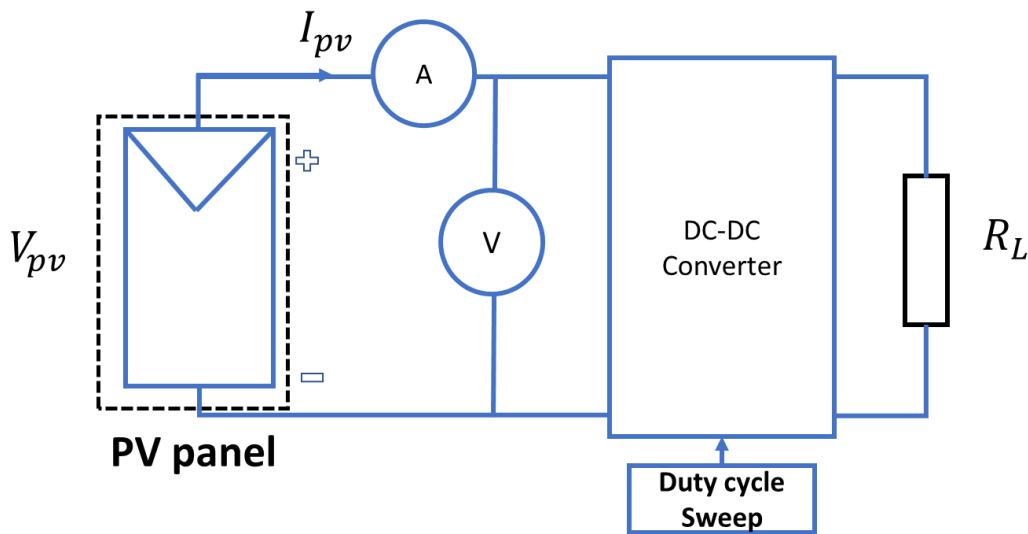


*Fig.I.8: DC-DC converter used as an I-V tracer*

The various topologies of DC-DC converters for measuring I-V curves were investigated. From the survey of the literature, several conclusions can be drawn:

- Buck-Boost-Derived structures are the only ones that enable a full curve sweep,
- Buck structures do not enable tracing curve points near  $I_{sc}$ , but Boost structures do not allow tracing of curve points near  $V_{oc}$ ,
- The reproduction of the I-V curve is obtained with reduced ripples with SEPIC (Single-Ended Primary Inductance Converter), and Cuk structures. According to experimental data, these topologies are optimum for this application [11].

A low-cost DC-DC Cuk converter was designed to measure I-V curves of PV modules up to 300W; the maximum values of open-circuit voltage and short circuit current are 50 V and 10A, respectively. The tracer was tested under different operating conditions, and the findings were compared to those of a commercial device. Even with simple electronic control circuitry and low-cost (265\$ per unit), low-resolution, it has exhibited sufficient accuracy [12]. In another study, a boost bidirectional DC-DC converter was employed to measure the I-V curves of a solar generator. These I-V curves were subsequently used to evaluate solar inverters by simulating these generators. A 15 kV prototype was developed and evaluated under real environmental conditions [17, 18]. Compared to its competitors, the technique using DC-DC converter has the best accuracy, sweep speed, maximum rating, and resolution performance. Furthermore, it might represent a future trend in I-V curve tracers since control techniques can

be applied to produce more stable and precise data. However, there are still challenges to fulfill market expectations in terms of volume and cost [2].

The comparison of the main techniques was done in [14], based on the following features: flexibility, fidelity, and response time to trace the curve, complexity, implementation cost, and application. The results are shown in *Table I.1*. The findings demonstrate that the electronic, capacitive, and DC-DC converter approaches have high fidelity, complexity, and applicability for PV cells, modules, and arrays. The DC-DC converter offers higher flexibility.

*Table I.1: Comparison of the I-V tracers [14]*

Method/Criteria(*)	Flexibility	Fidelity	Respond times	Cost	Complexity	Resolution	Applicability
Variable resistance	Medium	90.5%	11s	15.42\$	Low	247 points	Cells/Low power modules
Electronic load	Low	99%	22s	6.33\$	Medium	730 points	Cells/module/Array
Capacitive load	Low	98.8%	43s	12.44\$	High	747 points	Cells/modules/ low power array
DC-DC converter	High	98.1%	35s	15.98\$	High	70 points	Cells/modules/arrays

(\*)

- **Flexibility:** It addresses the capability of drawing the I-V curve from a certain point and drawing only specific areas of the curve. Flexibility is classified as high, medium, and low,
- **Fidelity:** Evaluates the error between the measured I-V curves and the reference curves obtained from the simulation,
- **Response time:** Refers to the measurement time of I-V curve unit in seconds,
- **Cost** of the microcontrollers and electronic parts used to implement the PV tracer,
- **Complexity:** refers to method implementation technique, considering the circuit designing, programming, etc. it is classified by high, medium, and low,
- **Resolution:** refers to the number of points on I-V curve,
- **Applicability:** refers to the applicability of the tracing I-V curve in the different level of application such as PV cells, modules, or arrays.

The I-V tracer based on a DC-DC converter was selected for our research based on the literature study. The next section will detail the proposal of a low-cost embedded I-V tracer. A logarithmic distribution of the points (LDP) on the I-V curve is selected to reduce the measurement time.

### I.3. Experimental Test Bench

The experimental test bench was installed in the Institut Universitaire de Technologie de Cachan (IUT de Cachan), Université Paris-Saclay. The simplified schematic diagram of the experimental system is shown in *Fig.I.9*. The main experimental setup consists of the measurement devices such as a low-cost I-V tracer, a PV module temperature sensor TC 74, a reference cell to measure the irradiance in the plane of area. It also includes a fault emulator of series ( $R_s$ ), and shunt ( $R_{sh}$ ) resistances degradation with several fault levels. A data acquisition



system (DAQ) described in more detail in section I.3.4, transfers the measurements stored in an Excel® file.

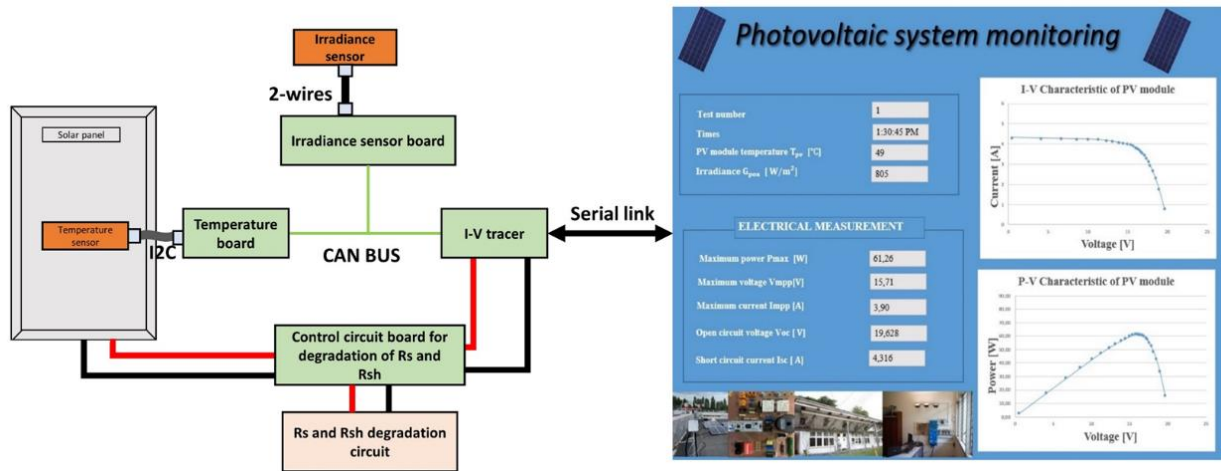


Fig.I.9: Schematic diagram of the testbed

### I.3.1. Low-cost I-V tracer

The proposed I-V tracer is designed to characterize the I-V curves of the PV module. The device installed on the back of the PV module allows measurement under real operating conditions. The PV module under test is of Type A (See Table.I.2); it consists of two strings, each one composed of 18 cells with a bypass diode.

Table.I.2: Characteristics under Standard Test Conditions (STC)

Maximum Power ( $P_{mp}$ )	87 W (+10%/-5%)
Maximum Power Voltage ( $V_{mp}$ )	17.4 V
Maximum Power Current ( $I_{mp}$ )	5.02 A
Open Circuit Voltage ( $V_{oc}$ )	21.7 V
Short Circuit Current ( $I_{sc}$ )	5.34 A
Temperature Coefficient of $V_{oc}$	-0.37 %/°C
Temperature Coefficient of $I_{sc}$	0.038 %/°C

Our first objective is to develop a PV module's low-cost I-V tracer. This will facilitate its deployment in a power plant consisting of several modules. The following PV module characteristics are retained for the design:  $P_{max} = 100$  W,  $I_{sc} = 10$  A,  $V_{oc} = 30$  V. Therefore, we opted for low-cost electronic equipment (especially the microcontroller, and the sensors) as follows:

- Microcontroller Nucleo 32 (model f303K8 with 32 bits, 72 MHz, 64kB of flash memory, and 16kB SRAM memory, with 12 channels of 12bits A/D converters). It is inexpensive and integrated with the CAN bus,

- PV Panel Isolation: two low-voltage electric relays are used to disconnect the PV panel during the measurement,
- Current measurement: shunt resistance [20],
- Voltage measurement: resistive voltage divider [22],
- Temperature measurement: TC 74 sensor.

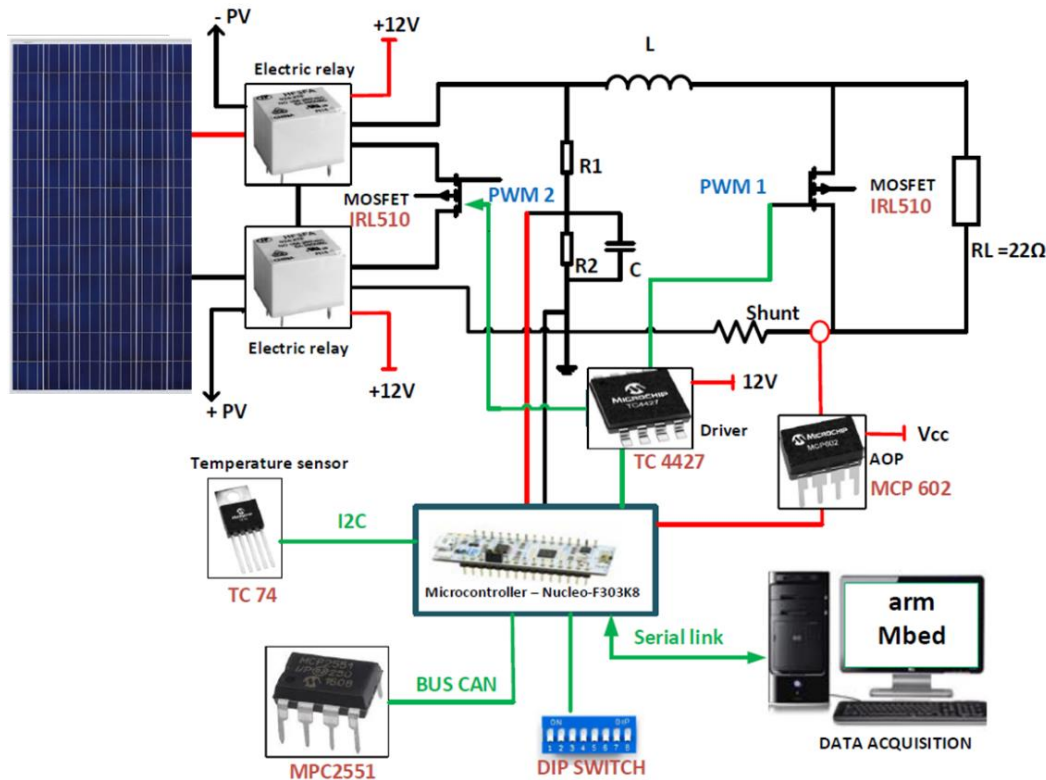


Fig.I.10: Main circuit design

The developed I-V tracer is shown in Fig.I.10. The TC74 sensor is used to measure the temperature of the PV module, which is transferred to the microcontroller through an I2C bus. A CAN transceiver MCP2551 allows communication between the different electronic boards and the other CAN transceivers in the system. The IP address of the I-V tracer can be accessed using the dip switch. Mbed online compiler is used to write and upload the code. The driver TC4427 controls the two MOSFET IRL350s, one of which is used to control the two electric relays and the other one to change the resistive load. The distribution of the points on the I-V curve is used to generate the duty cycle to control the load. Finally, the I-V characteristics and temperature are transferred to the computer via a serial link. The cost of the proposed I-V tracer is estimated at 35€/unit. The comparison with several commercially available I-V tracers is displayed in Table.I.3.

Table.I.3: Comparison with commercially available I-V tracers

Type	Response time	Cost (€)	Resolution	Acquisition	Application
Proposed I-V tracer	181 ms	35	26 points	Auto&Cont	Module
FTV 2000 IV tracer [15]	-	3650	500 points	Manual	Module
I-V 500W tracer [16]	-	4300	128 points	Manual&Auto	Module/String/Array
Electronic load Model 63600 series [17]	2 $\mu$ s to 40ms	> 4000	1- 4096 points	Manual&Auto	Module/String/Array
MP 11 IV checker [18]	5 s	-	400points	Manuel&Auto	Module
Huawei Smart I-V tracer Diagnosis [19]	1 s	-	128 points	Manual&Auto	Module/ String/Array
Solmetric PV analyzer I-V curve tracer [20]	0.05-2s	5690-11483	100 to 500 points	Manuel&Auto	Module/ String

- *Electric relay*

The I-V tracer must be first isolated from the PV system to ensure the efficiency of the PV characteristic. Two electric relays are presented in Fig.I.11 to provide electrical isolation. The relay is disconnected from the PV system when a 12 VDC is applied to the coil. These coils are activated by connecting one side to 12V and the other one to the drain of an IRL530. This one has its source connected to GND, so when we provide a 12V signal to the transistor's gate, it turns on, allowing the coils to switch their relays.

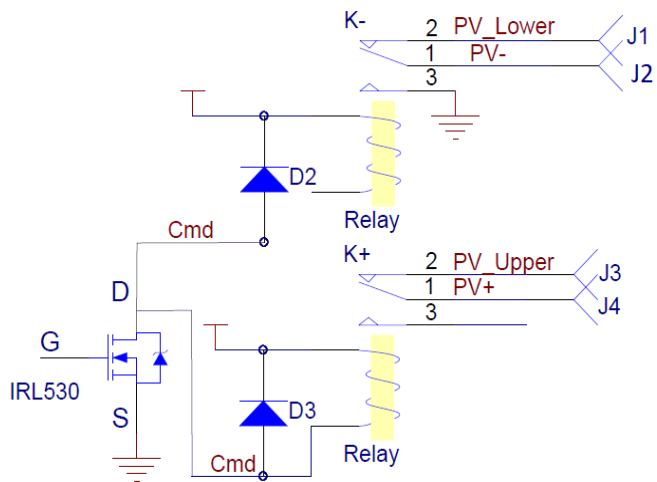


Fig.I.11 : Electric relay

- *load resistance ( $R_L$ )*

Fig.I.12 shows the load resistance circuit, where  $L$  is an inductance used to reduce the current ripples. The load resistance and the MOSFET are connected in parallel. The MOSFET works with a 50 kHz PWM signal. In

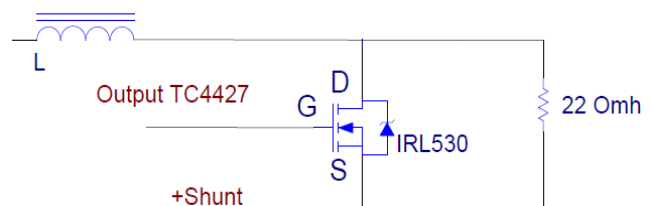
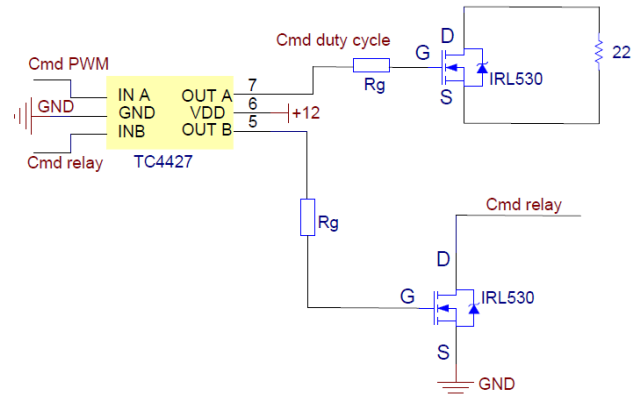


Fig.I.12 : Load resistance circuit

this technique, the I-V tracer works as a variable resistance from the short-circuit (when the duty cycle is 0) to the open circuit (when the duty cycle is 1).

- *Transistor control*

As known, the transistor works under 12 VDC, and the microcontroller Nucleo has only the output signal at 3.3V (Digital to analog outputs). Hence we need to upgrade these signals to 12 VDC. For this, we use a TC4427. The circuit is specially designed to control MOSFET. We connect the microcontroller's output to the TC4427's input and then associated outputs to the correct transistor's gates, using 12V from the power supply source, as shown in *Fig.I.13*.



*Fig.I.13 : Transistor control circuit*

- *Voltage and current measurements*

The voltage and current of the PV module are measured using a resistive voltage divider and a shunt resistance, respectively, as shown in *Fig.I.14*.

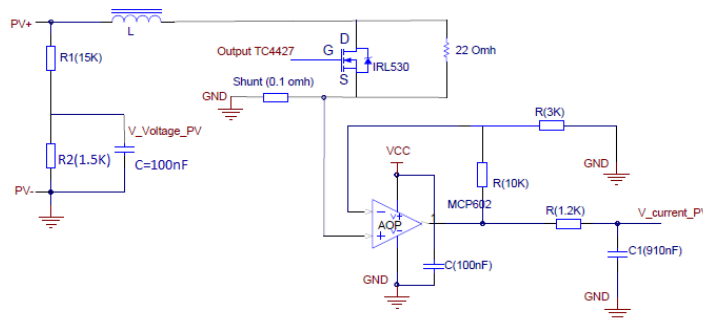


*Fig.I.14: Circuit for voltage and current measurements*

The two resistors  $R_1$  and  $R_2$  are connected in series, and the voltage divider is connected to the ground. The input voltage of these resistors is  $U_{in}$  and the output voltage  $U_{out}$  is measured at  $R_2$ 's terminals. The conversion rate is 30V to 3.3V. Hereby, the value of the resistors can be calculated as below :

$$U_{out(volt)} = \frac{R_2(volt)}{R_1(volt)+R_2(volt)} U_{in(volt)} \quad (I.1)$$

And

$$G = \frac{U_{out(volt)}}{U_{in(volt)}} = \frac{3.3}{30} \approx 0.1 \quad (I.2)$$

Therefore,

$$R_{2(volt)} = 1.5 \text{ k}\Omega$$

$$R_{1(volt)} = 15 \text{ k}\Omega$$

Where  $G$  is the gain of the resistive voltage divider.

A shunt resistance ( $0.1 \Omega$  in our case study) connected in series with the load resistance is used as a current sensor. The voltage across the shunt's resistance is amplified before usage. Indeed when the transistor short-circuits the load resistance, the current flowing into the shunt resistance is the short-circuit current sized at  $10A$ . Then, the maximum voltage ( $U_{max}$ ) can be calculated as below:

$$U_{max(curr)} = 0.1 \Omega \times 10 A = 1V. \quad (I.3)$$

Therefore, we have an amplifier gain of  $3.3$  to increase the voltage between  $0-3.3V$ . The calculation of the amplifier's resistors is:

$$U_{out(curr)} = \left(1 + \frac{R_{2(curr)}}{R_{1(curr)}}\right) U_{in(curr)} \quad (I.4)$$

$$\frac{R_{2(curr)}}{R_{1(curr)}} = \frac{U_{out(curr)}}{U_{in(curr)}} - 1 = 3.3 - 1 = 2.2 \quad (I.5)$$

So that,  $R_{1(curr)} = 1 \text{ k}\Omega$  and  $R_{2(curr)} = 2.2 \text{ k}\Omega$

### *I.3.2. Measurement of the PV module temperature and Irradiance*

A TC 74 sensor is glued on the backside of the PV module to measure the temperature ( $T_{pv}$ ) of the module. The operating range of this sensor is  $-40^\circ\text{C}$  to  $125^\circ\text{C}$  with  $\pm 3^\circ\text{C}$  accuracy from  $+25^\circ\text{C}$  to  $+85^\circ\text{C}$ . The plane of array irradiance ( $G_{POA}$ ) is measured with a reference cell (model Si-RS485TC-T-MB monocrystalline silicon irradiance sensors) with a tilt angle of  $25^\circ$ , the same as the PV panel support structure.

I.3.3. Emulation of  $R_s$  and  $R_{sh}$  degradation

To emulate the degradation of  $R_s$  and  $R_{sh}$ , additional resistors are connected in series or in parallel with the PV module, respectively. In order to evaluate different fault levels (three for each resistance in our case studies), an automatic emulator is designed as shown in *Fig.I.15*.

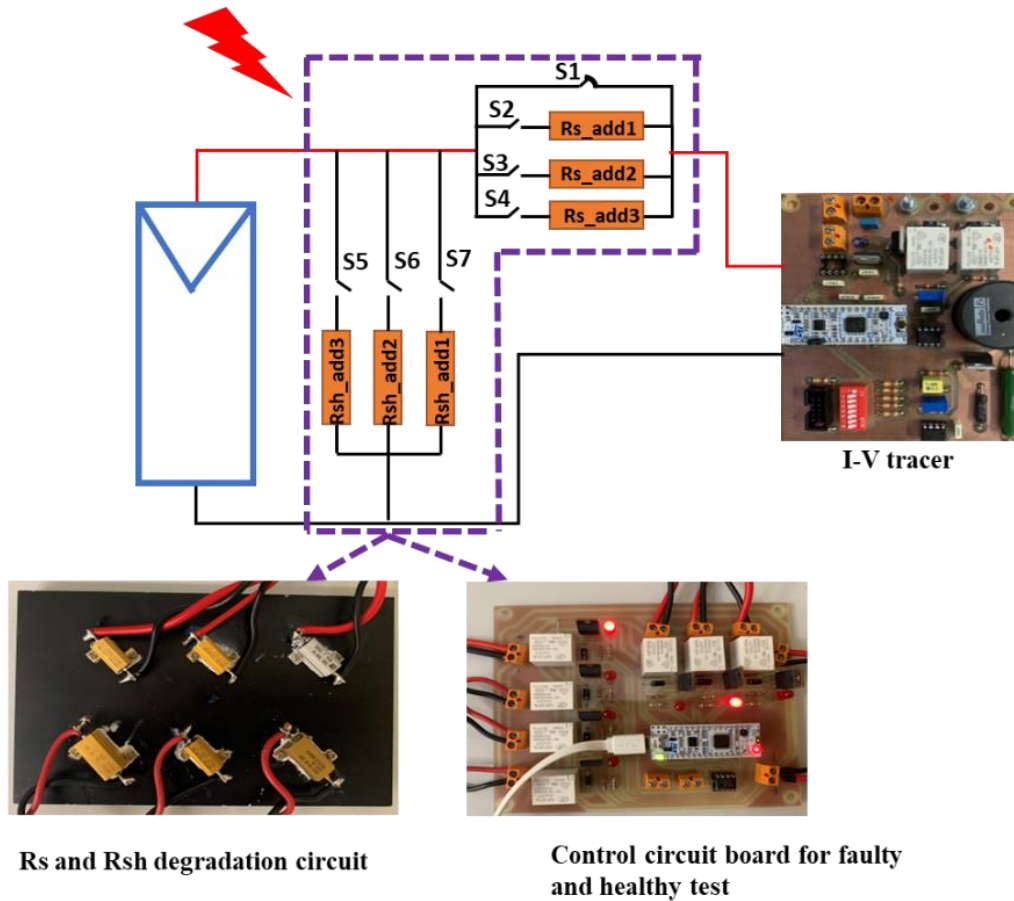


*Fig.I.15: Automatic emulator for  $R_s$  and  $R_{sh}$  degradation*

$R_{s\_add1}$ ,  $R_{s\_add2}$ ,  $R_{s\_add3}$  are the three additional resistances connected in series with the PV panel to emulate  $R_s$  degradation with three levels of severity; their values are 0.22, 0.33, and 0.39  $\Omega$ , respectively. And  $R_{sh\_add1}$ ,  $R_{sh\_add2}$ ,  $R_{sh\_add3}$  are the three additional resistances connected in parallel with the PV module; their values are 60, 50, and 39 $\Omega$ , respectively. The different configurations are set with the control of the seven switches (S1 to S7).

The whole system is shown in *Fig.I.16*.

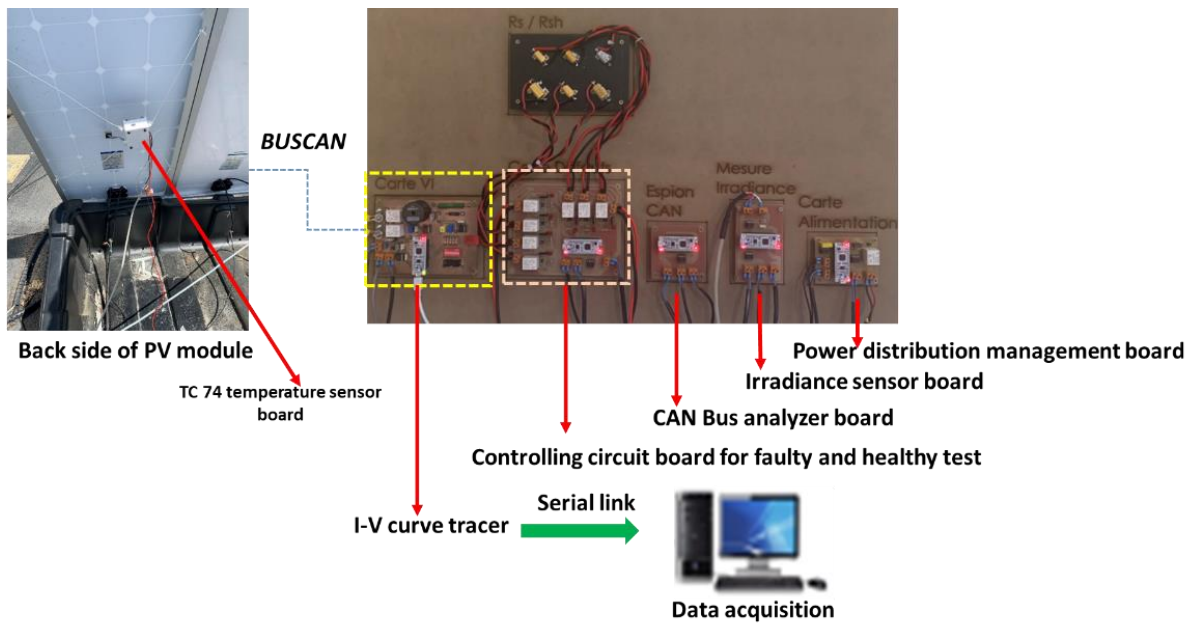


*Fig.I.16: Image of the experimental test bench*

#### *I.3.4. Data acquisition system*

The data acquisition system (DAQ) can be divided into four main parts: data acquisition and digitalization, data transmission, data storage, and data analysis. Analog signals from the sensors are converted into digital with ADC that is determined with its resolution and sampling frequency. In [21], a microcontroller with an 8-bit ADC was shown to be adequate for small and low-cost PV systems. There are several technologies available to interface the physical system with the DAQ (microcontroller, data logger, DAQcard) and for the communication (Peripheral Component Interconnect (PCI), Personal Computer Memory Card International Association (PCMCIA), USB, Ethernet, wifi). DAQ cards are more expensive than microcontrollers and data loggers. They are easy to use, and have already been utilized in a number of researches [22]–[25]. In our application, the CAN bus protocol is used to continuously collect the I-V characteristic, PV module temperature, and irradiance. The circuits of the CAN bus communication interface are composed of the microcontroller Nucleo32, which is used as the primary controller as well as a CAN bus node, a high-speed CAN transceiver MCP 2551 used as the interface between the protocol controller and the physical bus to enable data transmission and reception. Moreover, the connexion pins CAN H and CAN L are connected to the CAN bus through a resistor to prevent the CAN transceiver MCP 2551 from overcurrent. Our system has six communication nodes, as shown in *Fig.I.17*. To avoid any conflict, the data acquisition nodes have different priorities set with an ID (identifier).

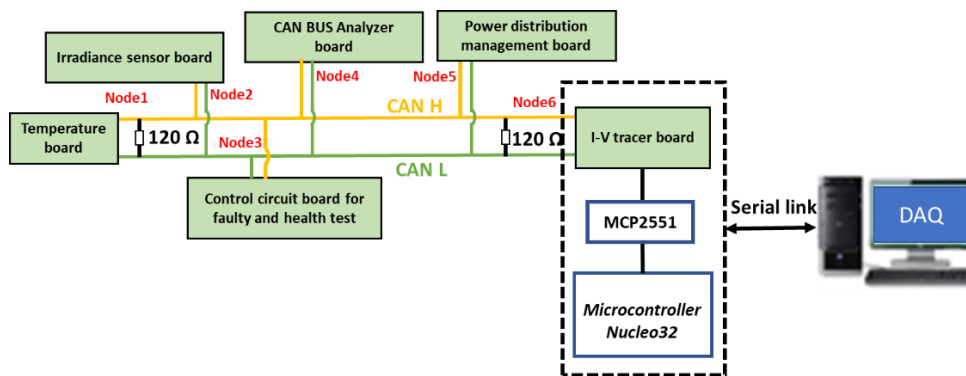


Fig.I.17: Block diagram of the data acquisition system

The microcontroller communicates with the PC via a serial link. Visual Studio and Excel are used to monitor, store, and display the incoming data of the PV module: current, voltage, temperature, irradiance, date, and times. The flowchart of the software is shown in Fig.I.18.

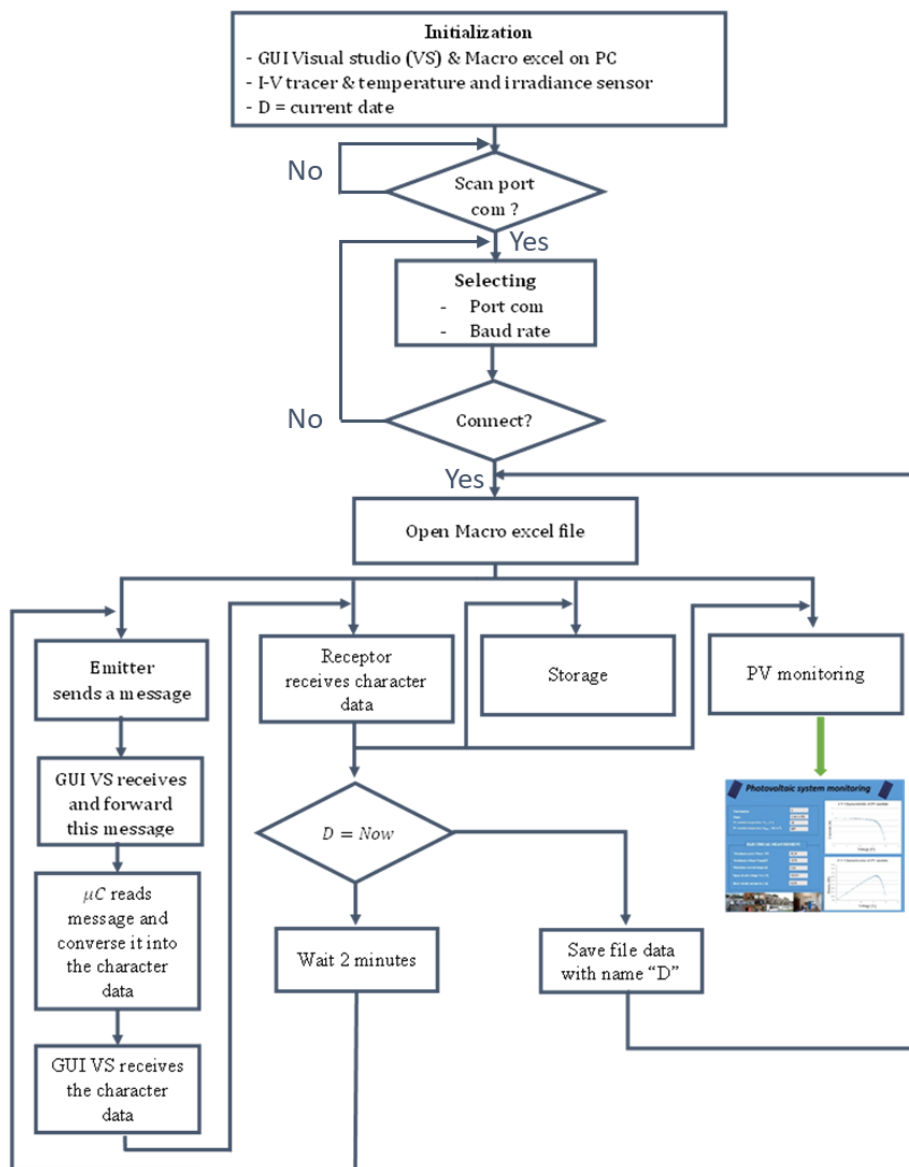


Fig.I.18: Flowchart of the software for data acquisition



#### I.4. The distribution of the points on the PV module's I-V curve

The measurement of the I-V curves, because it requires power interruption, must be done as fast as possible. Moreover, the I-V curve is highly sensitive to environmental conditions, e.g., irradiance, temperature, wind, and humidity. However, good accuracy is mandatory to obtain relevant information for health monitoring [26]–[28] or performance assessment (short-circuit current ( $I_{sc}$ ), open-circuit voltage ( $V_{oc}$ ), and maximum power point ( $P_{mpp}$ )), [29], [30], [31], [32]. So the sampling time, and the number distribution of the points are real issues.

In the healthy case, the I-V curve can be broadly decomposed into three zones; the constant current and constant voltage areas in which the characteristic is almost linear, and the area around the maximum power point (of high interest) where the characteristic is non linear. The distribution of the points along the curve can be even (uniform) or uneven, like the logarithmic distribution that is the most usual. Indeed, it is not necessary to measure many points in the constant current and constant voltage areas because the characteristic is linear. However, near the the maximum power point more points should be measured. In this regard, the Uniform distribution of points (UDP) and Logarithmic distribution of points (LDP) will be compared and analyzed to determine the optimal number of points, which depends on the variable load resistance that limits the I-V tracer's measurement range, which causes difficulty in distributing evenly the points along the I-V curve [2]. *Fig.I.19* shows the layout of the I-V curve with two domains, where  $NbPtV$  is the number of points when the output voltage varies from  $V_{pv_{min}}$  to  $V_{pv_{max}}$ , and  $NbPtI$  the number of points when output current varies from  $I_{pv_{min}}$  to  $I_{pv_{max}}$ .

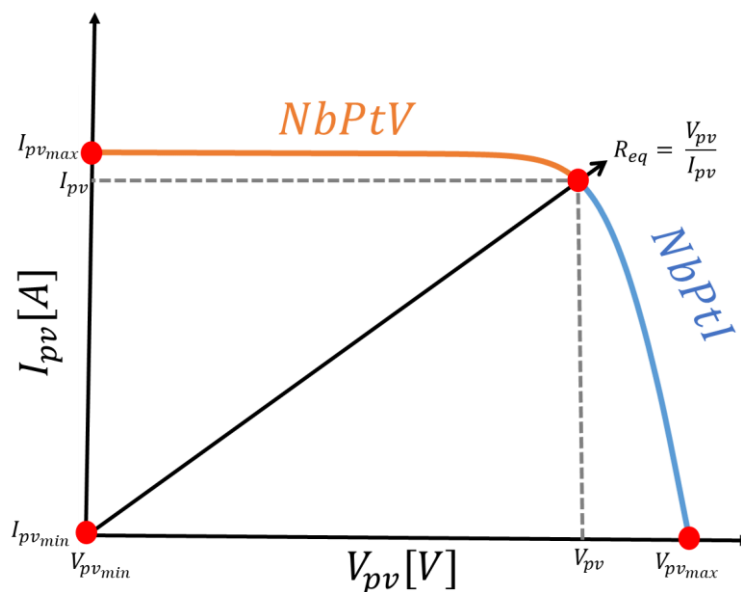


*Fig.I.19: Layout of I-V curve*

❖ LDP algorithm is described as below:

$$CoefLog(i)_{i \in [1, \dots, N]} = \log\left(1 + \frac{(i-1)*9}{N-1}\right) \quad (I.6)$$

where  $CoefLog$  is the logarithmic distribution coefficient for  $N$  points, and  $i$  is the sample number.

- *NbPtI* zone:

$$I_{pv}(i) = I_{pv_{min}} + [I_{pv_{max}} - I_{pv_{min}}] \times CoefLog[i] \quad (I.7)$$

$$V_{pv}(i) = V_{max} \quad (I.8)$$

$$Req_{NbPtI}(i) = \frac{V(i)}{I(i)} \quad (I.9)$$

- *NbPtV* zone:

$$I(i) = I_{max} \quad (I.10)$$

$$V(i) = V_{min} + [V_{max} - V_{min}] \times CoefLog[i] \quad (I.11)$$

$$Req_{NbPtV}(i) = \frac{V_{pv}(i)}{I_{pv}(i)} \quad (I.12)$$

❖ UDP algorithm is described as below:

$$CoefU = \frac{X_{max} - X_{min}}{N-1} \quad (I.13)$$

where  $CoefU$  is the uniform distribution coefficient for  $N$  points, the subscript symbol  $X_{min}$  and  $X_{max}$  refer to the first and final points, respectively.  $X(i)$  can be either identified as the current  $I_{pv}(i)$  or the voltage  $V_{pv}(i)$ , and  $i$  is the sample number.

- *NbPtI* zone:

$$I_{pv}(i) = (i - 1) + CoefU[i] \quad (I.14)$$

$$V_{pv}(i) = V_{max} \quad (I.15)$$

$$Req_{NbPtI}(i) = \frac{V_{pv}(i)}{I_{pv}(i)} \quad (I.16)$$

- *NbPtV* zone:

$$I_{pv}(i) = I_{max} \quad (I.17)$$

$$V_{pv}(i) = (i - 1) + CoefU[i] \quad (I.18)$$

$$Req_{NbPtV}(i) = \frac{V_{pv}(i)}{I_{pv}(i)} \quad (I.19)$$

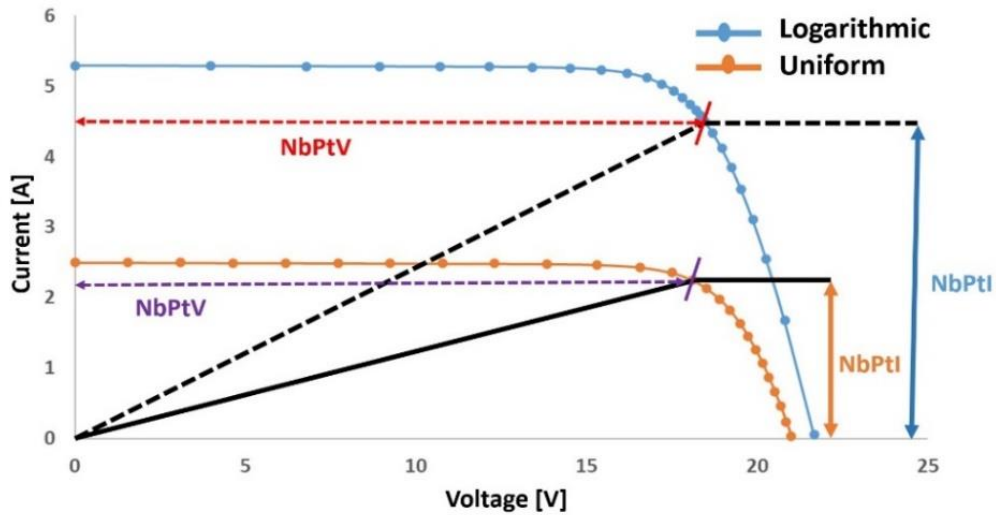


Fig.I.20: Logarithmic and uniform distribution of points on the I-V curve

I.4.1. *Qualitative analysis of the sensitivity of the five parameters of the single diode model to the number of points on the I-V curve*

❖ Methodology

A methodology is developed to study the sensitivity of the five extracted electrical parameters of PV single diode model's (SDM) to the number of points on the I-V curve. The methodology, which flowchart is shown in Fig.I.22 is described below :

First, the SDM with five parameters developed by NREL and available in Matlab/Simulink is used to simulate 1000 sampling data in STC. The characteristics of the simulated PV module are displayed in Table.I.2. The obtained I-V characteristic, denoted  $I(V)_{ref1000}$ , will be used as reference vector. The simulation result is shown in Fig.I.21.

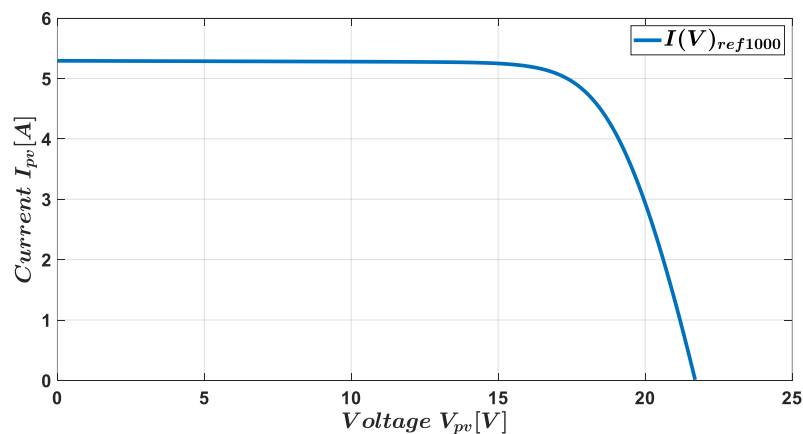


Fig.I.21: I-V characteristic of PV module type A

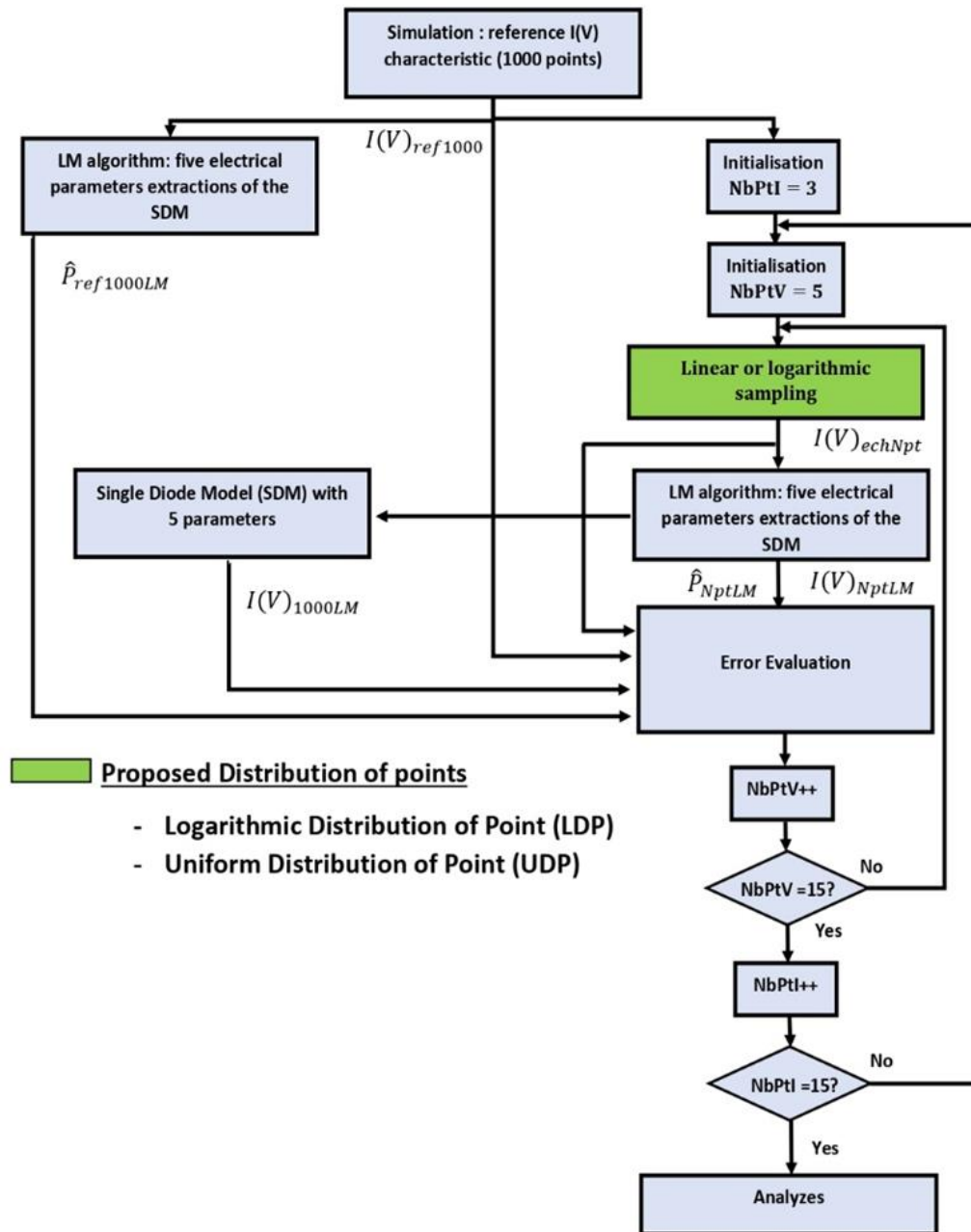


Fig.I.22: Flowchart of the methodology

Second, the vector  $I(V)_{ref1000}$  is used with LM approach to extract the five parameters of the PV model's. Their values are shown in [Table.I.4](#).

Table.I.4: Extracted parameters from the reference vector

$\hat{P}_{ref1000LM}(\hat{I}_{phref}, \hat{R}_{sref}, \hat{R}_{shref}, \hat{I}_{0ref}, \hat{n}_{ref})$					
$\hat{P}_{ref1000LM}$	$\hat{I}_{phref}$ [A]	$\hat{R}_{sref}$ [m $\Omega$ ]	$\hat{R}_{shref}$ [ $\Omega$ ]	$\hat{I}_{0ref}$ [A]	$\hat{n}_{ref}$
<b>Extracted values</b>	5.294	323.3	759.87	$3.39 \times 10^{-10}$	1

LDP and UDP algorithms are used to resample the vector  $I(V)_{ref1000}$ . The new vector is called  $I(V)_{echNpt}$ . By using this sampling vector as input for the extraction method (LM), five new

electrical parameters (named  $\hat{P}_{NptLM}(\hat{I}_{phNptLM}, \hat{R}_{sNptLM}, \hat{R}_{shNptLM}, \hat{I}_{0NptLM}, \hat{n}_{NptLM})$ ) and a new sampling vector (named  $I(V)_{NptLM}$ ) are obtained. The values of  $\hat{P}_{NptLM}$  are then used to re-simulate a new I-V curve called  $I(V)_{1000LM}$ .

Finally, by varying the number of points between 8 and 30 ( $NbPtI \in [3,15]$ ) and 5 to 15 points ( $NbPtV \in [5,15]$ ), the errors between the vectors  $I(V)_{ref1000LM}$  and  $I(V)_{1000LM}$ ,  $\hat{P}_{ref1000LM}$  and  $\hat{P}_{NptLM}$ ,  $I(V)_{echNpt}$  and  $I(V)_{NptLM}$  are computed and analyzed.

The mean absolute percentage error of the photovoltaic current ( $MAPE_{I_{pv}}$ ), and the absolute relative error of the PV model's parameters ( $ARE_{\hat{p}}$ ) are calculated as follows:

$$MAPE_{I_{pv}}(\%) = \frac{100}{N} \sum_{i=1}^m \left| \frac{I_{pv\_ref}(V_i) - I_{pv\_ex}(V_i)}{I_{pv\_ref}(V_i)} \right| \quad (I.20)$$

$$ARE_{\hat{p}}(\%) = 100 \left| \frac{\hat{p}_{ref}(i) - \hat{p}_{ex}(i)}{\hat{p}_{ref}(i)} \right| \quad (I.21)$$

The subscripts "ref" and "ex" correspond to reference and extracted data, respectively.  $V_i$  is the  $i^{th}$  simulated voltage, and  $m$  is data point.

#### I.4.2. Results and Analysis

##### a) Sensitivity of the series resistances ( $R_s$ )

Fig.I.23 illustrates the variation of  $R_s$  with  $NbPtI$  and  $NbPtV$ . LDP and UDP algorithms. The range of variations are  $[322.07m\Omega - 323.34m\Omega]$  for UDP and  $[318m\Omega - 322m\Omega]$  for LDP, respectively. The results also show that the values of  $R_s$  are relatively constant. Compared with the reference value of  $\hat{R}_{sref}$  ( $323.3 m\Omega$ ), the minimum and maximum relative deviations are in the ranges of  $[0.3\% - 1.23\%]$  and  $[0.3\% - 1.54\%]$ , respectively. These percentages of errors are acceptable.

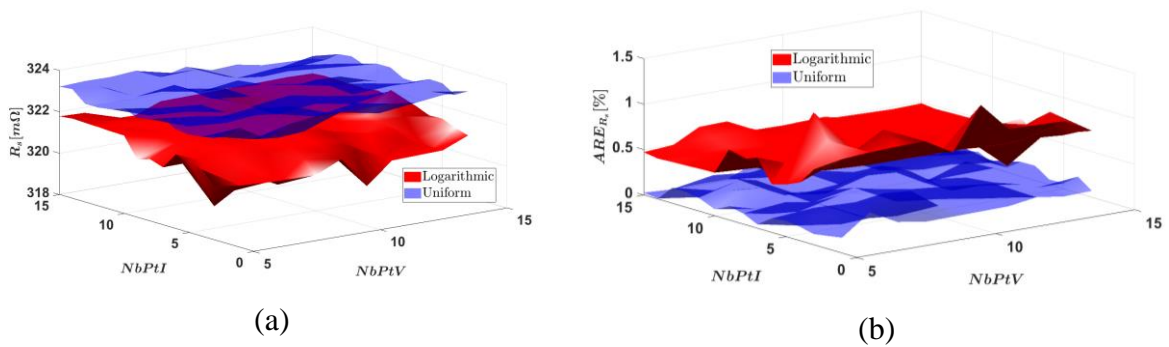


Fig.I.23: Variation of  $R_s$  and  $ARE_{R_s}$  with  $NbPtV$  and  $NbPtI$

b) Sensitivity analysis of the shunt resistance ( $R_{sh}$ )

The variations of  $R_{sh}$  and the relative deviation with  $NbPtI$  and  $NbPtV$  are shown in Fig.I.24. The results indicate that the minimum and maximum values of  $R_{sh}$  are in the range of [758.24  $\Omega$  - 854.93  $\Omega$ ] and [501.40  $\Omega$  - 853.52  $\Omega$ ] for LDP and UDP algorithms, respectively. Compared to the reference value of  $\hat{R}_{shref}$  (759.87  $\Omega$ ), the deviations are in the range of [0.21%- 12.51%] and [12.32 - 34.01%]. It can be concluded that  $R_{sh}$  is less sensitive to the number of points on the I-V curve when the LDP algorithm is used.

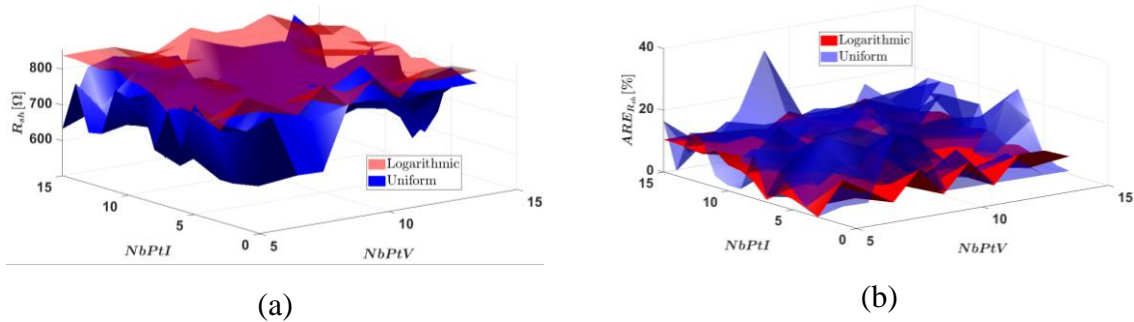


Fig.I.24: Variation of  $R_{sh}$  and  $ARE_{R_{sh}}$  with  $NbPtV$  and  $NbPtI$

c) Sensitivity analysis of the photocurrent ( $I_{ph}$ )

The variations of  $I_{ph}$  with  $NbptI$  and  $NbPtV$ , using the LDP and UDP algorithms are represented in Fig.I.25. The maximum and minimum values of  $I_{ph}$  are in the ranges of [5.291 A - 5.294 A] and [5.293 A - 5.298 A] in the case of LDP and UDP algorithms, respectively. Compared to the reference value of  $\hat{I}_{phref}$  (5.294 A), the minimum and maximum deviations are in the ranges of [0% - 0.05%] and [0- 0.07%], which shows that  $I_{ph}$  is very slightly impacted by the number of points on the I-V curve.

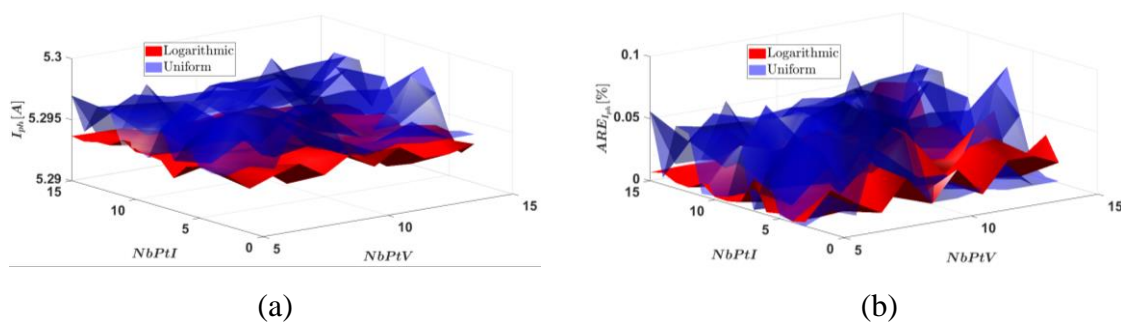


Fig.I.25: Variation of  $I_{ph}$  and  $ARE_{I_{ph}}$  with  $NbPtV$  and  $NbPtI$

d) Sensitivity analysis of the diode saturation current ( $I_0$ )

Fig.I.26 illustrates the variation of  $I_0$  with  $NbptI$  and  $NbPtV$  in the case of LDP and UDP algorithms. The results show the values of  $I_0$  are slowly increasing along with the number of

points. The minimum and maximum values of  $I_0$  are in the ranges of  $[3.37 \times 10^{-10} \text{ A} - 3.41 \times 10^{-10} \text{ A}]$  and  $[3.38 \times 10^{-10} \text{ A} - 3.46 \times 10^{-10} \text{ A}]$ , respectively. Compared with the reference value of  $\hat{I}_{0\text{ref}}$  ( $3.39 \times 10^{-10}$ ), the calculated relative deviations are in the range of  $[0.44\% - 0.58\%]$  and  $[0.14\% - 2.06\%]$ . These percentages of errors are relatively low, which means that  $I_0$  is also slightly impacted by the number of points.

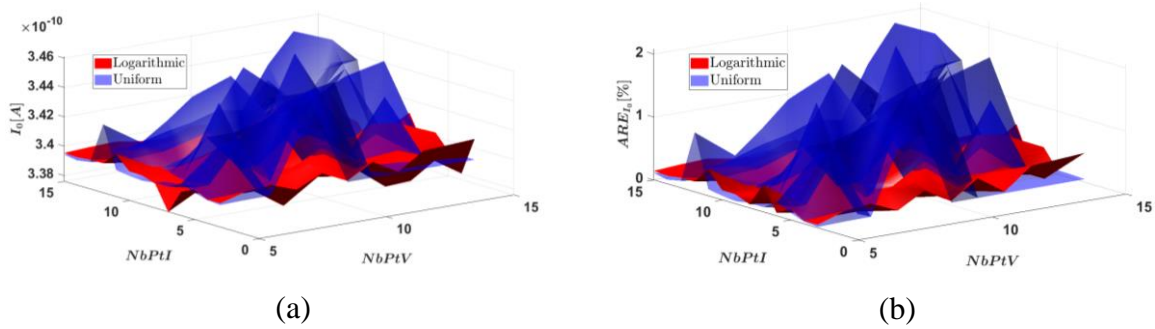


Fig.I.26: Variation of  $I_0$  and  $ARE_{I_0}$  with  $NbPtV$  and  $NbPtI$

e) Sensitivity analysis of the diode ideality factor ( $n$ )

The variations of  $n$  with  $NbPtI$  and  $NbPtV$  are shown in Fig.I.27. The relative deviation from the reference value is lower than 0.6 % for both algorithms, even if in the case of UDP, several peaks can be observed.

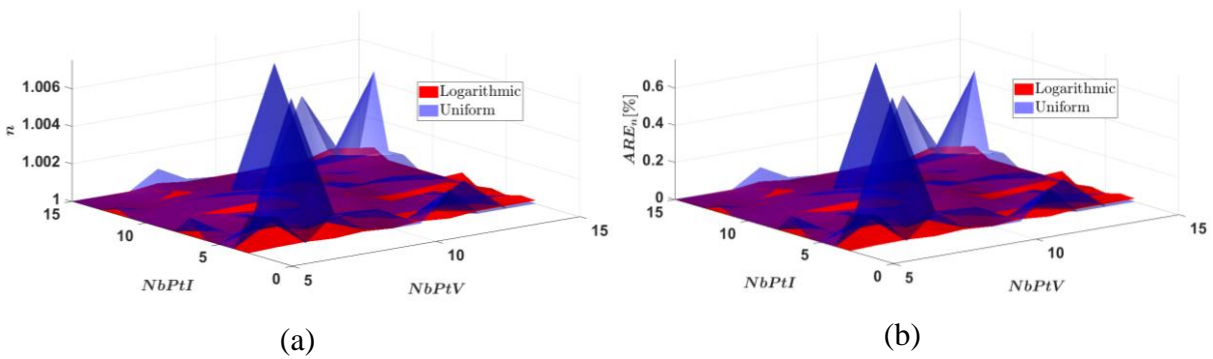


Fig.I.27: Variation of  $n$  and  $ARE_n$  with  $NbPtV$  and  $NbPtI$

f) Evaluation of  $I$ - $V$  characteristics between  $I(V)_{echNpt}$  and  $I(V)_{NptLM}$

Fig.I.28 shows the variations of  $MAPE_{I_{pv}}$  ( $I(V)_{echNpt}$  and  $I(V)_{NptLM}$ ) in the case of LDP and UDP algorithms. The results show that in both cases, the  $MAPE_{I_{pv}}$  increases when the number of points in the current variation area ( $NbPtI$ ) increases, but it decreases when the number of points in the voltage variation area ( $NbPtV$ ) increases. The minimum and maximum values of  $MAPE_{I_{pv}}$  are in the ranges of  $[0.165\% - 0.362\%]$  and  $[0.162\% - 0.523\%]$  in the case of LDP and UDP, respectively. It can be concluded that when  $NbPtI$  and  $NbPtV$  increase, the

sampling vector  $(I(V)_{echNpt})$  estimated from the extraction method is still accurate, reliable, and satisfactory.

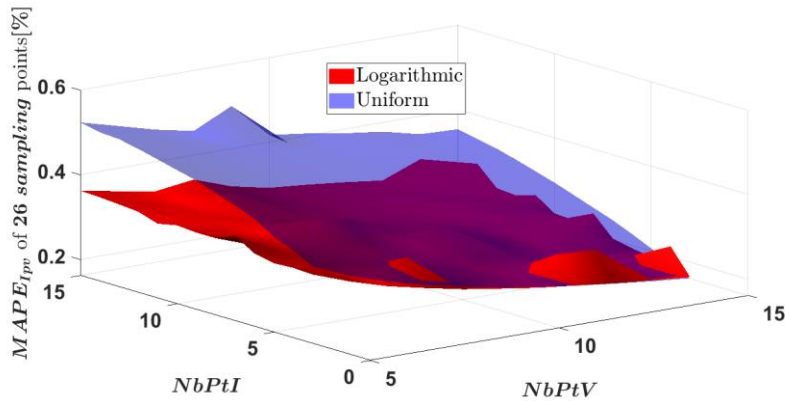


Fig.I.28: Variation of  $MAPE_{I_{pv}}$  (26 sampling points) with  $NbPtI$  and  $NbPtV$

g) Evaluation of I-V characteristics between  $I(V)_{ref1000}$  and  $I(V)_{1000LM}$

The variations of  $MAPE_{I_{pv}}$  ( $I(V)_{ref1000}$  and  $I(V)_{1000LM}$ ) with  $NbPtI$  and  $NbPtV$  for the LDP and UDP algorithms are represented in Fig.I.29. The results indicate that when  $NbPtI$  and  $NbPtV$  increase, the  $MAPE_{I_{pv}}$  remains very low mainly because the new extracted parameters used to simulate  $I(V)_{1000LM}$  slightly deviate from the reference ones, except for  $\hat{R}_{sh}$  in the case of the UDP algorithm. The lowest and highest values of  $MAPE_{I_{pv}}$  are in the ranges of [0.88% -1.204%] and [0.92% -1.081%] in the case of LDP and UDP algorithms, respectively.

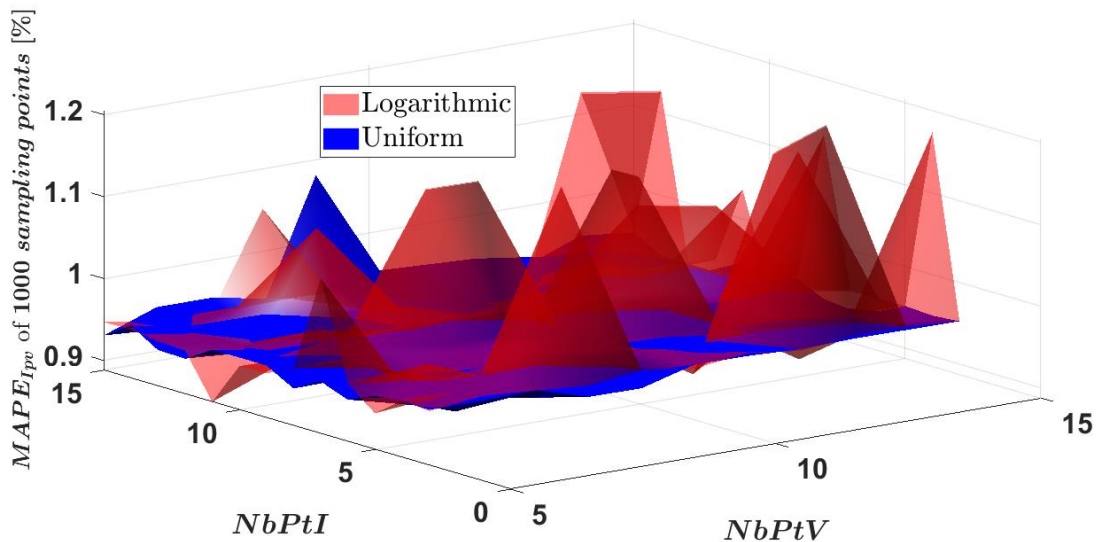


Fig.I.29: Evaluation of  $MAPE_{I_{pv}}$  (1000 sampling points) with  $NbPtV$  and  $NbPtI$



1.4.3. Summary of the sensitivity analysis

The sensitivity of the five electrical parameters of the PV model to the number of points on the I-V curve was investigated in this section. The ARE between the five new extracted parameters  $\hat{P}_{NptLM}$  and the reference ones  $\hat{P}_{1000LM}$  are displayed in [Table.I.5](#). Based on the findings, most of the AREs are lower when using the LDP instead of the UDP.

Table.I.5: Deviation of PV model parameters between reference and estimated data

Parameters of the PV model	$I_{ph}(A)$	$R_s(m\Omega)$	$R_{sh}(\Omega)$	$I_0 \times 10^{-10}(A)$	$n$	
Reference Parameters $\hat{P}_{ref1000}$	5.294	323.3	759.87	3.39	1	
Parameter estimated in the case of LDP algorithm	NbPtV $\in [5,15]$	5.291-5.294	322- 323	758.2-854.93	3.375-3.412	1-1.000
	NbPtI $\in [3,15]$					
Parameter estimated in the case of UDP algorithm	NbPtV $\in [5,15]$	5.293-5.298	318-322	501.4-853.52	3.385-3.461	1-1.007
	NbPtI $\in [3,15]$					
Absolute Relative Error (ARE) % in the case of LDP algorithm	0-0.05	0.3-1.23	0.21-12.51	0.44-0.58	0 - 0.05	
Absolute Relative Error (ARE) % in the case of UDP algorithm	0-0.07	0.3-1.54	12.32-34.01	0.14-2.06	0 - 0.75	

The  $MAPE_{I_{pv}}$  between the  $I(V)_{echNpt}$  and  $I(V)_{NptLM}$  ;  $I(V)_{ref1000}$  and  $I(V)_{1000LM}$  , are displayed in [Table.I.6](#). These deviations are relatively very low. It can be concluded that both methods of sampling points on the I-V curve are accurate, reliable, and acceptable for retrieving the I-V curve. But LDP as it is the most stable will be used in our I-V tracer.

Table.I.6 :  $MAPE_{I_{pv}}$  between the reference and estimated vectors

Description of detailed	Mean Absolute Percentage Error (MAPE) %
$I(V)_{echNpt}$ and $I(V)_{NptLM}$ in the case of the LDP algorithm	NbPtV $\in [5,15]$
	NbPtI $\in [3,15]$
$I(V)_{echNpt}$ and $I(V)_{NptLM}$ in the case of the UDP algorithm	NbPtV $\in [5,15]$
	NbPtI $\in [3,15]$
$I(V)_{ref1000}$ and $I(V)_{1000LM}$ in the case of the LDP algorithm	0.1653-0.3629
$I(V)_{ref1000}$ and $I(V)_{1000LM}$ in the case of the UDP algorithm	0.162-0.5238
$I(V)_{ref1000}$ and $I(V)_{1000LM}$ in the case of the LDP algorithm	0.88-1.204
$I(V)_{ref1000}$ and $I(V)_{1000LM}$ in the case of the UDP algorithm	0.92-1.081

1.4.4. Implementation of the LDP in the I-V tracer.

As explained in the previous section, our I-V tracer is based on a DC-DC converter driven with a PWM duty cycle to sweep the load resistance. The schematic circuit of the I-V tracer is shown in [Fig.I.30](#). The duty cycle ( $\alpha$ ) varies from 0 to 1; when  $\alpha$  is equal to 0, the circuit provides the maximum voltage ( $V_{pv,max}$ ), and when  $\alpha$  is equal to 1, the circuit provides

the maximum current ( $I_{pv_{max}}$ ). The relation between the variable resistance ( $R_{eq}$ ), the load resistance ( $R_L$ ), and the duty cycle ( $\alpha$ ) can be expressed as below:

$$\alpha(i) = 1 - \left(\frac{R_{eq}(i)}{R_L}\right) \quad (I.22)$$

Where  $i$  is the sample's number on the I-V curve.  $R_L$  the load resistance is set at  $22 \Omega$ . The LDP algorithm embedded in the microcontroller generates the optimal duty cycle ( $\alpha$ ) to control the MOSFET switch. *Fig.I.31* shows the flowchart of the software for the I-V tracer.

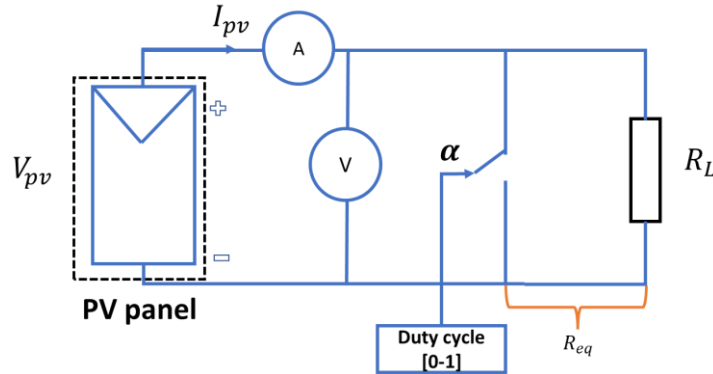


*Fig.I.30: Schematic circuit of the I-V tracer*

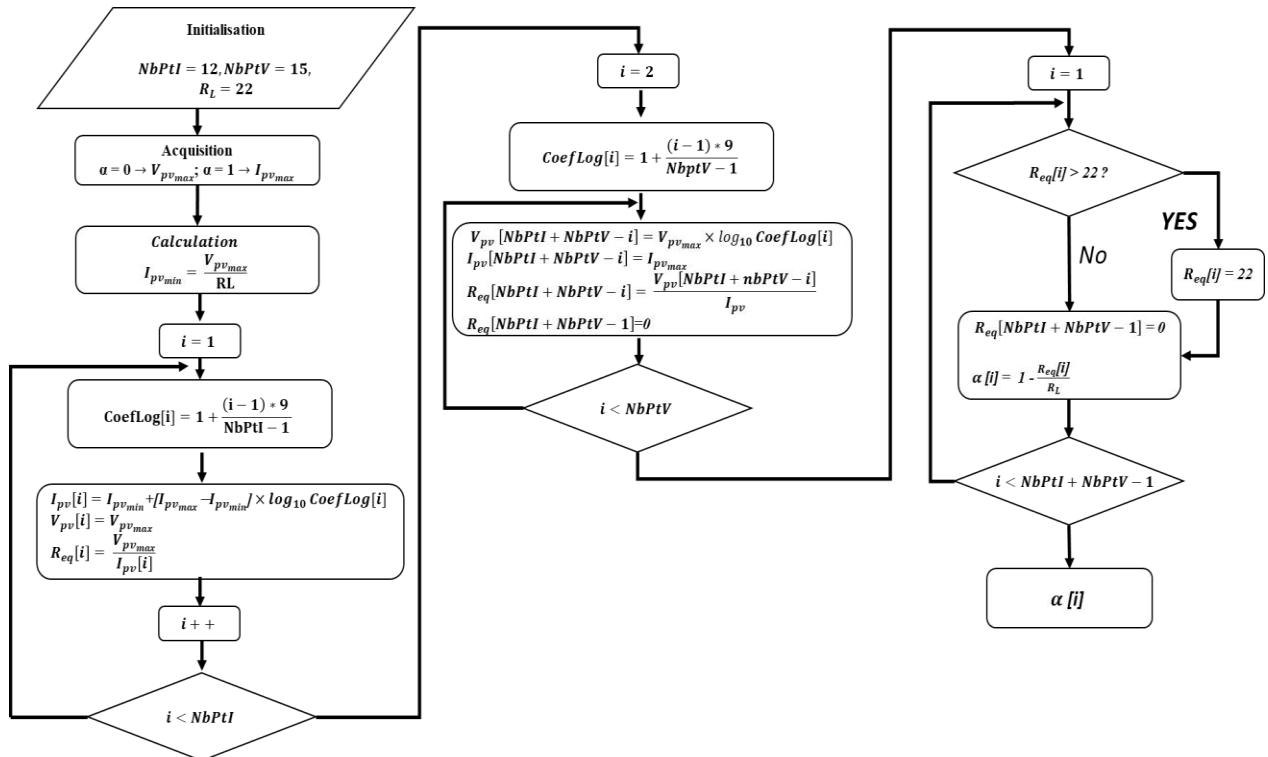


*Fig.I.31: Software flowchart of the I-V tracer using the logarithmic distribution of points*

❖ Sweep time of I-V tracer

The sweep time or sampling time interval is critical for the quality of the obtained I-V curves. It should be small enough to guarantee that voltage and current measurements are taken

under constant solar irradiation and temperature but large enough to ensure they are collected in steady state. In our case,  $NbPtV$  and  $NbPtI$  are set to 15 and 12 respectively.

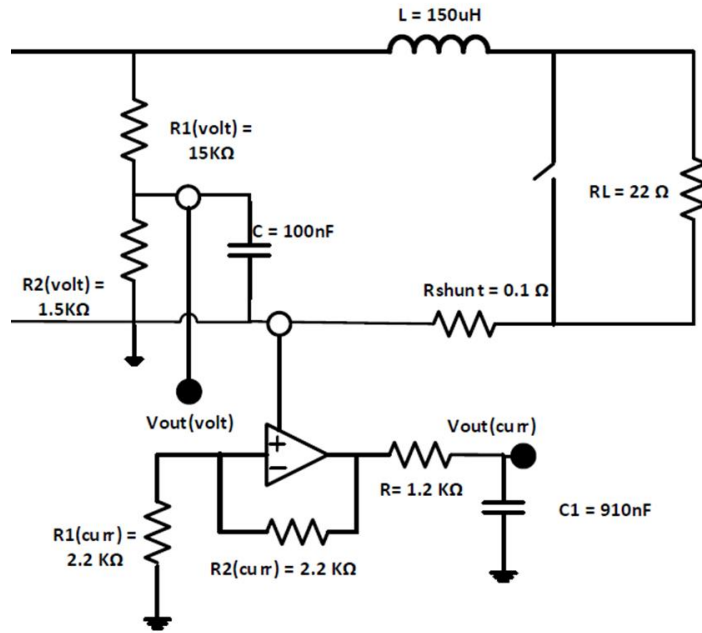


Fig.I.32: Simplified the main circuit of the I-V tracer

To determine the sweep time of the I-V tracer, its response time must be calculated first. Fig.I.32 shows the simplified main circuit of the I-V tracer, which indicates that there are three time constants: the time constant of the primary circuit called “ $\tau_1$ ”, the time constant of the voltage divider called “ $\tau_2$ ”, and the time constant of the amplifier operator (AOP) of the current sensor called “ $\tau_3$ ”. The time responses of the I-V tracer can be calculated as below:

$$\tau_1 = \frac{L}{R_L} = \frac{150 \times 10^{-6}}{22} = 0.006 \text{ ms} \quad (\text{I.23})$$

$$\tau_2 = \frac{R_{1(volt)}R_{2(volt)}C}{R_{1(volt)}+R_{2(volt)}} = \frac{1.5 \times 10^3 \times 15 \times 10^3 \times 100 \times 10^{-9}}{(1.5 \times 10^3 + 15 \times 10^3)} = 0.136 \text{ ms} \quad (\text{I.24})$$

$$\tau_3 = R \times C1 = 1.092 \text{ ms} \quad (\text{I.25})$$

Therefore, the global time response ( $t_r$ ) can be estimated as :

$$t_r = (\tau_1 + \tau_2 + \tau_3) \times 5 \approx 6.17 \text{ ms}$$

Based on this result, 7 ms will be retained in the microcontroller for the acquisition of one point. Fig.I.33 shows the PWM signal measurement using the Picoscope Digital Oscilloscope, and the result indicates that the I-V tracer needs 181.2 ms to capture 26 points on the I-V curve (let us recall that the switching frequency  $f_s = 50 \text{ kHz}$ ).

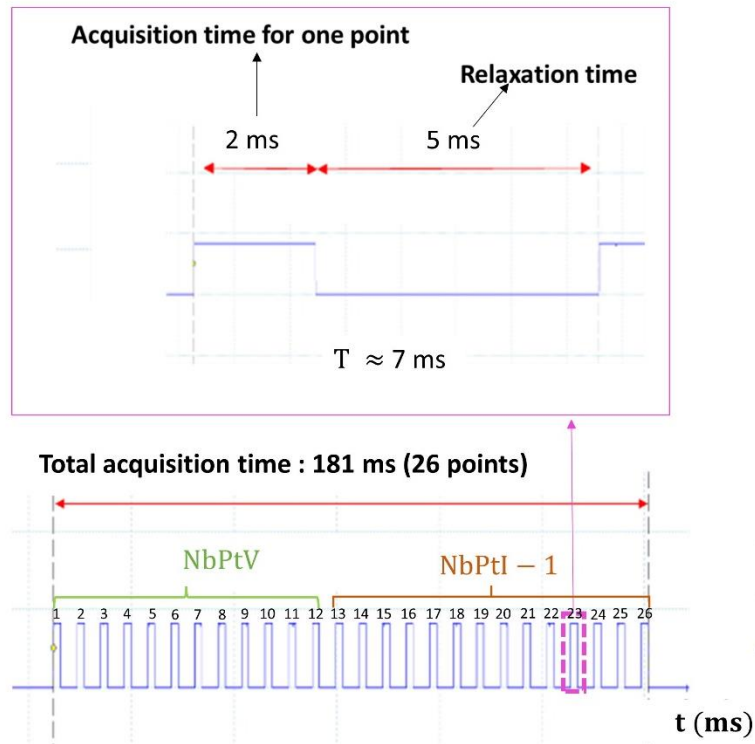


Fig.I.33: Acquisition time

### I.5. Calibration and validation of the I-V tracer

The approach for validating the calibration of the I-V tracer is detailed in this section. To perform all the measurements and ensure accuracy, the I-V tracer is usually compared to a commercially available I-V tracer[12], [33]. But in our case, the E4360 Modular Solar Array Simulator (MSAS) from Keysight Technologies, Inc is used as the main device to calibrate and validate the developed I-V tracer. *Fig.I.34* and *Fig.I.35* show the I-V tracer calibration and validation methodology and the I-V tracer and SAS test bench, respectively.

The mean absolute percentage error (MAPE) and absolute relative error (ARE) are used to evaluate the accuracy of the I-V tracer. The calculation uses the formula below :

- $X_1 = [I_{pv}], \text{ or } [V_{pv}]$

$$MAPE(X_1) = \frac{100}{m} \sum_{i=1}^m \left| \frac{X_{1MSAS} - X_{1meas}}{X_{1MSAS}} \right| \quad (I.26)$$

- $X_2 = [P_{mpp}, \text{ or } I_{sc}, \text{ or } V_{oc}]$

$$ARE(X_2) = 100 \frac{|X_{2MSAS} - X_{2meas}|}{X_{2MSAS}} \quad (I.27)$$

$X_1$  and  $X_2$  are obtained from the MSAS and the developed I-V tracer. The subscripts "MSAS" and "meas" denote MSAS and measurement. Where  $X_1$  can be the vector of  $I_{pv}$  or  $V_{pv}$  and  $X_2$  is a scalar ( $P_{mpp}$ ,  $I_{sc}$  or  $V_{oc}$ )

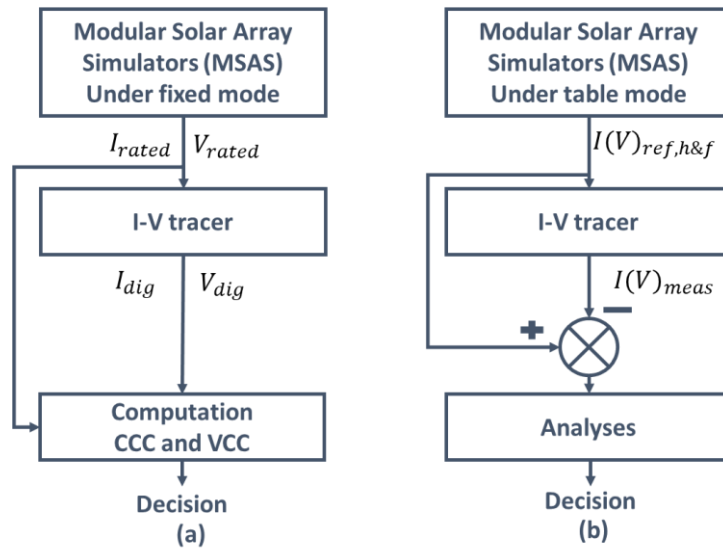


Fig.I.34: Methodology for I-V tracer calibration (a) and validation (b)

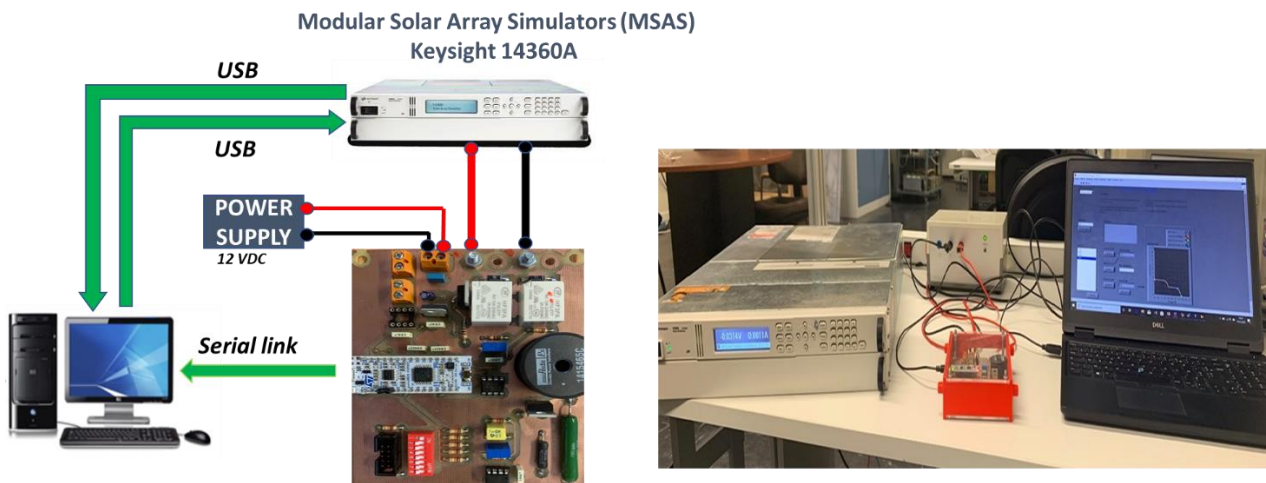


Fig.I.35: Experimental test bench for calibration and validation of I-V tracer at GeePs

The SAS is a dual output programmable DC power source that can generate the output characteristics of a solar cell/module/array. Furthermore, the E4360 SAS is a generator current source with a very low output capacitance that can rapidly simulate the I-V curve in various conditions (ex., temperature, age, etc.). It produces up to 2 outputs and up to 1200 W with three modes of operation: Simulator (SAS), Table, and Fixed. SAS or table modes are used to model the I-V curve of a solar module correctly, and fixed mode is used when a conventional power source is required. A LabVIEW interface developed by Instrument National (IN) is used to control and monitor this instrument.

- *Simulator (SAS) mode*

The power supply output characteristic in SAS mode is shown in *Fig.I.36*. The E4360 SAS creates a 4096 I-V points database. An I-V curve is approximated using an internal method. This can be done without a PC via the I/O ports or from the front panel. In this mode, four input parameters are needed to generate a curve:

- Open circuit voltage ( $V_{oc}$ )
- Short circuit current ( $I_{sc}$ )
- Current at maximum power point ( $I_{mpp}$ )
- Voltage at maximum power point ( $V_{mpp}$ )

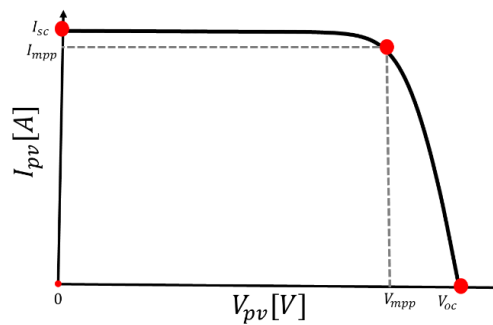


*Fig.I.36: Power supply output characteristic in SAS mode*

- *Fixed mode*

When the device is turned on, this is the default mode with a conventional power supply's rectangular I-V characteristics. *Fig.I.37* show Power supply output characteristic in fixed mode.  $I_{rated}$  and  $V_{rated}$  are the reference values of current and voltage.

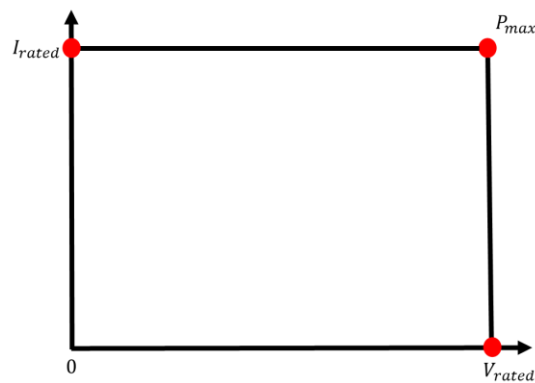


*Fig.I.37: Power supply output characteristic in Fixed mode*

- *Table mode*

In this mode, the user can define the table data to determine the I-V curve. The table can have a minimum and maximum of 3 to 4000 points, respectively. Each point corresponds to one current value and voltage value(I,V). The E4360 SAS memory can store up to 30 tables.

*I.5.1. I-V tracer calibration*

*Fig.I.34* (a) shows the methodology used to calibrate the I-V tracer. The I-V tracer uses two sensors to measure the current and voltage of the PV module. To ease the analyses, the sensors will be calibrated directly in ampere and volt for the current and voltage, respectively. *Fig.I.38* shows the block diagram for the calibration of the current and voltage sensors. The sensor's output signal is an analog signal in the range of 0-3.3V. The microcontroller converts it into a digital signal in the range of 0-1. To eliminate the noise and the current ripples, 100 samples are averaged. Hence, the microcontroller's digital output is in the range of 0-100. The calibration coefficient of current (CCC) and calibration coefficient of voltage (CCV) are then obtained as below :

$$ICC = \frac{I_{rated}}{I_{dig}} \quad (I.28)$$

$$CCV = \frac{V_{rated}}{V_{dig}} \quad (I.29)$$

Where  $I_{rated}$  and  $V_{rated}$  are the current and voltage references introduced into the MSAS under the fixed mode.  $I_{dig}$  and  $V_{dig}$  are the values measured from the current and voltage sensors.

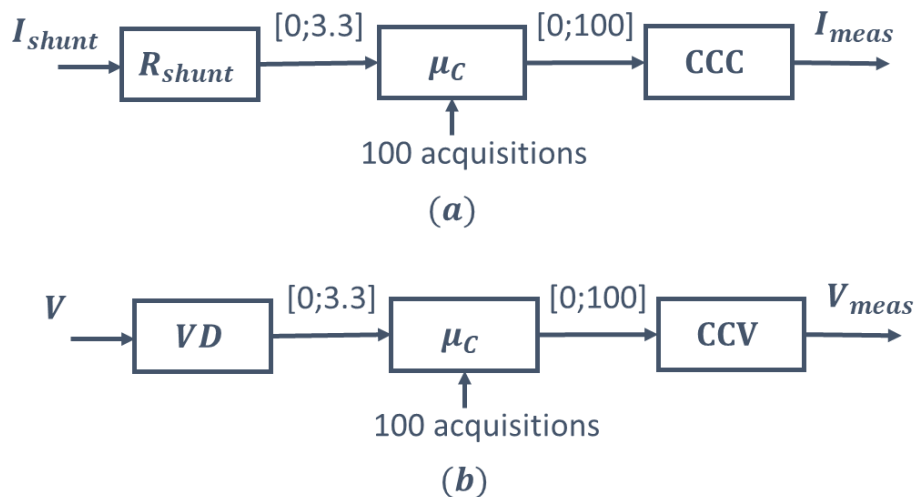


*Fig.I.38: Scale-up process*

To ensure the reliability of this process, the CCC and CCV are calculated for eight different cases, as shown in *Table.I.7*. The finding demonstrates that the CCC and CCV from the eight

different cases are relatively stable, which means that these coefficients can work under different conditions. The average of these eight samples will be used as coefficients set directly into the microcontroller of the I-V tracer.

Table.I.7: Eight different configurations for CCC and CCV calculation

No	MSAS : $I_{rated} - V_{rated}$	I-V tracer		Calibration coefficient	
		$I_{dig}$	$V_{dig}$	CCC	CCV
1	1,5 A – 10 V	14,1	39,2	0,1064	0,2551
2	2 A – 12 V	19,4	47,4	0,1031	0,2532
3	2,5 A – 14 V	24,7	55,7	0,1012	0,2513
4	3 A – 16 V	30,1	63,7	0,0997	0,2512
5	3,5 A – 18 V	35,4	72	0,0989	0,2500
6	4 A – 20 V	40,7	80,2	0,0983	0,2494
7	4,5 A – 22 V	46,1	88,5	0,0976	0,2486
8	5 A – 24 V	51,4	96,7	0,0973	0,2482
<b>Average</b>				<b>0,1003</b>	<b>0,2509</b>

In the fixed mode, we played different scenarios with different voltage and current values such as 10V-1.5A, 12V-2A, 14V-2.5A, 16V-3A, 18V-3.5A, 20V-4A, 22V-4.5A, and 24V-5A. Fig.I.39 shows the different I-V curves for calibration obtained from the reference (data obtained from MSAS) and the measured data (data obtained from I-V tracer); the scatter with a smooth line and the marker represent the reference and measured data, respectively. The results show a good agreement between the data obtained from MSAS and the one from the developed I-V tracer. The calculated deviations are shown in Table.I.8. The result show that the relative deviations are relatively higher for low values of current and voltage (1.5A -10V and 2A-12 V) compared to the case with higher values of current and voltage (2.5A-14V to 5A-24V).

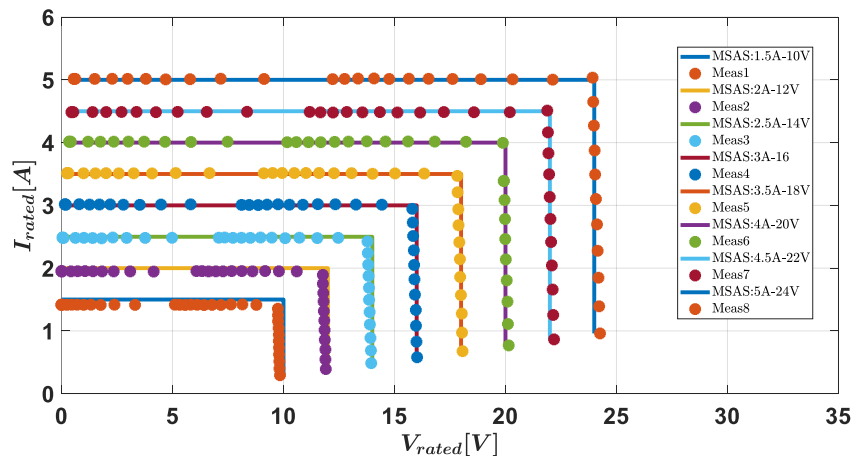


Fig.I.39: I-V curves of MSAS and I-V tracer in the fixed mode for various scenarios



Table.I.8: Relative calibration deviations

Case (C)	C1	C2	C3	C4	C5	C6	C7	C8
Current(A)	1.5	2	2.5	3	3.5	4	4.5	5
Voltage(V)	10	12	14	16	18	20	22	24
MAPE of Current (%)	5.56	2.49	0.67	0.42	0.34	0.33	0.32	0.28
MAPE of voltage (%)	2.11	1.37	0.96	0.6	0.44	0.34	0.38	0.46

Repeatability, defined as the ability to compare a given result to another measurement taken under the same condition is highly recommended for instruments. The scenario 3.5A-18V is retained (valued set into the MSAS under the fixed mode) to test the measurement repeatability of the I-V tracer. The scenario was repeated five times. The relative deviations between the data obtained from MSAS and I-V tracer shown in Table.I.9, demonstrate that the MAPE of current and voltage are stable. It can be concluded that the I-V tracer exhibits an acceptable repeatability.

Table.I.9 : Evaluation of the repeatability

Case (C)	C5	C5	C5	C5	C5
Current(A)	3.5	3.5	3.5	3.5	3.5
Voltage(V)	18	18	18	18	18
MAPE of current (%)	0.348	0.349	0.333	0.340	0.346
MAPE of voltage (%)	0.397	0.419	0.432	0.432	0.446

### I.5.2. I-V tracer validation

The methodology used to validate the I-V tracer is shown in Fig.I.34 (b). The MSAS under the table mode is used to establish the I-V curve (used as reference), which will be compared to the I-V curve obtained from the I-V tracer. To ensure that the I-V tracer can characterize the I-V curve of the PV module in both healthy and faulty conditions (partial shading,  $R_s$  and  $R_{sh}$  degradations), the table used to create the  $I(V)_{ref}$  must represent healthy and faulty conditions. First, the SDM with five parameters developed by NREL and available in Matlab/Simulink is used to generate  $I(V)_{ref}$  curves in healthy and faulty conditions. These I-V curves will be introduced into the MSAS under the table mode and used as the references. Then I-V tracer will be used to measure the I-V curve of MSAS. The data obtained from the I-V tracer will finally be compared to the reference one.

- *Healthy case*

To begin, we introduced the healthy I-V curve  $I(V)_{ref,h}$  in MSAS, then the  $I(V)_{meas}$  can be measured using the I-V tracer. Fig.I.40 shows the reference I-V and P-V curves and the ones measured with the I-V tracer. The values of the relative errors  $MAPE_{I_{pv}}$ ,  $MAPE_{P_{pv}}$ ,

$ARE_{P_{mpp}}$ ,  $ARE_{I_{sc}}$  and  $ARE_{V_{oc}}$  are 0.4%, 1.33%, 1.05%, 0.44% and 0.40%, respectively. They indicate a good performance of the I-V tracer with a high accuracy.

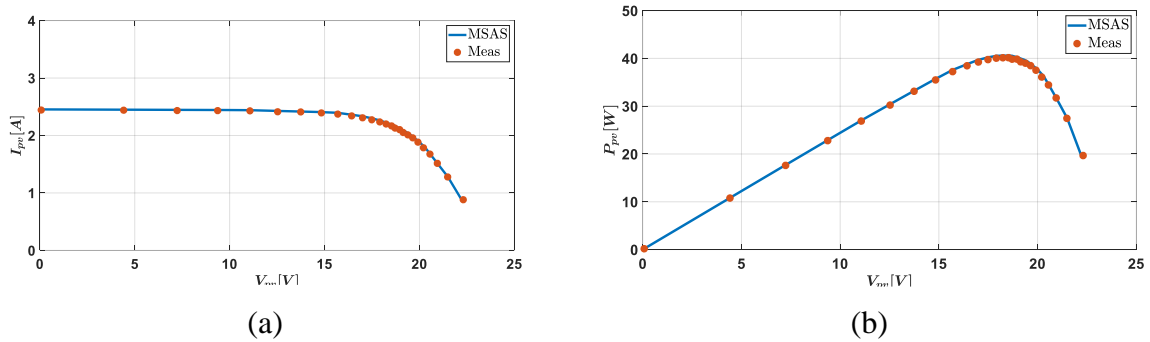


Fig.I.40: I-V and P-V curves obtained from I-V tracer and MSAS in the healthy case

Because of the limited load resistance ( $R_L = 22\Omega$ ) the I-V tracer cannot reach the open-circuit point  $V_{oc}$ . There are several solutions to address this issue: change the elements in the circuit (load resistance, MOSFETs) or use linear interpolation. The first solution is tedious and time consuming. The second one is more suitable for small data analysis. For big data, a more accurate method would be necessary, which is beyond the scope of this work. Finally, for sake of simplicity, we assume that the last point on the I-V curve, which corresponds to a resistance of  $22\Omega$ , is the open-circuit point (at  $V_{oc}$ ).

- *Partial shading case*

The I-V and P-V curves obtained from the I-V tracer and MSAS are displayed in Fig.I.41. The relative deviations  $MAPE_{I_{pv}}$ ,  $MAPE_{V_{pv}}$ ,  $ARE_{P_{mpp}}$ ,  $ARE_{I_{sc}}$  and  $ARE_{V_{oc}}$  are 3.65%, 5.51%, 8.57%, 0.47% and 0.36%, respectively. The results show that there is a mismatch around the inflexion points near the maximum operating point. The error could be reduced with the increase of the number of points in the current-varying region or with a different distribution of the points. However, despite this error around the MPP, the I-V tracer has an acceptable performance in the reproduction of the I-V curve in partial shading conditions.

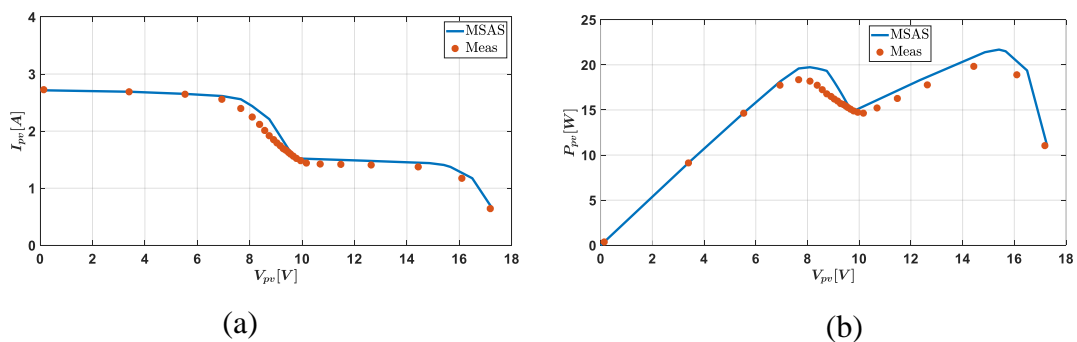


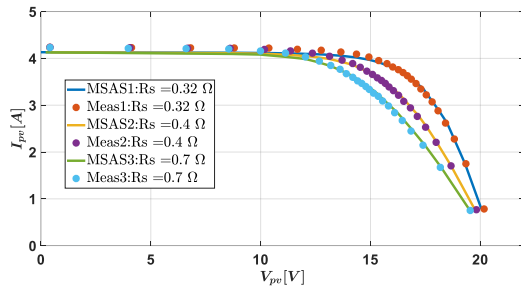
Fig.I.41: I-V and P-V curves obtained from I-V tracer and MSAS in partial shading case

- $R_s$  and  $R_{sh}$  degradations

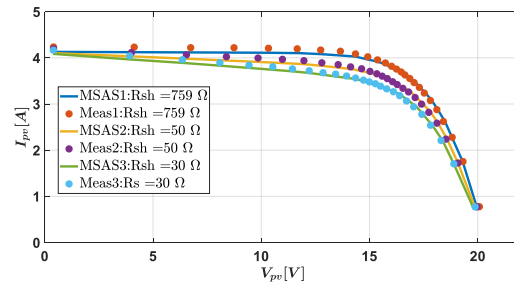
$R_s$  and  $R_{sh}$  degradation in PV modules occur due to ageing effects or aggressive external conditions affect the shape of the I-V characteristic [34][35]. The reference I-V curves in these faulty conditions are obtained by connecting additional resistances in series (in parallel) with the PV model (the SDM with five parameters available in the Matlab/Simulink). The information used in the simulation is summarized in *Table.I.10*. The results are plotted in *Fig.I.42*. There is a good agreement between the measured and reference data under the faulty conditions. The deviations are summarized in *Table.I.11*

*Table.I.10: Data used in the simulation to create the I-V curves for  $R_s$  or  $R_{sh}$  degradation*

$G_{poa} = 770 \text{ W/m}^2$ and $T_{pv} = 39^\circ\text{C}$	Healthy case	case1	case2
$R_s$ degradation (connected the additional resistance in series with PV model )	323 m $\Omega$	400 m $\Omega$	700m $\Omega$
$R_{sh}$ degradation (connected the additional resistance in parallel with the PV model )	759.6 $\Omega$	50 $\Omega$	30 $\Omega$



(a)  $R_s$  degradation



(b)  $R_{sh}$  degradation

*Fig.I.42: I-V curves obtained from I-V tracer and MSAS in case of  $R_s$  and  $R_{sh}$  degradation*

*Table.I.11: Deviations in the case of  $R_s$  and  $R_{sh}$  degradation*

$R_s$ degradation			
Deviation	Healthy case ( $R_s = 0.32 \Omega$ )	case1( $R_s = 0.4 \Omega$ )	case( $R_s = 0.7 \Omega$ )
$MAPE_{I_{pv}}(\%)$	0.94	0.82	0.74
$MAPE_{V_{pv}}(\%)$	0.79	0.88	0.86
$ARE_{P_{mpp}}(\%)$	0.11	0.03	0.183
$ARE_{V_{oc}}(\%)$	0.61	0.33	0.06
$ARE_{I_{sc}}(\%)$	1.12	1.14	1.15
$R_{sh}$ degradation			
Deviation	Healthy case ( $R_{sh} = 759 \Omega$ )	Case1( $R_{sh} = 50 \Omega$ )	Case2( $R_{sh} = 30 \Omega$ )
$MAPE_{I_{pv}}(\%)$	0.98	0.73	0.87
$MAPE_{V_{pv}}(\%)$	0.46	0.41	0.42
$ARE_{P_{mpp}}(\%)$	0.70	0.43	0
$ARE_{V_{oc}}(\%)$	0.62	0.49	0.49
$ARE_{I_{sc}}(\%)$	1.13	1.12	1.13

### *I.5.3. Summary of the validation*

The methodologies for the calibration and validation of the I-V tracer with the E4360 Modular Solar Array Simulator (MSAS) from Keysight Technologies, Inc were presented, and evaluated.

The current and voltage of the I-V tracer were calibrated in ampere and volt, respectively. For the calibration, various current (1.5A to 5A) and voltage (10V -24 V) values were employed. The result reveal that the deviations are relatively higher for low current and voltage (1.5A -10V and 2A-12 V) compared to higher values of current and voltage 2.5A-14V to 5A-24V. The repeatability has also been successfully evaluated.

For the validation, healthy case, partial shading (PS) ,  $R_s$  and  $R_{sh}$  degradations were considered. The findings indicate that the I-V tracer can accurately measure the I-V characteristic of the PV module in healthy and faulty cases, even if the accuracy is lower in the case of PS.

Finally, it can be concluded that the developed I-V tracer is reliable, has a low cost and a short response time. It is therefore suitable for monitoring a PV module.

## **I.6. Elimination of abnormal I-V curves due to over-illumination**

### *I.6.1. Observation of abnormal curves*

*Fig.I.43* shows several I-V curves measured in healthy case on sunny days. We observed every day, round noon, the occurrence of abnormal I-V curves (circled in red), in the low voltage zone. These abnormal I-V curves exhibit inflexion points as in the case of partial shading and the triggering of bypass diodes [36]–[38], which was not obviously the case. After visual inspection, we found that the aluminum tube next to the PV module, was responsible round noon of an overillumination of one part of the PV module, as shown in *Fig.I.44*. As a consequence, the PV module was receiving a non uniform irradiance, triggering the bypass diode! To avoid any misinterpretation, the abnormal I-V curves must be eliminated before processing the data. As the PV module behaves like in partial shading conditions, the partial shading detection techniques could be used to eliminate the abnormal curves. They are investigated in this section.

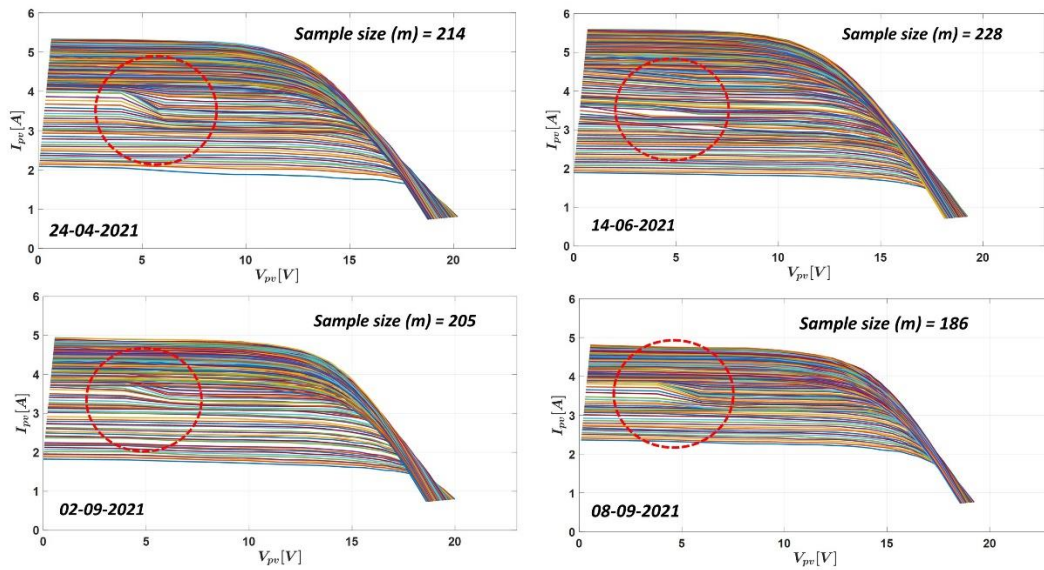


Fig.I.43: I-V curves measured in healthy case on 24<sup>th</sup> April, 14<sup>th</sup> June, 2<sup>nd</sup> and 8<sup>th</sup>, September 2021

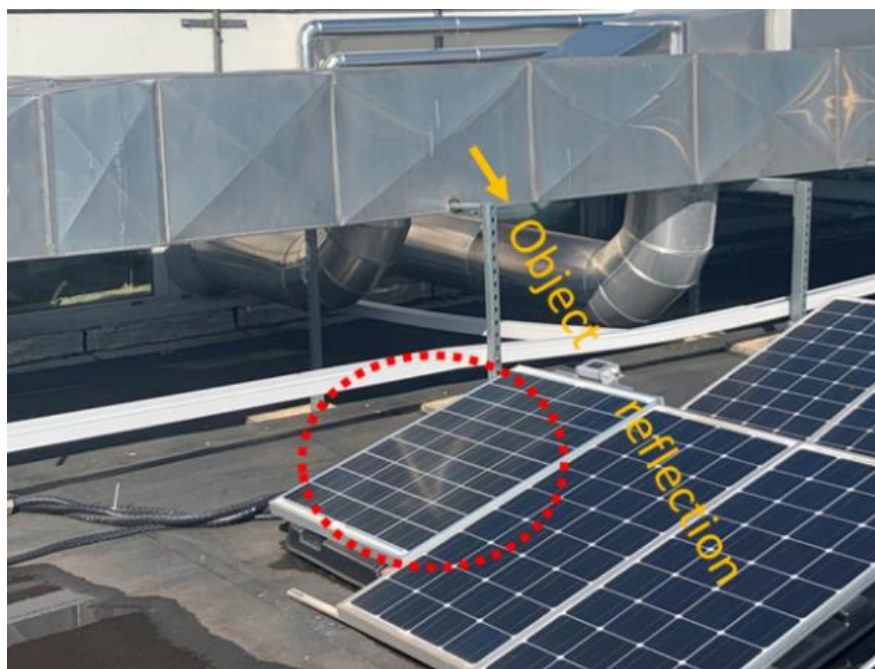


Fig.I.44: Reflection on the PV panel

### I.6.2. Partial shading detection methods using the I-V curve

In PV systems, shading is a significant issue. It occurs when the PV module is partially shaded. The current generated by the shaded cells is reduced, limiting the maximum current generated by the other series-connected cells. The bypass diodes are triggered to reduce shading impacts by preventing healthy cells from going into reverse bias, which can cause reverse

breakdown voltage and hot spots. Beside bypass diodes, the detection of such a mismatch is still essential as the partial shading can be due to dust soiling or bird droppings for example.

This section presents the partial shading detection techniques based on I-V characteristics. The first technique exploits the inflection point by calculating the first and second order derivatives of the I-V characteristic [38], [39]. The second technique calculates the irradiance values from the short-circuit current, and the current measured at the maximum power point (MPP) [40], [41]. The third uses a linear interpolation that is compared with the measured data in the low voltage zone. *Fig.I.45* depicts the flowcharts of the three techniques.

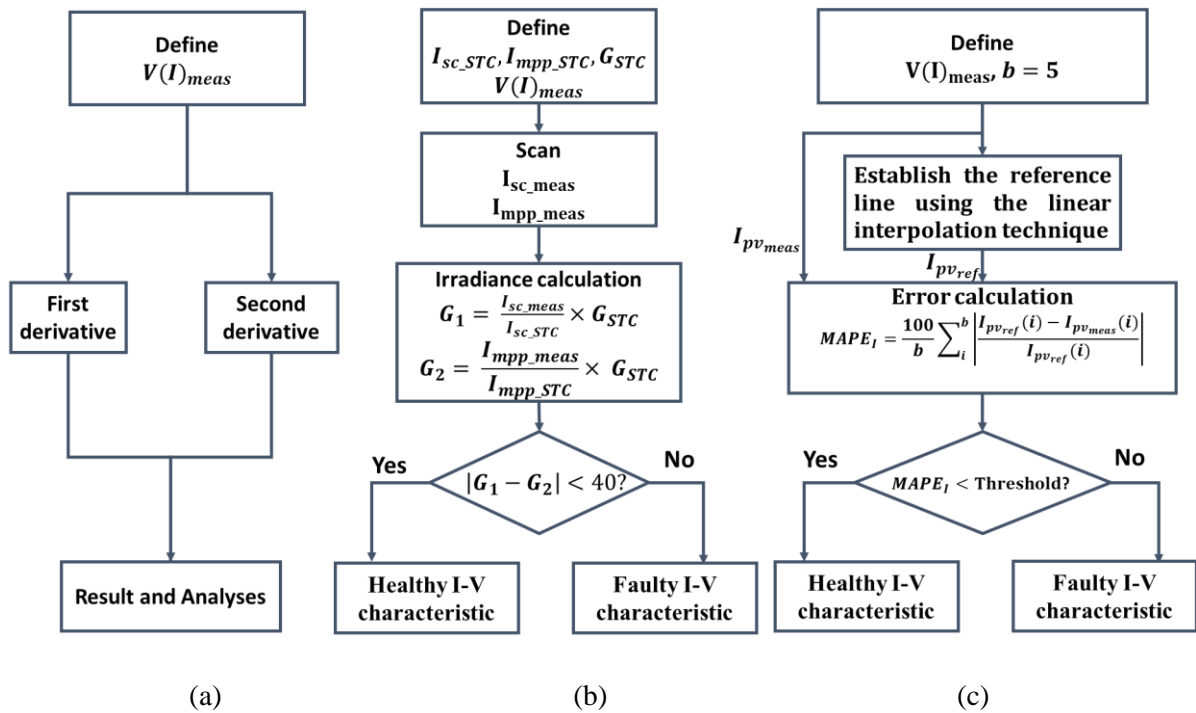


*Fig.I.45: Flowcharts of partial shading detection techniques based on I-V characteristics*

The calculation of derivatives is highly sensitive to the accuracy of the measurement and the number of samples. In our case, we have compromised the I-V curve measurement with only 26 samples distributed logarithmically. There are only five points in the low-voltage zone mainly affected by over-illumination. Therefore, this technique will not be suitable for our application.

#### 1.6.2.1. Calculation of the irradiance value with $I_{sc}$ and $I_{mpp}$

One of the partial shading detection methods proposed in [40] consists in calculating the values of the irradiance with  $I_{sc}$  and  $I_{mpp}$  denoted  $G_1$  and  $G_2$ , respectively. Under the assumption that the temperature remains constant, we can write:

$$G_1 = \frac{I_{sc}}{I_{sc\_STC}} G_{STC}, \quad G_2 = \frac{I_{mpp}}{I_{mpp\_STC}} G_{STC} \quad (I.30)$$

Where  $I_{sc\_STC}$ ,  $I_{mpp\_STC}$  and  $G_{STC}$  are retrieved from [Table.I.2](#), while  $I_{sc}$ , and  $I_{mpp}$  are taken from the I – V curve measurement. Under uniform illumination conditions, the current at the maximum power points ( $I_{mpp}$ ) is close to  $I_{sc}$  (approximately 90%)[40], [42]. As a consequence,  $|G_1 - G_2| < \Delta G_{th}$  where  $\Delta G_{th}$  is a threshold.

The flowchart of the technique is represented in [Fig.I.45](#) (b). The threshold is first set at  $40 W/m^2$ , as in [49].

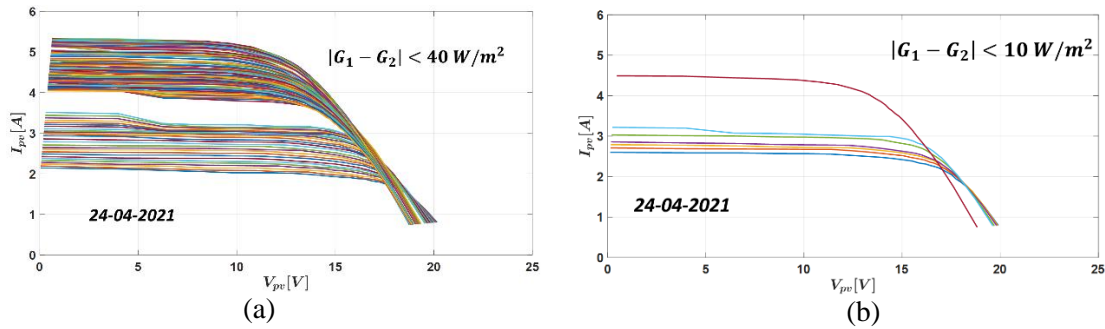


[Fig.I.46](#): I-V characteristics of PV panel after applying the partial shading detection method 2

[Fig.I.46](#) shows the results of the application of this technique to measured I-V curves. The results show that despite an improvement, there are still several abnormal I-V curves, even with a lower threshold ( $10 W/m^2$  in [Fig.I.46](#) (b)). It can be concluded that this technique would be more suitable to detect high over-illumination.

### I.6.2.2 Linear interpolation technique

The proposed method uses the linear interpolation method to draw a reference line from the five points measured in the low-voltage zone, as shown in [Fig.I.47](#), for healthy and faulty conditions. The reference lines 1 and 2 were created from the measured I-V curves in the healthy and faulty cases. The mean absolute percentage error of current ( $MAPE_I$ ) between the linear interpolation and the actual measurements is calculated to evaluate the distortion due to over-illumination.

$$MAPE_I = \frac{100}{b} \sum_i^b \left| \frac{I_{pv_{ref}}(i) - I_{pv_{meas}}(i)}{I_{pv_{ref}}(i)} \right| \quad (I.31)$$

Where  $I_{pv_{ref}}$ ,  $I_{pv_{meas}}$  are the reference and measured line, respectively,  $b$  is the measurement data points at low voltage zone.

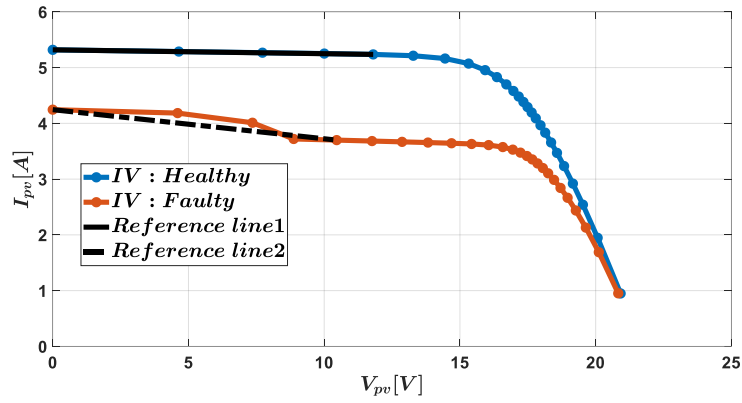


Fig.I.47: I-V characteristics of PV module using the logarithmic distribution of points in the healthy and shading cases

- Evaluation of the technique with synthetic data

The single diode model (at the cell level) developed in [43] is used to simulate the PV module to evaluate the proposal. Fig.I.48 displays the methodology with the following conditions: a difference of  $50 \text{ W/m}^2$  is introduced to emulate the over-illumination. The LDP is used to retain only 26 points from the 1000 ones obtained from the simulation of the PV current vector denoted as  $I_{PV_{sim26}}$  in healthy and faulty cases. The vector is used for the linear interpolation to get  $I_{PV_{ref}}$ . Then, the  $MAPE_I$  is computed for analysis.

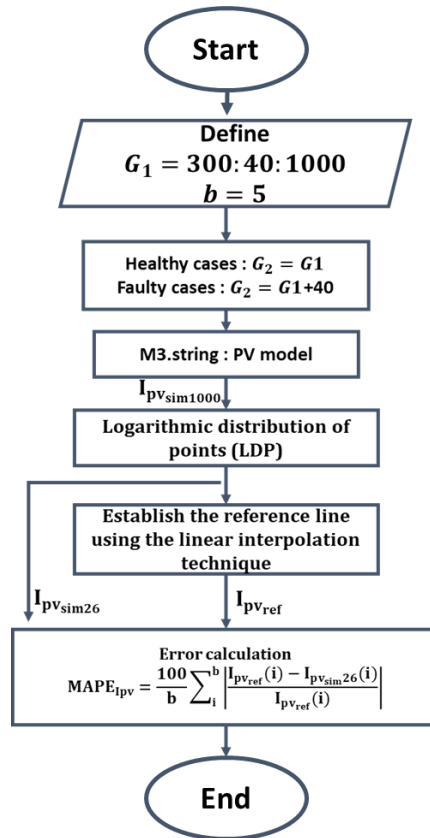


Fig.I.48: Flowchart for the evaluation of the linear interpolation.



Fig.I.49(a) and Fig.I.49 (b) illustrate the results for the healthy and faulty cases, respectively. In the healthy case, the linear interpolation fits almost perfectly with the I-V curve. Fig.I.50 shows that in this case, the  $MAPE_I < 0.4\%$ . In the case of over-illumination, the  $MAPE_I > 0.98\%$ . These results will be used to set the threshold to eliminate abnormal curves.

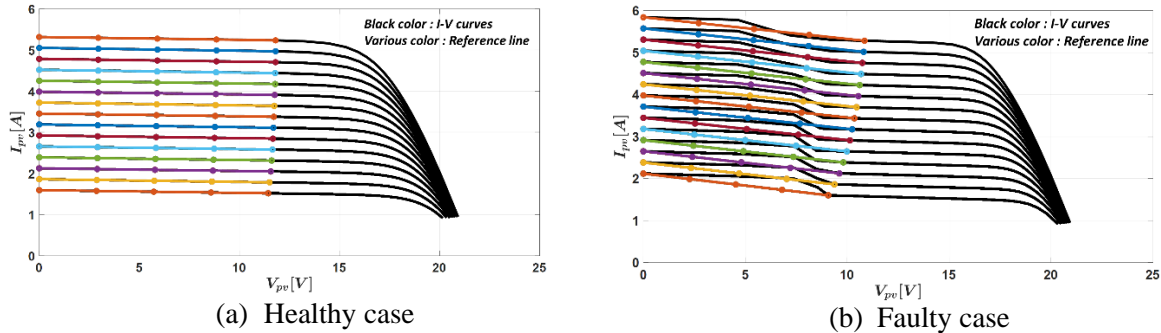


Fig.I.49: I-V characteristics and linear interpolations.

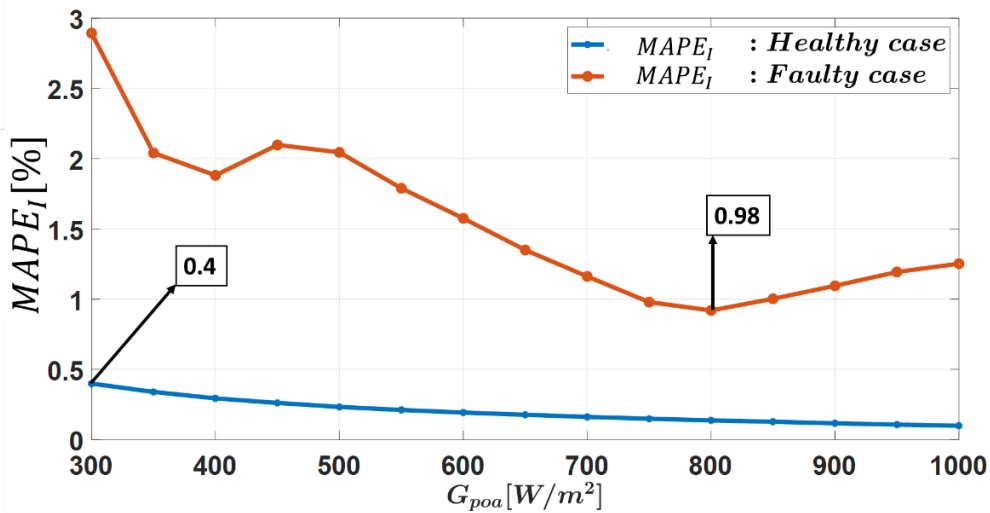
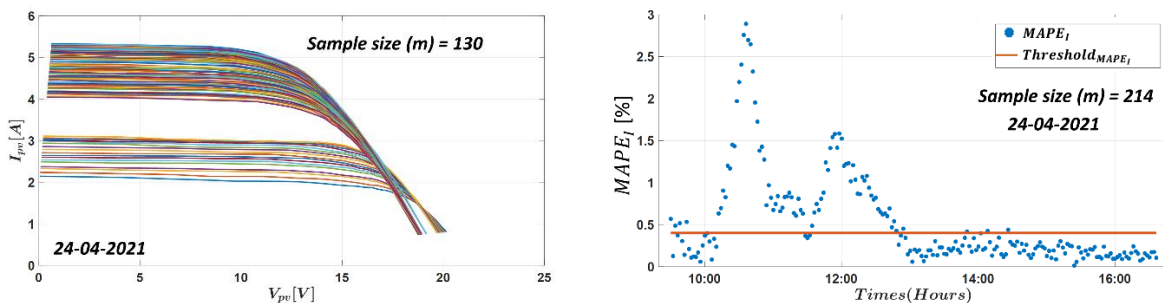


Fig.I.50: Mean Absolute Percentage Error of current ( $MAPE_I$ ).

- Evaluation of the technique with experimental data

The I-V curves are collected on April 24<sup>th</sup>, June 14<sup>th</sup>, September 2<sup>nd</sup>, and 8<sup>th</sup>.



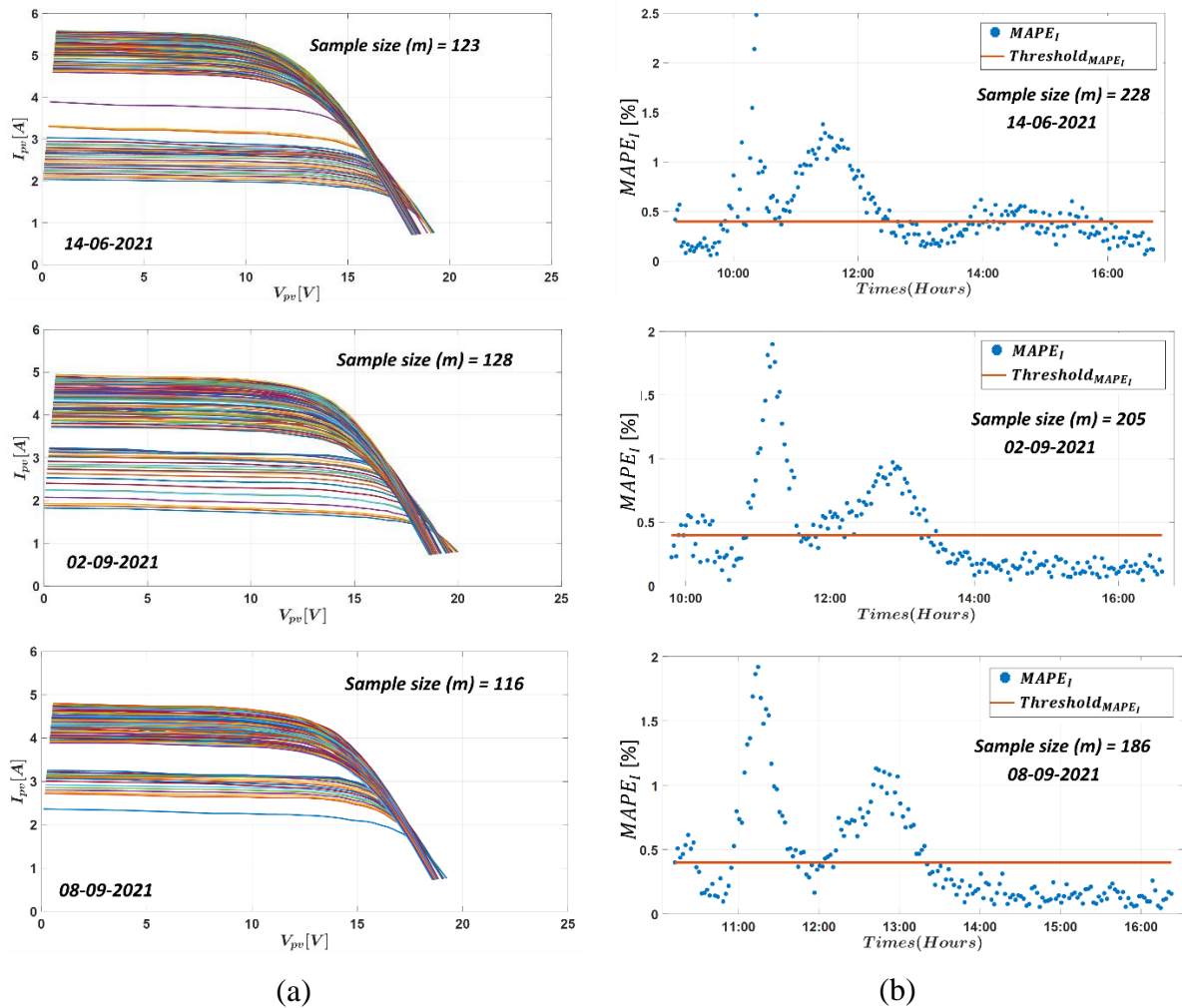


Fig.I.51: I-V characteristics of PV panel and MAPE of current profiles after eliminating the abnormal I-V curves using the MAPE threshold of 0.4%

Fig.I.51(a) displays the remaining I-V characteristics after the elimination of the abnormal curves when the threshold is set at 0.4% for the  $MAPE_I$ . We can see in Fig.I.51 (b) that the over-illumination that occurs everyday at the same time (from 11 AM to 1 PM) leads the MAPE to cross the detection threshold. Finally, we can conclude that the proposed method can eliminate the abnormal I-V curves due to over-illumination. Therefore, the proposal will process all the measured I-V curves before being used to extract the parameters.

## I.7. Conclusion

This chapter was mainly dedicated to developing the experimental test bench, which consists of a low-cost I-V tracer, TC 74 temperature sensor, reference cell for irradiance measurement, and fault emulator. Based on the literature review on I-V tracers, the I-V tracer based on a DC-DC converter was selected for our study.

The number of points is a compromise between the duration of the measurement, which should be as short as possible to minimize the power losses due to the interruption, and the

required accuracy for post-processing. In this regard, the logarithmic distribution of points (LDP) and the uniform distribution of points (UDP) algorithms were evaluated, analyzed and compared to determine the optimal number of points on the I-V curve. The results demonstrated that the absolute relative error (*ARE*) is lower for the LDP algorithm, which was selected for the I-V tracer.

The I-V tracer was calibrated and validated via a high-efficiency E4360A Modular Solar Array Simulator (MSAS) Keysight with an accuracy of 1.33% in the healthy case. We have also shown that it can also measure the I-V curves of faulty PV modules (partial shading,  $R_s$  degradation and  $R_{sh}$  degradation). This I-V tracer has a low cost, a short response time, a good repeatability. It is therefore suitable for monitoring PV modules in PV power plant.

During the acquisition, we noticed that some I-V curves exhibit an abnormal shape due to the activation of a bypass diode of the PV module that is periodically overilluminated by an aluminium tube. Thanks to a partial shading detection technique based on linear interpolation, the abnormal curves were successfully withdrawn to avoid any misinterpretation and wrong identification of the single diode parameters. In the following, all the measurement curves are preprocessed before being used.

## References of chapter I

- [1] E. Duran, M. Piliouguine, M. Sidrach-De-Cardona, J. Galan, and J. M. Andujar, "Different methods to obtain the I-V curve of PV modules: A review," 33rd IEEE Photovoltaic Specialist Conference, 11-16 May, San Diego, CA, USA, 2008.
- [2] Y. Zhu and W. Xiao, "A comprehensive review of topologies for photovoltaic I-V curve tracer," *Sol. Energy*, vol. 196, no. May 2019, pp. 346–357, 2020.
- [3] E. E. Van Dyk, A. R. Gxasheka, and E. L. Meyer, "Monitoring current-voltage characteristics and energy output of silicon photovoltaic modules," *Renew. Energy*, vol. 30, no. 3, pp. 399–411, 2005.
- [4] A. Q. Malik and S. J. B. H. Damit, "Outdoor testing of single crystal silicon solar cells," *Renew. Energy*, vol. 28, no. 9, pp. 1433–1445, 2003.
- [5] S. Sarikh, M. Raoufi, A. Bennouna, A. Benlarabi, and B. Ikken, "Implementation of a plug and play I-V curve tracer dedicated to characterization and diagnosis of PV modules under real operating conditions," *Energy Convers. Manag.*, vol. 209, no. October 2019, p. 112613, 2020.
- [6] Y. Kuai and S. Yuvarajan, "An electronic load for testing photovoltaic panels," *J. Power Sources*, vol. 154, pp. 308–313, 2006.
- [7] F. Spertino, J. Ahmad, A. Ciocia, P. Di Leo, A. F. Murtaza, and M. Chiaberge, "Capacitor charging method for I-V curve tracer and MPPT in photovoltaic systems," *Sol. Energy*, vol. 119, pp. 461–473, 2015.
- [8] Z. Chen, W. Lin, L. Wu, C. Long, P. Lin, and S. Cheng, "A capacitor based fast I-V characteristics tester for photovoltaic arrays," *Energy Procedia*, vol. 145, pp. 381–387, 2018.
- [9] F. Spertino, J. Ahmad, P. Di Leo, and A. Ciocia, "A method for obtaining the I-V curve of photovoltaic arrays from module voltages and its applications for MPP tracking," *Sol. Energy*, vol. 139, pp. 489–505, 2016.
- [10] L. A. Hecktheuer, A. Krenzinger, and C. W. M. Prieb, "Methodology for Photovoltaic Modules Characterization and Shading Effects Analysis," *J. Brazilian Soc. Mech. Sci.*, vol. 24, pp. 26–32, 2002.
- [11] E. Durán, J. Galán, J. M. Andújar, D. D. I. Electrónica, D. S. Infor, and U. De Huelva, "A new application of the Buck -Boost -Derived Converters to obtain the I-V curve of photovoltaic modules," pp. 413–417, 2007.
- [12] T. A. Pereira, L. Schmitz, W. M. Dos Santos, D. C. Martins, and R. F. Coelho, "Design of a Portable Photovoltaic I-V Curve Tracer Based on the DC-DC Converter Method," *IEEE J. Photovoltaics*, vol. 11, no. 2, pp. 552–560, 2021.
- [13] P. Sanchis, I. Echeverría, A. Ursúa, O. Alonso, E. Gubía, and L. Marroyo, "Electronic converter for the analysis of photovoltaic arrays and inverters," 34th IEEE Annual Conference on Power Electronics Specialist, 15-19 June 2003, Acapulco, Mexico, vol. 4, pp. 1748–1753, 2003.
- [14] J. T. de Carvalho Neto, "A Comparative Analysis of the Main Methods for Tracing PV Characteristic Curve Through Experimental Tests," pp. 1–6, 2022.
- [15] "FTV 2000 I-V tracer"[online]. Available : [https://chauvin-arnoux.fi/wp-content/uploads/2014/07/FTV200\\_GB.pdf](https://chauvin-arnoux.fi/wp-content/uploads/2014/07/FTV200_GB.pdf). [Accessed: 12-May-2022].

- [16] “I-V 500W tracer.”[Online]. Available:<https://www.ht-instruments.com/en/products/i-v525w/download/brochure/>. [Accessed: 12-May-2022].
- [17] “Electronic load Model 63600 series.” [Online]. Available: <https://www.chromaate.com/downloads/catalogue/Power/63600-EN.pdf>. [Accessed: 12-May-2022].
- [18] “MP-11 I-V Checker | EKO Instruments.” [Online]. Available: <https://eko-eu.com/products/solar-energy/iv-measurements/mp-11-i-v-checker>. [Accessed: 12-May-2022].
- [19] Huawei. Smart I-V Curve Diagnosis; 2020. Available : <https://solar.huawei.com/en-GB/download?p=%252F-%252Fmedia%252FSolar%252Fattachment%252Fpdf%252F%252Fdatasheet%252FIV-Curve.pdf>. [Accessed:12-May2022].
- [20] “Solmetric PV Analyzer I-V Curve Tracer User’s Guide with SolSensor TM 200 PVA-600 + with SolSensor TM.” [Online]. Available: [www.solmetric.com](http://www.solmetric.com). [Accessed: 12-May-2022].
- [21] R. Mukaro and X. F. Carelse, “A serial communication program for accessing a microcontroller-based data-acquisition system,” *Comput. Geosci.*, vol. 23, no. 9, pp. 1027–1032, 1997.
- [22] L. M. Ayompe, A. Duffy, S. J. McCormack, and M. Conlon, “Measured performance of a 1.72 kW rooftop grid connected photovoltaic system in Ireland,” *Energy Convers. Manag.*, vol. 52, no. 2, pp. 816–825, 2011.
- [23] M. Gagliarducci, D. A. Lampasi, and L. Podestà, “GSM-based monitoring and control of photovoltaic power generation,” *Meas. J. Int. Meas. Confed.*, vol. 40, no. 3, pp. 314–321, 2007.
- [24] E. Koutroulis and K. Kalaitzakis, “Development of an integrated data-acquisition system for renewable energy sources systems monitoring,” *Fuel Energy Abstr.*, vol. 44, no. 3, p. 163, 2003.
- [25] M. E. Andreoni López, F. J. Galdeano Mantiñan, and M. G. Molina, “Implementation of wireless remote monitoring and control of solar photovoltaic (PV) system, 6th IEEE/PES Transmission and Distribution: Latin America Conference and Exposition (T&D-LA), 3-5 September, Montevideo, Uruguay, pp. 1–6, 2012.
- [26] C. W. Riley and L. M. Tolbert, “An online autonomous I-V tracer for PV monitoring applications,” *IEEE Power & Energy Society General Meeting*, 26-30 July, Denver, CO, USA, pp.1-5, 2015
- [27] Z. Chen, Y. Chen, L. Wu, S. Cheng, and P. Lin, “Deep residual network based fault detection and diagnosis of photovoltaic arrays using current-voltage curves and ambient conditions,” *Energy Convers. Manag.*, vol. 198, no. May, p. 111793, 2019.
- [28] B. Li, C. Delpha, A. Migan-Dubois, and D. Diallo, “Fault diagnosis of photovoltaic panels using full I-V characteristics and machine learning techniques,” *Energy Convers. Manag.*, vol. 248, p. 114785, 2021.
- [29] X. Ma, W. H. Huang, E. Schnabel, M. Kohl, J. Brynjarsdottir, J. L. Braid, R. H. French, “Data-Driven I-V Feature Extraction for Photovoltaic Modules,” *IEEE J. Photovoltaics*, vol. 9, no. 5, pp. 1405–1412, 2019.
- [30] M. D. Yandt, J. P. D. Cook, M. Kelly, H. Schriemer, and K. Hinzer, “Dynamic Real-Time I-V Curve Measurement System for Indoor/Outdoor Characterization of Photovoltaic Cells and Modules,” *IEEE J. Photovoltaics*, vol. 5, no. 1, pp. 337–343, 2015.

- [31] Z. Chen, L. Wu, S. Cheng, P. Lin, Y. Wu, and W. Lin, "Intelligent fault diagnosis of photovoltaic arrays based on optimized kernel extreme learning machine and I-V characteristics," *Appl. Energy*, vol. 204, pp. 912–931, 2017.
- [32] B. K. Atay and U. Eminoğlu, "A new approach for parameter estimation of the single-diode model for photovoltaic cells/modules," *Turkish J. Electr. Eng. Comput. Sci.*, vol. 27, no. 4, pp. 3026–3039, 2019.
- [33] A. Vega, V. Valiño, E. Conde, A. Ramos, and P. Reina, "Double sweep tracer for I-V curves characterization and continuous monitoring of photovoltaic facilities," *Sol. Energy*, vol. 190, no. March, pp. 622–629, 2019.
- [34] E. E. van Dyk and E. L. Meyer, "Analysis of the effect of parasitic resistances on the performance of photovoltaic modules," *Renew. Energy*, vol. 29, no. 3, pp. 333–344, 2004.
- [35] C. Huang and L. Wang, "Simulation study on the degradation process of photovoltaic modules," *Energy Convers. Manag.*, vol. 165, no. October 2017, pp. 236–243, 2018.
- [36] M. R. Maghami, H. Hizam, C. Gomes, M. A. Radzi, M. I. Rezaadad, and S. Hajighorbani, "Power loss due to soiling on solar panel: A review," *Renew. Sustain. Energy Rev.*, vol. 59, pp. 1307–1316, 2016.
- [37] S. Fadhel, M. Trabelsi, I. Bahri, D. Diallo, and M. F. Mimouni, "Faults effects analysis in a photovoltaic array based on current-voltage and power-voltage characteristics," *17th International Conference on sciences and Technique of Automatic Control and Computer Engineering(STA)*, 19-21 December, Sousse, Tunisia, pp. 223–228, 2017.
- [38] Long BUN, "Détection et Localisation de Défauts pour un Système PV", PhD thesis Electrical Engineering, University of Grenoble, 2011.
- [39] M. Bressan, "Développement d'un outil de supervision et de contrôle pour une installation solaire photovoltaïque," PhD thesis Electronic, University of Perpignan" 2014.
- [40] J. Ahmed and Z. Salam, "An Accurate Method for MPPT to Detect the Partial Shading Occurrence in a PV System," *IEEE Trans. Ind. Informatics*, vol. 13, no. 5, pp. 2151–2161, 2017.
- [41] J. Gosumbonggot and G. Fujita, "Partial shading detection and global maximum power point tracking algorithm for photovoltaic with the variation of irradiation and temperature," *Energies*, vol. 12, no. 2, 2019.
- [42] K. Kobayashi, I. Takano, and Y. Sawada, "A study of a two-stage Maximum Power Point Tracking control of a photovoltaic system under partially shaded insolation conditions," *Electr. Eng. Japan (English Transl. Denki Gakkai Ronbunshi)*, vol. 153, no. 4, pp. 39–49, 2005.
- [43] V. Kongphet, A. Migan-dubois, C. Delpha, and D. Diallo, "Photovoltaic Fault Detection and Diagnosos: Which level of Granularity for PV Modeling?," *Prognostics and Health Management Conference (PHM-Besancon)*, 4-7 May 2020, Besancon, France, pp.180-186,2020.

## List of figures of chapter I

Fig.I.1: Variable load resistance technique .....	4
Fig.I.2: Electronic load technique for the I-V tracer .....	4
Fig.I.3: The I-V curve and the MOSFET characteristics [2].....	5
Fig.I.4: Capacitor load technique for I-V tracer .....	5
Fig.I.5: I-V capacitor: technologies and voltage ranges [2] .....	6
Fig.I.6: I-V curve and four-quadrant power supply .....	7
Fig.I.7: Basic circuit for an I-V tracer using the four-quadrant power supply technique.....	7
Fig.I.8: DC-DC converter used as an I-V tracer.....	8
Fig.I.9: Schematic diagram of the testbed .....	10
Fig.I.10: Main circuit design .....	11
Fig.I.11 : Electric relay circuit.....	12
Fig.I.12 : Load resistance circuit.....	12
Fig.I.13 : Transistor control circuit.....	13
Fig.I.14: Circuit for voltage and current measurements .....	13
Fig.I.15: Automatic emulator for $R_s$ and $R_{sh}$ degradation.....	15
Fig.I.16: Image of the experimental test bench .....	16
Fig.I.17: Block diagram of the data acquisition system .....	17
Fig.I.18: Flowchart of the software for data acquisition .....	17
Fig.I.19: Layout of I-V curve .....	18
Fig.I.20: Logarithmic and uniform distribution of points on the I-V curve .....	20
Fig.I.21: I-V characteristic of PV module type A .....	20
Fig.I.22: Flowchart of the methodology .....	21
Fig.I.23: Variation of $R_s$ and $ARER_s$ with $NbPtV$ and $NbPtI$ .....	22
Fig.I.24: Variation of $R_{sh}$ and $ARER_{sh}$ with $NbPtV$ and $NbPtI$ .....	23
Fig.I.25: Variation of $I_{ph}$ and $AREI_{ph}$ with $NbPtV$ and $NbPtI$ .....	23
Fig.I.26: Variation of $I_0$ and $AREI_0$ with $NbPtV$ and $NbPtI$ .....	24
Fig.I.27: Variation of $n$ and $AREn$ with $NbPtV$ and $NbPtI$ .....	24
Fig.I.28: Variation of $MAPEI_{pv}$ (26 sampling points )with $NbPtV$ and $NbPtI$ .....	25
Fig.I.29: Evaluation of $MAPEI_{pv}$ (1000 sampling points) with $NbPtV$ and $NbPtI$ .....	25
Fig.I.30: Schematic circuit of the I-V tracer.....	27
Fig.I.31: Software flowchart of the I-V tracer using the logarithmic distribution of points .....	27
Fig.I.32: Simplified the main circuit of the I-V tracer .....	28
Fig.I.33: Acquisition time .....	29
Fig.I.34: Methodology for I-V tracer calibration (a) and validation (b).....	30
Fig.I.35: Experimental test bench for calibration and validation of I-V tracer at GeePs .....	30
Fig.I.36: Power supply output characteristic in SAS mode.....	31

Fig.I.37: Power supply output characteristic in Fixed mode .....	31
Fig.I.38: Scale-up process .....	32
Fig.I.39: I-V curves of MSAS and I-V tracer in the fixed mode for various scenarios .....	33
Fig.I.40: I-V and P-V curves obtained from I-V tracer and MSAS in the healthy case.....	35
Fig.I.41: I-V and P-V curves obtained from I-V tracer and MSAS in partial shading case.....	35
Fig.I.42: I-V curves obtained from I-V tracer and MSAS in case of $R_s$ and $R_{sh}$ degradation .....	36
Fig.I.43: I-V curves measured in healthy case on 24 <sup>th</sup> April, 14 <sup>th</sup> June, 2 <sup>nd</sup> and 8 <sup>th</sup> . September 2021..	38
Fig.I.44: Reflection on the PV panel .....	38
Fig.I.45: Flowcharts of partial shading detection techniques based on I-V characteristics .....	39
Fig.I.46: I-V characteristics of PV panel after applying the partial shading detection method 2.....	40
Fig.I.47: I-V characteristics of PV module using the logarithmic distribution of points in the healthy and shading cases .....	41
Fig.I.48: Flowchart for the evaluation of the linear interpolation. ....	41
Fig.I.49: I-V characteristics and linear interpolations. ....	42
Fig.I.50: Mean Absolute Percentage Error of current ( <i>MAPEI</i> ). ....	42
Fig.I.51: I-V characteristics of PV panel and MAPE of current profiles after eliminating the abnormal I-V curves using the MAPE threshold of 0.4% .....	43



List of tables of chapter I

Table I.1: Comparison of the I-V tracers [14]..... 9

Table.I.2: Characteristics under Standard Test Conditions (STC) ..... 10

Table.I.3: Comparison with commercially available I-V tracers ..... 12

Table.I.4: Extracted parameters from the reference vector ..... 21

Table.I.5: Deviation of PV model parameters between reference and estimated data ..... 26

Table.I.6 :  $MAPEI_{pv}$  between the reference and estimated vectors ..... 26

Table.I.7: Eight different configurations for CCC and CCV calculation ..... 33

Table.I.8: Relative calibration deviations..... 34

Table.I.9 : Evaluation of the repeatability ..... 34

Table.I.10: Data used in the simulation to create the I-V curves for  $R_s$  or  $R_{sh}$  degradation ..... 36

Table.I.11: Deviations in the case of  $R_s$  and  $R_{sh}$  degradation ..... 36

# Chapter II

## Modeling, extraction, and validation of electrical PV model in healthy cases

### Tables of contents

Chapter II: Modeling, extraction, and validation of Electrical PV model in healthy cases .....	64
II.1. Introduction .....	64
II.2. State of the art on electrical PV model.....	64
II.2.1. Ideal model .....	67
II.2.2. Single diode model with series resistance (four parameters).....	67
II.2.4. Two diode model (seven parameters).....	69
II.2.5. Three diode model (nine parameters) .....	70
II.2.6. Bishop model .....	70
II.2.6. Summary of PV model .....	71
II.3. Description of the SDM five parameters and their variation with environmental operating conditions .....	73
II.3.1. The photo-generated current ( $I_{ph}$ ) .....	73
II.3.2. The diode saturation current ( $I_0$ ).....	74
II.3.3. The series resistance ( $R_s$ ) .....	75
II.3.4. Shunt resistance ( $R_{sh}$ ) .....	75
II.3.5. The diode ideality factor ( $n$ ).....	76
II.3.6. Summary of parameter model variation with environmental conditions .....	76
II.4. Parameters extraction methods.....	77
II.4.1. Analytical approach .....	77
II.4.2. Numerical approach.....	77
II.4.3. Metaheuristic approach .....	78
II.4.4. Hybrid approach .....	78
II.4.5. Summary of extraction methods .....	78
II.5. Levenberg-Marquardt optimization algorithm description .....	79
II.5.1. Implementation in MATLAB.....	79
II.6. Description and validation of the analytical models .....	82
II.6.1. The training step.....	84

- II.6.2. *The validation step* ..... 95
- II.7. Description and validation of the hybrid PV model ..... 97
  - II.7.1. *Resampling I-V curves of simulation*..... 98
  - II.7.2. *Hybrid PV model validation*..... 100
- II.8. Analysis of sensitivity to errors due to variations of PV module temperature ( $T_{pv}$ ) ..... 103
- II.9. Conclusion..... 108
- References of chapter II ..... 110
- List of figures of chapter II..... 117
- List of tables of chapter II ..... 119

## Chapter II: Modeling, extraction, and validation of Electrical PV model in healthy cases

### II.1. Introduction

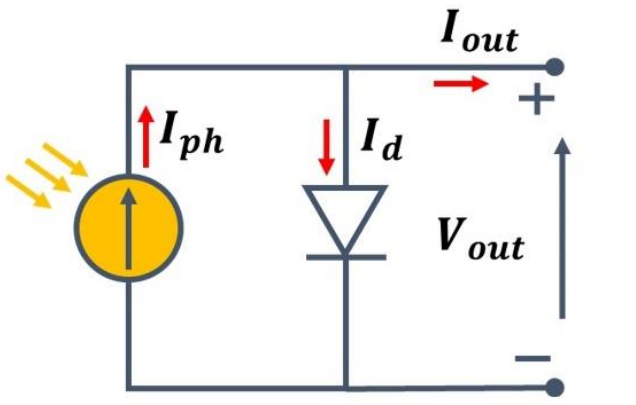
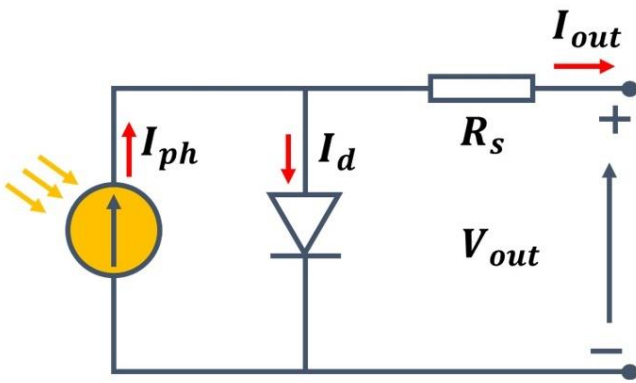
The previous chapter has highlighted the need to develop an experimental platform that can measure the I-V characteristic of healthy or faulty PV modules, including the characterization of the environment. In order to analyze the performance of a PV installation and make Fault Detection and Diagnosis (FDD), it is necessary to compare the measured values with those obtained by an accurate model, the FDD approach proposed is based on the complete I(V) characteristic, and only an equivalent electrical circuit will allow to simulate it, while the other types of modeling only give access to the MPP. This chapter presents the equivalent electrical model, and the objective is to define the model's parameters that best represent the I-V characteristics of the measured PV module. The PV module manufacturers' specifications do not allow for accurate modeling of PV performance under general and real environmental conditions. That's why we propose to extract electrical parameters from measured I-V characteristics. Consequently, accessibility to an accurate and reliable PV model is critical for FDD. The PV model will be used as the reference in health monitoring systems based on the comparison between the measured and the estimated current-voltage (I-V) characteristics. Hence, this chapter aims to identify and validate the PV model that we will use for FDD. In section II.2, we first present the state of the art on the electrical model equivalent of a PV module. The parameters used in the model are environment-dependants. As a consequence, analytical models of those parameters are described in section II.3. The parameters' extraction methods are cited in section II.4. The implementation of the numerical method based on Levenberg Marquardt is explained in section II.5. Thus, in section II.6 a method is proposed to extract the PV model parameters and validate the single diode model (SDM), including error analysis. Section II.7 introduces the exploitation, utilization, and validation of a hybrid PV model, associating the analytical parameters model and numerical SDM. The influence of the PV module temperature on the PV model is explained in section II.8. The last section of this chapter is a conclusion.

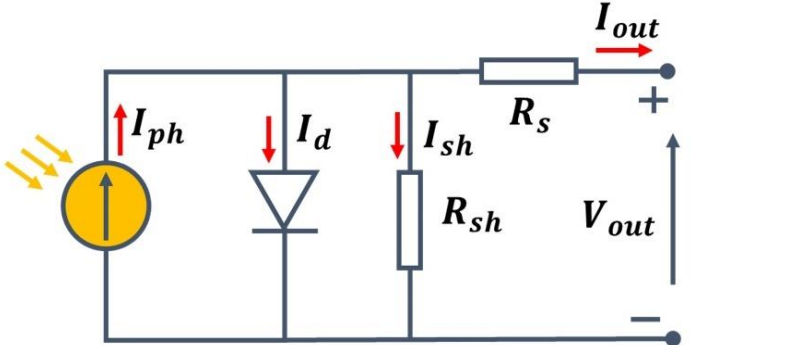
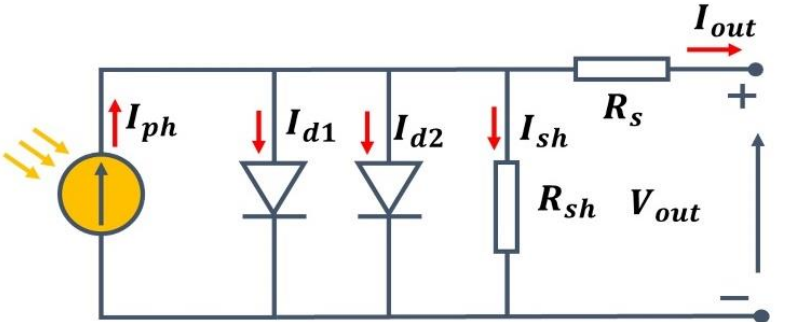
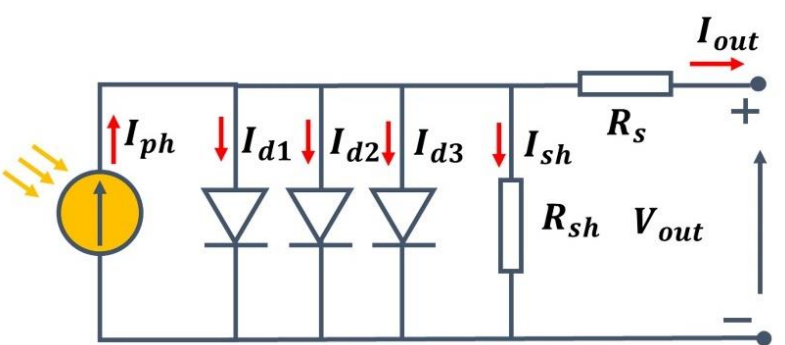
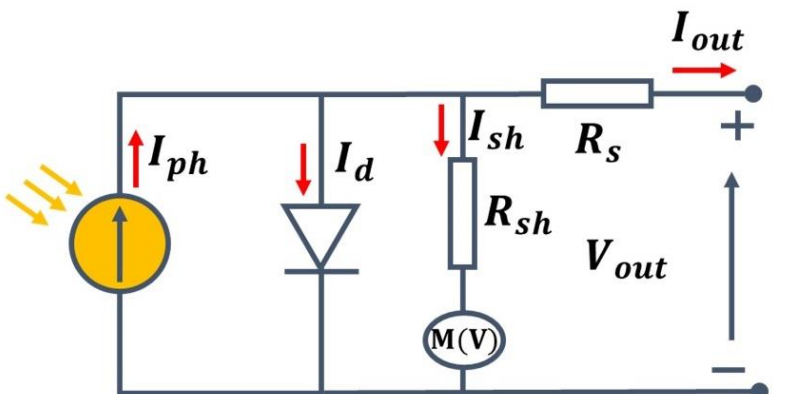
### II.2. State of the art on electrical PV model

The modeling of PV modules necessarily involves a judicious choice of equivalent electrical circuits, taking more or less details. Numerous mathematical models have been

developed to reproduce the highly nonlinear behavior resulting from the semiconductor PN junction, the basis of the photoelectric effect. Many approaches are used to simulate the performance of PV cells/modules/strings/arrays. In our study, we have decided to focus on the module level. Artificial networks have been proposed in [1]. However, the equivalent electrical circuit is the most commonly used. In the literature, several electrical models have been proposed to estimate photovoltaic module performance and energy productivity in real operating conditions [2]–[6]. The complexity of the models depends on the number of elements in the circuit and, consequently, on the number of parameters to identify. Each model is essentially an improvement of the ideal model, which contains a current source representing the photo-current and a diode that models the PN junction; the most widely used electrical circuit models are summarized in Table. II. 1, which will be presented and compared in the next parts.

Table. II. 1: Different electrical models

Model	Circuit model	Parameters	Accuracy Computation time
Ideal Model		$I_{ph}, n, I_0$	Low Fast
Single diode model with series resistance		$I_{ph}, n, I_0, R_s$	Quite good Fast

<p>Single diode model with series and parallel resistances (SDM)</p>		<p><math>I_{ph}, n, I_0,</math> <math>R_s, R_{sh}</math></p>	<p>Good Fast</p>
<p>Two diodes model</p>		<p><math>I_{ph}, n_1,</math> <math>I_{01}, n_2,</math> <math>I_{02}, R_s, R_{sh}</math></p>	<p>Very good High</p>
<p>Three diodes model</p>		<p><math>I_{ph}, n_1,</math> <math>I_{01}, n_2,</math> <math>I_{02}, n_3, I_{03},</math> <math>R_s, R_{sh}</math></p>	<p>Very good High</p>
<p>Bishop model</p>		<p><math>I_{ph}, n, I_0,</math> <math>R_s, R_{sh},</math> <math>V_{br}, a, m</math></p>	<p>Good High</p>

$I_{ph}$  is the generated photo-current,  $n$  or  $n_i$  is the ideality factor of the diode  $d$  or  $d_i$  and  $I_0$  or  $I_{0i}$  is the saturation current.  $R_s$  and  $R_{sh}$  are the series and shunt resistances, respectively.  $V_{br}$  is

the breakdown voltage,  $a$  is the avalanche fraction, and  $m$  is the avalanche exponent for Bishop model.

### II.2.1. Ideal model

Fig.II. 1 illustrates an ideal PV cell, which consists of a single diode connected in anti-parallel with a photo-generated current source ( $I_{ph}$ ).

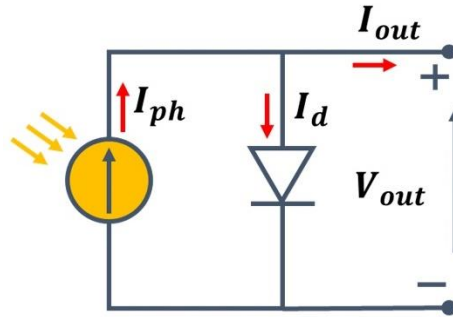


Fig.II. 1: Ideal PV circuit model (3 parameters)

The relationship between the output current and voltage has been investigated [3], and the output current can be expressed as below:

$$I_{out} = I_{ph} - I_d = I_{ph} - I_0 \left[ \exp \left( \frac{qV_{out}}{nKT} \right) - 1 \right] \quad (II.1)$$

Where  $I_{out}$  refers to the PV output current,  $I_{ph}$  defines the photo-generated current,  $I_0$  denotes diode saturation current,  $K$  is the Boltzmann constant ( $1.3806 \times 10^{-23} JK^{-1}$ ),  $q$  represents the electron's charge ( $1.602 \times 10^{-19} C$ ),  $V_{out}$  denotes the PV output voltage,  $n$  is the diode ideality factor, and  $T$  refers to the temperature of the P-N junction in Kelvin; this temperature is usually assumed to be equal to the PV module temperature ( $T_{pv}$ ) [7].

### II.2.2. Single diode model with series resistance (four parameters)

The ideal PV model is rarely used to model PV and is only utilized to explain the theory of PV cell modeling. When establishing a more realistic PV model, the contact resistance, the current flow resistance in the silicon material, and contact resistance between silicon and conductive surfaces are all taken into account by inserting a resistance ( $R_s$ ) in series in the ideal model [4], [8]. Fig.II. 2 shows this electrical circuit called the four-parameter model [2], [3], [9].

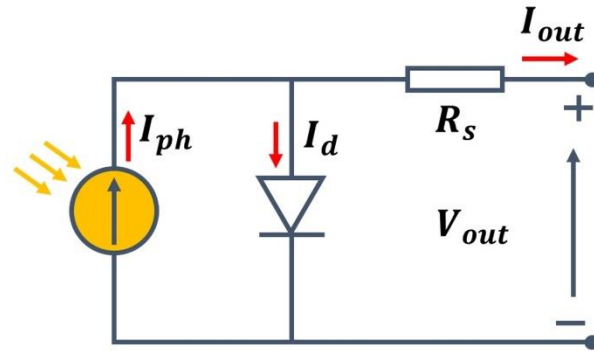


Fig.II. 2: Single diode model with series resistance (Four parameters)

The output current can be presented as below:

$$I_{out} = I_{ph} - I_d = I_{ph} - I_0 \left[ \exp \left( q \frac{V_{out} + I_{out} R_s}{nKT} \right) - 1 \right] \quad (II.2)$$

In [10], the four-parameters model was used to simulate three different PV technology: CIS, multi-crystalline silicon, and mono-crystalline silicon. The four-parameter model was also used to develop a mathematical model for PV modules that simply uses parameters from manufacturers' datasheets [11]. Even though this model is more accurate than the ideal model in simulating the behavior of physical PV modules, it's still insufficient for our FDD purpose.

### II.2.3. Single diode model with series and shunt resistances (SDM, 5 parameters)

A shunt resistance ( $R_{sh}$ ) is added to the PV model to take into account the leakage current of the P-N junction. The electrical circuit is shown in Fig.II. 3. This model is known as the five-parameters model and is widely used especially because of its reasonable compromise between accuracy and simplicity [12].

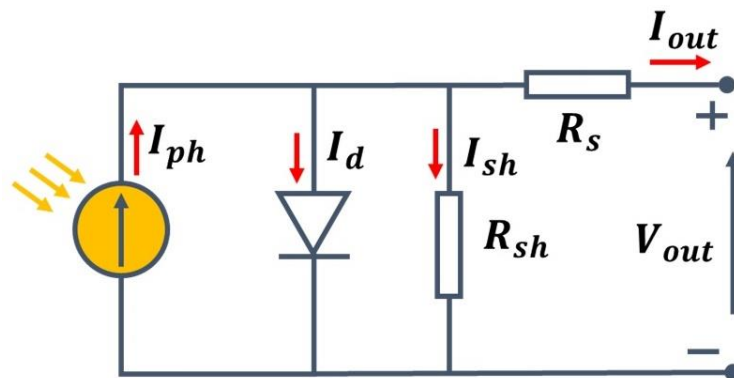


Fig.II. 3: Single diode model with series and shunt resistances (SDM, five parameters)

The output current can be re-written as below:



$$I_{out} = I_{ph} - I_d - I_{sh} = I_{ph} - I_0 \left[ \exp \left( q \frac{V_{out} + I_{out} R_s}{nKT} \right) - 1 \right] - \frac{V_{out} + I_{out} R_s}{R_{sh}} \quad (\text{II.3})$$

The addition of  $R_{sh}$  increased the number of parameters to five, namely  $I_{ph}$ ,  $R_s$ ,  $R_{sh}$ ,  $I_0$ , and  $n$ . The comparison between the four parameters and five parameters models was studied in [13], [14]. The result obtained from the PV module simulation and an optimal ANN model has been validated experimentally. The authors also demonstrated that the four-parameter model seems unable to describe the influence of high temperature on current, leading to a less accurate model than the five-parameter model. Another comparative study in [15] has demonstrated that the five-parameters model has a better fit with the experimental data than the four-parameters model.

#### II.2.4. Two diode model (seven parameters)

The single diode model is widely used, which can achieve acceptable accuracy. However, the single diode model essentially ignores the impact of current recombination loss in the depletion zone. Consequently, a second diode (d2) is added to the SDM to take into account for this loss, and this model provides reasonable precision under low irradiance [4]. The electrical circuit of the two diode model is shown in Fig.II. 4.

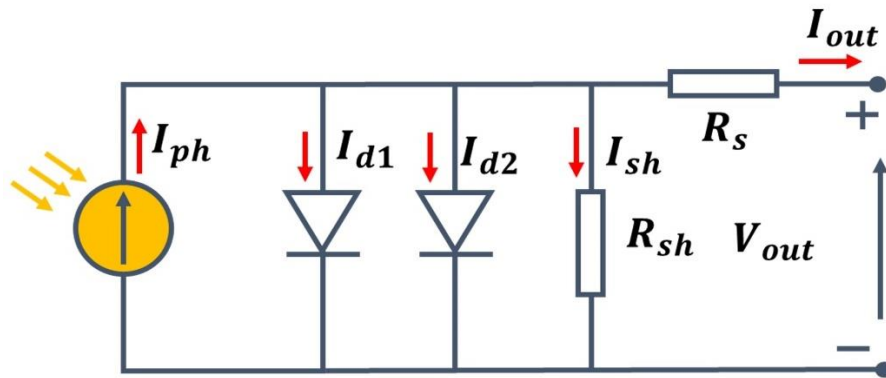


Fig.II. 4: Two diode model (seven parameters)

The output current can be expressed as below:

$$I_{out} = I_{ph} - I_{d1} - I_{d2} - I_{sh}$$

$$I_{out} = I_{ph} - I_{01} \left[ \exp \left( q \frac{V_{out} + I_{out} R_s}{n_1 K T} \right) - 1 \right] - I_{02} \left[ \exp \left( q \frac{V_{out} + I_{out} R_s}{n_2 K T} \right) - 1 \right] - \frac{V_{out} + I_{out} R_s}{R_{sh}} \quad (\text{II.4})$$

Where  $I_{d1}$  and  $I_{d2}$  are the current pass through the corresponding diode;  $n_1$  and  $n_2$  are diode ideality factors of the respective diode, and the saturation current of diode1 and diode2 are  $I_{01}$  and  $I_{02}$ , respectively. On the other hand, adding a second diode increases the number of

parameters that have to be computed. As equation (II.4) shows, this model is complicated since it is a nonlinear and explicit equation with two exponential parts and up to seven parameters. Consequently, the computation time is relatively long [6], [16]. Many approaches have been attempted to minimize the computational complexity, but they seem unsatisfactory [6].

### II.2.5. Three diode model (nine parameters)

Fig.II. 5 shows the three diode model. The first diode would provide the diode current ( $I_{d1}$ ) due to diffusion and recombination in the quasi-neutral regions (QNRs) of the emitter and bulk regions with  $n_1 = 1$ , and the second diode would provide a contribution to the diode current ( $I_{d2}$ ) due to recombination in the space charge region (SCR) with  $n_2 = 2$  and the third diode in parallel to the two diodes would provide the diode current component ( $I_{d3}$ ) due to the recombination in the defect regions, grain sites, etc., with  $n_3 > 2$  [17].

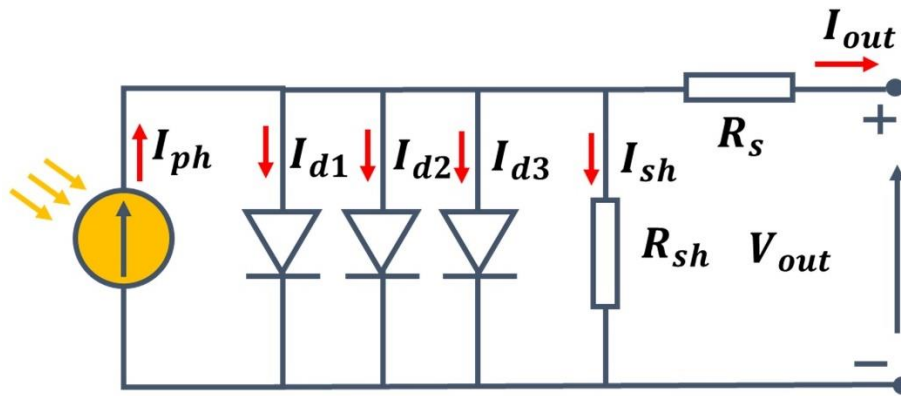


Fig.II. 5: Three diode model (nine parameters)

The following is an expression for the output current:

$$\begin{aligned}
 I_{out} &= I_{ph} - I_{d1} - I_{d2} - I_{d3} - I_{sh} \\
 I_{out} &= I_{ph} - I_{01} \left[ \exp \left( q \frac{V_{out} + I_{out} R_s}{n_1 K T} \right) - 1 \right] - I_{02} \left[ \exp \left( q \frac{V_{out} + I_{out} R_s}{n_2 K T} \right) - 1 \right] - \\
 &I_{03} \left[ \exp \left( q \frac{V_{out} + I_{out} R_s}{n_3 K T} \right) - 1 \right] - \frac{V_{out} + I_{out} R_s}{R_{sh}} \quad (II.5)
 \end{aligned}$$

### II.2.6. Bishop model

When one PV cell is occulted, it operates in the opposite regime (quadrant III). The SDM does not represent the behavior in this region, and it can be done by adding a nonlinear multiplier ( $M(V)$ ) that describes the avalanche effect (Bishop effect) in series with the shunt resistance [18]–[23]. The electrical circuit of this model is shown in Fig.II. 6.

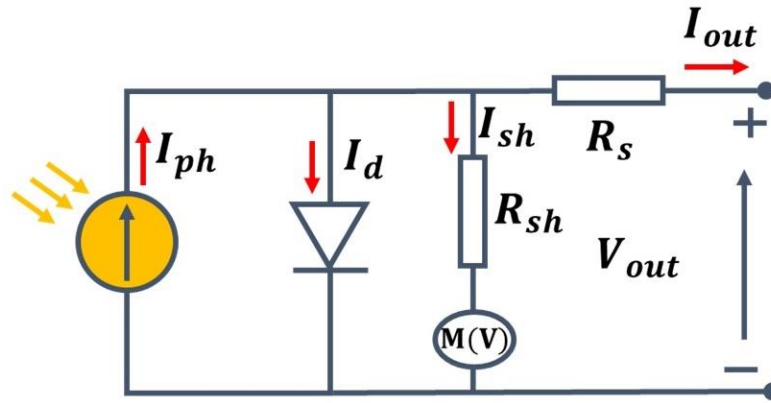


Fig.II. 6: PV electrical circuit of Bishop model

The output current can be written as below:

$$I_{out} = I_{ph} - I_d - I_{sh}$$

$$I_{out} = I_{ph} - I_0 \left[ \exp \left( q \frac{V_{out} + I_{out} R_s}{nKT} \right) - 1 \right] - \frac{V_{out} + I_{out} R_s}{R_{sh}} \left[ 1 + a \left( 1 - \frac{V_{out} + I_{out} R_s}{V_{br}} \right)^{-k} \right] \quad (\text{II.6})$$

$$\text{With } M(V) = 1 + a \left( 1 - \frac{V_{out} + I_{out} R_s}{V_{br}} \right)^{-k} \quad (\text{II.7})$$

When the Bishop model is added to the five parameters model, the number of parameters increases to eight parameters, and these three additional parameters are :

- $V_{br}$  : Breakdown voltage of the cell (-10 V to -30 V)
- $k$  : Avalanche breakdown coefficient (3.4 to 4)
- $a$  : Avalanche breakdown fraction ( $\sim 0.1$ )

### II.2.6. Summary of PV model

The three diode, two diodes and Bishop models are not selected for our study for the following two reasons:

- The addition of a second and third diodes dominates at low voltage and low irradiance. For FDD purposes, measurements can be selected in order not to be affected by low irradiance levels.
- The Bishop model enables PV cells to operate in an inverse regime. Nowadays, PV modules are protected by bypass diodes which prevent them from working as a load, that is, in an inverse regime.

The main drawback of the SDM is that the needed five parameters are not given in the datasheet of the PV module. They should be deduced from the current-voltage characteristic (given by the manufacturer or measured under controlled conditions). New methods for extracting these five parameters are regularly proposed in the scientific literature (e.g., [24], [25]).

Based on the literature review, many researchers considered the development of the SDM and made some suggestions for improvement and simplification to obtain the needed five parameters. Study results show acceptable performance in terms of accuracy [14], [26]–[32]. Therefore, the SDM is selected for our study.

The PV cell is the basic element of a PV module. Generally,  $N_s$  PV cells are interconnected in series to form the PV module. The SDM can model a PV cell, a PV module, and even a PV string or array. To be sure of the notations used in this manuscript, below are summarized the relationships we used to model a PV module from the five parameters of the SDM of a PV cell.

Fig.II. 7 illustrates the association of  $N_s$  PV cells connected in series to form a PV module, each one being represented by its SDM and the equivalent SDM of the PV module.

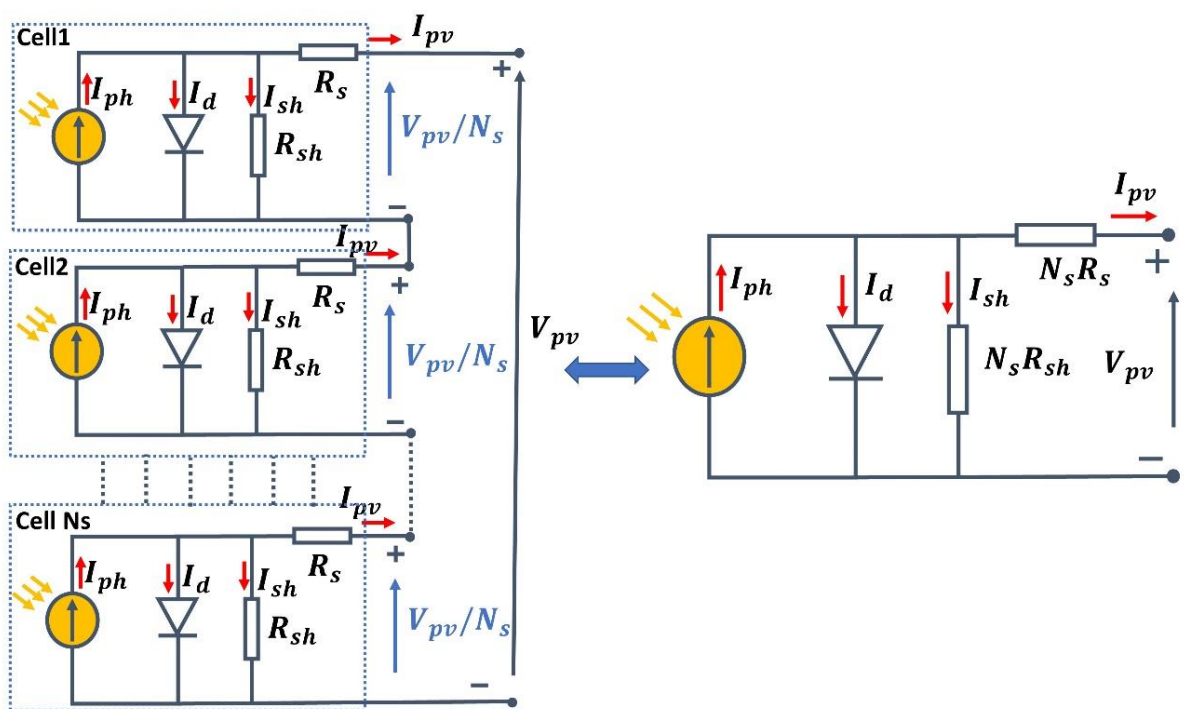


Fig.II. 7: SDM of  $N_s$  PV cells connected in series to form a PV module (left) and SDM of the same PV module (right)

According to equation (II.3) applied to a PV cell, the output current of the PV module is represented in the left part of Fig.II. 7 can be expressed as below:

$$I_{pv} = I_{ph} - I_0 \left[ \exp \left( q \frac{V_{pv} + I_{pv} R_s}{n_s k T} \right) - 1 \right] - \left( \frac{V_{pv} + I_{pv} R_s}{R_{sh}} \right) \quad (II.8)$$

$$I_{pv} = I_{ph} - I_0 \left[ \exp \left( q \frac{V_{pv} + I_{pv} R_s N_s}{n N_s k T} \right) - 1 \right] - \left( \frac{V_{pv} + I_{pv} R_s N_s}{R_{sh} N_s} \right) \quad (II.9)$$

Where  $I_{pv}$  refers to the PV output current of the PV module,  $V_{pv}$  denotes the PV output voltage of the PV module.

### II.3. Description of the SDM five parameters and their variation with environmental operating conditions

For the model to be even more precise, it is important to also take into account the variation of the SDM parameters with the environmental operating conditions and, more particularly, the irradiance in the plane of array ( $G_{POA}$ ) and the operating temperature of the PV module ( $T_{pv}$ ).

#### II.3.1. The photo-generated current ( $I_{ph}$ )

The output current at the standard test condition (STC) of Fig.II. 1 is :

$$I_{pv} = I_{ph} - I_0 \left[ \exp \left( \frac{q V_{pv}}{n k T} \right) - 1 \right] \quad (II.10)$$

This equation (II.10) allows quantifying  $I_{ph}$  which cannot be determined otherwise [33]. When PV cell is short-circuited ( $V_{pv} = 0$ ):

$$I_{sc} = I_{ph} - I_0 \left[ \exp \left( \frac{0}{n k T} \right) - 1 \right] \quad (II.11)$$

This equation is valid only in the ideal case. Therefore, equation (II.11) has to be written as:

$$I_{sc} \approx I_{ph} \quad (II.12)$$

The photo-generated current ( $I_{ph}$ ) is directly proportional to the irradiance and depends on the temperature via the short-circuit current temperature coefficient ( $K_{I_{ref}}$ , expressed in  $\% ^\circ C^{-1}$ ).

It can be expressed as below [34], [35] :

$$I_{ph} \approx I_{sc_{ref}} \left[ 1 + K_{I_{ref}} (T_{pv} - T_{STC}) \right] \frac{G_{POA}}{G_{STC}} \quad (II.13)$$

Where  $T_{pv}$  and  $T_{STC}$  represent the temperatures of the PV module in operating conditions and in standard test conditions (STC), respectively, in °C.  $G_{POA}$  and  $G_{STC} = 1000 \text{ W m}^{-2}$  in plane of array and STC irradiances.  $I_{sc\_ref}$  and  $K_{I\_ref}$  will be tuned according to our measurements and operating environmental conditions for the proposed hybrid model (see part II.7). Their initial values are obtained from the datasheet (Table I.2).

### II.3.2. The diode saturation current ( $I_0$ )

The diode saturation current ( $I_0$ ) is the asymptotic value of the current in reverse bias. It depends only on the temperature. It can be given through Eq (II.11) as below, according to [36]:

$$I_0 = I_{0\_ref} \left( \frac{T}{T_n} \right)^3 \exp \left[ \frac{qE_g N_s}{Kn} \left( \frac{1}{T} - \frac{1}{T_n} \right) \right] \quad (\text{II.14})$$

Where  $I_{0,STC}$  and  $T_n$  are the nominal diode saturation current and temperature in Kelvin at STC and  $E_g$  is the bandgap of the PV semiconductor in eV.  $I_{0,STC}$  can be derived from Eq (II.8) of the ideal model (neglecting series and shunt resistances), expressed in open-circuit conditions and STC ( $I_{pv} = 0$  and  $V_{pv} = V_{oc\_ref}$ ):

$$0 = I_{ph} - I_{0,STC} \left[ \exp \left( q \frac{V_{oc\_ref}}{nN_s K T_{pv}} \right) - 1 \right]$$

$$I_{0\_ref} = \frac{I_{ph}}{\exp \left( \frac{qV_{oc\_ref}}{nN_s K T} \right) - 1} \quad (\text{II.15})$$

But in this study, the formula of the saturation diode current ( $I_0$ ) that fits and matches the most to the proposed approach is presented as follows [7], [37]:

$$I_0 = \frac{I_{ph\_ref} [1 + K_{I\_ref} (T_{pv} - T_{STC})]}{\exp \left( \frac{qV_{oc\_ref} [1 + K_{V\_ref} (T_{pv} - T_{STC})]}{nN_s K T} \right) - 1} \quad (\text{II.16})$$

$V_{oc\_ref}$  is the open-circuit voltage measured in STC and  $K_{V\_ref}$  is the  $V_{oc}$  thermal coefficient in  $\% \text{ } ^\circ\text{C}^{-1}$ . Their value will be tuned according to our measurements and operating environmental conditions for the proposed hybrid model (see part II.7). Their initial values are taken from the datasheet (Table I.2).

### II.3.3. The series resistance ( $R_s$ )

Several methods tried to model the effect of the temperature and the irradiance on  $R_s$ . Among others, the author in [38] propose the following equation:

$$R_s = R_{s\_ref} [1 + K_{R\_ref} (T - T_n)] \left( \frac{G_{POA}}{G_{STC}} \right)^{-B_{ref}} \quad (II.17)$$

Where  $K_{R\_ref}$  defines the linear temperature coefficient (varying from 0 to 0.5% °C<sup>-1</sup>), and  $B_{ref}$  denotes the exponential solar irradiance coefficient of  $R_s$  (0.78)

Some other authors assume that  $R_s$  only depends on irradiance so that it can be written as the equation below [39], [40]:

$$R_s = R_{s\_ref} \times \frac{G_{STC}}{G_{POA}} \quad (II.18)$$

Where  $R_{s\_ref}$  is the series resistance at STC.

Finally, we can also find in the literature that  $R_s$  increases with temperature and decreases with irradiance [41], [42], as follows:

$$R_s = R_{s\_ref} \left[ \frac{T}{T_n} \times \left( 1 - \beta_{ref} \ln \left( \frac{G_{POA}}{G_{STC}} \right) \right) \right] \quad (II.19)$$

With  $\beta_{ref} = 0.217$ .

The coefficients  $K_{R\_ref}$ ,  $B_{ref}$ ,  $R_{s\_ref}$  and  $\beta_{ref}$  will be tuned according to our measurements and operating environmental conditions for the proposed hybrid model (see part II.7). The initial value of  $R_{s\_ref}$  is estimated from a one-shot I-V curve measurement, while the initial values of  $K_{R\_ref}$ ,  $B_{ref}$ ,  $\beta_{ref}$  are taken from the literature.

### II.3.4. Shunt resistance ( $R_{sh}$ )

In the research of [43], [44], the author presents a formula for shunt resistance ( $R_{sh}$ ) variation with the irradiance level from PVSYST software [45] as below:

$$R_{sh} = R_{sh\_ref} + [R_{sh}(0) - R_{sh\_ref}] \exp \left( -R_{shexp} \frac{G_{POA}}{G_{STC}} \right) \quad (II.20)$$

According to the software reference guide (PVSYST, 2012),  $R_{sh}(0)$  is equal to four times  $R_{sh\_ref}$  for crystalline silicon.  $R_{shexp}$  is the exponential parameter, usually 5.5.

$$R_{sh} = R_{sh\_ref} \left[ 1 + 3 \exp \left( -R_{sh\_exp} \frac{G_{POA}}{G_{STC}} \right) \right] \quad (\text{II.21})$$

Another research considers  $R_{sh}$  as constant, it can be written as below [46]:

$$R_{sh} = R_{sh\_ref} \quad (\text{II.22})$$

$R_{sh}$  can also be taken proportional to the irradiance, represented as following [26], [40], [47] :

$$R_{sh} = R_{sh\_ref} \times \frac{G_{STC}}{G_{POA}} \quad (\text{II.23})$$

The coefficients  $R_{sh\_ref}$  and  $R_{sh\_exp}$  will be tuned according to our measurements and operating environmental conditions for the proposed hybrid model (see part II.7).  $R_{sh\_ref}$  initial values is estimated from a one-shot I-V curve, while the initial value of  $R_{sh\_exp}$  is taken from the literature.

### II.3.5. The diode ideality factor ( $n$ )

The diode ideality factor ( $n$ ) is proportional to the PV module temperature. It can be expressed in the equation as below [48], [49]:

$$n = n_{ref} \times \frac{T}{T_n} \quad (\text{II.24})$$

Where  $n_{ref}$  is the diode ideality factor. Its initial value is set to 1.

The coefficients  $n_{ref}$  will be tuned according to our measurements and operating environmental conditions for the proposed hybrid model (see part II.7).

### II.3.6. Summary of parameter model variation with environmental conditions

The FDD method that we propose is based on the comparison between the measurement in real conditions, and the simulation, under the same conditions, of a PV module. To do this, we have chosen to use the SDM, whose five electrical parameters define the output PV voltage and current. We have just synthesized the main analytical laws of variation of these parameters as a function of the irradiance in the plane of array ( $G_{POA}$ ) and of the operating temperature of the PV module ( $T_{pv}$ ). These laws were extracted from the literature. They will be empirically tuned to our measurements in part II.7 to obtain a hybrid model (analytical modelling of the parameters with environmental conditions and numerical modelling of the SDM) that best suits the characterized PV modules.



## II.4. Parameters extraction methods

Following the choice of an acceptable model with five electrical parameters, and the presentation of their variation with environmental conditions, we will now explain how their values are setted. Determining them on the basis of information from the datasheet or experimental measurements is still a challenge, and yet, it is essential to find the most accurate parameters allowing better precisions in the simulations. As a consequence, this issue has attracted the interest of many researchers. In recent years, several accurate parameter extraction methods have been proposed to deal with the nonlinear I-V characteristic of PV cells, modules, strings, or arrays. They can be classified into four main approaches [4], [50], which are described bellow.

### II.4.1. Analytical approach

Analytical approaches provide formulas to obtain model parameters from the datasheets or from I-V curve measurements. The analytical method proposes to solve a set of transcendental algebraic equations to extract the parameters. These equations are derived from (II.8) expressed for remarkable points (open-circuit voltage ( $V_{oc}$ ), short-circuit current ( $I_{sc}$ ), current ( $I_{mpp}$ ) and voltage ( $V_{mpp}$ ) at the maximum power point (MPP)) specified in the manufacturer's datasheet or from I-V curves measurements. The SDM parameters extraction is described in references [41], [51], [52], which provide approximate equations using various simplification methodologies. This analytical method needs the value of  $I_{sc}$ ,  $V_{oc}$ ,  $I_{mpp}$  and  $V_{mpp}$ . This lead to a set of three equations for five unknown parameters. The slopes of the I-V curve can be added to the current source and voltage source zones. From them,  $R_{sh}$  and  $R_s$  can be derived. While using the whole I-V curve, the number of samples is also a limitation, particularly when the MPP and the slopes have to be calculated. This approach is feasible if the key points are accurate, but the MPP is subject to sampling noise. Therefore, these analytical methods are not suited for high-accuracy calculations and are time-consuming.

### II.4.2. Numerical approach

Due to the drawbacks of the analytical approach, numerical methods for solving the implicit nonlinear transcendental equation with better accuracy have been developed. The numerical methods are based on iterative techniques or optimization algorithms such as Gauss-Seidel [53], Newton Raphson [54], Levenberg Marquardt (LM) [2], and so on. These methods typically use gradient-descent-based techniques to minimize an objective function between the

measured and calculated I-V curves. This minimization aids in the optimization of parameter values. The numerical methods provide fast convergence, high computation efficiency, and sufficient accuracy. Any inappropriate choice of initial values may cause these methods to be trapped in the local search instead of the global search [55].

### *II.4.3. Metaheuristic approach*

To mitigate the disadvantages of numerical methods, metaheuristic methods have been proposed for solving complex optimization problems to extract the parameter of PV models in terms of global search capability. These methods rely on evolutionary, probabilistic, population-based optimization algorithms developed from nature-inspired [56]. Metaheuristic algorithms, including Genetic Algorithm, Differential Evolution, and Particle Swarm Optimization, in general, do not require any initial value condition for the parameters or gradient descent-based information [57], [58]. Even if metaheuristic methods have high accuracy, they also require a high computation due to the large stochastic population's complexity, which remains the main problem of these methods [59].

### *II.4.4. Hybrid approach*

Another method is known as hybrid methods, which combines the merits of two methods, e.g., numerical-metaheuristic [60], analytical-numerical [61], and metaheuristic-metaheuristic [62], to improve the efficiency of parameters extraction. For example, a combination of the analytical and metaheuristic method was studied to identify PV cells' single diode model parameters. By using metaheuristics algorithms, the values of series and shunt resistances ( $R_s, R_{sh}$ ) were optimized. While the analytical method is applied to estimate the values of the ideality diode factor ( $n$ ), diode saturation current ( $I_0$ ), and photocurrent ( $I_{ph}$ ) [63]. Even though hybrid methods feature the accuracy and convergence speed of parameter extraction, they also need huge computing resources, which are not suitable for implementing real-time parameter extraction [64].

### *II.4.5. Summary of extraction methods*

To sum up, a useful parameter extraction method must include accuracy and low computational time. In our study, we have chosen the numerical method based on the LM algorithm because it requires a full range of measured I-V curves. Moreover, the LM algorithm combines two minimization methods (Gradient Descent and Gauss-Newton) which give

robustness and makes the algorithm faster [65]. In [2], the authors proposed a numerical method based on the LM algorithm to extract PV models' electrical parameters from among the five most commonly used ones, including PV models with three, four, five, six, and seven parameters. The result showed that the single diode model with five electrical parameters gives a very good accuracy when using the LM algorithm. Furthermore, this algorithm offers the best trade-off between sufficient accuracy and the speed of calculation. For all of these reasons, this extraction method was chosen to extract the single diode model's five electrical parameters.

## II.5. Levenberg-Marquardt optimization algorithm description

The parameters extraction method based on the Levenberg-Marquardt (LM) optimization algorithm is chosen in our study to extract the five unknown parameters of the PV model. LM algorithm provides a numerical solution to the problem of minimizing an objective function that is nonlinear and dependent on several variables. Its main application is the progression through the least-squares method [2], [60].

### II.5.1. Implementation in MATLAB

Assuming that we have the observation of  $m$  measurement data points along an I-V curve of PV modules  $(V_{meas_i}, I_{meas_i}), i = 1:m$ , the PV model characterized by five parameters is described by equation (II.8), as follows:

$$I_{pred_i}(\theta, V_{meas_i}) = \theta(1) - \theta(4) \left[ \exp \left( q \frac{V_{meas_i} + I_{pred_{(i-1)}} \cdot \theta(2) \cdot N_s}{\theta(5) \cdot N_s \cdot K \cdot T} \right) - 1 \right] + \left( \frac{V_{meas_i} + I_{pred_{(i-1)}} \cdot \theta(2) \cdot N_s}{\theta(3) \cdot N_s} \right) \quad (II.25)$$

Where  $\theta = [I_{ph}, R_s, R_{sh}, I_0, n]$  is a vector composed of the five unknown parameters of the SDM.  $I_{pred_i}(\theta, V_{meas_i})$  is the predicted current as of the function of  $\theta$  and the measured voltage  $V_{meas_i}$ . Then, the absolute error vector between the predicted and measured current is calculated, which is written as follows:

$$e(\theta) = \begin{pmatrix} I_{meas_1} - I_{pred_1}(\theta, V_{meas_1}) \\ I_{meas_2} - I_{pred_2}(\theta, V_{meas_2}) \\ \vdots \\ I_{meas_i} - I_{pred_i}(\theta, V_{meas_i}) \\ \vdots \\ I_{meas_m} - I_{pred_m}(\theta, V_{meas_m}) \end{pmatrix} = \begin{pmatrix} e_1(\theta) \\ e_2(\theta) \\ \vdots \\ e_i(\theta) \\ \vdots \\ e_m(\theta) \end{pmatrix} \quad (II.26)$$

The objective here is to find the optimal vector  $\theta$ , which minimizes the function  $f(\theta)$  calculated with the vector  $e(\theta)$ .

$$f(\theta) = \frac{1}{2} \sum_{i=1}^m [e_i(\theta)]^2 \quad (II.27)$$

The function  $f(\theta)$  becomes the objective function to be minimized by least squares and thanks to the LM algorithm under MATLAB. Fig.II. 8 shows the L-M flowchart implemented in MATLAB.

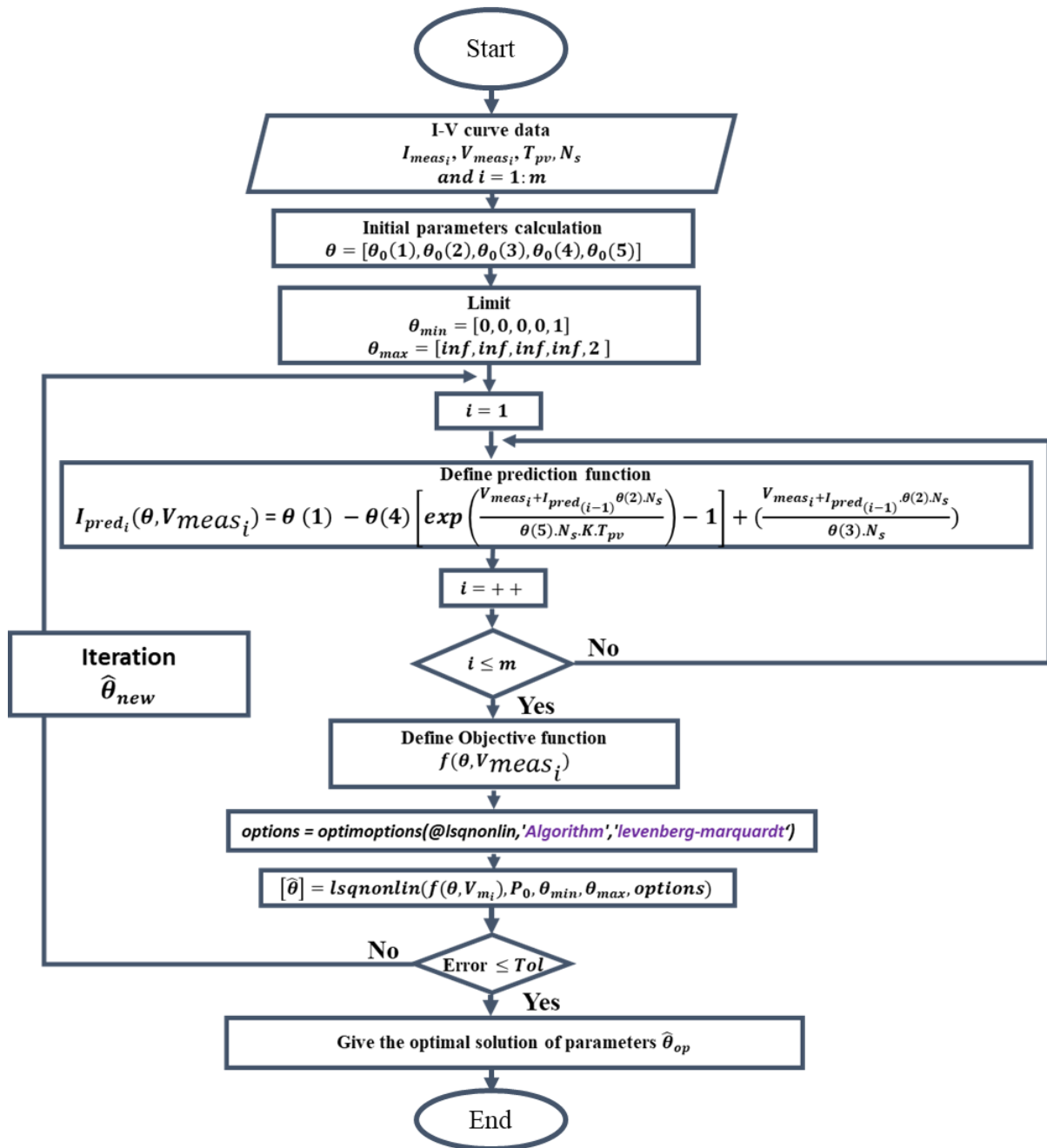


Fig.II. 8 : Levenberg-Marquardt approach flowchart

### II.5.2. Initial condition

Initial values play a crucial part in the numerical optimization method, especially in the LM algorithm. Any wrong initial value choice of a parameter may affect the results, which can be trapped in any local optimum instead of the global one. Poor initial values, for example, may lead to a significant increase in the number of iterations and, in some cases, a divergence of the optimization algorithm [2]. Therefore, the initial values of the SDM parameters must be taken into account very seriously.

#### II.5.2.1. Initial value of the photo-generated current ( $I_{ph0}$ )

The research proposed in [2] indicates that a good starting point for the initial value for  $I_{ph}$  is approximated by the short-circuit current at the operation condition. It can be defined as below:

$$I_{ph0} = I_{sc_{meas}} \quad (II.28)$$

#### II.5.2.2. Initial value of diode ideality factor ( $n_0$ )

Depending on the fabrication process and semiconductor material, the ideality factor  $n$  usually ranges from 1 to 2 [2]. Therefore, the initial value of  $n$  can be set to 1.

$$n_0 = 1 \quad (II.29)$$

#### II.5.2.3. Initial value of the diode saturation current ( $I_{00}$ )

Considering the ideal model, that is to say, the Eq (II.9) with  $R_s = 0$  and  $R_{sh} = \infty$ , expressed for a voltage equal to the open-circuit one ( $V_{pv} = V_{oc_{meas}}$  and  $I_{pv} = 0$ ) and in operating conditions and with the hypothesis that  $I_{ph} = I_{sc_{meas}}$ , the diode saturation current initial value can be expressed as bellowing [2], [26], [66] :

$$I_{00} = \frac{I_{sc_{meas}}}{\exp\left(\frac{V_{oc_{meas}}}{nN_sKT}\right) - 1} \quad (II.30)$$

#### II.5.2.4. Initial value of the series resistance ( $R_{s0}$ )

The equation below uses the slope of the measured I-V curve, close to the open circuit point, to determine the initial value of  $R_s$  [2], [67], [68]:

The two couples of points closest to the open circuit ( $V_{oc}, 0$ ) on the measured I-V curve, are indicated as  $(V_1, I_1)$  and  $(V_2, I_2)$ . By making the following assumptions, we can calculate the initial value of  $R_s$  as below

$$R_{s0} = n_0 \times \frac{N_s K T}{q} \times \frac{1}{I_2 - I_1} \times \ln \left( \frac{I_{ph0} - I_2}{I_{ph0} - I_1} \right) - \frac{V_2 - V_1}{I_2 - I_1} \quad (\text{II.31})$$

$I_{ph0}$  is the initial value of photo generated current and  $n_0$  is the initial value of the ideality factor.

#### II.5.2.5 Initial value of the shunt resistance ( $R_{sh0}$ )

According to research on PV array modeling and circuit-based simulation [69], the Eq (II.31) is one of the most suitable equations to have a good initial guess value of  $R_{sh}$ , because the initial value of  $R_{sh}$  started from the minimum value of  $R_{sh}$  by using the expression here follow :

$$R_{sh_0} = \frac{V_{mppmeas}}{I_{scmeas} - I_{mppmeas}} - \frac{V_{ocmeas} - V_{mppmeas}}{I_{mppmeas}} \quad (\text{II.32})$$

Where,  $V_{ocmeas}$  and  $I_{scmeas}$ , are open-circuit voltage and short-circuit current,  $V_{mppmeas}$  and  $I_{mppmeas}$  are voltage and current at the MPP, respectively, in experimental operating conditions.

## II.6. Description and validation of the analytical models

Manufacturers often provide information under standard test conditions (STC, 25°C, 1000 W m<sup>-2</sup>, AM1.5), which is insufficient for determining overall PV performance. PV cells, modules, strings, and arrays do, in fact, work under a variety of meteorological conditions far from the STC. For FDD, accurate and reliable modeling of the PV system under every environmental condition is required. Furthermore, the PV model's extracted parameters must be precise and accurate in order to simulate the PV system. Many numerical techniques have recently been presented for several weather conditions to determine the optimal extracted parameters that minimize the objective function and provide the lowest quadratic errors; these extracted parameters are then utilized as constant values in the PV model. The precision and dependability are not as high as they should be. When the irradiance and temperature of the PV model are changed, the extracted parameters of the PV model also change substantially. In the following, a 4-step methodology, described in Fig.II. 9, is developed to extract the parameters of the SDM. The first two steps are devoted to the training, while the last two ones are for validation.

- Step 1: For training data  $(T_{pv}, G_{POA})_{\text{training}}$ , extraction of the parameters  $\hat{\theta}_{(I-V)} = [I_{ph}, R_s, R_{sh}, I_0, n]$  from measured I-V curves,

- Step 2: Identification of the reference values for the analytical models  $\delta_{ref} = [R_{sh\_ref}, R_{s\_ref}, \beta_{ref}, V_{oc\_ref}, k_{V\_ref}, k_{I\_ref}, I_{sc\_ref}, n_{ref}]$ . The cross-effect between  $G_{POA}$  and  $T_{pv}$  will be considered,
- Step 3: Extraction of  $\hat{\theta}_{analy} = [\hat{I}_{pv}, \hat{R}_s, \hat{R}_{sh}, \hat{I}_0, \hat{n}]$  with the analytical models using the reference values  $\delta_{ref}$  and validation dataset  $(T_{pv}, G_{POA})_{validation}$ ,
- Step 4: Analyses for each of the  $M$  I-V curves the mean absolute percentage error ( $MAPE_{\theta}$ ) between  $\hat{\theta}_{(I-V)}$  and  $\hat{\theta}_{analy}$  to validate the analytical model.

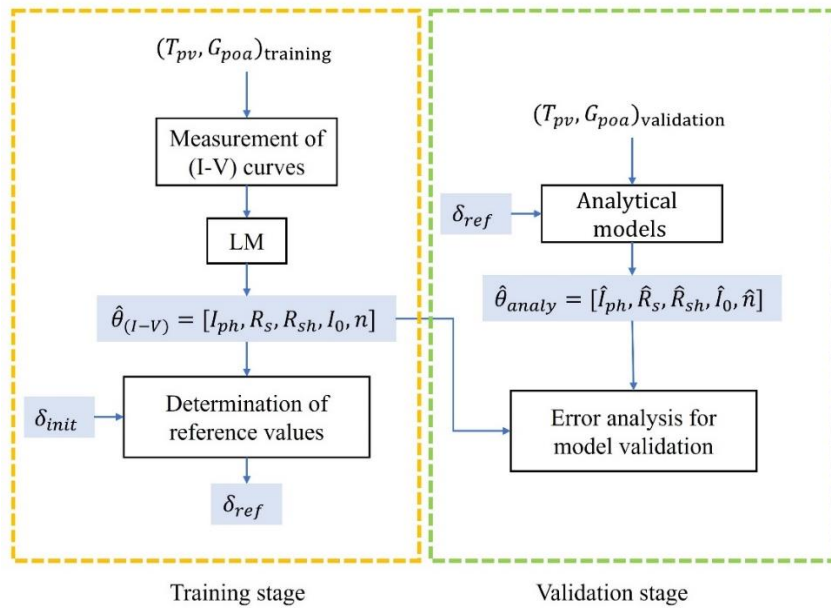


Fig.II. 9: Training and validating methodology

To evaluate the accuracy of our methods, parameters extracted from I-V curves measurements and estimated by the analytical models for a validation dataset (which is different from the training dataset used to adjust the analytical models) are compared. The mean absolute percentage error between those two sets of parameters ( $MAPE_{\theta}$ ) is calculated using the formulas below:

$$MAPE_{\theta} = \frac{1}{m} \sum_{i=1}^m \left| \frac{\hat{\theta}_{(I-V)_i} - \hat{\theta}_{analy_i}}{\hat{\theta}_{(I-V)_i}} \right| \quad (II.33)$$

- $\hat{\theta}_{(I-V)}$  is the five unknown parameters, which are extracted from I-V curves measurement using the LM optimization algorithm
- $\hat{\theta}_{(analy)}$  is the five unknown parameters, which are calculated from the analytical model of parameters
- $m$  is the number of I-V curves
- $i$  refers to  $i^{th}$  measurement

The two next parts present in detail how are trained the analytical models to get the best reference parameters  $\delta_{ref}$ , using I-V curves measured under training conditions  $(G_{POA}, T_{pv})_{training}$  and how the models are validated by comparison between the parameters analytically calculated  $\hat{\theta}_{(analy)}$  and extracted from measured I-V curves  $\hat{\theta}_{(I-V)}$ , both in validation conditions  $(G_{POA}, T_{pv})_{validation}$ . Once the proposed hybrid model is validated, it can be used to simulate PV healthy modules in FDD processes.

### II.6.1. The training stage

During the training step, the five unknown parameters  $\hat{\theta}_{(I-V)}$  of the SDM are extracted from measured I-V curves under real conditions. The curves used in this step are selected only if they have been measured under an irradiance greater than or equal to  $600 \text{ W m}^{-2}$  in order to avoid low irradiance conditions. An example of an I-V curve measured on 8<sup>th</sup> September 2021, at 2:12 pm with an irradiance of  $698 \text{ W m}^{-2}$  and a module temperature of  $47^\circ\text{C}$  is presented in Fig.II. 10 with blue dot markers. We applied the LM algorithm as described in section II.5; the parameters are written in the figure. The red marker and yellow line in Fig.II. 10 are the I-V curve obtained from the LM algorithm and PV model, respectively. This figure shows a good agreement between measurements and simulation. To ensure that the extracted parameters of the PV model will be reliable, accurate, and work under any weather condition, many I-V curves measured under different conditions are investigated, and the five parameters are extracted for each one. The training dataset is composed of 488 measurements that have been carried out under different weather conditions, as shown in Table.II. 2.

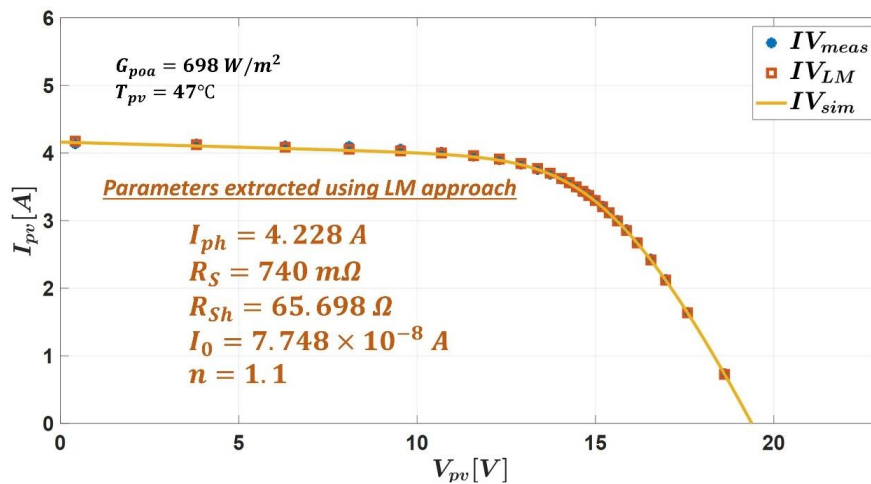


Fig.II. 10: Measured and simulated I-V curve, in real operation condition; this data was measured on 08-09-2021 at 14:12; the SDM was configured with the extracted parameters



Table.II. 2 : Dataset used for the training step

Date of acquisition	Weather	Number of I-V curves, $G_{pOA} \geq 600Wm^{-2}$	
1	02/09/2021	Sunny	94
2	08/09/2021	Sunny	86
3	10/09/2021	Partly cloudy	29
4	14/09/2021	Partly cloudy	45
5	15/09/2021	Partly cloudy	42
6	19/09/2021	Partly cloudy	44
7	20/09/2021	Partly cloudy	27
8	23/09/2021	Partly cloudy	58
9	24/09/2021	Sunny	63
Total			488

The analytical expressions mentioned in section II.3 are used to model the variation of the five SDM parameters with irradiance and temperature. As can be seen in these equations, some reference values need to be estimated. They are represented by  $\delta_{ref} = [R_{sh\_ref}, R_{s\_ref}, \beta_{ref}, V_{oc\_ref}, k_{V\_ref}, k_{I\_ref}, I_{sc\_ref}, n_{ref}]$ . Those reference values are obtained during the training step with the fitting of the analytical models to the real parameters variations. The flowchart of this step is shown in *Fig.II. 11*. The least square error method is proposed to minimize the absolute error between the measured and the estimated parameter. The absolute error vector is shown below:

$$e(\delta) = \begin{pmatrix} \hat{\theta}_{(I-V)_1} - \hat{\theta}_{analy_1}(\delta) \\ \hat{\theta}_{(I-V)_2} - \hat{\theta}_{analy_2}(\delta) \\ \vdots \\ \hat{\theta}_{(I-V)_i} - \hat{\theta}_{analy_i}(\delta) \\ \vdots \\ \hat{\theta}_{(I-V)_M} - \hat{\theta}_{analy_M}(\delta) \end{pmatrix} = \begin{pmatrix} e_1(\delta) \\ e_2(\delta) \\ \vdots \\ e_i(\delta) \\ \vdots \\ e_M(\delta) \end{pmatrix} \quad (II.34)$$

The goal here is to find the  $\delta_{ref}$  vector which minimize the function  $f(\delta)$  defined as bellow:

$$f(\delta) = \frac{1}{2} \sum_i^M [e_i(\delta)]^2 \quad (II.35)$$

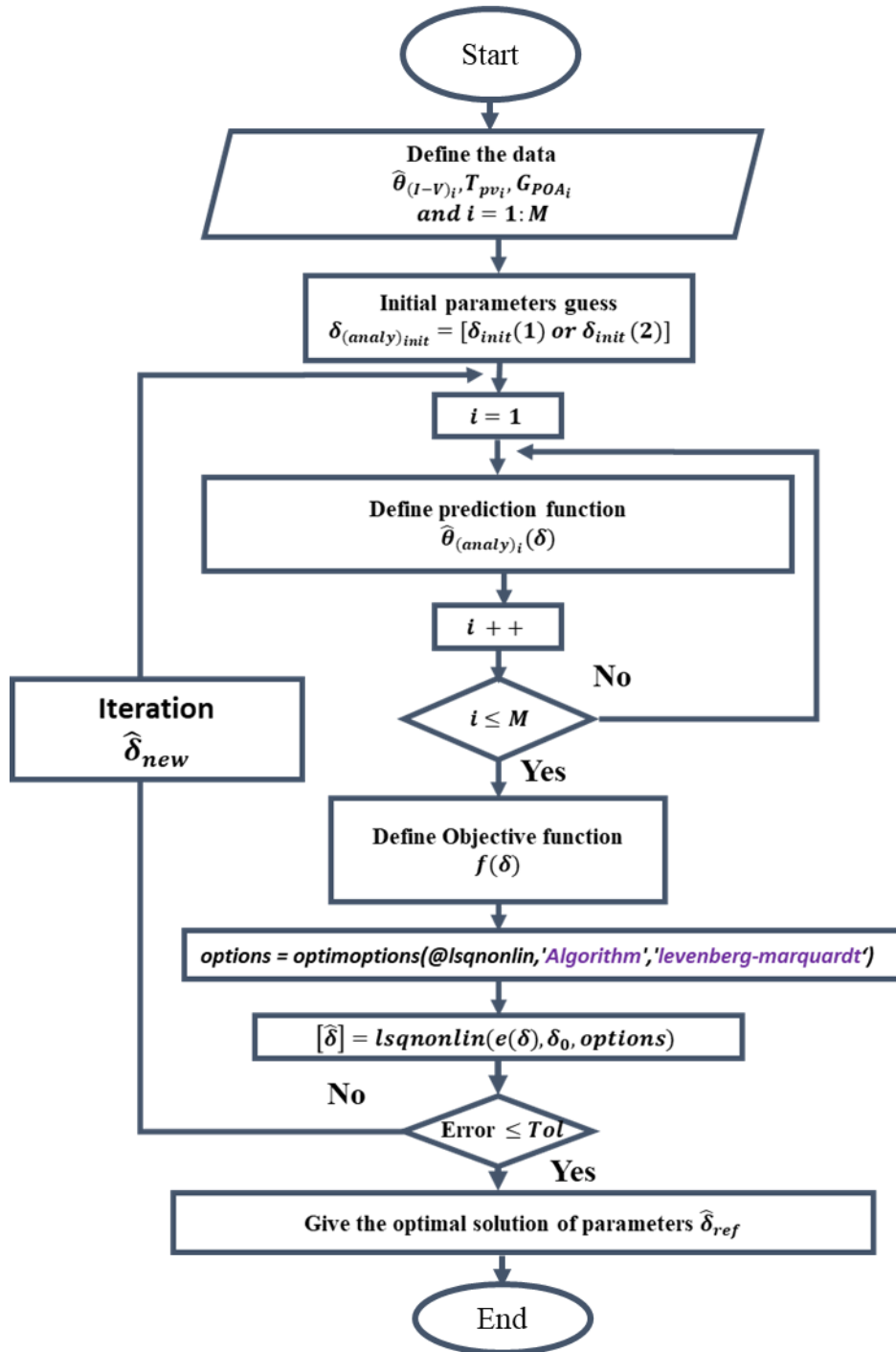


Fig.II. 11 : Flowchart approach for calculating the reference values of the analytical model

### II.6.1.1. Analytical model of the photocurrent ( $I_{ph}$ )

According to Eq (II.13), the photocurrent depends on the reference values  $K_{I_{ref}}$  and  $I_{sc_{ref}}$ . Their initial values are determined using the datasheet or information found in the literature, and then they are tuned to minimize the objective function defined in (II.35) and use the LM algorithm. The photocurrent depends not only on the irradiance but also on the

temperature. To avoid the cross-effect between  $G_{POA}$  and  $T_{pv}$ ,  $K_{I_{ref}}$  is tuned at constant irradiance ( $G_{POA} = 765 \text{ W/m}^2 \pm 2\%$ ) and  $I_{sc_{ref}}$  at constant  $T_{pv}$ . Under different irradiances for  $T_{pv} = 56^\circ\text{C}$ , the reference parameters are estimated. The results are shown in Table.II. 3.

Table.II. 3 : Estimated reference value from Eq (II.13) for constant  $T_{pv} = 56^\circ\text{C}$

	$I_{sc_{ref}}$ [A]	$K_{I_{ref}}$ [%/°C]	$MAPE_{I_{ph}}$ [%]
Initial reference values	5.34	0.038	8.34
Optimal reference values of 1 <sup>st</sup> step	5.817	0.061	6.01

The evolution of  $I_{ph}$  with  $G_{pOA}$  is shown in Fig.II. 12. The analytical model converges toward the measured values. The  $MAPE_{I_{ph}}$  is 6.01%.

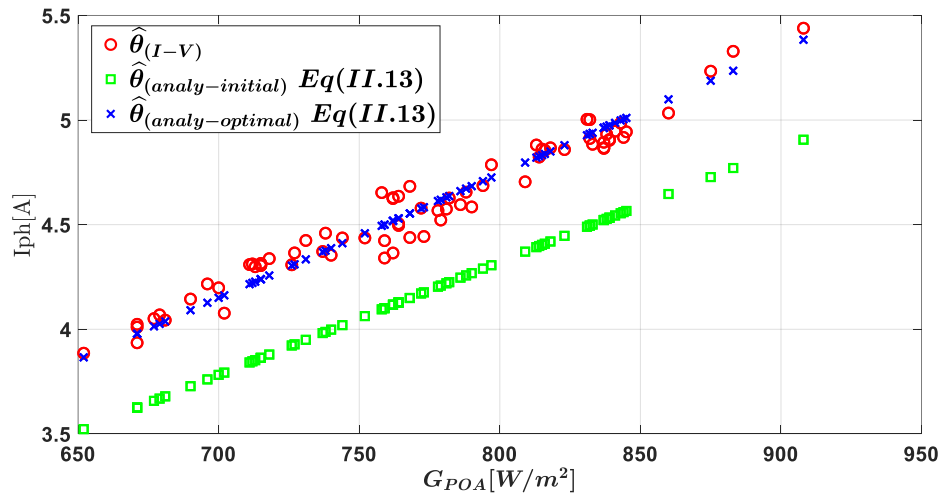


Fig.II. 12 : Evolution of the photo-generated current ( $I_{ph}$ ) with irradiance, for constant  $T_{pv} = 56^\circ\text{C}$

Once the reference temperature coefficient ( $K_{I_{ref}}$ ) is estimated for constant  $T_{pv}$ , its value is set in Eq (II.13). Then  $I_{sc_{ref}}$  can be estimated for constant  $G_{POA}$ . We assume that  $750 \text{ W/m}^2 \leq G_{POA} \leq 780 \text{ W/m}^2$  (i.e. 4% variations). The results are summarised in Table.II. 4.

Table.II. 4: Extracted reference values of Eq (II.13) for constant  $G_{POA} = 765 \text{ W/m}^2 \pm 2\%$

	$I_{sc_{ref}}$ [A]	$K_{I_{ref}}$ [%/°C]	$MAPE_{I_{ph}}$ [%]
Optimal reference values of 1 <sup>st</sup> step	5.817	0.061	6.01
Optimal reference values	5.799	0.061	1.49

The evolution of  $I_{ph}$  as the function of  $T_{pv}$  for constant irradiance ( $G_{POA} = 765 \text{ W/m}^2 \pm 2\%$ ) is shown in Fig.II. 13 . It can be observed that the module temperature  $T_{pv}$  has a slight influence on  $I_{ph}$ . The  $MAPE_{I_{ph}}$  is equal to 1.49%.

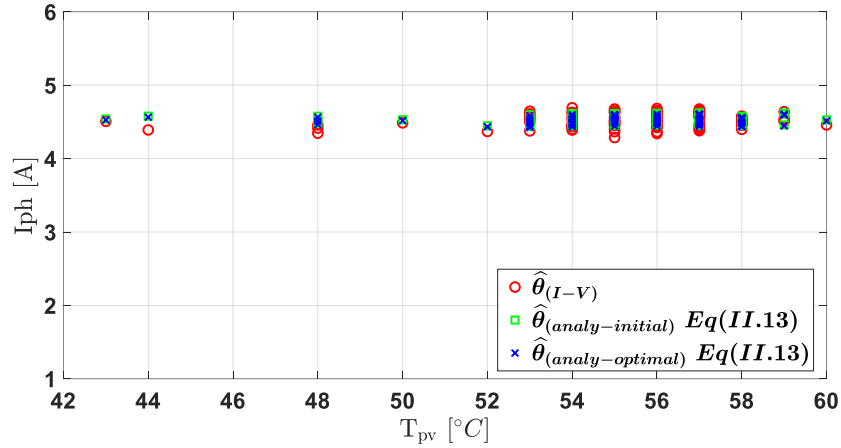


Fig.II. 13 : Evolution of the photo-generated current ( $I_{ph}$ ) with  $T_{pv}$  for constant  $G_{POA} = 765 \text{ W/m}^2 \pm 2\%$

Once the optimal reference values of  $I_{sc\_ref}$  and  $K_{I\_ref}$  are estimated, its values is set in Eq (II.13). Then  $\hat{I}_{ph(analy)}$  can be calculated for all measured in training stage (488 values) under the difference of  $T_{pv}$  and  $G_{POA}$ . The evolution of  $\hat{I}_{ph(analy)}$  and  $\hat{I}_{ph(I-V)}$  as function of  $G_{POA}$  and  $T_{pv}$  is illustrated in Fig.II. 14. This figure shows a good agreement. The  $MAPE_{I_{ph}}$  is equal to 1.57%.

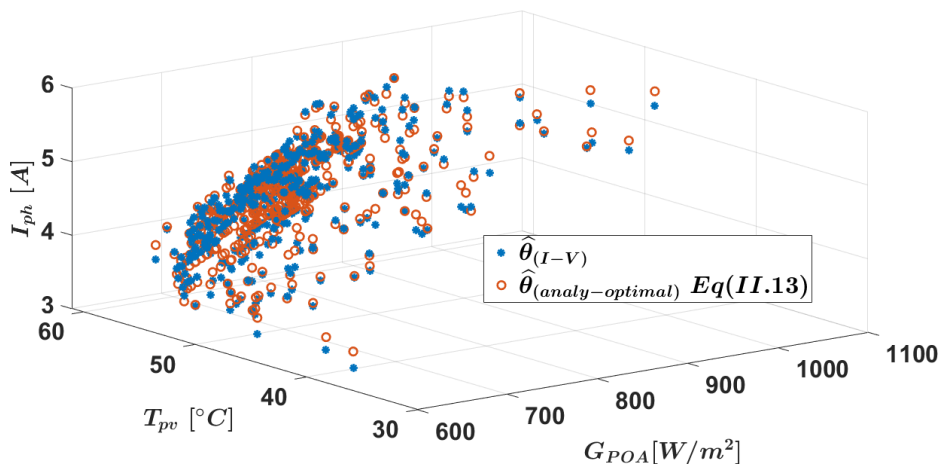


Fig.II. 14: Evolution of the photo generated current ( $I_{ph}$ ) with  $G_{POA}$  and  $T_{pv}$  for all the measured values in the training stage.

### II.6.1.2. Analytical model of the diode saturation current ( $I_0$ )

$I_0$  is exclusively affected by temperature, as shown in Eq (II.16). The impact of irradiance is not considered here. The reference values are  $V_{oc\_ref}$ ,  $K_{V\_ref}$ ,  $I_{sc\_ref}$ , and  $K_{I\_ref}$ .

The last two ones have been determined in the previous section. *Table.II. 5* and *Fig.II. 15* show the estimated reference values and the evolution of  $I_0$  as a function of temperature, respectively.  $I_0$  slightly increases with  $T_{pv}$ . The evolution of  $\hat{I}_{0(analy)}$  and  $\hat{I}_{0(I-V)}$  as function of  $G_{POA}$  and  $T_{pv}$  in 3D is illustrated in *Fig.II. 16*. The results shows a good agreement and the  $MAPE_{I_0}$ , is equal to 10.5 %.

*Table.II. 5 : Extracted reference values of Eq (II.16)*

	$V_{oc\_ref}$ [V]	$K_{V\_ref}$ [%/°C]	$MAPE_{I_0}$ [%]
Initial reference values	21.7	-0.387	60.4
Optimal reference values	20.68	-0.519	10.5

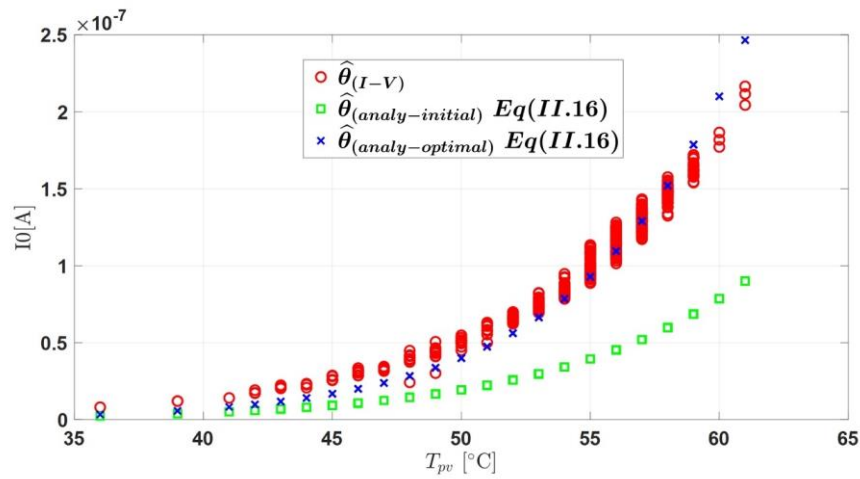


*Fig.II. 15: Evolution of the diode saturation current ( $I_0$ ) with  $T_{pv}$*

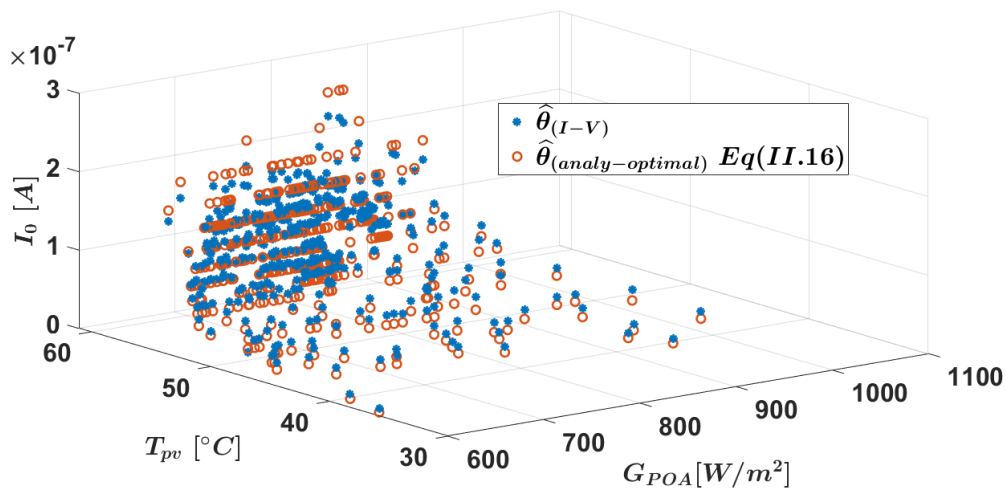


*Fig.II. 16: Evolution of the diode saturation current ( $I_0$ ) with  $G_{POA}$  and  $T_{pv}$  for all the measured values in the training stage.*

II.6.1.3. Analytical model of diode ideality factor ( $n$ )

Eq (II.24) explains that the diode ideality factor ( $n$ ) is exclusively affected by temperature. Hence, only the influence of temperature is considered. The estimation of the reference value is shown in *Table.II. 6*. The  $MAPE_n$  and  $n_{ref}$  calculated are 0.831% and 1.01 respectively. *Fig.II. 17* represents the evaluation of  $n$  as function of  $T_{pv}$ , the result shows that  $n$  is relatively constant. The evolution of  $\hat{n}_{(analy)}$  and  $\hat{n}_{(I-V)}$  as function of  $G_{POA}$  and  $T_{pv}$  in 3D is illustrated in *Fig.II. 18*, the finding shows a good agreement.

*Table.II. 6 : Estimated reference value of Eq (21) while  $G_{POA}$  are constant*

	$n_{ref} [-]$	$MAPE_n [\%]$
Initial reference value	1	0.851
Optimal reference value	1.01	0.831

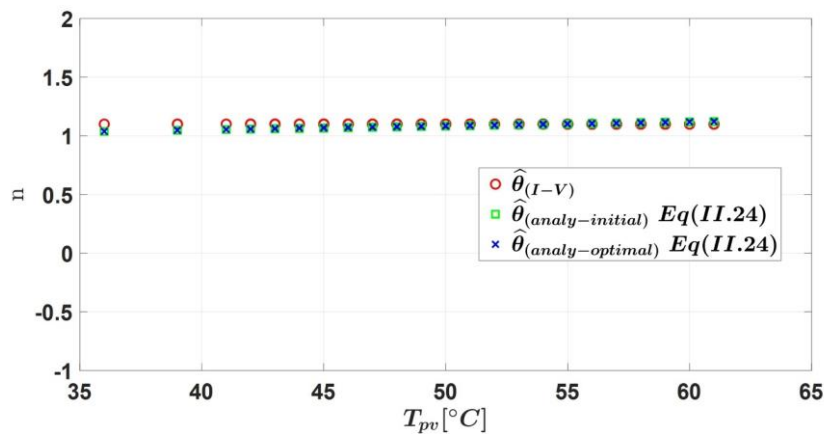


*Fig.II. 17 : Evolution of  $n$  with  $T_{pv}$  while  $G_{poa}$  are constant*

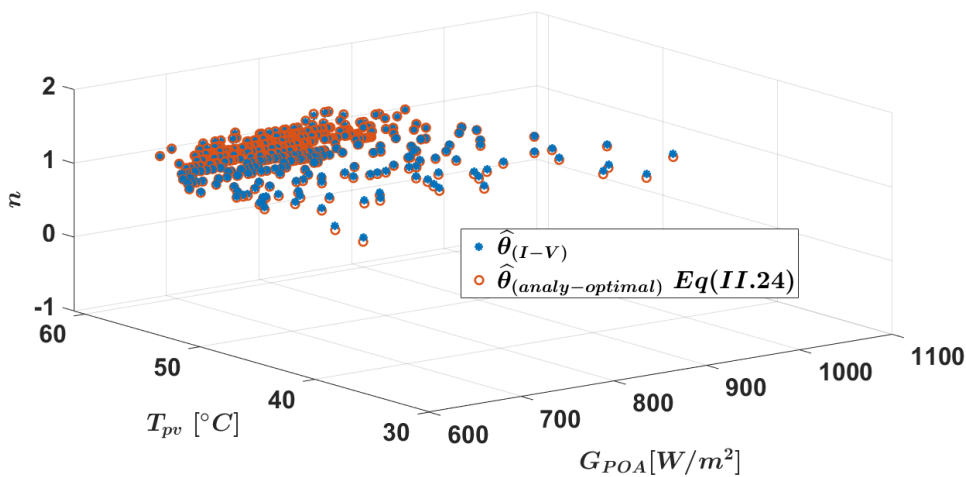


*Fig.II. 18 : : Evolution of  $n$  with with  $G_{POA}$  and  $T_{pv}$  for all the measured values in the training stage.*

II.6.1.4. Analytical model of the series resistance ( $R_s$ )

Based on the literature review mentioned in section II.3 for the series resistance ( $R_s$ ), three analytical models are considered and compared with the extracted one. The best analytical model will be selected based on determining the lowest of  $MAPE_{R_s}$ . Eq. (II.17), in which reference values are  $R_{s\_ref}$ ,  $R_{R\_ref}$ ,  $B_{ref}$  and Eq. (II.18) which depend only on the irradiance and its reference value is  $R_{s\_ref}$ . Furthermore, Eq.(19), which reference values are  $R_{s\_ref}$ ,  $\beta_{ref}$  modelise  $R_s$  dependence with irradiance and temperature.

Firstly, the reference values of each model are determined for constant  $T_{pv} = 56^\circ\text{C}$ . The results are shown in *Table.II. 7* and *Fig.II. 19*. We can notice that the models represented by Eq. (II.17) and Eq. (II.18) do not converge to the measured value. From the Eq. (II.19), the result demonstrates a good agreement with measured values. The  $MAPE_{R_s}$  are 6.1%, 4.65% and 0.88% respectively for Eq. (II.17), Eq. (II.18) and Eq. (II.19),. Therefore, the model of (II.19) is selected for our study.

*Table.II. 7: Estimation reference values of Eq(II.17.18.19) for constant  $T_{pv} = 56^\circ\text{C}$*

	Eq.	$R_{s\_ref}$ [m $\Omega$ ]	$\beta_{ref}$ [-]	$K_{R\_ref}$ [%/ $^\circ\text{C}$ ]	$B_{ref}$ [-]	$MAPE_{R_s}$ [%]
Initial reference values	II.17	800	-	0.001	0.77	28.836
	II.18	800	-	-	-	32.876
	II.19	800	0.217	-	-	18.972
Optimal ref. values of 1 <sup>st</sup> step	II.17	602	-	0.006	0.768	4.651
	II.18	799	-	-	-	6.101
	II.19	<b>708</b>	<b>0.036</b>	-	-	0.880

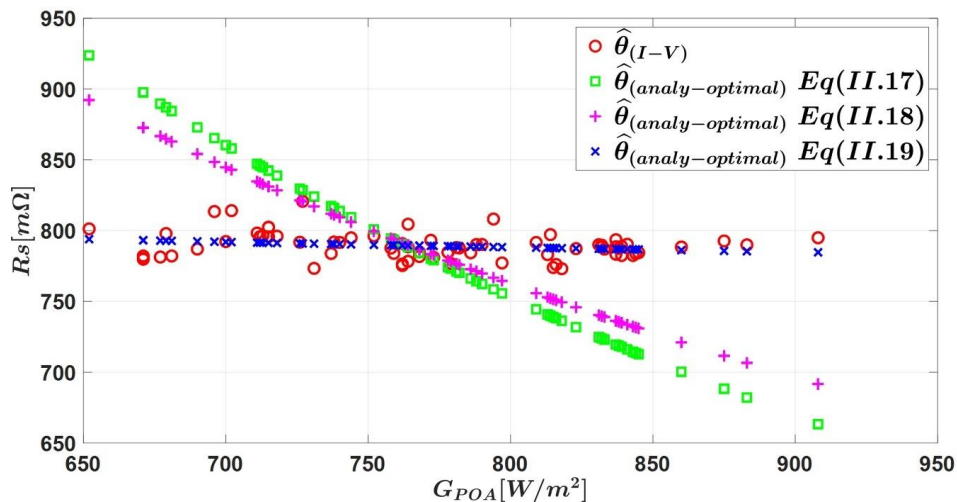


*Fig.II. 19 : Evolution of  $R_s$  with  $G_{poa}$  for constant  $T_{pv} = 56^\circ\text{C}$*

The value of  $\beta_{ref}$  is set in Eq (II.19) to analyze the influence of the temperature. The extraction results for constant irradiation are shown in *Table.II. 8* and *Fig.II. 20*. The result demonstrates that  $R_s$  linearly increases with  $T_{pv}$ . Furthermore, the calculated deviation of  $MAPE_{R_s}$  is 0.925%.

*Table.II. 8: Extracted reference value of Eq(II.19) for constant  $G_{POA} = 765 \frac{W}{m^2} \pm 2\%$*

	$R_{s\_ref}$ [m $\Omega$ ]	$\beta_{ref}$ [-]	$MAPE_{R_s}$ [%]
Optimal reference values of 1 <sup>st</sup> step	708	0.036	0.880
Optimal reference values	<b>709</b>	<b>0.036</b>	0.925

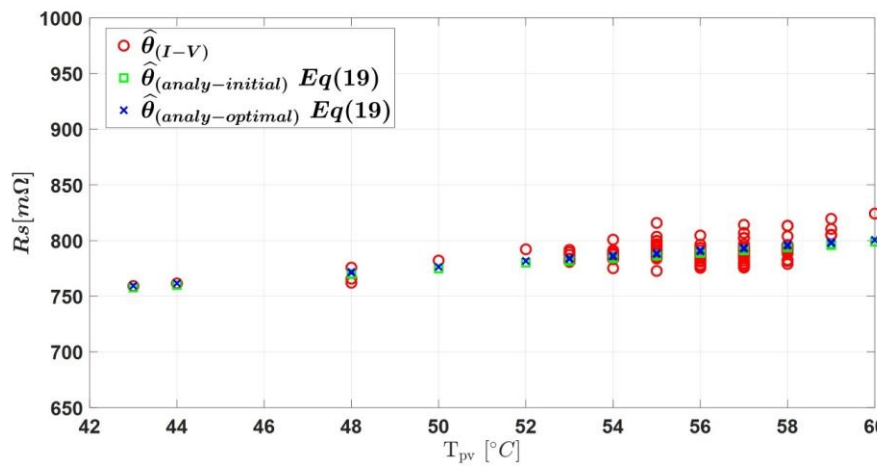


*Fig.II. 20 : Evolution of  $R_s$  with  $T_{pv}$  for constant  $G_{POA} = 765 \text{ W/m}^2 \pm 2\%$*

Once the optimal reference values of  $R_{s\_ref}$  and  $\beta_{ref}$  are estimated, its values is set in Eq (II.19). Then  $\hat{R}_{s(analy)}$  can be calculated for all measured under the difference of  $T_{pv}$  and  $G_{POA}$ . The evolution of  $\hat{R}_{s(analy-optimal)}$  and  $\hat{R}_{s(I-V)}$  as function of  $G_{POA}$  et  $T_{pv}$  in 3D is illustrated in *Fig.II. 21* This figure show a good agreement . The  $MAPE_{R_s}$  is equal to 1.175 %.

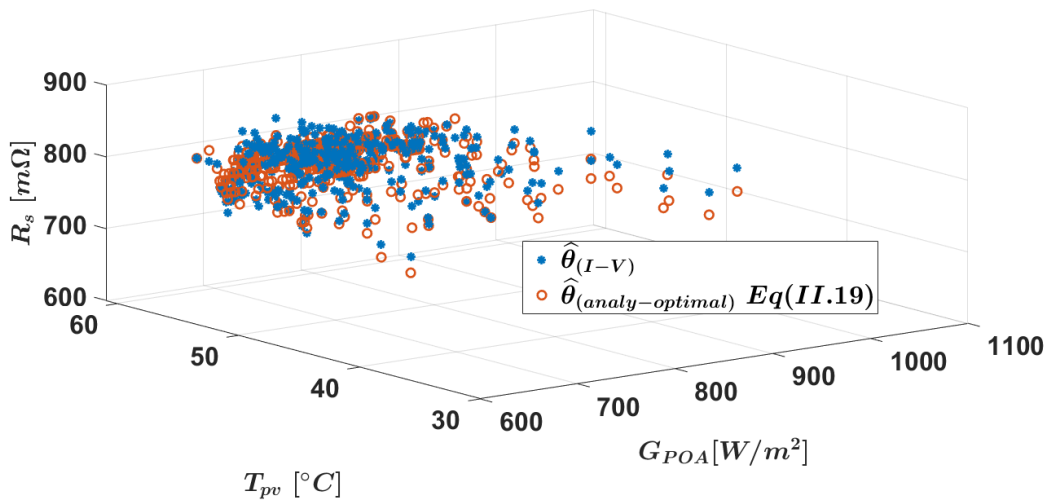


*Fig.II. 21: Evolution of  $R_s$  with  $G_{POA}$  for all the measured values in the training stage*

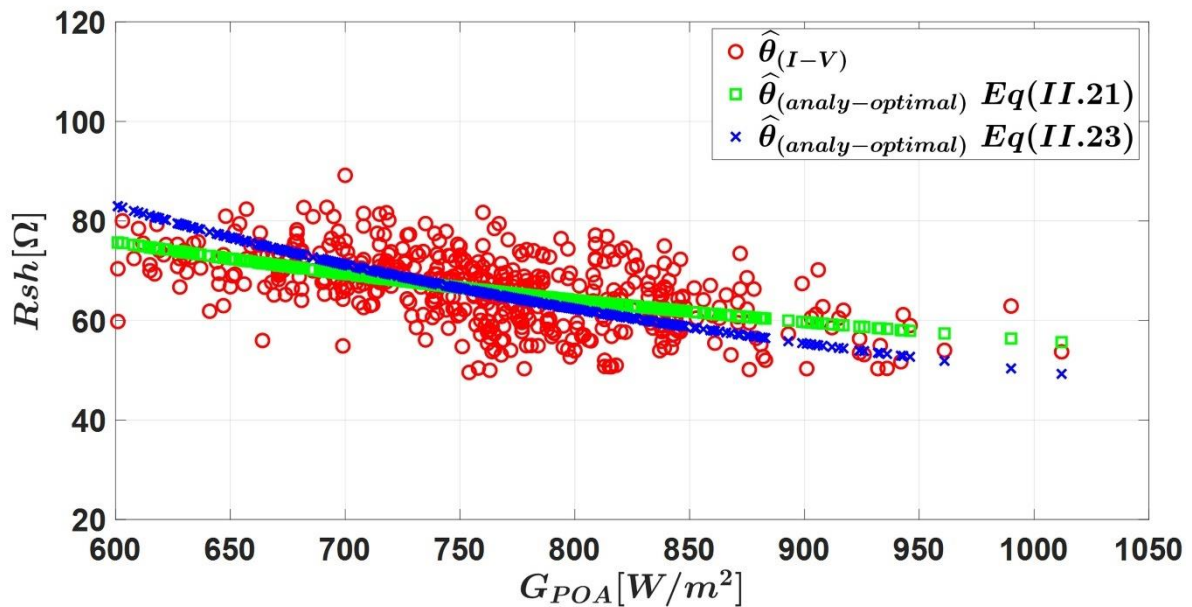


II.6.1.5. Analytical model of the shunt resistance ( $R_{sh}$ )

In this section, the analytical model described by Eq. (II.21) and Eq. (II.23) are investigated to estimate the reference value of  $R_{sh\_ref}$  and  $R_{shexp\_ref}$ . According to Eq. (II.21) and Eq.(II.23), we don't see any term of importance related to the PV module temperature. Only the influence of irradiance on  $R_{sh}$  is considered in this case. The evolution of  $R_{sh}$  as function of  $G_{POA}$  is shown in Fig.II. 22. The result demonstrates that the shunt resistance is inversly proportional to the irradiance. The reference values are extracted as shown in Table.II. 9 . The  $MAPE_{R_{sh}}$  calculated are 8.061% and 7.518% for the Eq. (II.21) and (II.23), respectively. And the model described by the Eq. (II.23) is selected for our case study. The evolution of  $\hat{R}_{sh(analy-optimal)}$  and  $\hat{R}_{sh(I-V)}$  as function of  $G_{POA}$  et  $T_{pv}$  in 3D is illustrated in Fig.II. 23. This figure show a good agreement.

Table.II. 9: Estimated value of Eq (II.21,23)

	Eq.	$R_{sh\_ref}$ [ $\Omega$ ]	$R_{shexp\_ref}$ [ $\Omega$ ]	$MAPE_{R_{sh}}$ [%]
Initial reference values	II.21	80	5.5	92.65
	II.23	80	-	55.99
Optimal reference values	II.21	38.17	1.86	8.06
	II.23	49.85	-	7.52


 Fig.II. 22: Evolution of  $R_{sh}$  with  $G_{poa}$

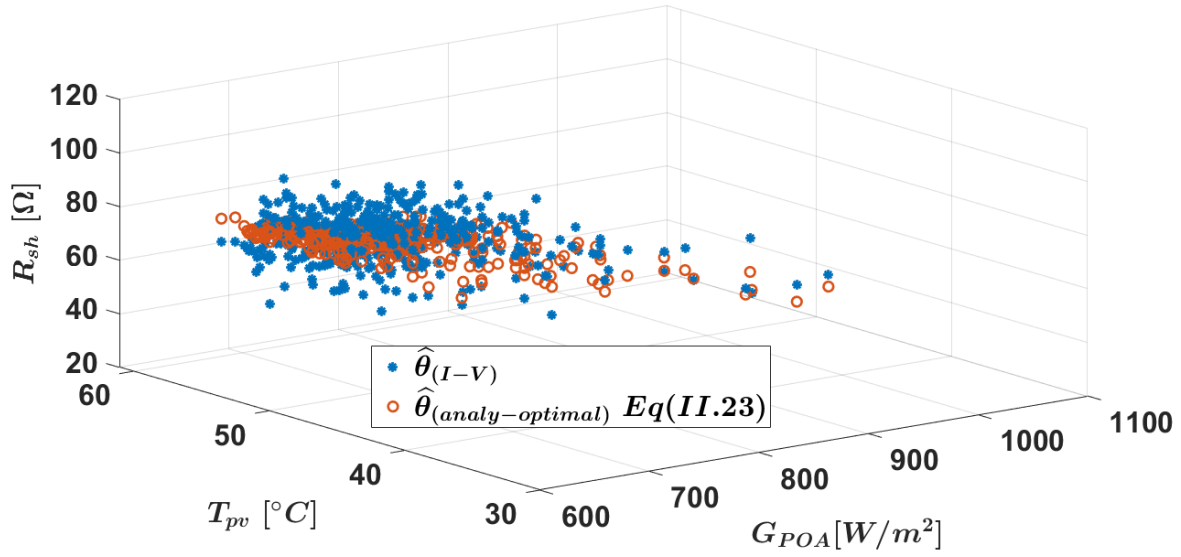


Fig.II. 23 : Evolution of  $R_{sh}$  with  $G_{POA}$  for all the measured values in the training stage

#### II.6.1.5. Summary of the training step

Table.II. 10 summarizes the eight reference values of  $\delta_{ref}$ , extracted from the 488 measurements of the training dataset. These values will now be used to estimate the five parameters of the SDM  $\hat{\theta}$  through the analytical models for all possible environmental conditions.

Table.II. 10: Summary of the eight reference values tuned during the training step and used by the analytical modelling

The single diode of PV model with five electrical parameters and eight reference values									
$I_{pv} = I_{ph} - I_0 \left[ \exp\left(\frac{q(V_{pv} + I_{pv}R_s N_s)}{nN_s K T}\right) - 1 \right] - \left(\frac{V_{pv} + I_{pv}R_s N_s}{R_{sh} N_s}\right)$									
Five electrical parameters	Analytical model	The eight reference values							
		$I_{sc,ref}$ [A]	$K_{l,ref}$ [%/°C]	$V_{oc,ref}$ [V]	$K_{v,ref}$ [%/°C]	$R_{s,ref}$ [mΩ]	$\beta_{ref}$ [-]	$R_{sh,ref}$ [Ω]	$n_{ref}$ [-]
$I_{ph}$	$I_{ph} = I_{sc,ref} [1 + K_{l,ref} (T_{pv} - T_{STC})] \frac{G_{POA}}{G_{STC}}$	5.79	0.061	-	-	-	-	-	-
$I_0$	$I_0 = \frac{I_{sc,ref} + K_{l,ref} (T_{pv} - T_{STC})}{\exp\left(\frac{qV_{oc,ref} [1 + K_{v,ref} (T_{pv} - T_{STC})]}{nKN_s T}\right)} - 1$	5.79	0.061	20.68	-0.519	-	-	-	-
$R_s$	$R_s = R_{s,ref} \left[ \frac{T}{T_n} \left( 1 - \beta_{ref} \ln\left(\frac{G_{POA}}{G_{STC}}\right) \right) \right]$	-	-	-	-	709	0.036	-	-
$R_{sh}$	$R_{sh} = R_{sh,ref} \frac{G_{STC}}{G_{POA}}$	-	-	-	-	-	-	49.85	-
$n$	$n = n_{ref} \frac{T}{T_n}$	-	-	-	-	-	-	-	1.01

### II.6.2. The validation stage

After the training stage, the validation stage will compare the analytically calculated five parameters of the SDM with extracted ones using the LM algorithm. The dataset of measurements is different for the validation than for the training and is summed up in [Table.II. 11.](#)

*Table.II. 11: Dataset used for the validation stage*

	Date of acquisition	Weather	Number of I-V curve $G_{POA} \geq 600 \text{ W/m}^2$
1	03/09/2021	Partly cloudy	100
2	09/09/2021	Partly cloudy	21
3	12/09/2021	Partly cloudy	9
4	13/09/2021	Partly cloudy	42
5	22/09/2021	Partly cloudy	12
6	08/10/2021	Partly cloudy	44
7	09/10/2021	Partly cloudy	71
8	10/10/2021	Partly cloudy	56
9	11/10/2021	Partly cloudy	47
10	15/10/2021	Partly cloudy	27
Total			429

In order to evaluate the performance of the proposed analytic models of the SDM parameters, we compute residuals, which are defined as the difference between the SDM parameters extracted from measured I-V curves with the LM algorithm ( $\hat{\theta}_{(I-V)}$ ) and the estimated ones ( $\hat{\theta}_{analy}$ ). The errors ( $\varepsilon$ ) and the standard deviation ( $\sigma$ ) are calculated with the formulas below:

$$\varepsilon_i = \text{abs}(\hat{\theta}_{(I-V)_i} - \hat{\theta}_{analy_i}) \quad (\text{II.35})$$

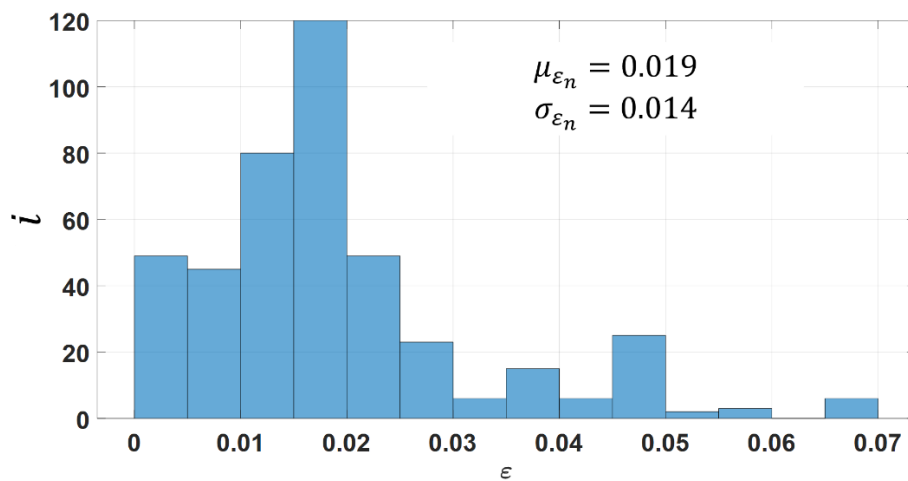
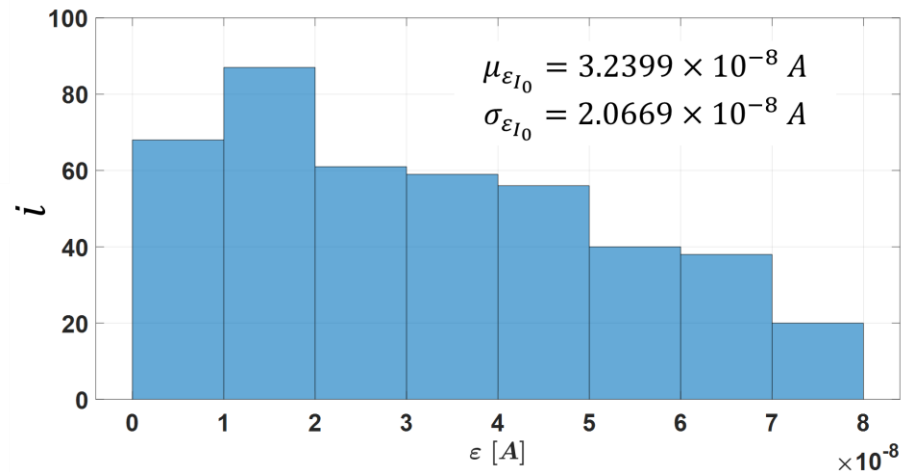
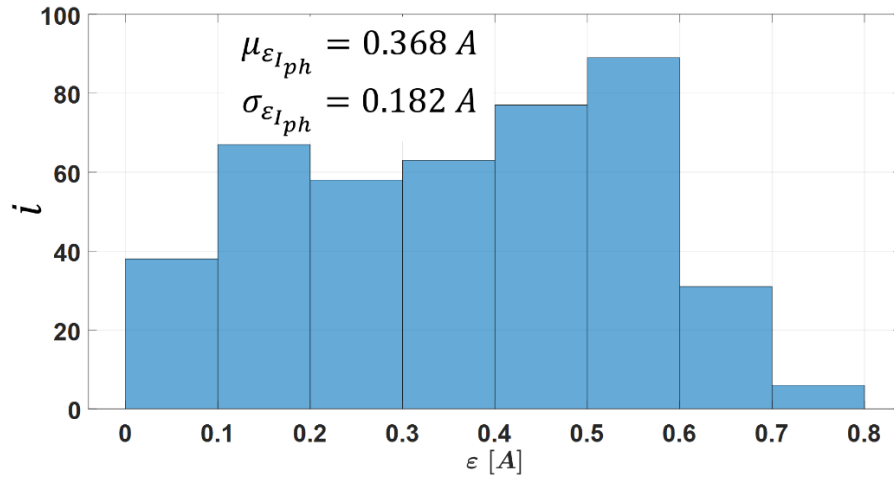
$$\mu = \frac{\sum x_i}{M} \quad (\text{II.36})$$

$$\sigma = \sqrt{\frac{(x_i - \mu)^2}{M-1}} \quad (\text{II.37})$$

Where,  $x_i$  is observation value, which may be  $\varepsilon_i$

[Fig.II. 24](#) shows the uncertainties in the estimation errors of the different parameters. The finding showed significant dispersion for all the parameters, mostly due to the variable environmental conditions. Despite the scattered uncertainties in the estimation errors of the five parameters, the analytical models remain valid. In fact, the measurement could only be used to identify four parameters. There was, therefore, a degree of freedom to obtain the correct I-V

characteristic for several parameters combination. Finally, the vector of parameters estimated from the analytical models can be used to make a diagnosis at the PV cell/model/string or array level, under different irradiance and temperature.



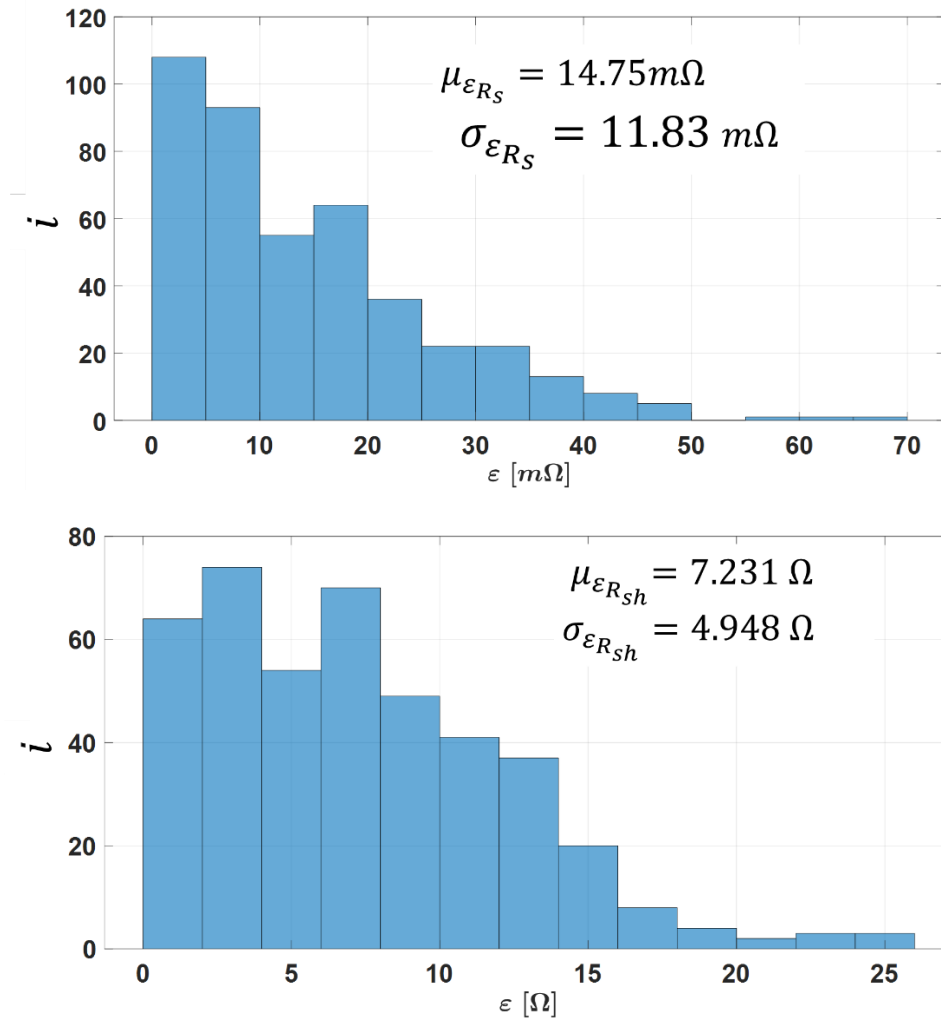


Fig.II. 24 : Error analysis ( $\epsilon = \text{abs}(\hat{\theta}_{(I-V)} - \hat{\theta}_{analy})$ ) during the validation step ( $M=429$ )

## II.7. Description and validation of the hybrid PV model

The hybrid model is developed to accurately simulate a PV array in real conditions and compare the results to measurements for FDD. It includes the analytical models described in the previous section combined with a numerical PV model in Matlab/Simulink for the SDM, as shown in *Fig.II. 25*. The detail is described in Appendix. The I-V curves obtained from the hybrid model are compared to the measured ones to evaluate its accuracy in *Fig.II. 26*.

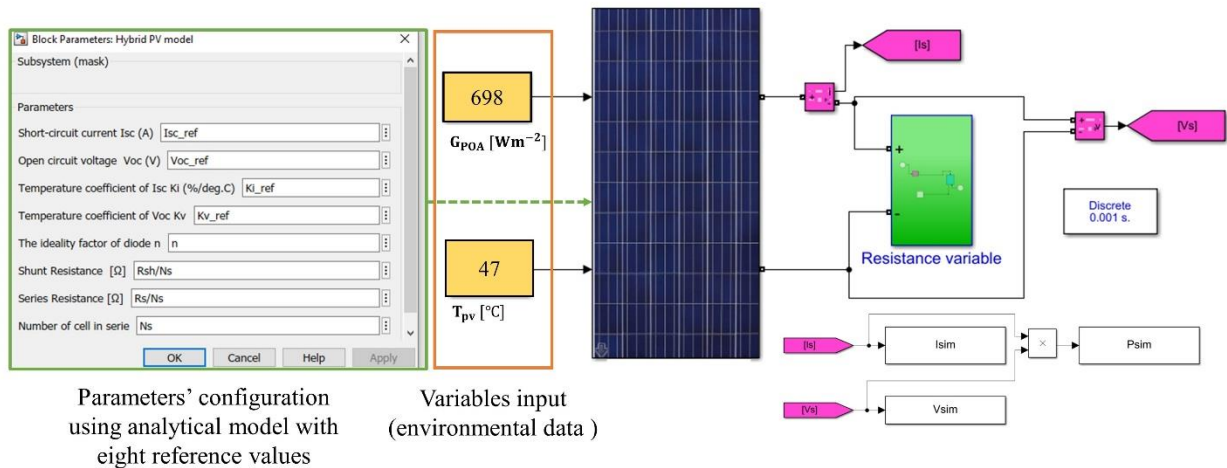


Fig.II. 25 : Presentation of the whole hybrid PV model with the variable input of environment ( $G_{POA} = 689 \text{ Wm}^{-2}$  and  $T_{pv} = 47^\circ\text{C}$ )

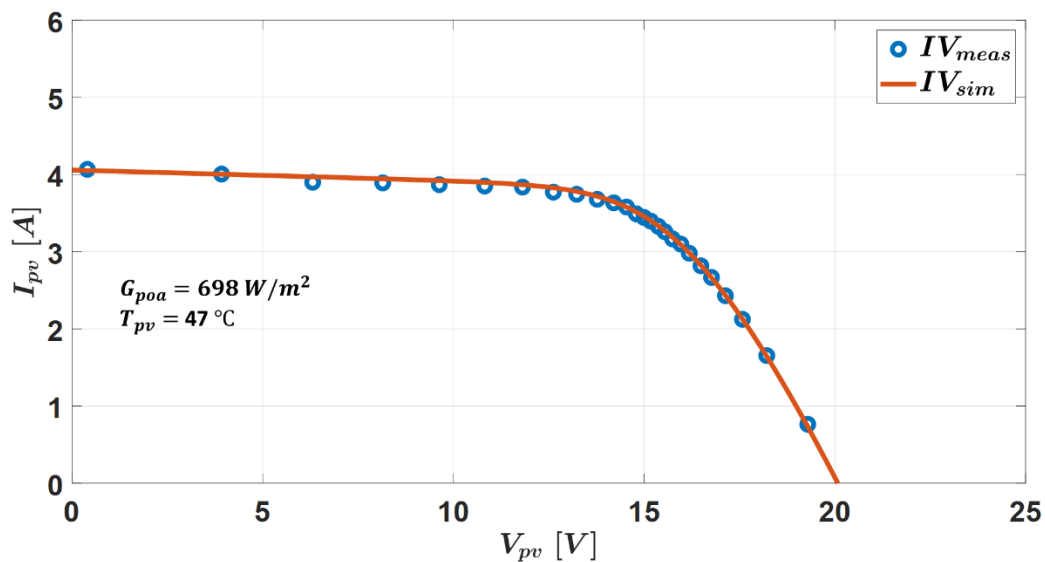


Fig.II. 26: Measured (I-V tracer) and simulated (Hybrid PV model) I-V curve of a PV module

Fig.II. 26 shows the I-V characteristic of the PV module obtained from the measurement (26 sampling points) and the simulation (1000 sampling points). As the number of points on the I-V curve in both cases is different, herein, the comparison between them is impossible. Therefore, the resampling of the simulated I-V curves is proposed in next sub-section.

### II.7.1. Resampling I-V curves of simulation

As mentioned in chapter I, the logarithmic distribution of points (LDP) with 26 optimal numbers of points is applied with the low-cost I-V tracer to measure the I-V curves of the PV modules. The I-V curve can be divided into two zones, such as a constant current zone, where the number of points is called  $NbPtV$  (1<sup>st</sup> to 15<sup>th</sup> sampling points of the I-V curve), and a

constant voltage zone where the number of points is called  $NbPtI$  (15<sup>th</sup> to 26<sup>th</sup> sampling points of I-V curve). The simulated I-V curve is obtained with 1000 uniformly distributed points. In order to compare point to point, the simulated and the measured I-V curves (e.g., to calculate MAPE), these I-V curves need to have the same number of points and the same distribution on the voltage axis.

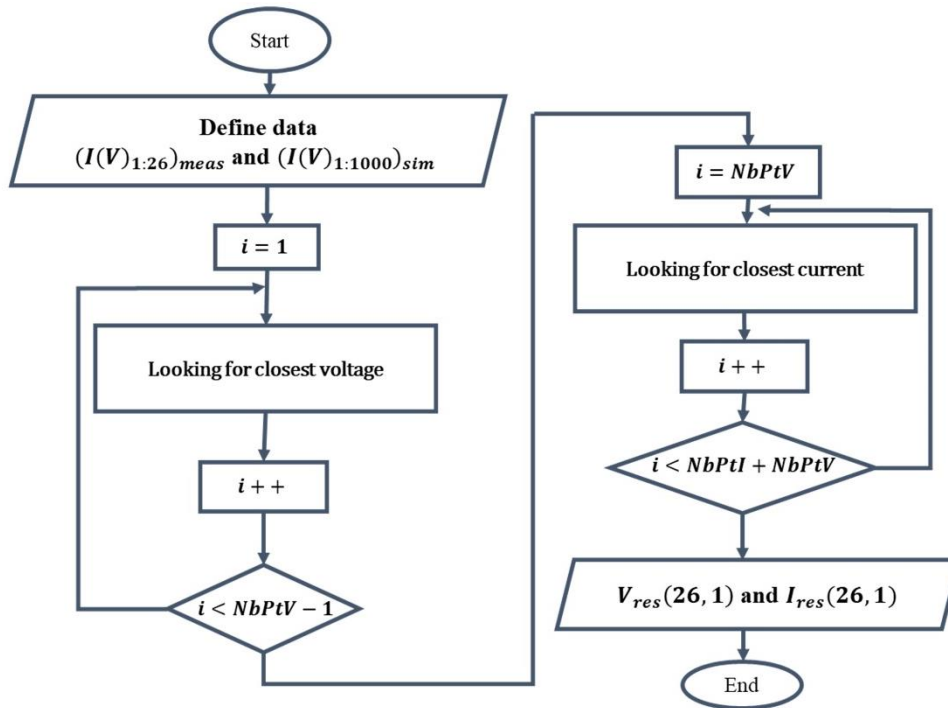


Fig.II. 27 : Flowchart for the resampling of the simulated I-V curve to the same format of the measured I-V curve

Fig.II. 27 illustrates the flowchart for resampling the 1000 points of the simulated I-V curve to 26 samples with the same distribution as the measured I-V curve. In the constant voltage zone ( $NbPtI$ ), the voltage is almost constant so the closest simulated point is determined by looking for the closest measured current value. Reciprocally, in the constant current zone ( $NbPtV$ ), it the current that is almost constant. Herein, the closest point is determined by looking for the closest measured voltage value. Fig.II. 28 shows the I-V curve of the PV module obtained from measured (26 points, blue markers), simulation (1000 points, red line), and resampling (26 points, yellow markers). This figure demonstrates that the I-V curve obtained from measured and resampling simulation can be compared and analyzed; the sampling points on I-V curves are the same.

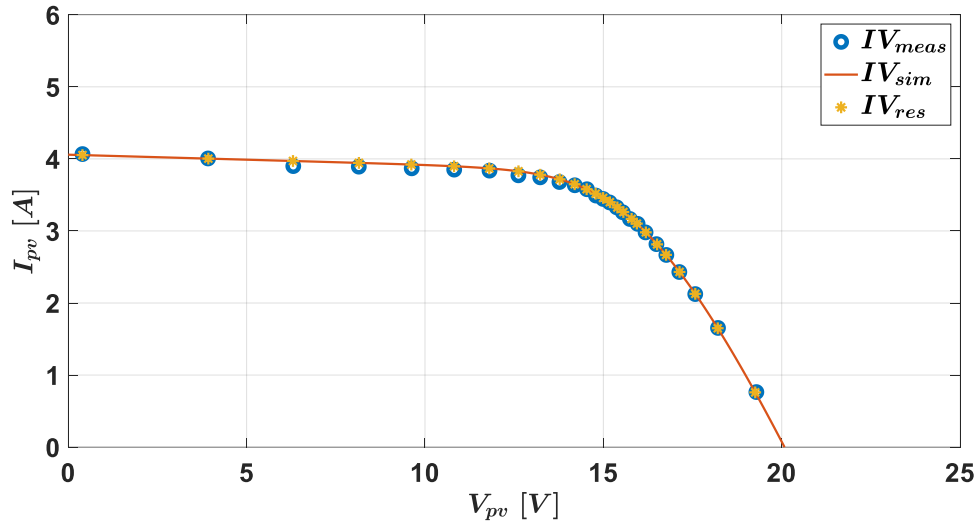


Fig.II. 28: I-V curve of PV module obtained from measured (26 samples), simulation (1000 samples), and resampling (26 samples)

### II.7.2. Hybrid PV model validation

The validation process for the hybrid PV model is shown in the flowchart in [Fig.II. 29](#); the input variables of this model are  $G_{POA}$  and  $T_{pv}$  from the measured conditions. The output of the model is the I-V curve, then  $X_{1_{res}}$  and  $X_{2_{res}}$  can be derived from this simulated I-V curve. To evaluate the hybrid PV model's accuracy, the data obtained from the simulation are then compared to the measured one ( $X_{1_{meas}}$  and  $X_{2_{meas}}$ ). The mean absolute percentage error ( $MAPE(X_1)$ ), the absolute relative errors ( $ARE(X_2)$ ) are computed as formulas below:

- $X_1 = [I_{pv}], [V_{pv}]$  (26 couples)

$$MAPE(X_1) = \frac{100}{m} \sum_{i=1}^m \left| \frac{X_{1_{meas}}(i) - X_{1_{res}}(i)}{X_{1_{meas}}(i)} \right| \quad (II.38)$$

- $X_2 = [P_{mpp}, I_{sc}, V_{oc}]$

$$ARE(X_2) = 100 \frac{|X_{2_{meas}} - X_{2_{res}}|}{X_{2_{meas}}} \quad (II.39)$$

The average and the standard deviation are calculated according to Eq. (II. 36) et (II.37).

The subscripts “meas” and “res” denote measurement and resampling after simulation. Where  $X_1$  can be the vector of  $I_{pv}$  or  $V_{pv}$  and  $X_2$  can be scalar of  $P_{mpp}$  or  $I_{sc}$  or  $V_{oc}$ .  $M$  is the number of the I-V curve, and  $m$  is the number of points on the I-V curve ( $m = 26$ ).



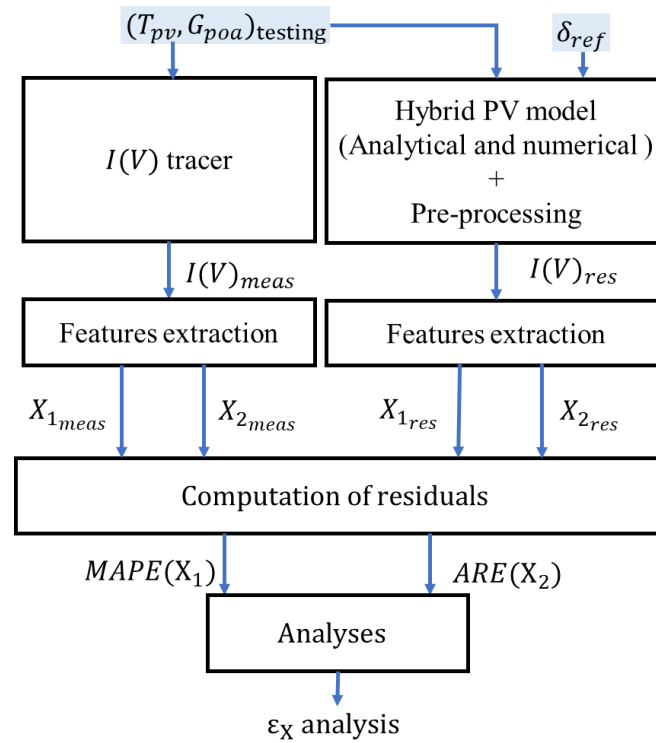
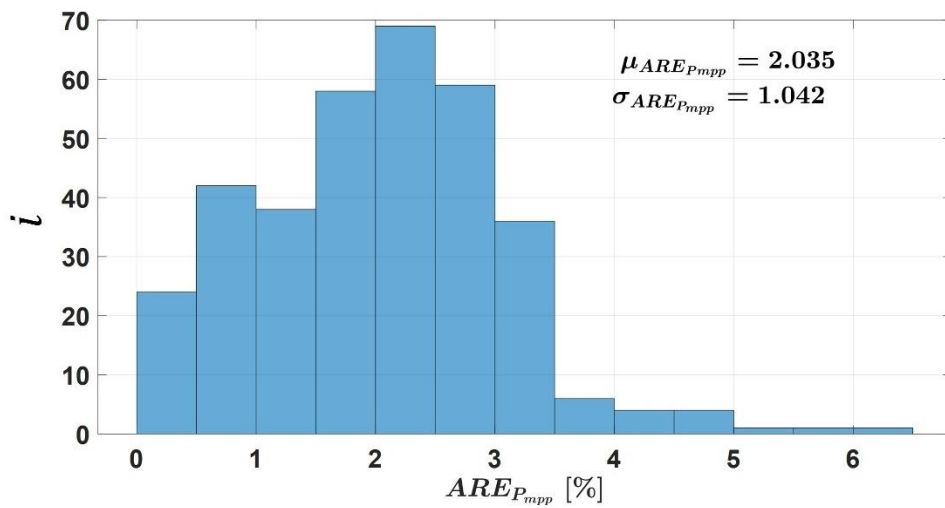
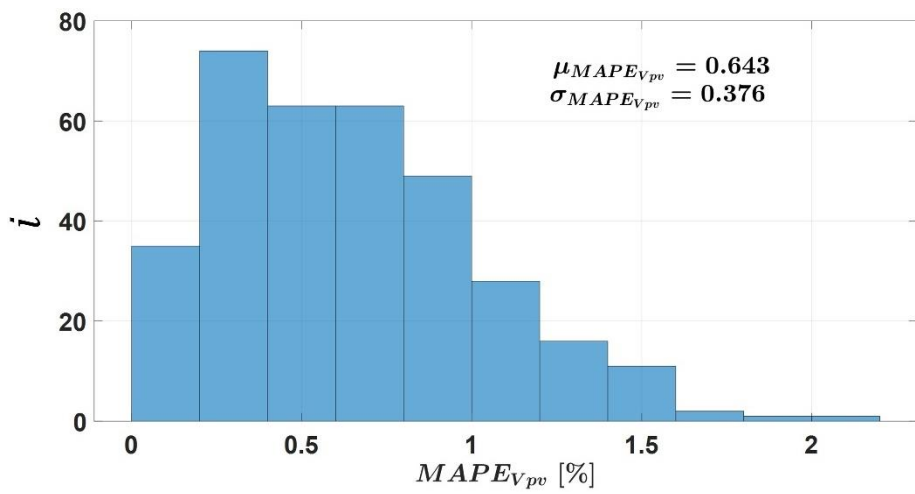
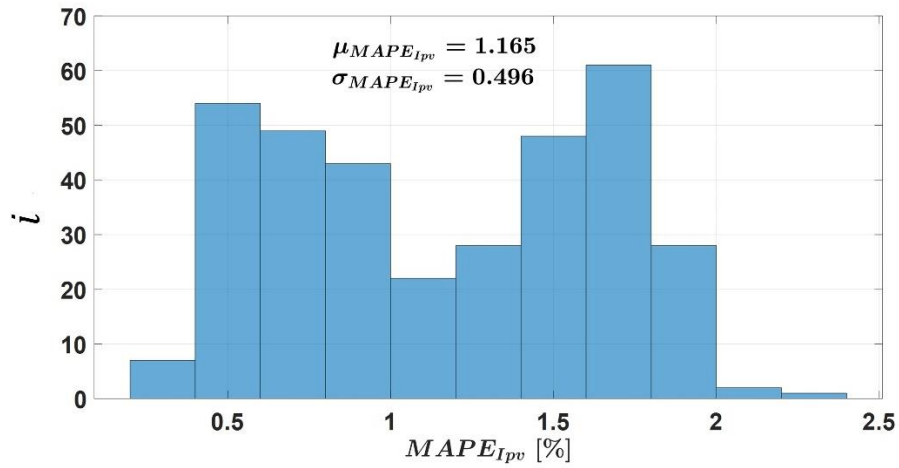


Fig.II. 29: Flowchart of the hybrid PV model validation

The Testing dataset shown in *Table.II. 12*, which are different from the training dataset, is used to test and validate the hybrid PV model. The histogram plotted in *Fig.II. 30*. It shows that the errors between the experimental values, and the simulated ones, are lower than 3%. Therefore, the hybrid model is accurate and robust to various environmental conditions. It is suitable for health monitoring and FDD.

Table.II. 12: Data acquisition used for validation of the hybrid PV model

Date of acquisition		Weather	Number of I-V curves $G_{poa} \geq 600 \text{ W/m}^2$
1	03/09/2021	Partly cloudy	100
2	09/09/2021	Partly cloudy	21
3	12/09/2021	Partly cloudy	9
4	13/09/2021	Partly cloudy	42
5	22/09/2021	Partly cloudy	12
6	08/10/2021	Partly cloudy	44
7	09/10/2021	Partly cloudy	71
8	10/10/2021	Partly cloudy	44
Total			343



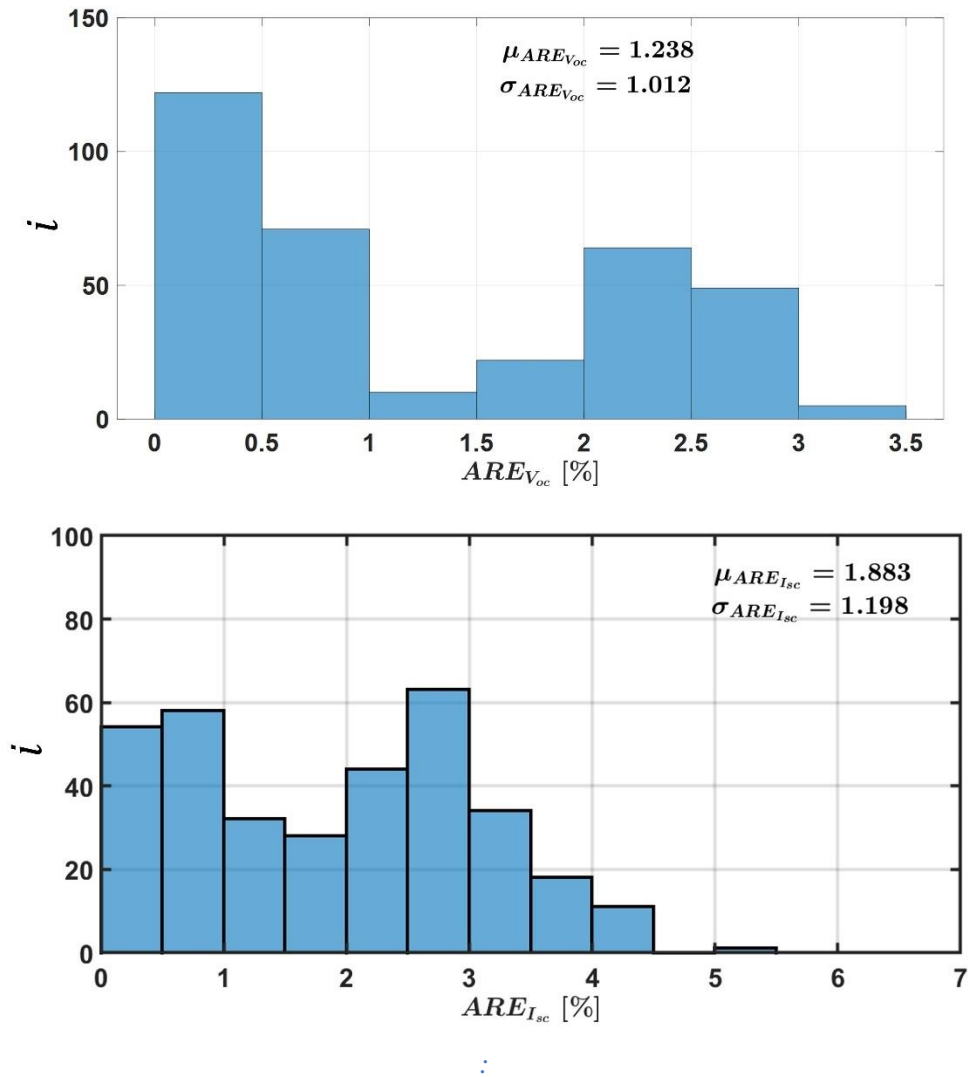


Fig.II. 30: Histogram of error distribution between measurements and simulation with the hybrid model ( $M = 343$ ) and all units of the average and standard deviation in %

## II.8. Analysis of sensitivity to errors due to variations of PV module temperature ( $T_{pv}$ )

The temperature of the PV module ( $T_{pv}$ ) is one of the critical parameters that impact the I-V characteristics. Therefore, this section aims to analyze the error sensitivity with the variation of  $T_{pv}$ .

*Fig.II. 31* explains the methodology of this sensibility analysis by varying  $T_{pv}$ . The dataset used in this study is the same as the hybrid model validation dataset (*Table II.12*), but only the last 208<sup>th</sup> measurements. The values of  $G_{poa}$  will be kept at the same values as the measurements, while the values of  $T_{pv}$  will be varied from (measurement -10°C) to

(measurement +10°C, by 2°C step). The profile of irradiance and temperature used in this study are shown in Fig.II. 32.

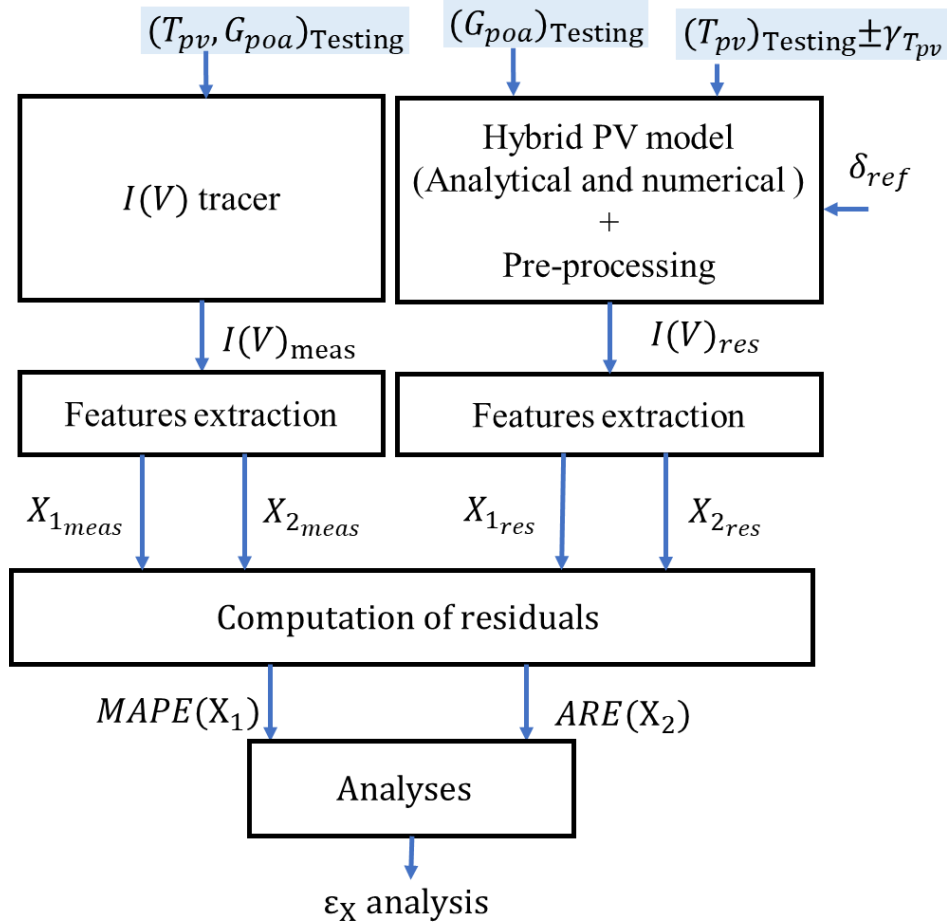


Fig.II. 31: Flowchart of the sensitivity analysis of errors due to changes in  $T_{pv}$

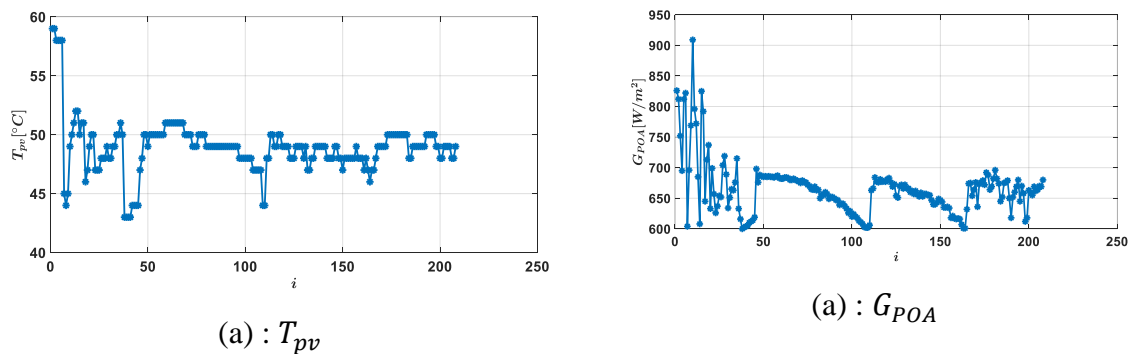
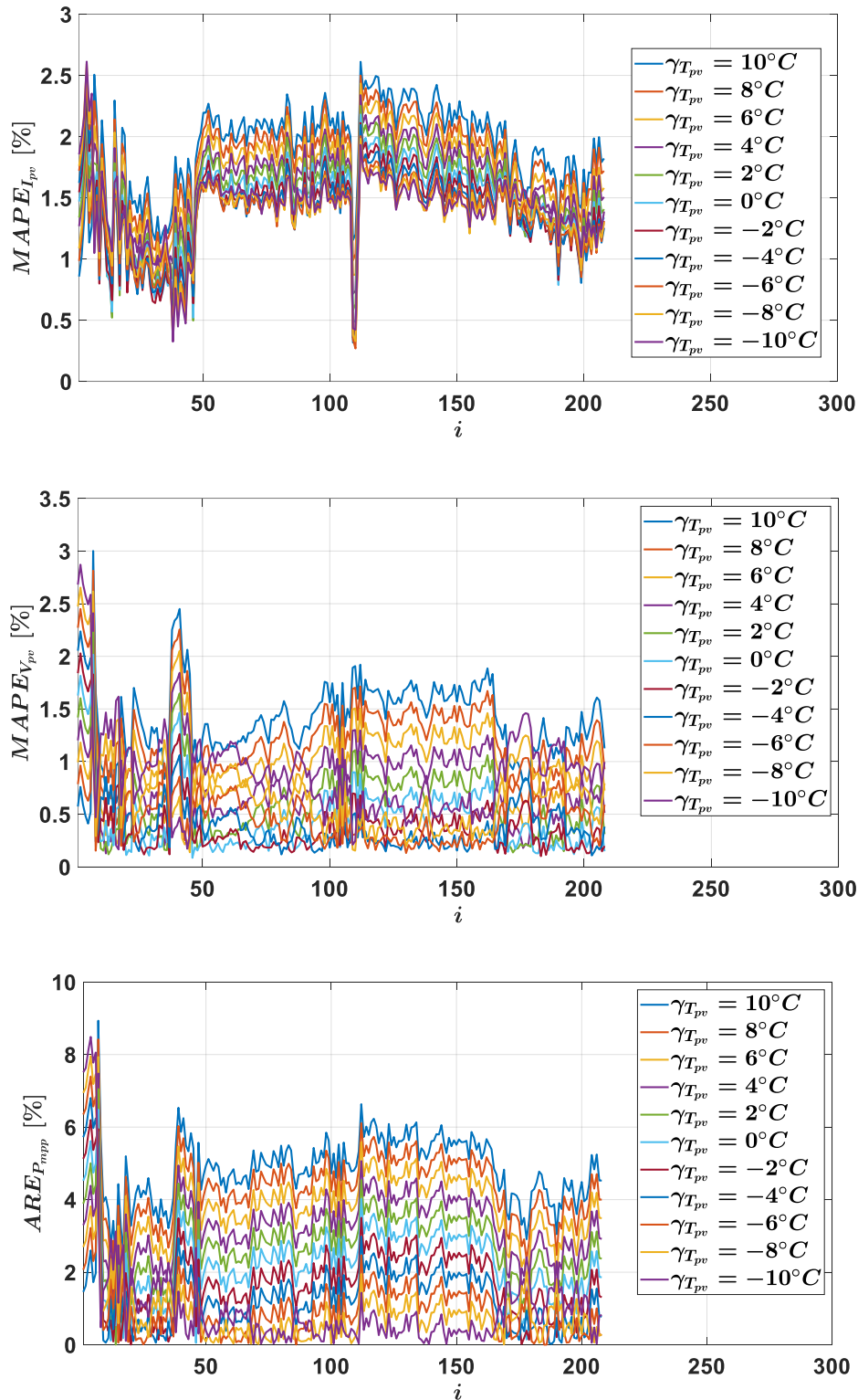


Fig.II. 32: Profile of  $T_{pv}$  and  $G_{POA}$

The same analysis as in the hybrid model validation (section II.7) is done here, but instead of having one simulated curve for one measurement, they are eleven (measure  $T_{pv} \pm 10^\circ\text{C}$ , by step of  $2^\circ\text{C}$ ). Fig.II. 33 shows the error evolution as a function of the number of the measured I-V curves.



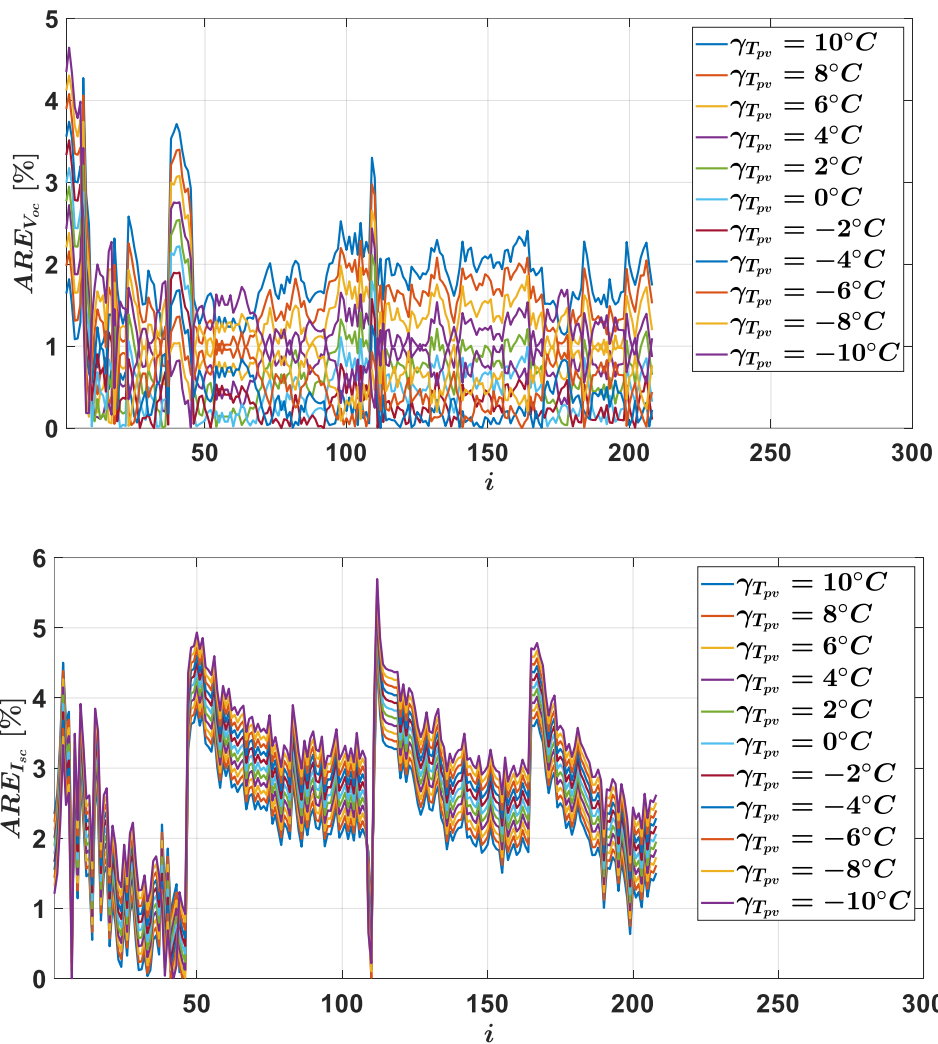
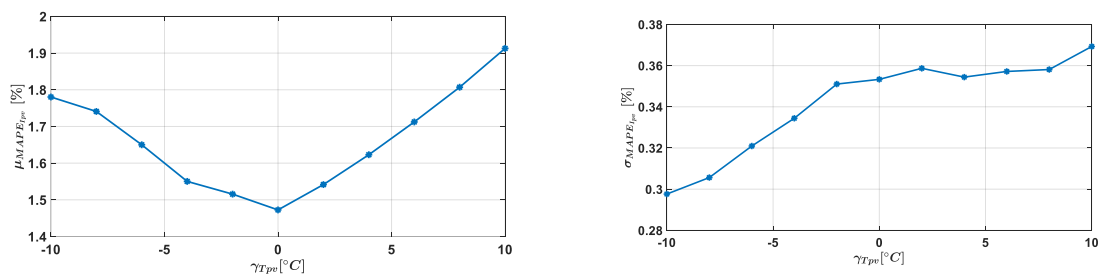


Fig.II. 33: Error analyses while  $T_{pv}$  vary of  $\pm 10^\circ C$  from its measured value and  $G_{POA}$  is the measured one

For each temperature, the average ( $\mu$ ) and standard deviation ( $\sigma$ ) of the errors are calculated, for one temperature and all the 208 measurements. Fig.II. 34 shows the evolution of  $\mu$  and  $\sigma$  according to the added temperature ( $\gamma_{T_{pv}}$ ).



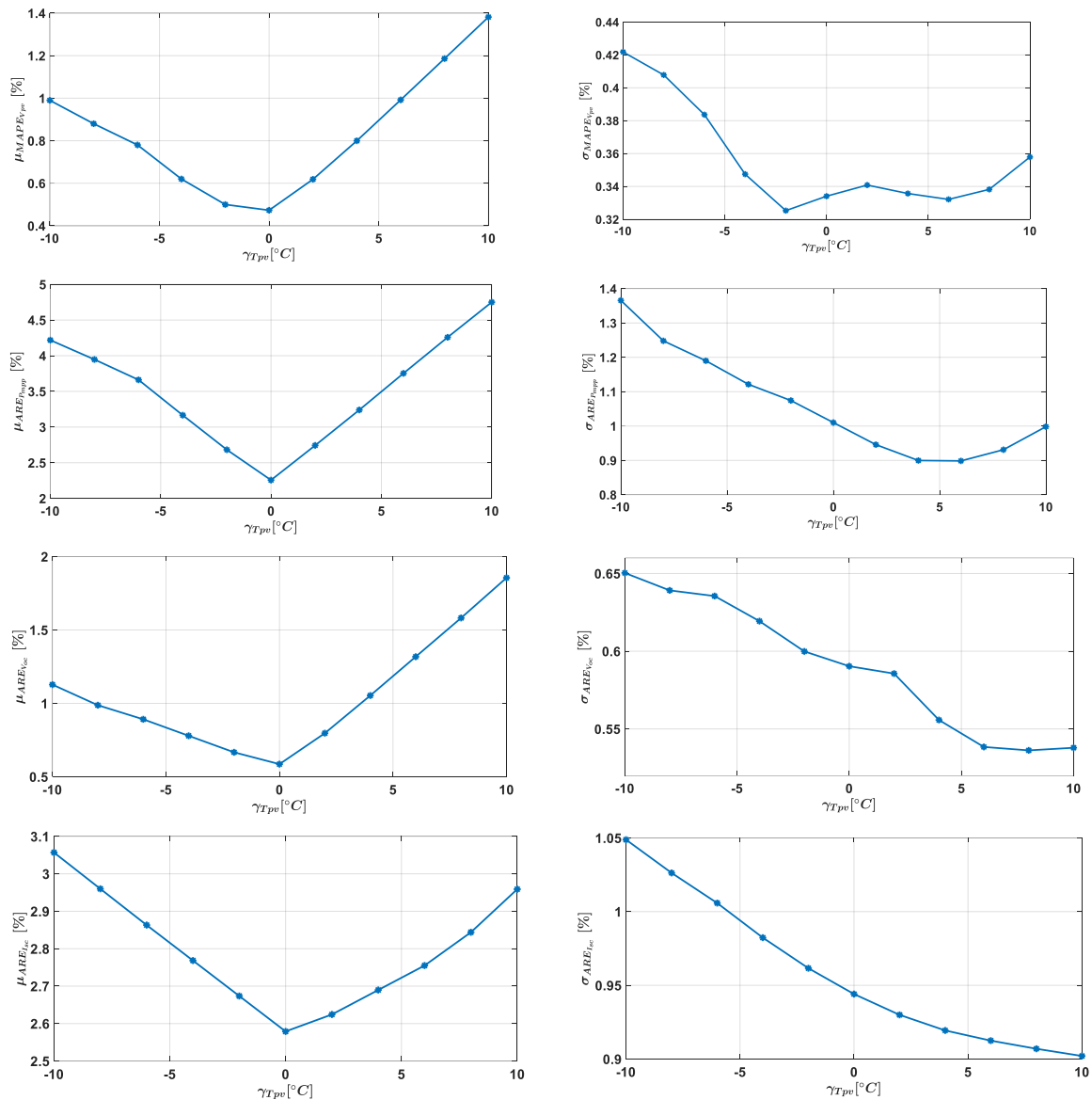
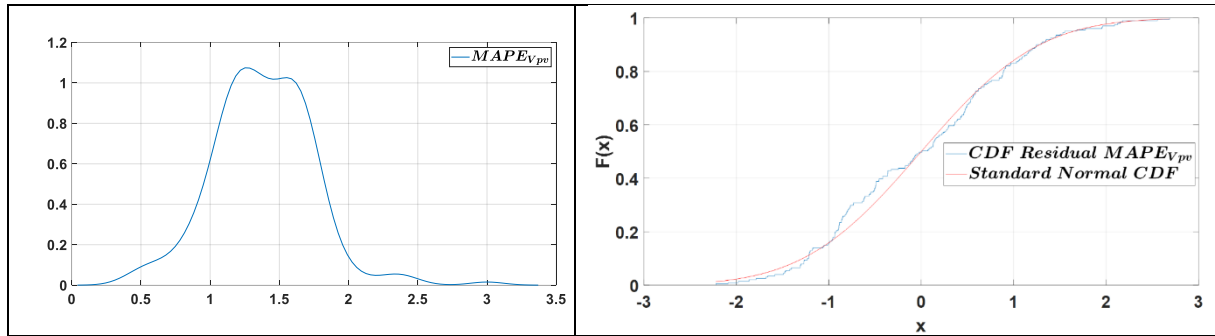


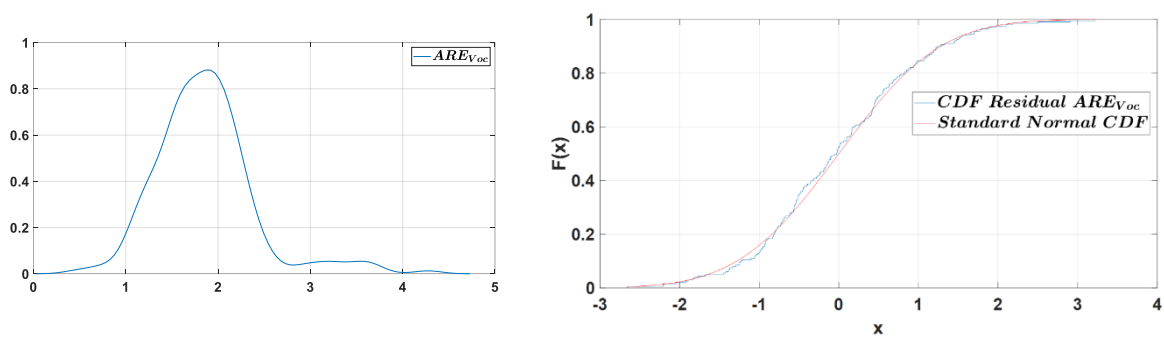
Fig.II. 34 : Average (left) and standard deviation (right) of errors as a function of the added temperature ( $\gamma_{T_{pv}} = \pm 10^{\circ}\text{C}$ )

Fig.II. 34 shows that the average of each error is obtained for  $\gamma_{T_{pv}} = 0^{\circ}\text{C}$ , which is rather reassuring because it means that the difference between the simulation and the measurement is minimal when the simulation is led under exactly the same temperature and irradiance conditions as the measurement. The standard deviation has an acceptable low value except for  $I_{sc}$ ,  $I_{pv}$  and  $P_{mpp}$ . This may be a consequence of the strong dependence of the current and power on the operating irradiance. Therefore, they are not selected as a fault indicator for diagnosis. On the other hand, the results highlight that the  $MAPE_{V_{pv}}$  and  $ARE_{V_{oc}}$  related to the voltage, there are more stable and can be used as a fault indicator. The density and the cumulative density

function of  $MAPE_{I_{pv}}$  and  $ARE_{V_{oc}}$  are displayed in *Fig.II. 35* and *Fig.II. 36*, respectively. they shows that this two functions follow normal distributions.



*Fig.II. 35 : Distribution (left) and cumulative distribution (right) of  $MAPE_{V_{pv}}$*



*Fig.II. 36 : Distribution (left) and cumulative distribution (right) of  $ARE_{V_{oc}}$*

We also evaluate successfully the normality of the distribution through the Kolmogorov-Smirnov's test. We have set the threshold according to a normal law at  $(\varepsilon_{\mu})_{th} = \mu + 3\sigma$ . This gives the following values :  $(\varepsilon_{\mu_{MAPE_{V_{pv}}}})_{th} = \mu_{MAPE_{V_{pv}}} + 3\sigma_{MAPE_{V_{pv}}} \approx 2.45\%$  and  $(\varepsilon_{\mu_{ARE_{V_{oc}}}})_{th} = \mu_{ARE_{V_{oc}}} + 3\sigma_{ARE_{V_{oc}}} \approx 3.46\%$ , for  $MAPE_{V_{pv}}$  and  $ARE_{V_{oc}}$ , respectively.

## II.9. Conclusion

In this chapter, the modeling, extraction, and validation of the PV model have been presented. First, we conducted a literature review of several common electrical PV models and extraction methods, which led us to choose the most appropriate methods for our study: Single Diode Model with 5 parameters for simulation, and Levenberg-Marquardt algorithm for parameters extraction based on measured I-V curves. These parameters are not constant with environmental conditions. This leads us to propose analytical models for those five parameters to take into account these environmental variations in simulation. To choose those best analytical models, a 4-step methodology was developed. The first two steps are devoted to the training, while the last two are for validation. The error between the parameters calculated from



the analytical model and those extracted from measured I-V curves are :  $0.356 \pm 0.205$  A for the photo-generated current  $I_{ph}$ ,  $9.21 \pm 16.09$  m $\Omega$  for the series resistance  $R_s$ ,  $4.423 \pm 7.568$   $\Omega$  for the shunt resistance  $R_{sh}$ ,  $2.90 \cdot 10^{-8} \pm 2.52 \cdot 10^{-8}$  A for the diode saturation current  $I_0$ , and  $1.08 \pm 0.019$  for the diode ideality factor. The analytical model of PV parameters includes eight reference values used in the physical PV model called the hybrid PV model under MATLAB/Simulink to generate the simulated I-V curves of a PV system. 343 I-V curves obtained from the hybrid model are compared to the 343 curves measured with an I-V tracer, and the relative error of the maximum power point is less than 3%. It can be concluded that our proposed PV model is extremely accurate, user-friendly for the simulation of PV modules in real operation conditions, and is suitable for health monitoring and FDD. Moreover, in the last part, the sensitivity to the temperature where evaluated. The  $ARE_{ISC}$ ,  $MAPE_{I_{pv}}$  and  $ARE_{P_{mpp}}$  are more sensitive to the variable environmental conditions and they can't be used as the fault indicator. In contrast, the  $MAPE_{V_{pv}}$  and  $ARE_{V_{oc}}$  can be used, and the thresholds are setted to 2.45% and 3.46 for  $MAPE_{V_{pv}}$  and  $ARE_{V_{oc}}$ , respectively.

## References of chapter II

- [1] F. Almonacid, C. Rus, L. Hontoria, M. Fuentes, and G. Nofuentes, "Characterisation of Si-crystalline PV modules by artificial neural networks," *Renew. Energy*, vol. 34, no. 4, pp. 941–949, 2009.
- [2] A. K. Tossa, Y. M. Soro, Y. Azoumah, and D. Yamegueu, "A new approach to estimate photovoltaic modules' performance and energy productivity in real operating conditions," *Sol. Energy*, vol. 110, pp. 543–560, 2014.
- [3] T. Ma, H. Yang, and L. Lu, "Solar photovoltaic system modeling and performance prediction," *Renew. Sustain. Energy Rev.*, vol. 36, pp. 304–315, 2014.
- [4] A. R. Jordehi, "Parameter estimation of solar photovoltaic (PV) cells: A review," *Renew. Sustain. Energy Rev.*, vol. 61, pp. 354–371, 2016.
- [5] E. Saloux, A. Teyssedou, and M. Sorin, "Explicit model of photovoltaic panels to determine voltages and currents at the maximum power point," *Sol. Energy*, vol. 85, no. 5, pp. 713–722, 2011.
- [6] K. Ishaque, Z. Salam, and H. Taheri, "Simple, fast and accurate two-diode model for photovoltaic modules," *Sol. Energy Mater. Sol. Cells*, vol. 95, no. 2, pp. 586–594, 2011.
- [7] M. G. Villalva, J. R. Gazoli, and E. R. Filho, "Comprehensive approach to modeling and simulation of photovoltaic arrays," *IEEE Trans. Power Electron.*, vol. 24, no. 5, pp. 1198–1208, 2009.
- [8] V. J. Chin, Z. Salam, and K. Ishaque, "Cell modeling and model parameters estimation techniques for photovoltaic simulator application: A review," *Appl. Energy*, vol. 154, pp. 500–519, 2015.
- [9] K. Ishaque and Z. Salam, "An improved modeling method to determine the model parameters of photovoltaic (PV) modules using differential evolution (DE)," *Sol. Energy*, vol. 85, no. 9, pp. 2349–2359, 2011.
- [10] R. Chenni, M. Makhlouf, T. Kerbache, and A. Bouzid, "A detailed modeling method for photovoltaic cells," *Energy*, vol. 32, no. 9, pp. 1724–1730, 2007.
- [11] A. Bellini, S. Bifaretti, V. Iacovone, and C. Cornaro, "Simplified model of a photovoltaic module," 2009 *Appl. Electron international conference*, 9-10 September, Pilsen, Czech Republic, pp. 47–52, 2009.
- [12] C. Carrero, J. Amador, and S. Arnaltes, "A single procedure for helping PV designers to select silicon PV modules and evaluate the loss resistances," *Renew. Energy*, vol. 32, no. 15, pp. 2579–2589, 2007.
- [13] M. Karamirad, M. Omid, R. Alimardani, H. Mousazadeh, and S. N. Heidari, "ANN-based simulation and experimental verification of analytical four- and five-parameters models of PV modules," *Simul. Model. Pract. Theory*, vol. 34, pp. 86–98, 2013.
- [14] A. N. Celik and N. Acikgoz, "Modelling and experimental verification of the operating current of monocrystalline photovoltaic modules using four- and five-parameter models," *Appl. Energy*, vol. 84, no. 1, pp. 1–15, 2007.
- [15] S. Dongue, D. Njomo, J. Tamba, and L. Ebengai, "Modeling Of Electrical Response of Illuminated Crystalline Photovoltaic Modules Using Four-And Five-Parameter Models," *Ijetae.Com*, vol. 2, no. 11, pp. 612–619, 2012.
- [16] K. Ishaque, Z. Salam, H. Taheri, and A. Shamsudin, "A critical evaluation of EA computational methods for Photovoltaic cell parameter extraction based on two diode

- model," *Sol. Energy*, vol. 85, no. 9, pp. 1768–1779, 2011.
- [17] V. Khanna, B. K. Das, D. Bisht, Vandana, and P. K. Singh, "A three diode model for industrial solar cells and estimation of solar cell parameters using PSO algorithm," *Renew. Energy*, vol. 78, pp. 105–113, 2015.
- [18] J. W. Bishop, "Computer simulation of the effects of electrical mismatches in photovoltaic cell interconnection circuits," *Sol. Cells*, vol. 25, no. 1, pp. 73–89, 1988.
- [19] L. Bun and A. Université, "Détection et localisation de défauts pour un système PV Long Bun To cite this version : HAL Id : tel-00647189 Détection et Localisation de Défauts pour un Système PV," 2012.
- [20] Y. El Basri, M. Bressan, L. Seguier, H. Alawadhi, and C. Alonso, "A proposed graphical electrical signatures supervision method to study PV module failures," *Sol. Energy*, vol. 116, pp. 247–256, 2015.
- [21] M. Bressan, Y. El Basri, A. G. Galeano, and C. Alonso, "A shadow fault detection method based on the standard error analysis of I-V curves," *Renew. Energy*, vol. 99, pp. 1181–1190, 2016.
- [22] M. Bressan, A. Gutierrez, L. Garcia Gutierrez, and C. Alonso, "Development of a real-time hot-spot prevention using an emulator of partially shaded PV systems," *Renew. Energy*, vol. 127, pp. 334–343, 2018.
- [23] A. G. Galeano, M. Bressan, F. J. Vargas, and C. Alonso, "Shading ratio impact on photovoltaic modules and correlation with shading patterns," *Energies*, vol. 11, no. 4, pp. 1–26, 2018.
- [24] D. Wei, M. Wei, H. Cai, X. Zhang, and L. Chen, "Parameters extraction method of PV model based on key points of I-V curve," *Energy Convers. Manag.*, vol. 209, no. March, p. 112656, 2020.
- [25] A. Singh, A. Sharma, S. Rajput, A. K. Mondal, A. Bose, and M. Ram, "Parameter Extraction of Solar Module Using the Sooty Tern Optimization Algorithm," *Electron.*, vol. 11, no. 4, 2022.
- [26] W. De Soto, S. A. Klein, and W. A. Beckman, "Improvement and validation of a model for photovoltaic array performance," vol. 80, pp. 78–88, 2006.
- [27] D. Sera, R. Teodorescu, and P. Rodriguez, "PV panel model based on datasheet values," *IEEE Int. Symp. Ind. Electron.*, no. 4, pp. 2392–2396, 2007.
- [28] E. Karatepe, M. Boztepe, and M. Colak, "Neural network based solar cell model," *Energy Convers. Manag.*, vol. 47, no. 9–10, pp. 1159–1178, 2006.
- [29] H. Tian, F. Mancilla-David, K. Ellis, E. Muljadi, and P. Jenkins, "A cell-to-module-to-array detailed model for photovoltaic panels," *Sol. Energy*, vol. 86, no. 9, pp. 2695–2706, 2012.
- [30] Y. Sukamongkol, S. Chungpaibulpatana, and W. Ongsakul, "A simulation model for predicting the performance of a solar photovoltaic system with alternating current loads," *Renew. Energy*, vol. 27, no. 2, pp. 237–258, 2002.
- [31] R. K. Kharb, S. L. Shimi, S. Chatterji, and M. F. Ansari, "Modeling of solar PV module and maximum power point tracking using ANFIS," *Renew. Sustain. Energy Rev.*, vol. 33, pp. 602–612, 2014.
- [32] T. Ma, H. Yang, L. Lu, and J. Peng, "Technical feasibility study on a standalone hybrid solar-wind system with pumped hydro storage for a remote island in Hong Kong," *Renew. Energy*, vol. 69, pp. 7–15, 2014.
- [33] H. Bellia, R. Youcef, and M. Fatima, "A detailed modeling of photovoltaic module using MATLAB," *NRIAG J. Astron. Geophys.*, vol. 3, no. 1, pp. 53–61, 2014.
- [34] M. C. Di Piazza, M. Luna, G. Petrone, and G. Spagnuolo, "Parameter translation for single-diode

- PV models based on explicit identification,” *Conf. Proc. - 2017 17th IEEE Int. Conf. Environ. Electr. Eng. 2017 1st IEEE Ind. Commer. Power Syst. Eur. IEEEIC / I CPS Eur. 2017*, 2017.
- [35] W. Xing, J. Zhou, and Z. Feng, “Effects of mounting geometries on photovoltaic module performance using CFD and single-diode model,” *Sol. Energy*, vol. 103, pp. 541–549, 2014.
- [36] E. A. Silva, F. Bradaschia, M. C. Cavalcanti, A. J. Nascimento, L. Michels, and L. P. Pietta, “An Eight-Parameter Adaptive Model for the Single Diode Equivalent Circuit Based on the Photovoltaic Module ’ s Physics,” vol. 7, no. 4, pp. 1115–1123, 2017.
- [37] M. K. Dave, “Modeling of PV arrays based on datasheet,” *1st IEEE Int. Conf. Power Electron. Intell. Control Energy Syst. ICPEICES 2016*, pp. 1–4, 2017.
- [38] E. A. Silva, F. Bradaschia, M. C. Cavalcanti, and A. J. Nascimento, “Parameter estimation method to improve the accuracy of photovoltaic electrical model,” *IEEE J. Photovoltaics*, vol. 6, no. 1, pp. 278–285, 2016.
- [39] G. Ciulla, V. Lo Brano, V. Di Dio, and G. Cipriani, “A comparison of different one-diode models for the representation of I-V characteristic of a PV cell,” *Renew. Sustain. Energy Rev.*, vol. 32, pp. 684–696, 2014.
- [40] V. Lo Brano, A. Orioli, G. Ciulla, and A. Di Gangi, “An improved five-parameter model for photovoltaic modules,” *Sol. Energy Mater. Sol. Cells*, vol. 94, no. 8, pp. 1358–1370, 2010.
- [41] J. Bai, S. Liu, Y. Hao, Z. Zhang, M. Jiang, and Y. Zhang, “Development of a new compound method to extract the five parameters of PV modules,” *Energy Convers. Manag.*, vol. 79, pp. 294–303, 2014.
- [42] H. Ibrahim and N. Anani, “Variations of PV module parameters with irradiance and temperature,” *Energy Procedia*, vol. 134, pp. 276–285, 2017.
- [43] C. S. Ruschel, F. P. Gasparin, and A. Krenzinger, “Experimental analysis of the single diode model parameters dependence on irradiance and temperature,” vol. 217, no. January, pp. 134–144, 2021.
- [44] A. Orioli and A. Di Gangi, “A procedure to calculate the five-parameter model of crystalline silicon photovoltaic modules on the basis of the tabular performance data,” *Appl. Energy*, vol. 102, pp. 1160–1177, 2013.
- [45] “PVsyst – Logiciel Photovoltaïque.” [Online]. Available: <https://www.pvsyst.com/>. [Accessed: 23-Aug-2022].
- [46] H. A. B. Siddique, P. Xu, and R. W. De Doncker, “Parameter extraction algorithm for one-diode model of PV panels based on datasheet values,” in *4th International Conference on Clean Electrical Power: Renewable Energy Resources Impact, ICCEP 2013*, pp. 7–13.
- [47] C. S. Ruschel, F. P. Gasparin, E. R. Costa, and A. Krenzinger, “Assessment of PV modules shunt resistance dependence on solar irradiance,” *Sol. Energy*, vol. 133, pp. 35–43, 2016.
- [48] A. Chouder, S. Silvestre, N. Sadaoui, and L. Rahmani, “Modeling and simulation of a grid connected PV system based on the evaluation of main PV module parameters,” *Simul. Model. Pract. Theory*, vol. 20, no. 1, pp. 46–58, 2012.
- [49] A. R. Jordehi, “Parameter estimation of solar photovoltaic ( PV ) cells : A review,” *Renew. Sustain. Energy Rev.*, vol. 61, pp. 354–371, 2016.
- [50] M. U. N. Khursheed, M. F. Nadeem Khan, G. Ali, and A. K. Khan, “A review of estimating solar photovoltaic cell parameters,” *2019 2nd Int. Conf. Comput. Math. Eng. Technol. iCoMET 2019*, 2019.
- [51] D. S. H. Chan and J. C. H. Phang, “Analytical Methods for the Extraction of Solar-Cell Single- and Double-Diode Model Parameters from I-V Characteristics,” *IEEE Trans. Electron Devices*,

- vol. 34, no. 2, pp. 286–293, 1987.
- [52] F. Khan, S. H. Baek, Y. Park, and J. H. Kim, “Extraction of diode parameters of silicon solar cells under high illumination conditions,” *Energy Convers. Manag.*, vol. 76, pp. 421–429, 2013.
- [53] A. O. ↑ K. Et-torabi, I. Nassar-eddine and M. A. , Y. Errami, R. Rmaily, S. Sahnoun, A. El fajri, “Parameters estimation of the single and double diode photovoltaic models using a Gauss–Seidel algorithm and analytical method: A comparative study,” *Energy Convers. Manag.*
- [54] H. A. Adel A. Elbaset, “Novel seven-parameter model for photovoltaic modules,” *Sol. Energy Mater. Sol. Cells.*
- [55] Z. S. Vun Jack Chin, “A New Three-point-based Approach for the Parameter Extraction of Photovoltaic Cells,” *Appl. Energy.*
- [56] “Important notes on parameter estimation of solar photovoltaic cell.”
- [57] K. Ishaque and Z. Salam, “An improved modeling method to determine the model parameters of photovoltaic ( PV ) modules using differential evolution ( DE ),” *Sol. Energy*, vol. 85, no. 9, pp. 2349–2359, 2011.
- [58] M. Zagrouba, A. Sellami, M. Bouaïcha, and M. Ksouri, “Identification of PV solar cells and modules parameters using the genetic algorithms: Application to maximum power extraction,” *Sol. Energy*, vol. 84, no. 5, pp. 860–866, 2010.
- [59] L. Wu *et al.*, “Parameter extraction of photovoltaic models from measured I-V characteristics curves using a hybrid trust-region reflective algorithm,” *a.*
- [60] F. Dkhichi, B. Oukarfi, A. Fakkar, and N. Belbounaguia, “Parameter identification of solar cell model using Levenberg – Marquardt algorithm combined with simulated annealing,” *Sol. Energy*, vol. 110, pp. 781–788, 2014.
- [61] A. Benahmida, R. Ben Maachou, and E. Jadida, “Parameter Identification of Photovoltaic Generators Using an Analytical Approach and Iterative Method,” pp. 1–5, 2019.
- [62] R. Bendaoud *et al.*, “New method for extracting physical parameters of PV generators combining an implemented genetic algorithm and the simulated annealing algorithm,” *Sol. Energy*, vol. 194, no. October, pp. 239–247, 2019.
- [63] M. R. Arabshahi, H. Torkaman, and A. Keyhani, “A method for hybrid extraction of single-diode model parameters of photovoltaics,” *Renew. Energy*, vol. 158, pp. 236–252, 2020.
- [64] Z. Chen, Y. Lin, L. Wu, S. Cheng, and P. Lin, “Development of a capacitor charging based quick I-V curve tracer with automatic parameter extraction for photovoltaic arrays,” *Energy Convers. Manag.*, vol. 226, no. June, p. 113521, 2020.
- [65] H. P. Gavin, “The Levenburg-Marquardt Algorithm For Nonlinear Least Squares Curve-Fitting Problems,” *Duke Univ.*, pp. 1–19, 2019.
- [66] F. Ghani and M. Duke, “Numerical determination of parasitic resistances of a solar cell using the Lambert W-function,” *Sol. Energy*, vol. 85, no. 9, pp. 2386–2394, 2011.
- [67] P. Wolf and V. Benda, “Identification of PV solar cells and modules parameters by combining statistical and analytical methods,” *Sol. Energy*, vol. 93, pp. 151–157, 2013.
- [68] J. Ding, X. Cheng, and T. Fu, “Analysis of series resistance and P-T characteristics of the solar cell,” *Vacuum*, vol. 77, no. 2, pp. 163–167, 2005.
- [69] M. G. Villalva, J. R. Gazoli, and E. Ruppert Filho, “Modeling and circuit-based simulation of photovoltaic arrays,” *2009 Brazilian Power Electron. Conf. COBEP2009*, pp. 1244–1254, 2009.
- [24] D. Wei, M. Wei, H. Cai, X. Zhang, and L. Chen, "Parameters extraction method of PV model

- based on key points of I-V curve," *Energy Convers. Manag.*, vol. 209, no. March, p. 112656, 2020.
- [25] A. Singh, A. Sharma, S. Rajput, A. K. Mondal, A. Bose, and M. Ram, "Parameter Extraction of Solar Module Using the Sooty Tern Optimization Algorithm," *Electron.*, vol. 11, no. 4, 2022.
- [26] W. De Soto, S. A. Klein, and W. A. Beckman, "Improvement and validation of a model for photovoltaic array performance," vol. 80, pp. 78–88, 2006.
- [27] D. Sera, R. Teodorescu, and P. Rodriguez, "PV panel model based on datasheet values," *IEEE Int. Symp. Ind. Electron.*, no. 4, pp. 2392–2396, 2007.
- [28] E. Karatepe, M. Boztepe, and M. Colak, "Neural network-based solar cell model," *Energy Convers. Manag.*, vol. 47, no. 9–10, pp. 1159–1178, 2006.
- [29] H. Tian, F. Mancilla-David, K. Ellis, E. Muljadi, and P. Jenkins, "A cell-to-module-to-array detailed model for photovoltaic panels," *Sol. Energy*, vol. 86, no. 9, pp. 2695–2706, 2012.
- [30] Y. Sukamongkol, S. Chungpaibulpatana, and W. Ongsakul, "A simulation model for predicting the performance of a solar photovoltaic system with alternating current loads," *Renew. Energy*, vol. 27, no. 2, pp. 237–258, 2002.
- [31] R. K. Kharb, S. L. Shimi, S. Chatterji, and M. F. Ansari, "Modeling of solar PV module and maximum power point tracking using ANFIS," *Renew. Sustain. Energy Rev.*, vol. 33, pp. 602–612, 2014.
- [32] T. Ma, H. Yang, L. Lu, and J. Peng, "Technical feasibility study on a standalone hybrid solar-wind system with pumped hydro storage for a remote island in Hong Kong," *Renew. Energy*, vol. 69, pp. 7–15, 2014.
- [33] H. Bellia, R. Youcef, and M. Fatima, "A detailed modeling of photovoltaic module using MATLAB," *NRIAG J. Astron. Geophys.*, vol. 3, no. 1, pp. 53–61, 2014.
- [34] M. C. Di Piazza, M. Luna, G. Petrone, and G. Spagnuolo, "Parameter translation for single-diode PV models based on explicit identification," 2017 IEEE International Conference on Environment and Electrical Engineering and 2017 IEEE Industrial and Commercial Power System Europe (EEEIC/I&CPS Europe), 6-9 June, Milan, Italy, 2017.
- [35] W. Xing, J. Zhou, and Z. Feng, "Effects of mounting geometries on photovoltaic module performance using CFD and single-diode model," *Sol. Energy*, vol. 103, pp. 541–549, 2014.
- [36] E. A. Silva, F. Bradaschia, M. C. Cavalcanti, A. J. Nascimento, L. Michels, and L. P. Pietta, "An Eight-Parameter Adaptive Model for the Single Diode Equivalent Circuit Based on the Photovoltaic Module's Physics," vol. 7, no. 4, pp. 1115–1123, 2017.
- [37] M. K. Dave, "Modeling of PV arrays based on the datasheet," 1st IEEE International Conference on Power Electronics, Intelligent Control and Energy Systems(ICPEICES), 4-6 July, Delhi, India, pp.1-4, 2017.
- [38] E. A. Silva, F. Bradaschia, M. C. Cavalcanti, and A. J. Nascimento, "Parameter estimation method to improve the accuracy of photovoltaic electrical model," *IEEE J. Photovoltaics*, vol. 6, no. 1, pp. 278–285, 2016.
- [39] G. Ciulla, V. Lo Brano, V. Di Dio, and G. Cipriani, "A comparison of different one-diode models for the representation of I-V characteristic of a PV cell," *Renew. Sustain. Energy Rev.*, vol. 32, pp. 684–696, 2014.
- [40] V. Lo Brano, A. Orioli, G. Ciulla, and A. Di Gangi, "An improved five-parameter model for photovoltaic modules," *Sol. Energy Mater. Sol. Cells*, vol. 94, no. 8, pp. 1358–1370, 2010.
- [41] J. Bai, S. Liu, Y. Hao, Z. Zhang, M. Jiang, and Y. Zhang, "Development of a new compound method to extract the five parameters of PV modules," *Energy Convers. Manag.*, vol. 79, pp.

- 294–303, 2014.
- [42] H. Ibrahim and N. Anani, "Variations of PV module parameters with irradiance and temperature," *Energy Procedia*, vol. 134, pp. 276–285, 2017.
- [43] C. S. Ruschel, F. P. Gasparin, and A. Krenzinger, "Experimental analysis of the single diode model parameters dependence on irradiance and temperature," vol. 217, no. January, pp. 134–144, 2021.
- [44] A. Orioli and A. Di Gangi, "A procedure to calculate the five-parameter model of crystalline silicon photovoltaic modules on the basis of the tabular performance data," *Appl. Energy*, vol. 102, pp. 1160–1177, 2013.
- [45] "PVsyst – Logiciel Photovoltaïque." [Online]. Available: <https://www.pvsyst.com/>. [Accessed: 23-Aug-2022].
- [46] H. Abu, B. Siddique, P. Xu, and R. W. De Doncker, "Parameter Extraction Algorithm for One-Diode Model of PV Panels based on Datasheet Values," *International Conference on Clean Electrical Power(ICCEP)*,11-13 June, Alghero, Italy, pp. 7–13, 2013.
- [47] C. S. Ruschel, F. P. Gasparin, E. R. Costa, and A. Krenzinger, "Assessment of PV modules shunt resistance dependence on solar irradiance," *Sol. Energy*, vol. 133, pp. 35–43, 2016.
- [48] A. R. Jordehi, "Parameter estimation of solar photovoltaic ( PV ) cells : A review," *Renew. Sustain. Energy Rev.*, vol. 61, pp. 354–371, 2016.
- [49] A. Chouder, S. Silvestre, N. Sadaoui, and L. Rahmani, "Modeling and simulation of a grid-connected PV system based on the evaluation of main PV module parameters," *Simul. Model. Pract. Theory*, vol. 20, no. 1, pp. 46–58, 2012.
- [50] M. U. N. Khursheed, M. F. Nadeem Khan, G. Ali, and A. K. Khan, "A review of estimating solar photovoltaic cell parameters," *2nd International Conference on Computing, Mathematics and Engineering Technologies(iCoMET)*,30-31 Jan, Sukkur, Pakistan,2019.
- [51] D. S. H. Chan and J. C. H. Phang, "Analytical Methods for the Extraction of Solar-Cell Single- and Double-Diode Model Parameters from I-V Characteristics," *IEEE Trans. Electron Devices*, vol. 34, no. 2, pp. 286–293, 1987.
- [52] F. Khan, S. H. Baek, Y. Park, and J. H. Kim, "Extraction of diode parameters of silicon solar cells under high illumination conditions," *Energy Convers. Manag.*, vol. 76, pp. 421–429, 2013.
- [53] A. Obbadi, Y. Errami, R. Rmaily, S. Sahnoun, A. El, and M. Agunaou, "Parameters estimation of the single and double diode photovoltaic models using a Gauss-Seidel algorithm and analytical method : A comparative study," *Energy Convers. Manag.*, vol. 148, pp. 1041–1054, 2017.
- [54] A. A. Elbaset, H. Ali, and M. A. Sattar, "Novel seven-parameter model for photovoltaic modules," *Sol. Energy Mater. Sol. Cells*, vol. 130, pp. 442–455, 2014.
- [55] Z. S. Vun Jack Chin, "A New Three-point-based Approach for the Parameter Extraction of Photovoltaic Cells," *Appl. Energy*.
- [56] P.J.Gnetchejo, S.N Essiane, P.Ele, R.Wamkeue, D.M.Wapet, S.P.Ngoffe,"Important notes on parameter estimation of solar photovoltaic cell." *Energy Convers. Manag.*, vol. 197, 2019.
- [57] K. Ishaque and Z. Salam, "An improved modeling method to determine the model parameters of photovoltaic ( PV ) modules using differential evolution ( DE )," *Sol. Energy*, vol. 85, no. 9, pp. 2349–2359, 2011.

- [58] M. Zagrouba, A. Sellami, M. Bouaïcha, and M. Ksouri, "Identification of PV solar cells and modules parameters using the genetic algorithms: Application to maximum power extraction," *Sol. Energy*, vol. 84, no. 5, pp. 860–866, 2010.
- [59] L.Wu, Z.Chen, C.Long, S.Cheng, P.Lin, Y.Chen, and H.Chen., "Parameter extraction of photovoltaic models from measured I-V characteristics curves using a hybrid trust-region reflective algorithm," *Appl. Energy*, vol. 232, pp. 36–53, 2018.
- [60] F. Dkhichi, B. Oukarfi, A. Fakkar, and N. Belbounaguia, "Parameter identification of solar cell model using Levenberg – Marquardt algorithm combined with simulated annealing," *Sol. Energy*, vol. 110, pp. 781–788, 2014.
- [61] A. Benahmida, R. Ben Maachou, and E. Jadida, "Parameter Identification of Photovoltaic Generators Using an Analytical Approach and Iterative Method," pp. 1–5, 2019.
- [62] R. Bendaoud, H. Amiry, M. Benhmida, B. Zohal, S. Yadir, S. Bounouar, C. Hajjaj, E. Baghaz, M. EL Aydi., "New method for extracting physical parameters of PV generators combining an implemented genetic algorithm and the simulated annealing algorithm," *Sol. Energy*, vol. 194, no. October, pp. 239–247, 2019.
- [63] M. R. Arabshahi, H. Torkaman, and A. Keyhani, "A method for hybrid extraction of single-diode model parameters of photovoltaics," *Renew. Energy*, vol. 158, pp. 236–252, 2020.
- [64] Z. Chen, Y. Lin, L. Wu, S. Cheng, and P. Lin, "Development of a capacitor charging based quick I-V curve tracer with automatic parameter extraction for photovoltaic arrays," *Energy Convers. Manag.*, vol. 226, no. June, p. 113521, 2020.
- [65] H. P. Gavin, "The Levenburg-Marquardt Algorithm For Nonlinear Least Squares Curve-Fitting Problems," *Duke Univ.*, pp. 1–19, 2019.
- [66] F. Ghani and M. Duke, "Numerical determination of parasitic resistances of a solar cell using the Lambert W-function," *Sol. Energy*, vol. 85, no. 9, pp. 2386–2394, 2011.
- [67] P. Wolf and V. Benda, "Identification of PV solar cells and modules parameters by combining statistical and analytical methods," *Sol. Energy*, vol. 93, pp. 151–157, 2013.
- [68] J. Ding, X. Cheng, and T. Fu, "Analysis of series resistance and P-T characteristics of the solar cell," *Vacuum*, vol. 77, no. 2, pp. 163–167, 2005.
- [69] M. G. Villalva, J. R. Gazoli, and E. Ruppert Filho, "Modeling and circuit-based simulation of photovoltaic arrays," *Brazilian Power Electronics Conference*, 27 September -1 October, Bonito-Mato Grosso do Sul, Brazil, pp. 1244–1254, 2009.



## List of figures of chapter II

Fig.II. 1: Ideal PV circuit model (3 parameters) .....	67
Fig.II. 2: Single diode model with series resistance (Four parameters) .....	68
Fig.II. 3: Single diode model with series and shunt resistances (SDM, five parameters) .....	68
Fig.II. 4: Two diode model (seven parameters) .....	69
Fig.II. 5: Three diode model (nine parameters).....	70
Fig.II. 6: PV electrical circuit of Bishop model .....	71
Fig.II. 7: SDM of $N_s$ PV cells connected in series to form a PV module (left) and SDM of the same PV module (right).....	72
Fig.II. 8 : Levenberg-Marquardt approach flowchart.....	80
Fig.II. 9: Training and validating methodology .....	83
Fig.II. 10: Measured and simulated I-V curve, in real operation condition; this data was measured on 08-09-2021 at 14:12; the SDM was configured with the extracted parameters .....	84
<i>Fig.II. 11</i> : Flowchart approach for calculating the reference values of the analytical model .....	86
Fig.II. 12 : Evolution of the photo-generated current ( $I_{ph}$ ) with irradiance, for constant $T_{pv} = 56^\circ\text{C}$	87
Fig.II. 13 : Evolution of the photo-generated current ( $I_{ph}$ ) with $T_{pv}$ for constant $G_{POA} = 765 \text{ W/m}^2 \pm 2\%$ .....	88
Fig.II. 14: Evolution of the photo generated current ( $I_{ph}$ ) with $G_{POA}$ and $T_{pv}$ for all the measured values in the training stage. ....	88
Fig.II. 15: Evolution of the diode saturation current ( $I_0$ ) with $T_{pv}$ .....	89
Fig.II. 16: Evolution of the diode saturation current ( $I_0$ ) with $G_{POA}$ and $T_{pv}$ for all the measured values in the training stage. ....	89
Fig.II. 17 : Evolution of $n$ with $T_{pv}$ while $G_{poa}$ are constant .....	90
Fig.II. 18 : : Evolution of $n$ with with $G_{POA}$ and $T_{pv}$ for all the measured values in the training stage. ....	90
Fig.II. 19 : Evolution of $R_s$ with $G_{poa}$ for constant $T_{pv} = 56^\circ\text{C}$ .....	91
Fig.II. 20 : Evolution of $R_s$ with $T_{pv}$ for constant $G_{POA} = 765 \text{ W/m}^2 \pm 2\%$ .....	92
Fig.II. 21: Evolution of $R_s$ with $G_{POA}$ for all the measured values in the training stage .....	92
Fig.II. 22: Evolution of $R_{sh}$ with $G_{poa}$ .....	93
Fig.II. 23 : Evolution of $R_{sh}$ with $G_{POA}$ for all the measured values in the training stage .....	94
Fig.II. 24 : Error analysis ( $\epsilon = \theta(I - V) - \theta_{analy}$ ) during the validation step ( $M=429$ ).....	97
Fig.II. 25 : Presentation of the whole hybrid PV model with the variable input of environment ( $G_{POA} = 689 \text{ Wm} - 2$ and $T_{pv} = 47^\circ\text{C}$ ).....	98
Fig.II. 26: Measured (I-V tracer) and simulated (Hybrid PV model) I-V curve of a PV module .....	98

Fig.II. 27 : Flowchart for the resampling of the simulated I-V curve to the same format of the measured I-V curve ..... 99

Fig.II. 28: I-V curve of PV module obtained from measured (26 samples), simulation (1000 samples), and resampling (26 samples) ..... 100

Fig.II. 29: Flowchart of the hybrid PV model validation ..... 101

Fig.II. 30 : Histogram of error distribution between measurements and simulation with the hybrid model (M = 343) and all unit of the average and standard deviation in % ..... 103

Fig.II. 31: Flowchart of the sensitivity analysis of errors due to changes in  $T_{pv}$  ..... 104

Fig.II. 32 : Profile of  $T_{pv}$  and GPOA ..... 104

Fig.II. 33: Error analyses while  $T_{pv}$  vary of  $\pm 10^{\circ}\text{C}$  from its measured value and GPOA is the measured one ..... 106

Fig.II. 34 : Average (left) and standard deviation (right) of errors as a function of the added temperature  $\gamma T_{pv} = \pm 10^{\circ}\text{C}$ ..... 107

*Fig.II. 35 : Distribution (left) and cumulative distribution (right) of MAPEV<sub>pv</sub>..... 108*

*Fig.II. 36 : Distribution (left) and cumulative distribution (right) of AREVoc ..... 108*

## List of tables of chapter II

Table.II. 1: Different electrical models .....	65
Table.II. 2 : Dataset used for the training step .....	85
Table.II. 3 : Estimated reference value from Eq (II.13) for constant $T_{pv} = 56^{\circ}\text{C}$ .....	87
Table.II. 4: Extracted reference values of Eq (II.13) for constant $G_{POA} = 765 \text{ W/m}^2 \pm 2\%$ .....	87
Table.II. 5 : Extracted reference values of Eq (II.16).....	89
Table.II. 6 : Estimated reference value of Eq (21) while $G_{poa}$ are constant.....	90
Table.II. 7: Estimation reference values of Eq(II.17.18.19) for constant $T_{pv}= 56^{\circ}\text{C}$ .....	91
Table.II. 8: Extracted reference value of Eq(II.19) for constant $G_{POA} = 765\text{Wm}^2 \pm 2\%$ .....	92
Table.II. 9: Estimated value of Eq (II.21,23) for constant $T_{pv}$ .....	93
Table.II. 10: Summary of the eight reference values tuned during the training step and used by th analytical modelling .....	94
Table.II. 11 : Dataset used for the validation stage .....	95
Table.II. 12 : Data acquisition used for validation of the hybrid PV model.....	101

# Chapter III

## PV panel fault detection and diagnosis

### Table of Contents

Chapter III: PV panel fault detection and diagnosis.....	122
III.1. Introduction .....	122
III.2. Faults in Photovoltaic systems .....	122
III.2.1. <i>Faults in PV module</i> .....	124
II.2.1.1. Encapsulation fault .....	124
II.2.1.2. Glass breakage.....	125
II.2.1.3. Corrosion of a PV module.....	125
II.2.1.4. Interconnection failure.....	125
II.2.1.5. Back sheet adhesion failure .....	125
II.2.1.6. Bubbles.....	126
II.2.1.8. Light-induced power degradation (LID) .....	126
II.2.1.9. Hot spots (HS).....	127
II.2.1.10. Shading and soiling .....	127
II.2.1.11. Bypass Diode failure (DF).....	128
II.2.1.12. Junction box failure (JBF).....	128
III.2.2. <i>Classification of defects according to their frequency of occurrence</i> .....	128
III.2.3. <i>Impact of the defect in terms of power losses</i> .....	130
III.3. Fault Detection and diagnosis of PV panel .....	132
III.3.1. <i>Introduction</i> .....	132
III.3.2. <i>Visual inspection</i> .....	132
III.3.3. <i>Automatic analysis method based on features analysis</i> .....	133
III.3.3.1. Power, energy, and maximum power point analysis approach .....	134
III.3.3.2. Analysis of the Current-Voltage (I-V) curve characteristics .....	134
III.3.4. <i>Fault detection and diagnosis proposal</i> .....	135
III.4. Results of fault detection and diagnosis with methods M1 and M2.....	136

- III.4.1. *Rs degradation* ..... 136
  - III.4.1.1. Simulation data..... 137
    - III.4.1.1.1. *Evaluation of method M1 with simulation data*..... 137
    - III.4.1.1.2. *Evaluation of method M2 with simulation data*..... 140
  - III.4.1.2. Experimental data..... 141
    - III.4.1.2.1. *Evaluation of method M1 with experimental data*..... 141
    - III.4.1.2.2. *Evaluation of method M2 with experimental data*..... 144
- III.4.2. *Rsh degradation*..... 145
  - III.4.2.1. Simulation data..... 145
    - III.4.2.1.1. *Evaluation of method M1 with simulation data*..... 145
    - III.4.2.1.2. *Evaluation of method M2 method with simulation data* ..... 148
  - III.4.2.2. Experimental data in case of *Rsh* degradation ..... 149
    - III.4.2.2.1. *Evaluation of method M1 with experimental data*..... 149
    - III.4.2.2.2. *Evaluation of method M2 method with experimental data* ..... 152
- III.4.3. *Partial shading* ..... 153
  - III.4.3.1. Evaluation of method M2 with simulation data ..... 153
  - III.4.3.2. Evaluation of method M2 with experimental data ..... 155
- III.5. Conclusion..... 157
- Reference of chapter III..... 159
- List of figures of chapter III ..... 162
- List of tables of chapter III ..... 164
- General Conclusion ..... 165
- Perspectives ..... 166
- Annex: Hybrid PV model based on the single diode with Rs and Rsh model*..... 168

## Chapter III: PV panel fault detection and diagnosis

### III.1. Introduction

Photovoltaic systems can suffer failures which, depending on their severity level, lead to loss of energy output or destruction by fire. Therefore, the increasing importance of photovoltaic energy in the energy mix requires the availability, quality and profitability of installations to be ensured. These goals will be achieved by continuously monitoring the health of the modules that make up the plants. Detection and diagnostic methods are at the heart of the monitoring systems. Their implementation requires a knowledge model of the system to be monitored and its failure modes.

In the case of our study, the knowledge model is the hybrid model developed and validated in chapter II. We will therefore start in section III.2 with a quick presentation of the main faults in photovoltaic systems. Then we will briefly describe in section III.3 the main detection and diagnosis methods. Section III.4 will be dedicated to the development and results of the method implemented for our application. Finally, we conclude in section III.5.

### III.2. Faults in Photovoltaic systems

Faults can affect a cell, a module (cell, junction block, bypass diode) or the inverter if the system is connected to an AC grid. The classification of faults in photovoltaic systems can be made according to several criteria: cause (intrinsic or extrinsic), location, permanent or intermittent character, degree of severity [1]–[7]. They are summarized in *Table.III. 1*.

*Table.III. 1: Fault Classification in PV systems*

Ref	Classification criteria	Categories	PV fault
[1]	Location and components of the PV system	Cell-level faults	<ul style="list-style-type: none"> <li>Cell crack, Discoloration, Snail track, delamination,etc.</li> </ul>
		Module-level faults	<ul style="list-style-type: none"> <li>Shading/soiling, Frame breakage, Back sheet adhesion loss, Junction box fault, Diode fault, Burn Mark, Shunt hot spot, Short circuit and open circuit module, PID, Abnormal degradation,etc.</li> </ul>
		Array-level faults	<ul style="list-style-type: none"> <li>Ground fault(GF), Line to Line fault (LLF), Arc fault(AF), etc.</li> </ul>
[3], [4]	Cause and nature of PV faults	Physical	<ul style="list-style-type: none"> <li>Internal: Damage to PV module, Damage to bypass diode, etc.</li> <li>External: Crack PV module, degradation, etc.</li> </ul>
		Environment	<ul style="list-style-type: none"> <li>Permanent shading: Hot spot fault</li> <li>Temporary shading</li> </ul>
		Electrical	<ul style="list-style-type: none"> <li>Open circuit faults</li> </ul>

			<ul style="list-style-type: none"> <li>• LLF : Intra-string LLF, Inter-string LLF</li> <li>• AF: Series AF, Parallel AF</li> <li>• Ground fault: single line GF, Double line GF</li> </ul>
[5]	Duration and degree of severity	Permanent	<ul style="list-style-type: none"> <li>• Line to line, Line to ground, Bridging, Open circuit, Bypass diode, Grounding, Arc, Junction box, Interconnection, damage, etc.</li> </ul>
		Intermittent	<ul style="list-style-type: none"> <li>• Shading, Leaf, Bird drop, Dust, Contamination, Snow, Accumulation, High humidity., etc.</li> </ul>
		Incipient	<ul style="list-style-type: none"> <li>• Degradation, Corrosion, Interconnection, Partial damage, etc.</li> </ul>
[6]	Symptoms, effects, and consequences	PV module failures modes	<ul style="list-style-type: none"> <li>• Encapsulation failures, Back sheet adhesion loss, Cell cracking, Broken interconnection, shading and soiling, hot spots, Module corrosion, PID, LID, etc.</li> </ul>
		Inverter failure modes	<ul style="list-style-type: none"> <li>• Manufacturing and design problem.</li> <li>• Control problem</li> <li>• Electrical components failures</li> </ul>
		Other failure modes	<ul style="list-style-type: none"> <li>• Balance of system(BOS) failure</li> <li>• Junction Box failure</li> <li>• Bypass diode failure</li> <li>• Mismatch fault</li> <li>• Ground fault</li> <li>• Line-to-line fault</li> <li>• Arc fault</li> <li>•</li> </ul>
[7]	Component of PV system, Cause and effects	Cell/module	<ul style="list-style-type: none"> <li>• Hot spot(HP)</li> </ul>
		Bypass diode or Blocking diode	<ul style="list-style-type: none"> <li>• Diode faults (DF)</li> </ul>
		Junction box	<ul style="list-style-type: none"> <li>• Junction box fault (JBF)</li> </ul>
		Photovoltaic module	<ul style="list-style-type: none"> <li>• PV module fault</li> </ul>
		PV array or PV string	<ul style="list-style-type: none"> <li>• Grounding fault</li> </ul>
		PV string	<ul style="list-style-type: none"> <li>• Arc fault</li> </ul>
		PV array	<ul style="list-style-type: none"> <li>• Line to Line fault</li> </ul>

Transportation, manufacturing, installation, or environmental factors (temperature or humidity) are the main reasons for PV faults, as reported in [10]–[14]. *Fig. III.2* shows the most common structure for c-Si and thin-film PV modules with the different elements: solar cells, glass front cover, encapsulant, back sheet, internal circuit (electrodes, interconnects), bypass diodes, junction boxes, frame, cables, and connectors.

This section will give an overview of the different fault types, their frequency of occurrence, and their effects.

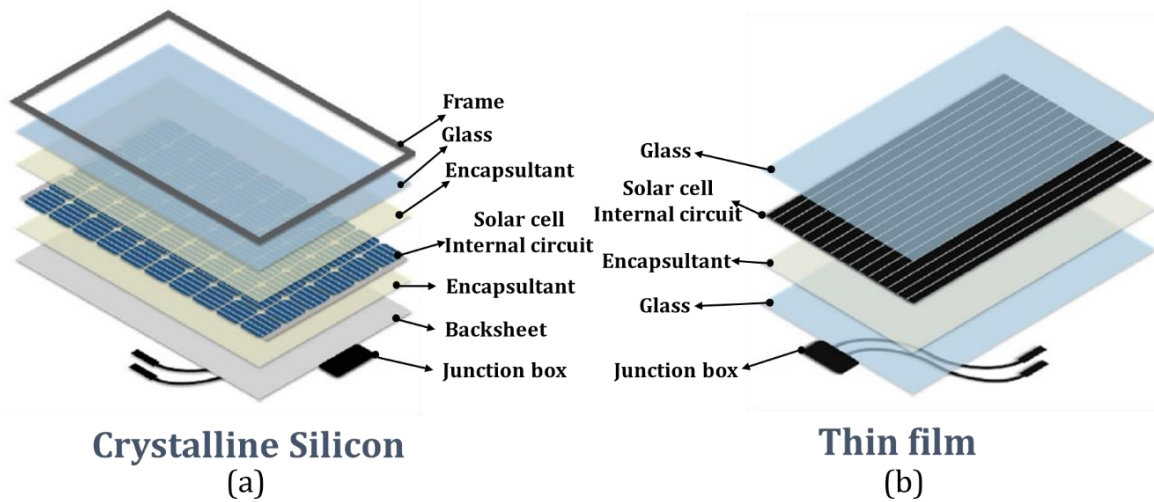
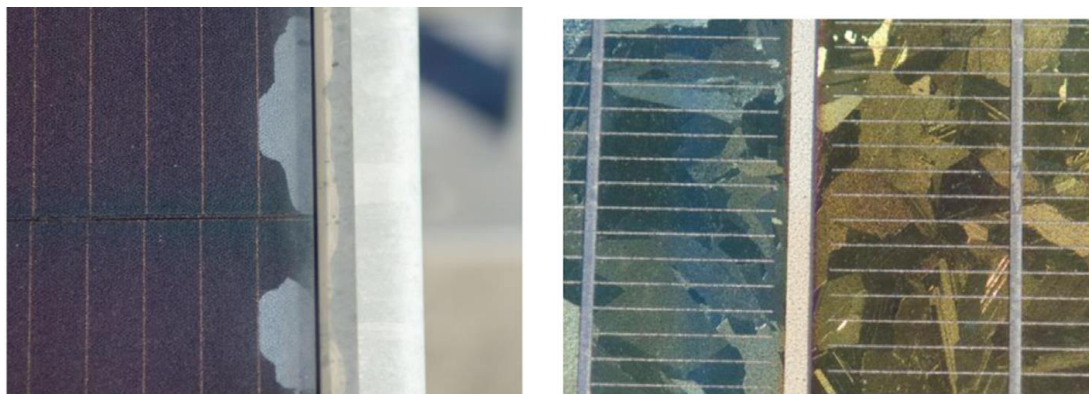


Fig. III.2: Structure of standard crystalline silicon and thin-film PV module [11]

### III.2.1. Faults in PV module

#### II.2.1.1. Encapsulation fault

The encapsulant is usually made with EVA (ethylene vinyl acetate). Delamination (*Fig.III.3 (a)*) and discoloration (*Fig.III.3 (b)*) are the most common encapsulation faults due to environmental factors such as humidity and heat [15], [16]. The delamination degrades the optical properties of the cells, which reduces the solar flux penetration, resulting in a loss of output power. Discoloration causes corrosion that results in an increase of the series resistance, degrading the performance [18], [19].



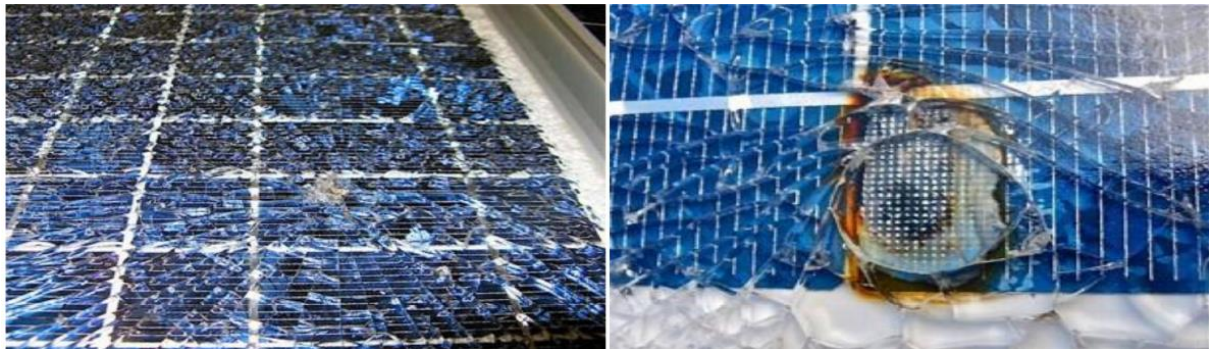
(a) Encapsulant delamination (a-Si) (b) Discolored solar cell-Yellowish (p-Si)

Fig.III.3: Encapsulation failure[20]



### II.2.1.2. Glass breakage

The breakage of the glass is mainly due to extrinsic factors. It can occur during manufacturing, transportation, installation, or during operation. The main consequence is a reduction of the output power, which depends on the damaged surface [1]. However, the module can still keep on operating, increasing the risk of electric shock and moisture penetration. as it can be observed in *Fig. III.4*.



*Fig. III.4: PV module with broken glass and cell burn [14]*

### II.2.1.3. Corrosion of a PV module

Aggressive environmental factors or insufficient maintenance are responsible for the corrosion of conductive components of the cells and interconnections via the encapsulant. This degradation induces changes in series and shunt resistance, leading to poor performance of the PV module [18], [21].

### II.2.1.4. Interconnection failure

The major causes of these disconnections are transportation stresses, hot areas, thermal cycling, or repetitive mechanical stress. They are responsible for failures of weak ribbon interconnections between the cells. A small space between cells can also induce fault interconnection leading to shorted or open-circuited cells.

### II.2.1.5. Back sheet adhesion failure

Faults in the backsheet can be caused by various factors, including temperature, moisture, mechanical stress, or delamination. An example is shown in *Fig. III.5*. The consequences can be insulation default and increasing exposure to active electrical components, particularly near the junction box or the edge of the module. The fault severity depends on the design, the structure, and the materials [2], [6].

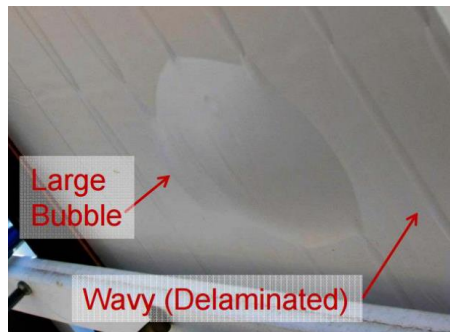


*Fig. III.5: Backsheet/encapsulation fault [22]*

#### II.2.1.6. Bubbles

A photovoltaic module with several bubbles on the back and front is shown in *Fig. III.6*. The bubbles in this kind of deprivation are similar to delaminating. The bubbles are caused by a chemical reaction that releases the gas stuck in the PV module. When this happens on the unit's backside, mobbing occurs in the encapsulated polymer, causing air bubbles and making it more difficult for solar cells to disperse heat, leading to higher temperatures and a shorter life lifetime [14].

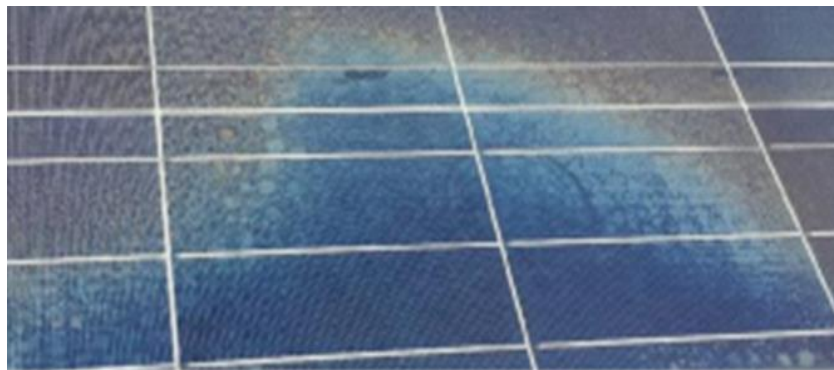


*Fig. III.6: Bubbles in a PV module [14]*

#### II.2.1.8. Light-induced power degradation (LID)

The LID is a natural deterioration of the p-n junction of a PV cell caused by a physical reaction. It exhibits a decrease in silicon solar cells' efficiency and a reduction in the solar cell's short circuit current and open-circuit voltage[6], [24]. *Fig.III.7* summarizes all of these failures. It depicts PV modules' primary aging and failure processes, categorized as infant failures, midlife failures, and wear-out failures [25].

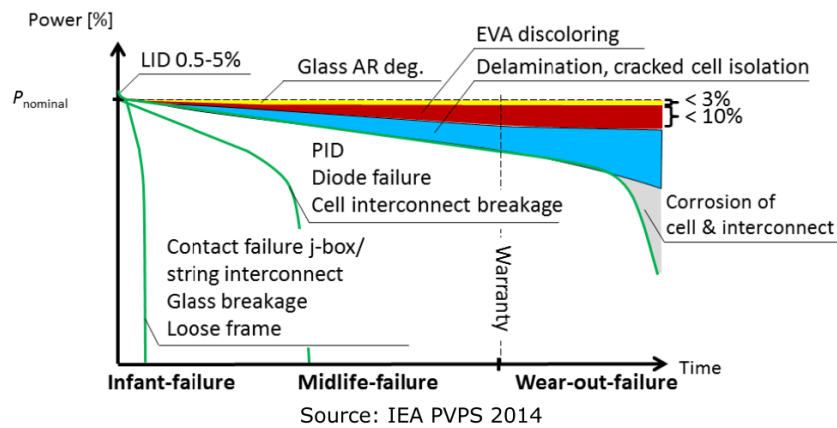


Fig.III.7: Aging mechanisms leading to PV module degradation [25]

### II.2.1.9. Hot spots (HS)

Hot spots can occur due, for example, to cell degradation, shading, bypass diode failure, and cell mismatches[27]. Hot spots are well-known to be one of the major causes of the degradation of performance or failures of PV modules. A hot spot appears when a cell, or a group of cells, operates in reverse bias, dissipating heat rather than creating electricity. Therefore, the local temperature increases, and the cell or the group of cells burns, as shown in Fig.III.8 [14], if the fault is not detected at its earliest stage [26].

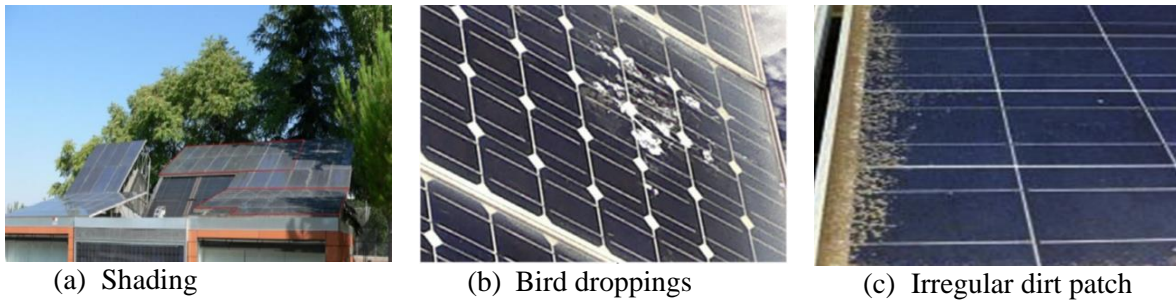


Fig.III.8: PV module with hot spot [14]

### II.2.1.10. Shading and soiling

Shading and soiling can be classified as hard or soft, permanent or temporary fault causes [26]. Partial shading and shading are typically caused by trees, buildings, passing clouds, etc. Soiling refers to dirt, dust, and snow covering the surface of the PV module. Fig.III.9 shows different cases of shading and soiling. They are responsible for non-uniform irradiation on the

PV module. They can be handled with the triggering of bypass diodes to avoid hotspots. However, the mismatch should be detected and preventive actions engaged to avoid any failure.



*Fig.III.9: Different cases of shading and soiling fault [26]*

#### II.2.1.11. Bypass Diode failure (DF)

The fault of the bypass diode is mainly due to human errors such as reverse or loose connection. Its failure may be catastrophic as it should be triggered to protect a module in case of non-uniform irradiation.

#### II.2.1.12. Junction box failure (JBF)

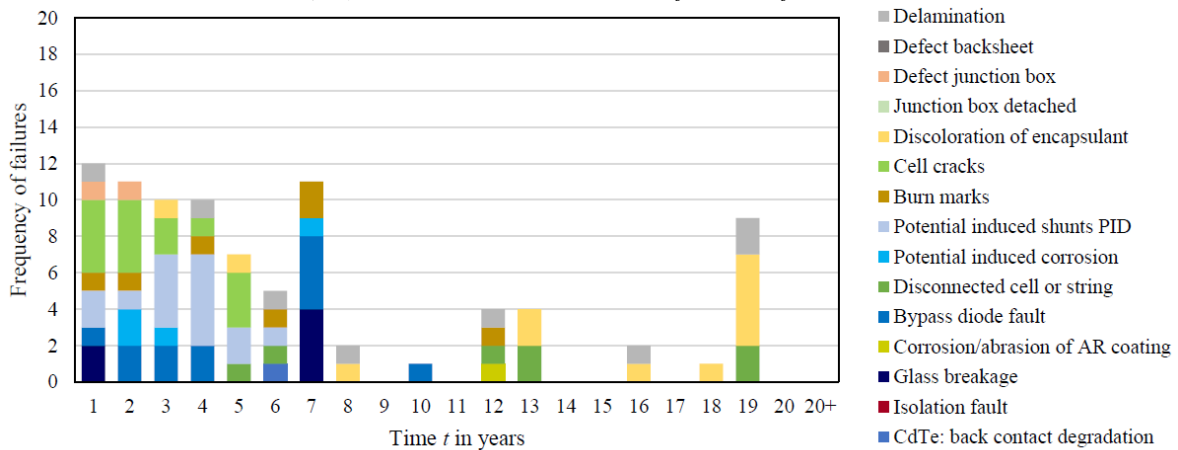
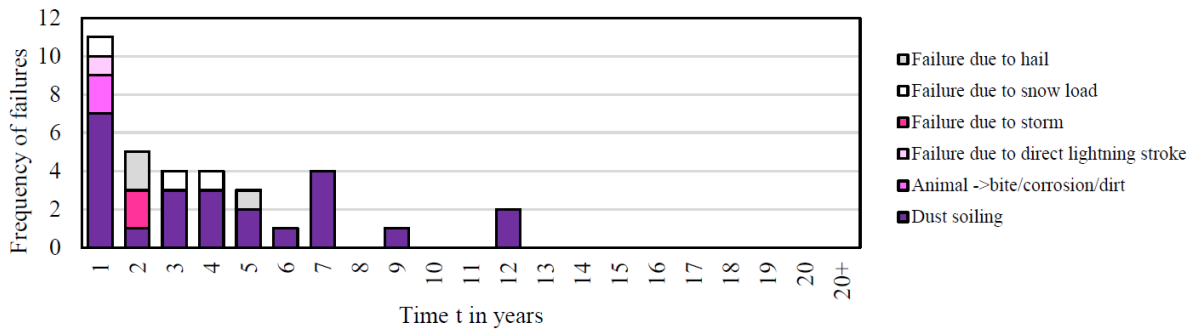
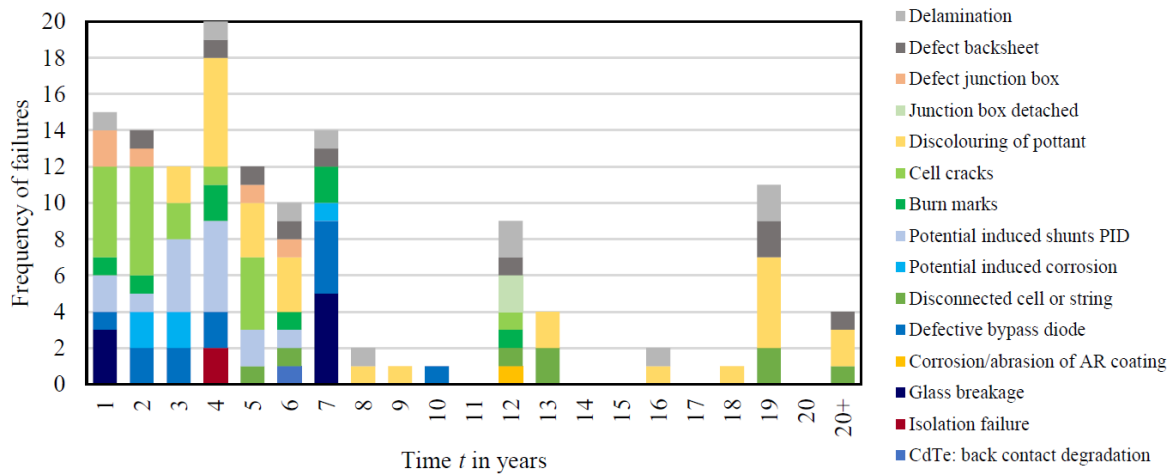
The junction box faults or failures are caused by moisture penetration, corrosion of connections, poor connections, improper wiring leading to internal arcing, improper mounting, or thermal degradation [2]. Approximately 85% of junction box failures are caused by system installation, and most of them happen during the first three months following PV system installation [28]. The failures are illustrated in *Fig.III.10* [14].

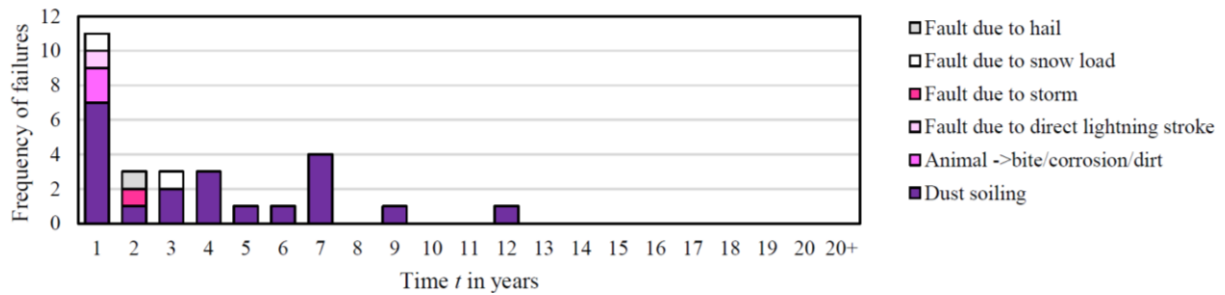


*Fig.III.10: Junction box failure [14]*

### III.2.2. Classification of defects according to their frequency of occurrence

The occurrence of these defects, as studied in [8], represents the frequency of occurrence of a defect as a function of the production year of the PV system.





(b2): Occurrence distribution of sudden occurring failure

Fig. III.11: Occurrence distribution of failures over the years of the PV system operation [8], (a1) and (a2): Total failure occurrence of all detected failures; (b1) and (b2): Occurrence of failures that cause measurable power losses

Fig. III.11 represents the frequency occurrence for two fault categories. The first category represents faults due to internal factors such as delamination, discoloring of pottant, corrosion called degrading faults. Their frequency of occurrence is represented in Fig. III.11 (a.1) and Fig. III.11.(b.1). The second category concerns the faults that occur suddenly due to an external factor such as hail, snow load storm. Their frequency of occurrence is represented in Fig. III.11.(a.2) and Fig. III.11.(b.2). The results show that the cell cracks appears mostly in the first two years. The disconnection of cells or strings appears from year five and is spread over the following years. The discoloration of the encapsulant appears as early as the third year of operation and recurs over the years with a strong accumulation that leads to significant power losses after 18 years of operation. Bypass diode faults are very common during the first ten years of operation. The reasons for sudden PV failures are more often related to environmental factors. When compared to the other types of defects, dust soiling is the most common sudden defect causing power losses, especially in the first 12 years.

### III.2.3. Impact of the defect in terms of power losses

The faults' power losses strongly depend on the PV module's environment and technology. Generally, the losses are constant at the beginning of the operation but increase with time. The study in [29] presents the photovoltaic failure and degradation mode. The degradation modes are ranked from 1 to 10, with 1 indicating no influence on performance and 10 indicating a substantial effect on power and safety. The results are summarized in Table.III. 2. It was mentioned in the same study that the defects with the highest severity are the hot spots and the back sheet insulation. Back sheet insulation compromise includes peeling, flaking, and cracking. This degradation has significant effects on the output power but also on the safety. The summary of degradation modes with their severity ranking is shown in Table.III. 3.

*Table.III. 2: Severity rating of the different degradation modes [29]*

Severity	Rating
Major effect on power safety	10
Major effect on power	8
Moderate effect on power	5
Slight deterioration of performance	3
No effect on performance	1

*Table.III. 3:Summary of degradation modes with their severity ranking [29]*

Mode	Severity
Encapsulant discoloration	3
Major Delamination	5
Minor Delamination	1
Backsheet insulation compromise	10
Backsheet other	1
Internal circuitry discoloration, series resistance increase	5
Internal circuitry failure, solder bond failure	8
Hot spots	10
Fractured cells	5
Diode /J-Box problem	5
Glass breakage	5
Permanent soiling	2
Potential induced degradation	8
Frame deformation	3

Pareto chart obtained by adding all modules affected by a specific degradation mode is shown in *Fig. III.12*, these degradations have been identified in the last ten years of installations, and the hot spots and PID are the most severe in the last ten years.

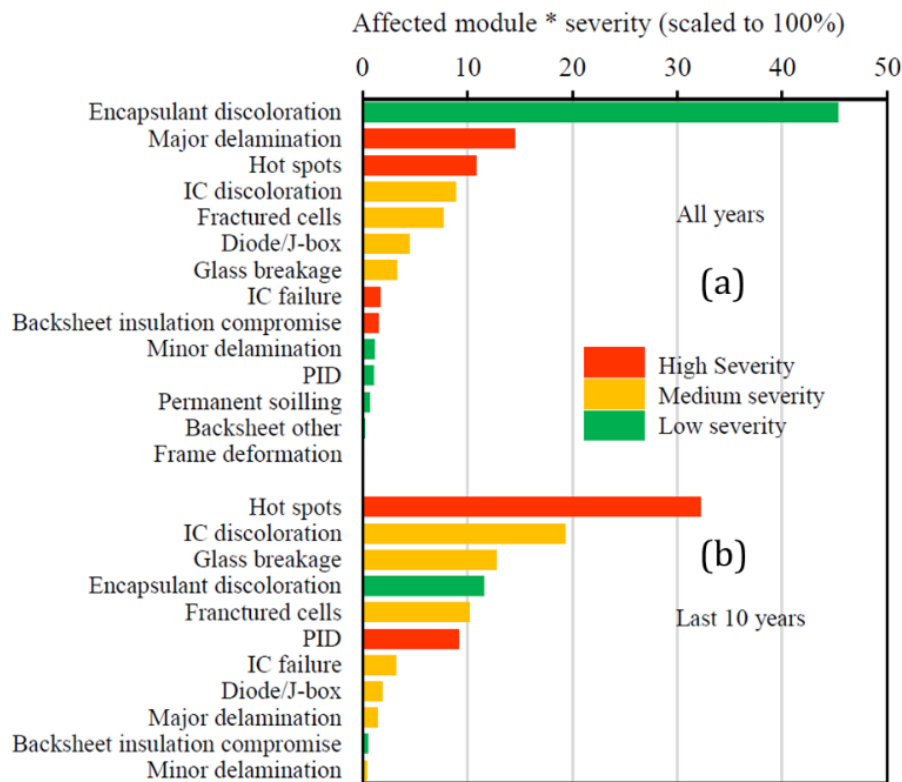


Fig. III.12: Pareto chart of the most significant modes: (a) All years, (b) System installed in the last ten years. The bars are color-coded by severity [29]

### III.3. Fault Detection and diagnosis of PV panel

#### III.3.1. Introduction

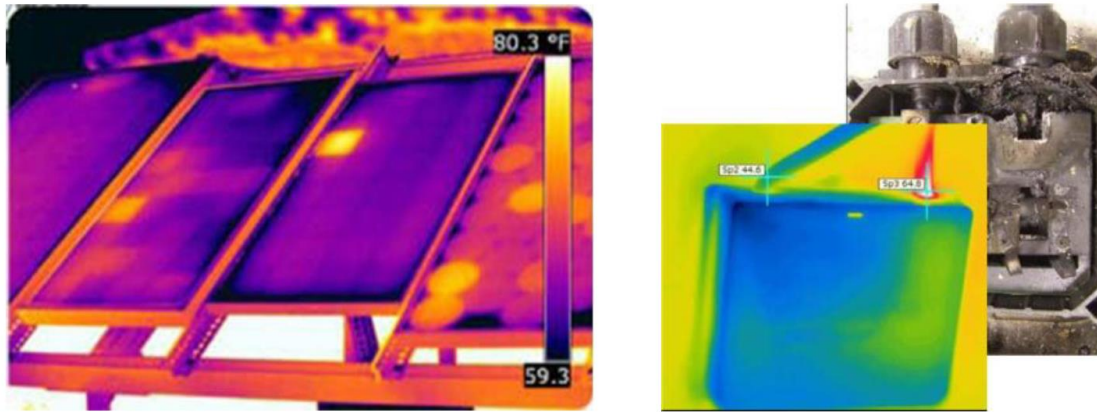
Condition-based maintenance based on continuous monitoring is suitable to limit the drop in performance and improve the reliability of photovoltaic modules. Fault detection and diagnosis (FDD) is at the heart of health monitoring. There are several FDD approaches reported in the literature [2], [7], [30]. They can be broadly classified in two categories: visual inspection or automatic analysis.

#### III.3.2. Visual inspection

Visual inspection and infrared and thermal imagery analysis are classified as non-electrical methods because they do not require the measurement of electrical data. Visual and thermal methods are used specifically to detect discoloration, browning, soiling, hot spot, breakage, and delamination of PV modules [7]. Visual inspection is suitable for small-scale PV systems but may require an expert to analyze the data. At the PV module level, the infrared imaging method (thermal camera) is widely used; this method is based on the fact that all



materials emit infrared radiation over a range of wavelengths that depends on its temperature. The anomalies can be located by examining the temperature distribution. *Fig.III.13* shows some examples of fault isolation with thermal images. *Table.III. 4* shows the list of the most detectable PV faults using visual inspection.



(a) Short circuit cell

(b) Corrosion in the junction box

*Fig.III.13: Some examples of fault isolation with thermal camera [31]*

*Table.III. 4: List of detectable PV module faults using visual inspection[1]*

PV module component	PV module fault
Front/Back of PV module	Bubbles, delamination, Yellowing, browning
PV cell	Cracked cell, discolored anti reflection
Cell metallization	Burned, oxidized
Frame	Bent, broken, misaligned
Junction box	Broken, loose, oxidation, corrosion
Wired, connectors	Detachment, broken, exposed electrical part
Bypass diode	Burned, broken connection

### III.3.3. Automatic analysis method based on features analysis

Automatic analysis methods are based on the analysis of fault features [32] obtained from measured or estimated information. The most usual informations captured from PV plants are the output power or energy, the maximum power, or the I-V curves obtained with I-V tracers.

### III.3.3.1. Power, energy, and maximum power point analysis approach

The approaches based on the analysis of the power, energy, and maximum power point are usually integrated into the commercial inverter, in which an algorithm for maximum power point tracking (MPPT) is embedded [33], [34].

The International Energy Agency (IEA) Photovoltaic Power System Program has defined four performance indicators in IEC standard 61724 [36] to characterize the overall system performance: energy output, solar energy, rated power, and total power impact on system losses. The methods are based on the analysis of residuals computed as the difference between the actual measurements and their predicted values. In [35], three residuals are calculated: current, voltage, and power at the maximum power point. The reference [37] analyses power losses to identify the fault types (faulty module in a string, faulty string, and a set of distinct faults such as partial shading, aging), and MPPT error. In the study conducted in [38], the analysis of the energy drop is used to identify component failure, inverter shutdown, shading, and MPPT error.

### III.3.3.2. Analysis of the Current-Voltage (I-V) curve characteristics

A change in the I-V characteristics occurs when there is a change in the PV state of health caused by environmental conditions (irradiance or temperature) or fault occurrence.

*Fig.III.14* shows the I-V curves of a PV module in different conditions.

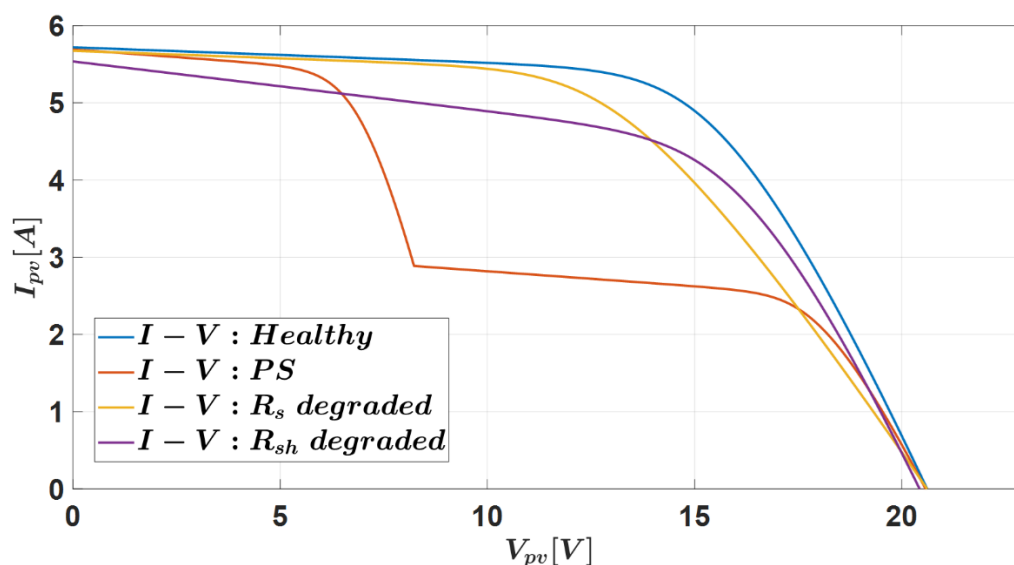


*Fig.III.14: Comparison of I-V characteristics in healthy and faulty cases*

The I-V curve can be used for fault diagnosis in two ways:

- *Partial usage:*

Only several points are analyzed to make a decision. For example (open-circuit voltage  $V_{oc}$ , short-circuit current  $I_{sc}$ , and the power at the MPP,  $P_{mpp}$ ) [39]. The disadvantages of this approach are the limited number of diagnosable faults and its high sensitivity to environmental conditions.

- *Full usage:*

In [40], the entire I-V curve is used as a fault feature for PV fault diagnosis under eight conditions (healthy and seven faults) with variable temperature and irradiance. Six machine learning techniques (artificial neural network, support vector machine, decision tree, random forest, k-nearest neighbors, and naive Bayesian classifier) have been evaluated. The main issues are the number of sampling points and the computational burden necessary to handle the data processing. The study [31] investigates the abrupt deviation of the faulty I-V characteristic in the case of shading and  $R_s$  degradation fault ; the results indicate that it is impossible to detect the presence of an inflexion point by observing the profile of the first derivative. The appearance of a positive peak in the second derivative makes it possible to detect the fault.

The entire I-V curve can also be used to extract the PV model parameters ( $I_{ph}$ ,  $I_0$ ,  $R_s$ ,  $R_{sh}$  and  $n$ ) considered as fault features. In [41], this approach is used with the double diode model. Various types of partial shading (PS) and degradation are diagnosed using threshold analysis. However, the effectiveness of this method strongly depends on the model's accuracy.

#### *III.3.4. Fault detection and diagnosis proposal*

Still, the I-V curve is a widely discussed topic [7] because the I-V curve contains several pieces of information on the PV module's health status. However, measuring the I-V curve requires interrupting power production and the availability of an I-V tracer. The deployment on a larger scale would be relevant if the I-V tracer has a low cost and interruption (measurement time) is limited. Based on the solution proposed in chapter I, the measured I-V curve will be used as input for two FDD methodologies that will be detailed in the following. The first one uses the parameters of the electrical equivalent circuit as fault features. It is based on the single diode model (SDM). The second one uses the extracted characteristics  $I_{pv}$ ,  $V_{pv}$ ,  $P_{mpp}$ ,  $I_{sc}$ , and  $V_{oc}$  as fault features. The first one denoted "M1", is displayed in [Fig.III.15\(a\)](#), while the second one "M2" is shown in [Fig.III.15 \(b\)](#).

❖ *Faults under study*

Due to natural aging or severe environmental conditions (e.g., a decrease in contact adhesion and the corrosive action of water vapor), the series resistance increases while the shunt resistance decreases. In the following, partial shading, degradation of series, and shunt resistances will be considered through three scenarios:

- Fault 1:  $R_s$  degradation
- Faulty 2:  $R_{sh}$  degradation
- Faulty 3: Partial shading

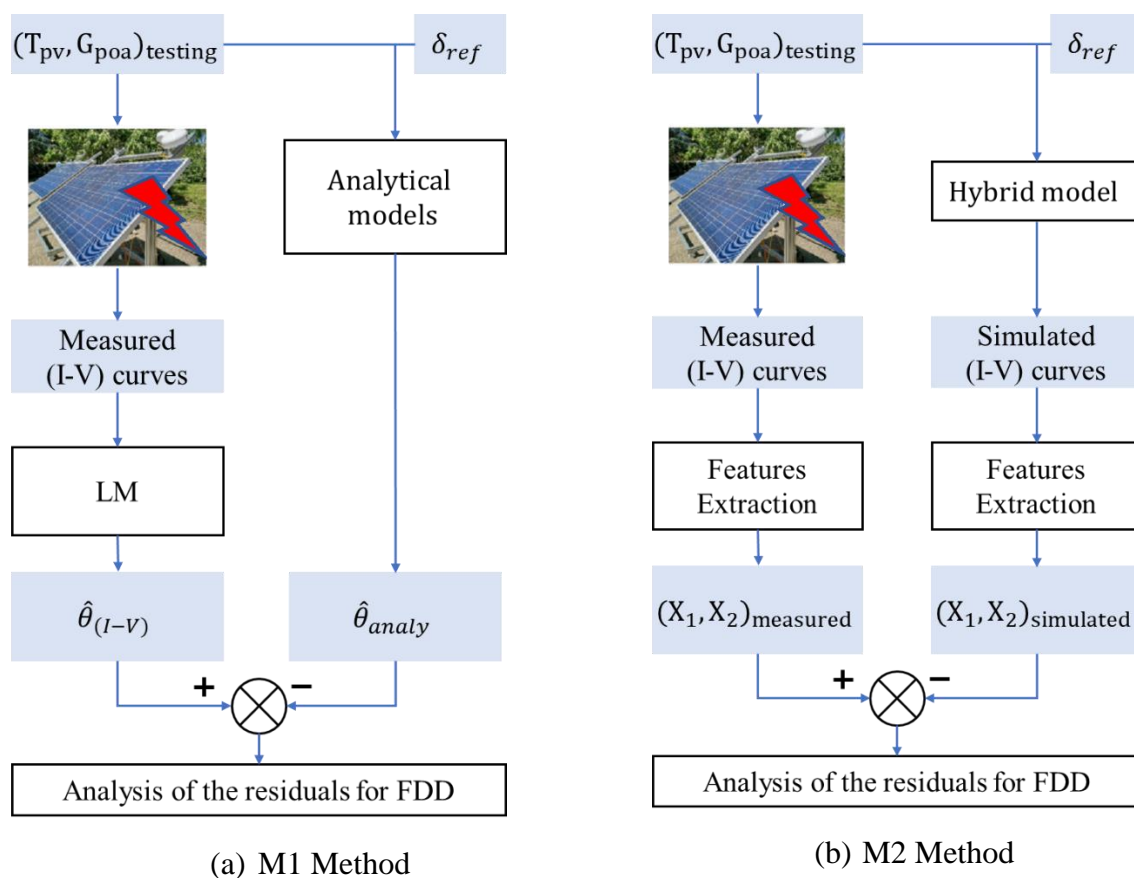


Fig.III.15: Flowchart of the FDD

### III.4. Results of fault detection and diagnosis with methods M1 and M2

#### III.4.1. $R_s$ degradation

The degradation of the series resistance  $R_s$  is mainly due to the aging of the PV module. In the PV model, the series resistance represents the resistance of the cell, the resistance of the contact between the metal and the semiconductor, and the interconnection resistance between

the cells. To evaluate the two methods, the degradation is emulated by connecting an additional variable resistance in series with the PV panel.

#### III.4.1.1. Simulation data

To evaluate the methods M1 and M2 with simulation data, the ‘measured I-V’ curves in the flowchart of Fig.III.14 are replaced with I-V curves obtained from the simulation of the hybrid model in which the faults are emulated.

##### III.4.1.1.1. Evaluation of method M1 with simulation data

The simulation uses the hybrid PV model presented in chapter I. The environmental measurement data for the testing stage ( $(G_{poa}$  and  $T_{pv})_{testing}$ ) consists of 343 samples. The additional resistance used to emulate the degradation varies from from 5% to 50% of the mean value of the series resistance of the healthy case ( $R_{s,mean,h} = 0.78 \Omega$ ), as shown in *Table.III. 5*. The five parameters ( $\hat{\theta}_{(I-V)}$ ) are extracted from the simulated faulty I-V curves, using the LM algorithm. These extracted parameters are compared to the estimated ones ( $\hat{\theta}_{analy}$ ) calculated from the analytical models in healthy conditions with the same environmental data. In the following, the lower script ‘*f*’ stands for faulty, and ‘*h*’ for healthy.

*Table.III. 5: Fault levels for  $R_s$  degradation*

No	Degradation percentage [%]	$\Delta R_s [\Omega]$	$R_{s_f} = R_{s,h} + \Delta R_s [\Omega]$
0	0	0	0,78
1	5	0,039	0,819
2	10	0,078	0,858
3	15	0,117	0,897
4	20	0,156	0,936
5	25	0,195	0,975
6	30	0,234	1,014
7	35	0,273	1,053
8	40	0,312	1,092
9	45	0,351	1,131
10	50	0,39	1,17

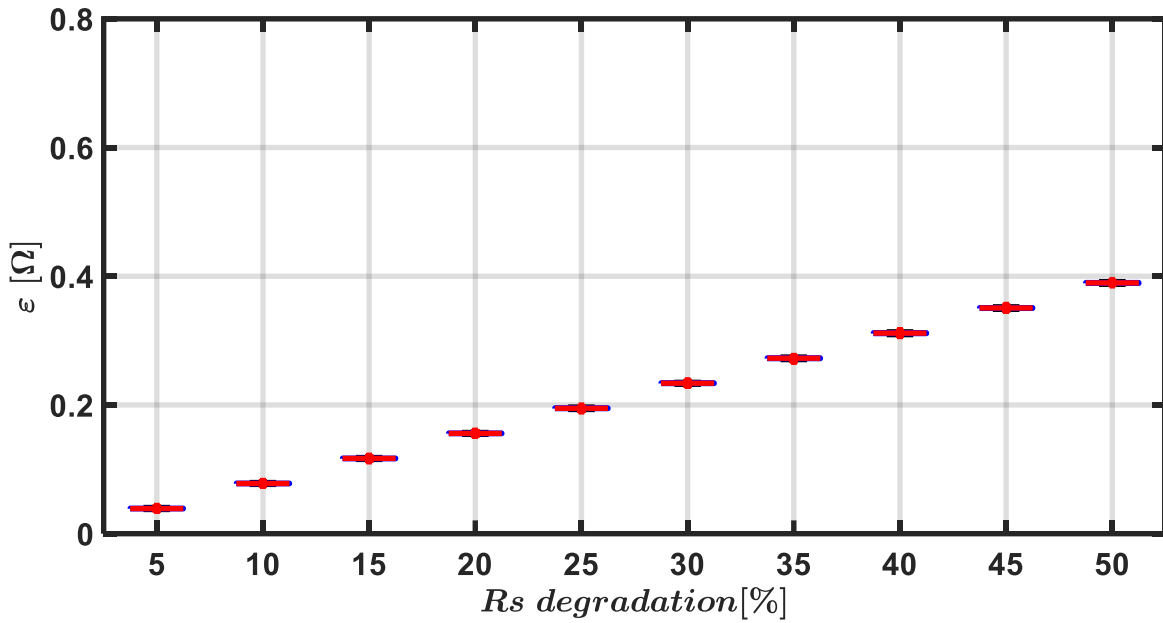
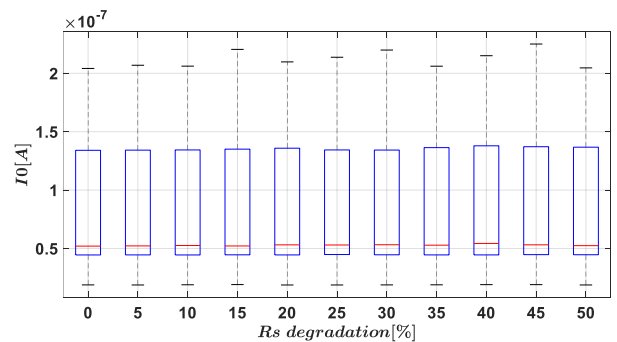
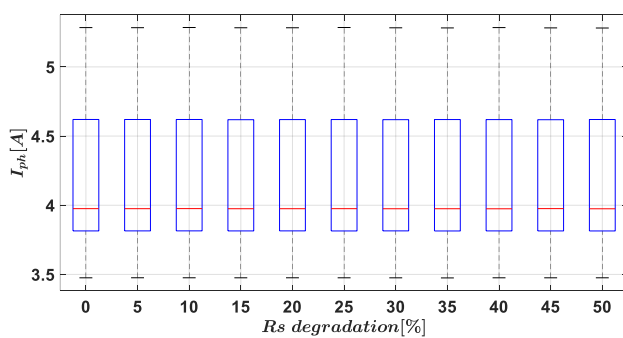


Fig.III.16: Boxplot of the residual for  $R_s$  degradation

The boxplot of the residuals is shown in Fig.III.16. The fault can be detected with the appropriate setting of a threshold. The severity levels can also be accurately estimated, as shown in Table.III. 6. It can be noted that the series resistance degradation does not affect the other parameters, as shown in Fig.III.17. The result show that while  $R_s$  increases, the extracted values of  $I_{ph}$ ,  $R_{sh}$ ,  $I_0$  and  $n$  remain constant.

Table.III. 6: Residuals for  $R_s$  degradation

Fault level	$f1$	$f2$	$f3$	$f4$	$f5$	$f6$	$f7$	$f8$	$f9$	$f10$
$\hat{R}_{s(I-V),h}(\Omega)$	0.782	0.782	0.782	0.782	0.782	0.782	0.782	0.782	0.782	0.782
$\hat{R}_{s(analy),f}(\Omega)$	0.821	0.860	0.899	0.938	0.977	1.016	1.055	1.094	1.133	1.172
$\varepsilon(\Omega)$	0,039	0,078	0,117	0,156	0,195	0,234	0,273	0,312	0,351	0,39



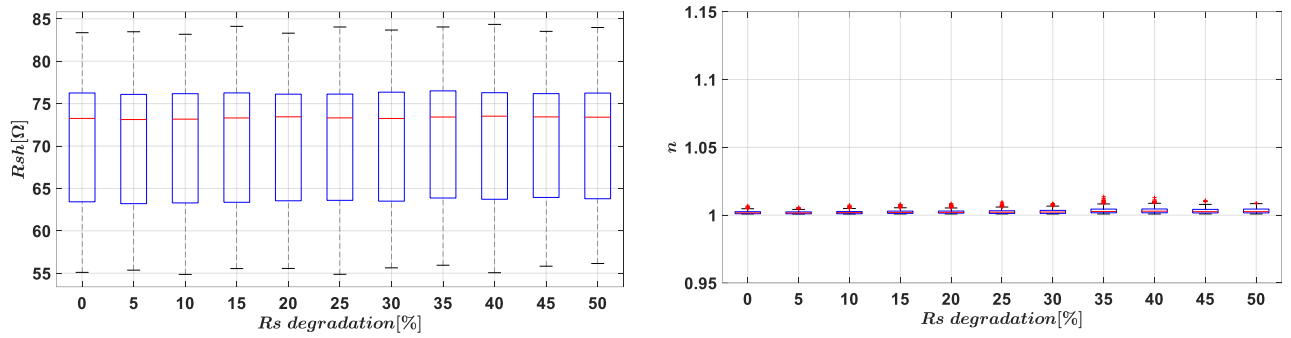


Fig.III.17: Effect of  $R_s$  degradation on the other parameters of the SDM

Fig.III.18 shows the I-V and P-V curves under the same environmental condition with different faulty conditions. It can be observed that the degradation of the series resistance mainly affects the maximum power points, while the  $V_{OC}$  and  $I_{SC}$  remain almost constant.

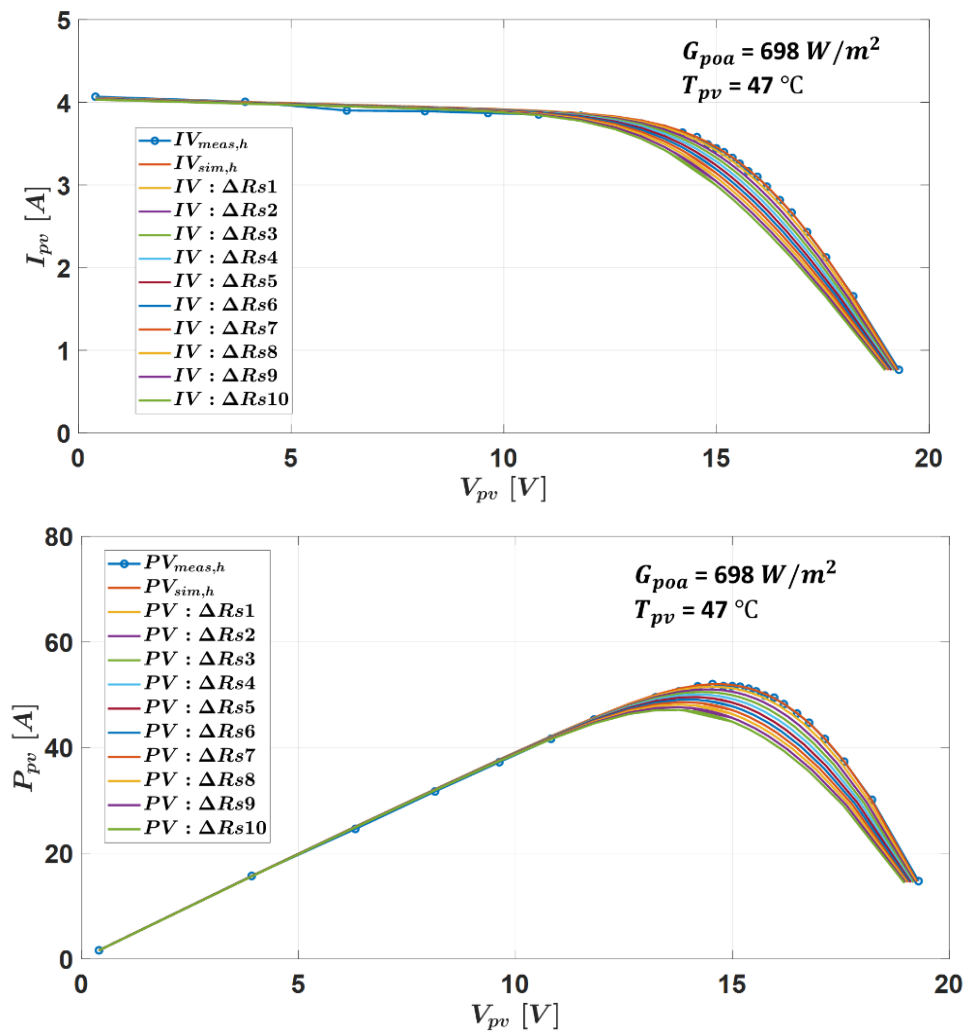


Fig.III.18: Effect of  $R_s$  degradation on I-V and P-V curves

III.4.1.1.2. Evaluation of method M2 with simulation data

As previously mentioned, FDD with the method M2 uses the characteristics  $I_{pv}$ ,  $V_{pv}$ ,  $P_{mpp}$ ,  $I_{sc}$ , and  $V_{oc}$  extracted from the actual I-V curves as fault features. They are compared with the characteristics extracted from the healthy I-V curves for the same environmental data. The results are displayed in Fig.III.19.

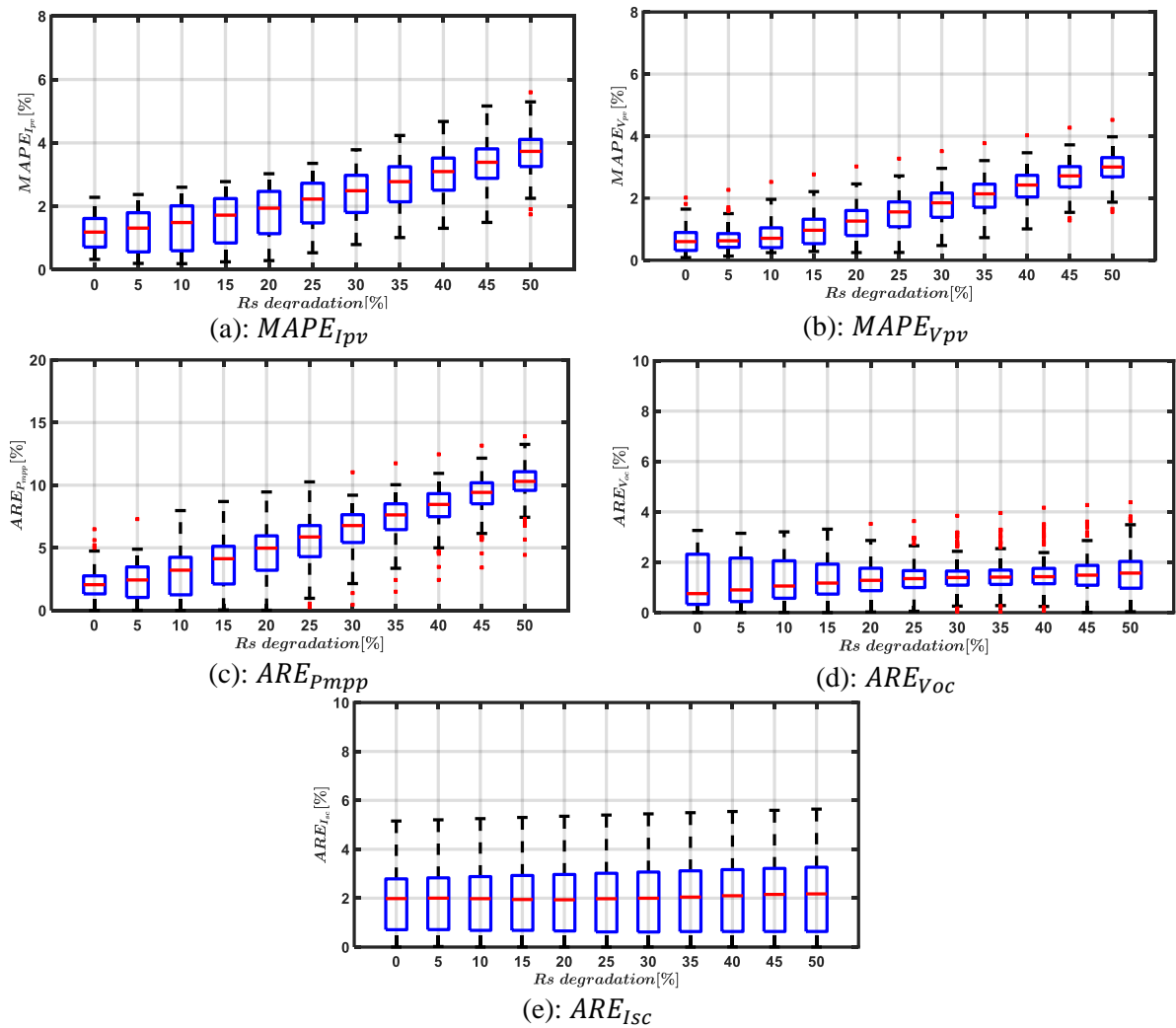


Fig.III.19: Effect of  $R_s$  degradation on I-V curve characteristics

The mean values of the relative residuals for the five characteristics are summarized in Table.III.7. We can draw the following conclusions: the maximum power point is the most sensitive feature to series resistance degradation, the voltage is more sensitive than the current, the short-circuit current and open-circuit voltage are barely affected. These findings are consistent as the series resistance mainly affects the voltage-source region of the I-V curve.



Table.III. 7 : Mean values of the residuals

Fault level	$f1$	$f2$	$f3$	$f4$	$f5$	$f6$	$f7$	$f8$	$f9$	$f10$
$\Delta\mu MAPE_{I_{pv}}(\%)$	0,045	0,156	0,343	0,562	0,800	1,052	1,316	1,589	1,870	2,158
$\Delta\mu MAPE_{V_{pv}}(\%)$	0,026	0,176	0,484	0,885	1,325	1,782	2,246	2,712	3,179	3,645
$\Delta\mu ARE_{P_{mpp}}(\%)$	<b>0,115</b>	<b>0,381</b>	<b>0,803</b>	<b>1,250</b>	<b>1,718</b>	<b>2,192</b>	<b>2,659</b>	<b>3,122</b>	<b>3,585</b>	<b>4,047</b>
$\Delta\mu ARE_{V_{oc}}(\%)$	0,007	0,023	0,048	0,072	0,102	0,128	0,153	0,183	0,209	0,242
$\Delta\mu ARE_{I_{sc}}(\%)$	0,006	0,013	0,021	0,029	0,038	0,048	0,058	0,070	0,083	0,097

### III.4.1.2. Experimental data

#### III.4.1.2.1. Evaluation of method M1 with experimental data

$\Delta R_{s1}$ ,  $\Delta R_{s2}$ ,  $\Delta R_{s3}$  are the three resistances added in series with the PV panel to emulate three fault levels ( $f1, f2, f3$ ), corresponding to an increase of 28%, 42%, and 50%, respectively. Table.III. 8 displays the fault scenarios, the environmental conditions, and the number of I-V curves measured with the I-V tracer. Temperature  $T_{pv}$  and irradiance  $G_{poa}$  are also provided. As described in Fig.III.15 (a), the FDD with the method M1 uses the vector of parameters as fault features.

Table.III. 8: Data acquisition in case of  $R_s$  degradation

Date of acquisition	Weather	Number of I-V curves $G_{poa} \geq 600 W/m^2$	Fault level
1   12/04/2021	Partly cloudy	38	$\Delta R_{s3} = 0.39 \Omega$
2   17/04/2021	Partly cloudy	16	$\Delta R_{s3} = 0.39 \Omega$
3   18/04/2021	Partly cloudy	56	$\Delta R_{s3} = 0.39 \Omega$
4   19/04/2021	Partly cloudy	34	$\Delta R_{s2} = 0.33 \Omega$
5   26/04/2021	Partly cloudy	61	$\Delta R_{s2} = 0.33 \Omega$
6   27/04/2021	Partly cloudy	61	$\Delta R_{s2} = 0.33 \Omega$
7   20/04/2021	Partly cloudy	104	$\Delta R_{s1} = 0.22 \Omega$

In the following,  $R_{s(I-V)}$  stands for the series resistance extracted from the measured I-V curve, while  $R_{s(analy)}$  is the series resistance estimated from the analytical model. The lower script ' $f$ ' stands for faulty, and ' $h$ ' for healthy. The histograms of the series resistances for the healthy and faulty cases are plotted in Fig.III.19.

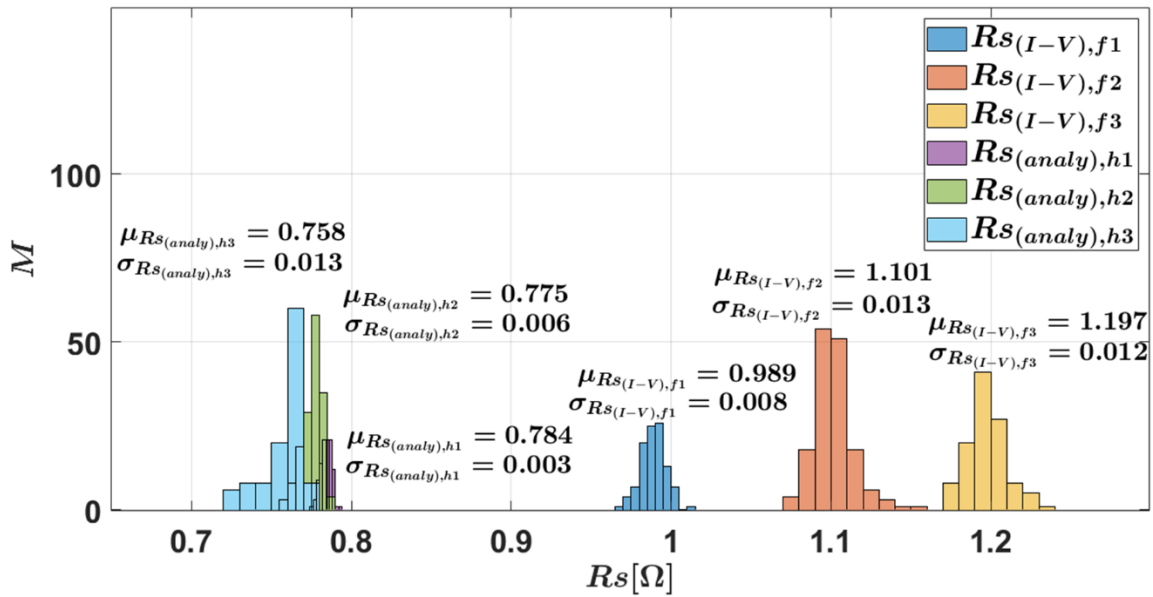


Fig.III.20: Histograms of the series resistance  $R_s$

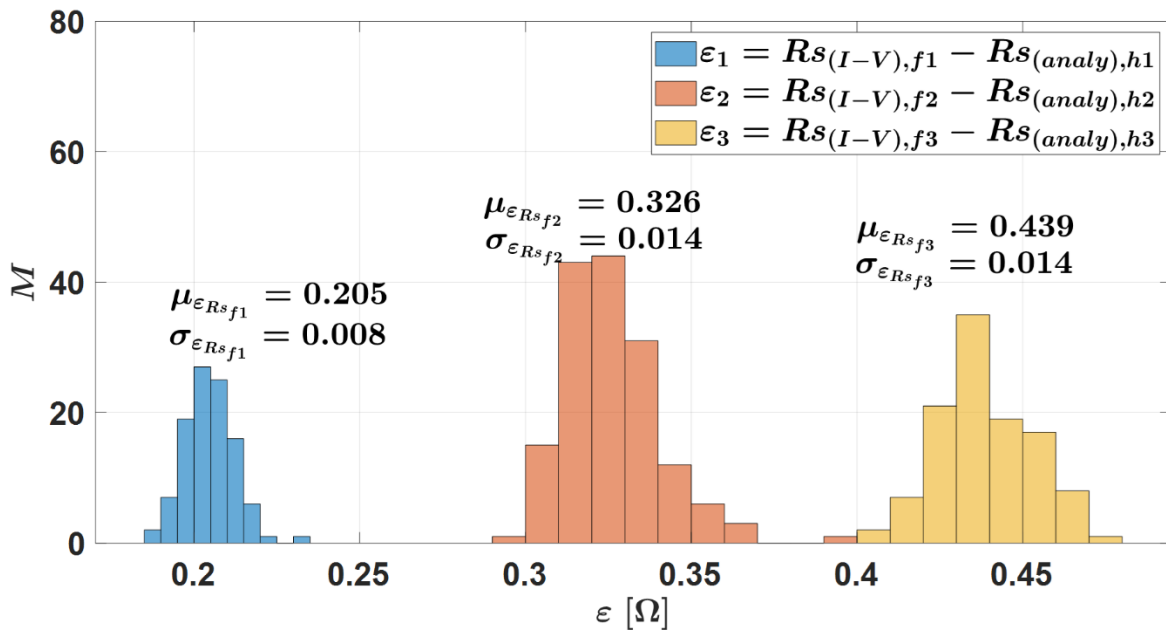


Fig.III.21: Histograms of the residuals for the three fault severities

The histograms of the residuals are plotted in Fig.III.21. From these results, we can conclude:

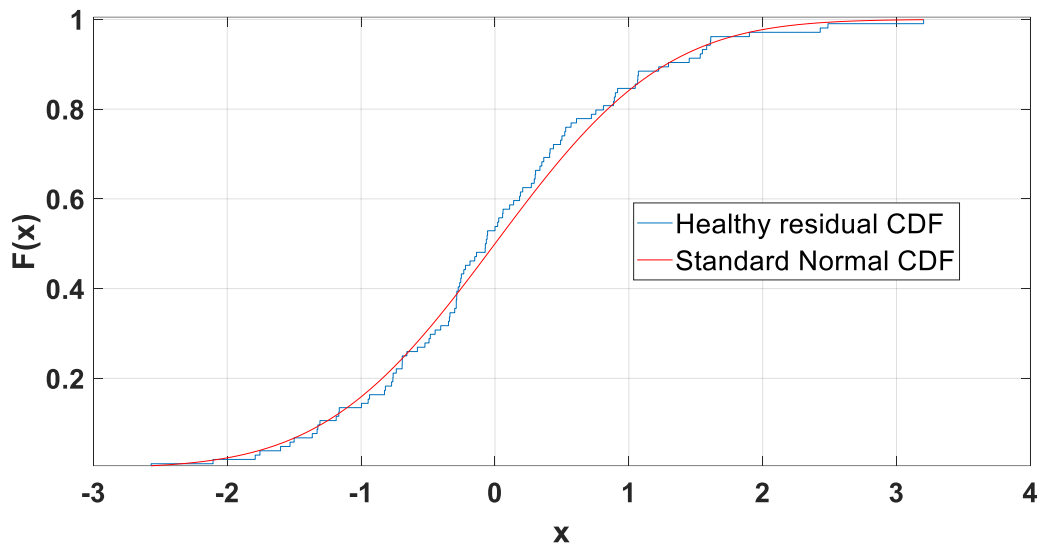
- in the healthy case, despite the variations of the environmental conditions (irradiance and temperature), the series resistance in healthy case  $R_{s,h} \in [0.737, 0.788]\Omega$  is almost constant,
- in faulty conditions, the series resistances are significantly different from the healthy case.

The severity levels can also be estimated with an acceptable accuracy, as shown in *Table.III. 9*.

*Table.III. 9: Accuracy of fault level estimation in case of  $R_s$  degradation*

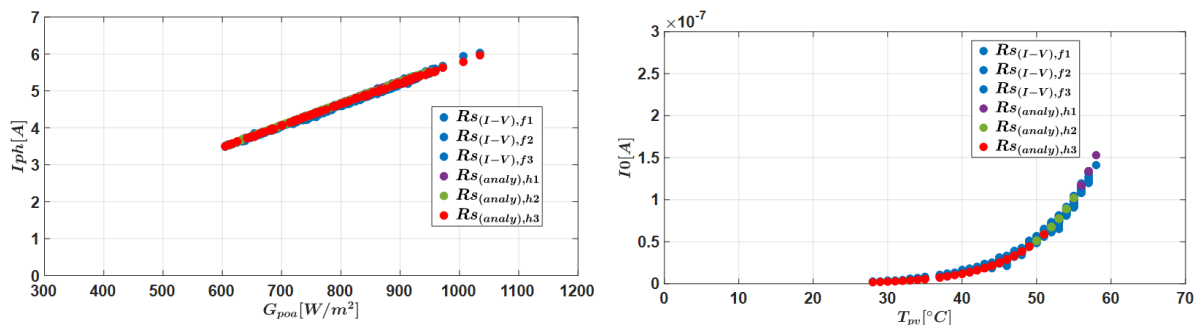
Fault level	$f1$	$f2$	$f3$
$\Delta R_{s\text{Experimental}}(\Omega)$	0.22	0.33	0.39
$\Delta R_{s\text{Estimated}}(\Omega)$	0.205	0.326	0.439
Relative error %	2.5	1.2	12.5

The cumulative density functions of a normal distribution and the residual in healthy conditions are displayed in *Fig.III.21*. We also successfully evaluate the normality of the distribution through the Kolmogorov-Smirnov test. Therefore, we can set the threshold at  $Th_{R_s} = \mu_{\epsilon_{R_s}} + 3 * \sigma_{\epsilon_{R_s}} = 0.036\Omega$ . The fault can be detected for each case as  $\Delta R_s > Th_{R_s}$ .



*Fig.III.22: Cumulative Distribution functions in case of  $R_s$*

From the results shown in *Fig.III.23*, we can observe that the fault has almost no effect on the other parameters.



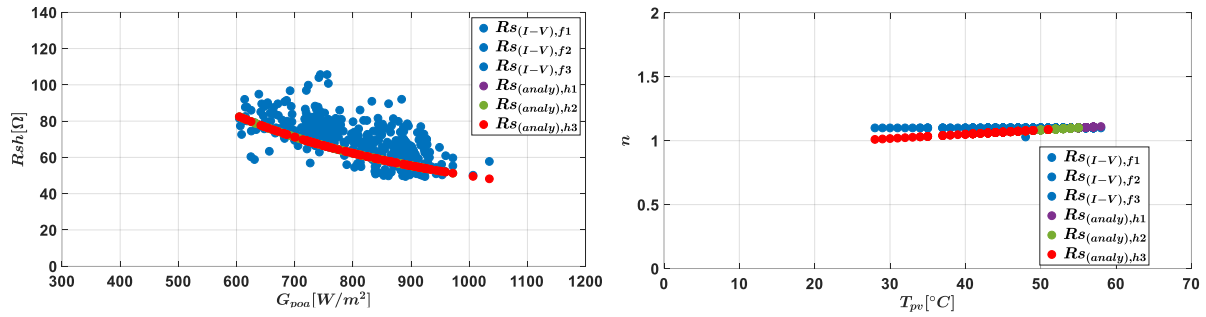
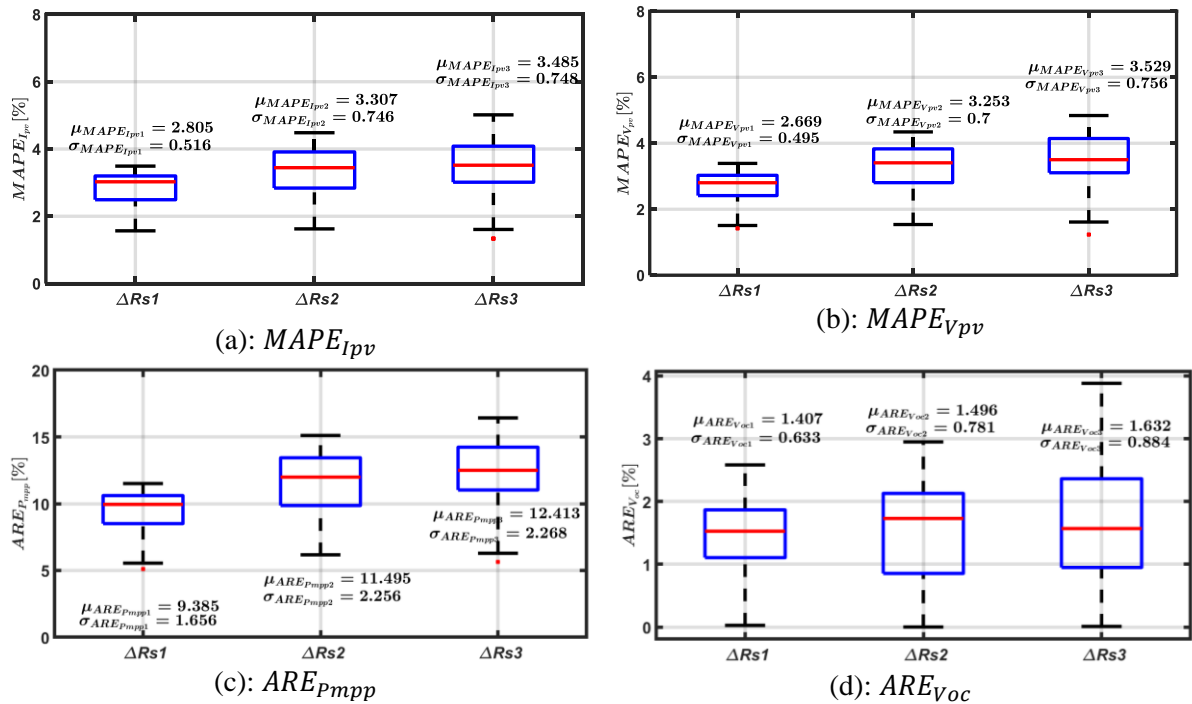


Fig.III.23: Effect of  $R_s$  degradation on the other parameters of the SDM

#### III.4.1.2.2. Evaluation of method M2 with experimental data

The method M2 compares the main characteristics extracted from measured I-V curves to those extracted from healthy I-V curves simulated with the hybrid model. The results are shown in Fig.III.24. The relative variations of the mean values (compared to the healthy case) for the five characteristics are displayed in Table.III. 10. We can deduce as in the case of simulated data, that the maximum power point is the most sensitive feature to the series resistance degradation. The voltage values are also more affected than the current values. The open-circuit voltage and the short-circuit current are barely affected. These results are consistent as the series resistance mainly affects the voltage-source region of the I-V curve.



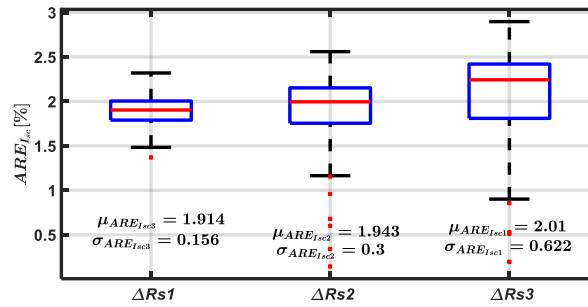

 (e):  $ARE_{Isc}$ 

 Fig.III.24: Effect of  $R_s$  on the I-V curve characteristics

Table.III. 10: Mean value relative variation of the residuals

Fault level	f1	f2	f3
$\Delta\mu MAPE_{I_{pv}}(\%)$	1.4	1.84	1.99
$\Delta\mu MAPE_{V_{pv}}(\%)$	3.15	4.06	4.48
$\Delta\mu ARE_{P_{mpp}}(\%)$	<b>3.6</b>	<b>4.64</b>	<b>5.1</b>
$\Delta\mu ARE_{V_{oc}}(\%)$	0.13	0.21	0.32
$\Delta\mu ARE_{I_{sc}}(\%)$	0.01	0.032	0.067

### III.4.2. $R_{sh}$ degradation

The parallel resistance represents all the paths crossed by the leakage current, either in parallel with the cell or at the cell's border. It results from damage in the crystal or impurities in or near the junction. The degradation of the shunt resistance  $R_{sh}$  is due to the aging of the PV module. In order to investigate the FDD for this type of degradation, the PV panel's resistance is decreased by connecting in parallel an additional resistance, which value is varied to emulate several fault levels.

#### III.4.2.1. Simulation data

##### III.4.2.1.1. Evaluation of method M1 with simulation data

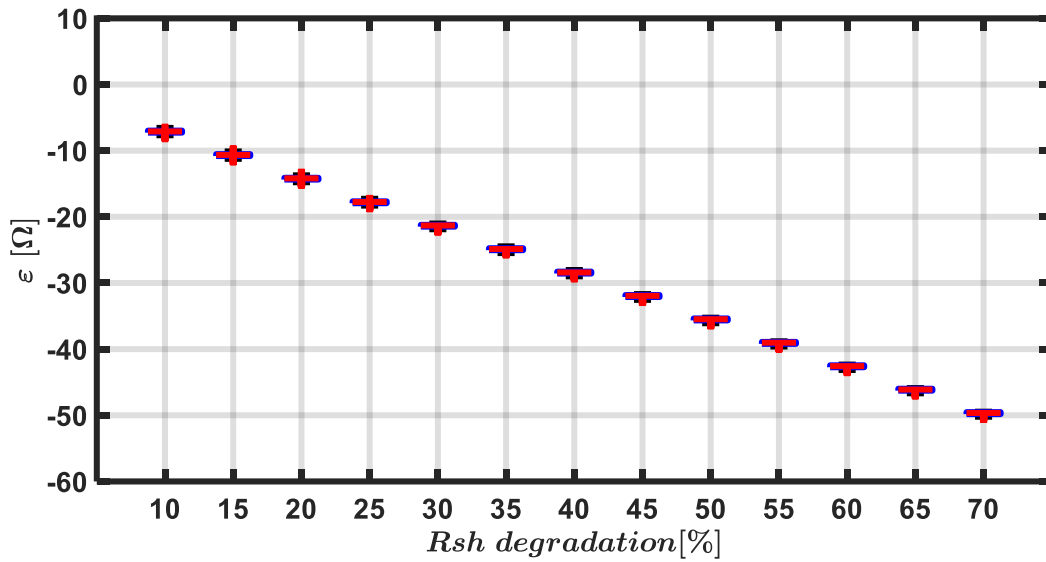
For the simulation, the shunt resistance will be decreased by 10 to 70% of the healthy value measured in the healthy case:  $R_{sh,mean}$  ( $R_{sh,mean,h} = 70.71 \Omega$ ). The values of  $R_{sh_f}$  are reported in *Table.III. 11*.

Table.III. 11: Shunt resistance fault levels used in the PV hybrid model

No	Degradation percentage [%]	$\Delta R_s [\Omega]$	$R_{sh_f} = R_{sh,h} - \Delta R_{sh} [\Omega]$
0	0	0	70,71
1	10	7,072	63,648
2	15	10,608	60,112
3	20	14,144	56,576
4	25	17,68	53,04

5	30	21,216	49,504
6	35	24,752	45,968
7	40	28,288	42,432
8	45	31,824	38,896
9	50	35,36	35,36
10	55	38,896	31,824
11	60	42,432	28,288
12	65	45,968	24,752
13	70	49,504	21,216

The boxplot of the residuals are shown in *Fig.III.25*. It can be concluded from the results in *Table.III. 12*, that even with a decrease of 10%, the fault can be detected and its severity assessed. We can also observe, as illustrated in *Fig.III.26*, that the fault has no effect on the other parameters,  $I_{ph}$ ,  $I_0$ ,  $R_s$ , and  $n$ , which remain almost unchanged.



*Fig.III.25 : Boxplot of residuals for Rsh*

*Table.III. 12: Residuals for Rsh*

Fault level	$f1$	$f2$	$f3$	$f4$	$f5$	$f6$	$f7$	$f8$	$f9$	$f10$	$f11$	$f12$	$f13$
$Rsh, h(\Omega)$	70,7	70,7	70,7	70,7	70,7	70,7	70,7	70,7	70,7	70,7	70,7	70,7	70,7
$Rsh_{Estimated} (\Omega)$	63,6	60,0	56,5	52,9	49,4	45,8	42,3	38,7	35,2	31,6	28,1	24,6	21,0
$\varepsilon (\Omega)$	7,1	10,7	14,2	17,8	21,4	24,9	28,5	32,0	35,5	39,1	42,6	46,2	49,7

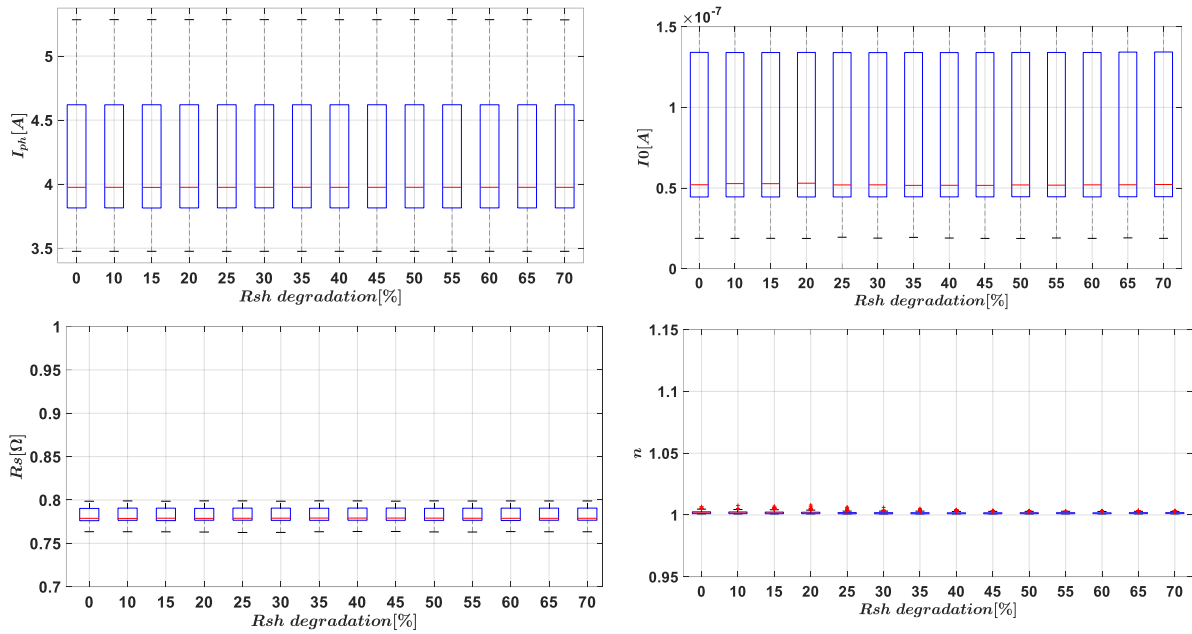


Fig.III.26 : Effect of  $R_{sh}$  degradation on the other parameters

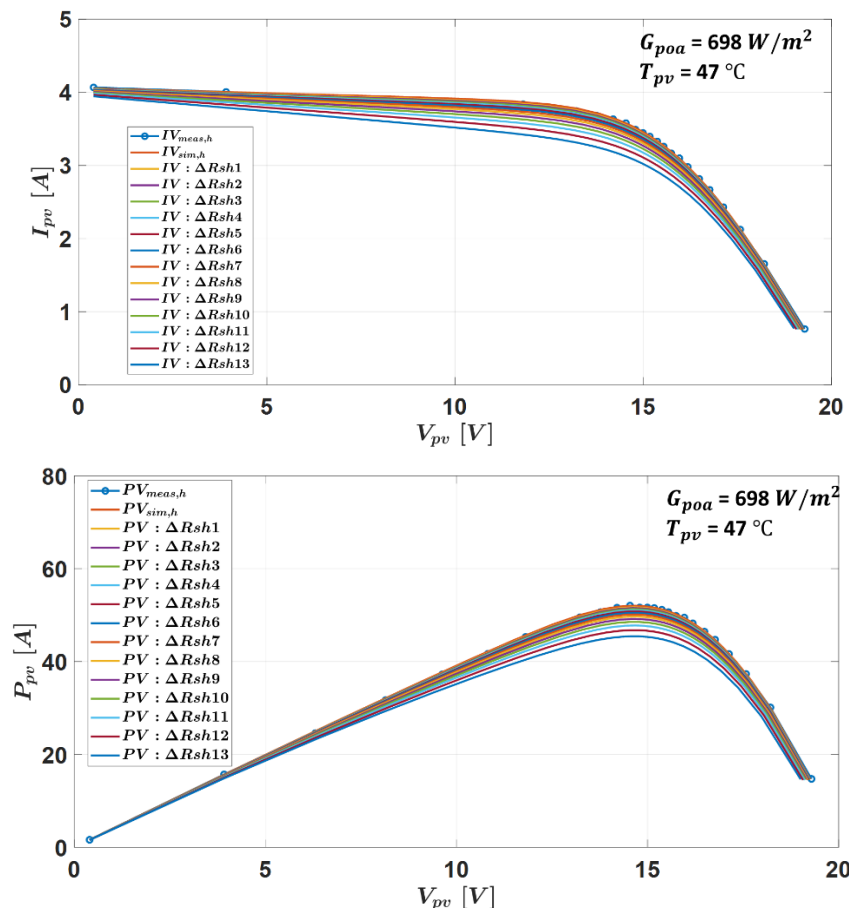


Fig.III.27: Effect of  $R_{sh}$  degradation on I-V and P-V curves

Fig.III.27 illustrates the influence of  $R_{sh}$  degradation on I-V and P-V curves under the same environmental conditions. We can observe that the variations of  $R_{sh}$  mainly affect the maximum power points, while  $V_{oc}$  and  $I_{sc}$  are almost constant.

III.4.2.1.2. Evaluation of method M2 method with simulation data

The effects of  $R_{sh}$  degradation on the characteristics of the I-V curve are shown in Fig.III.28. Looking at the relative mean values displayed in

Table.III. 13, it can be concluded that the maximum power point is the most sensitive feature, the current is more significantly affected than the voltage, and the open-circuit voltage and short-circuit current are barely impacted. These results are consistent because the shunt resistance mainly affects the current-source region of the I-V curve.

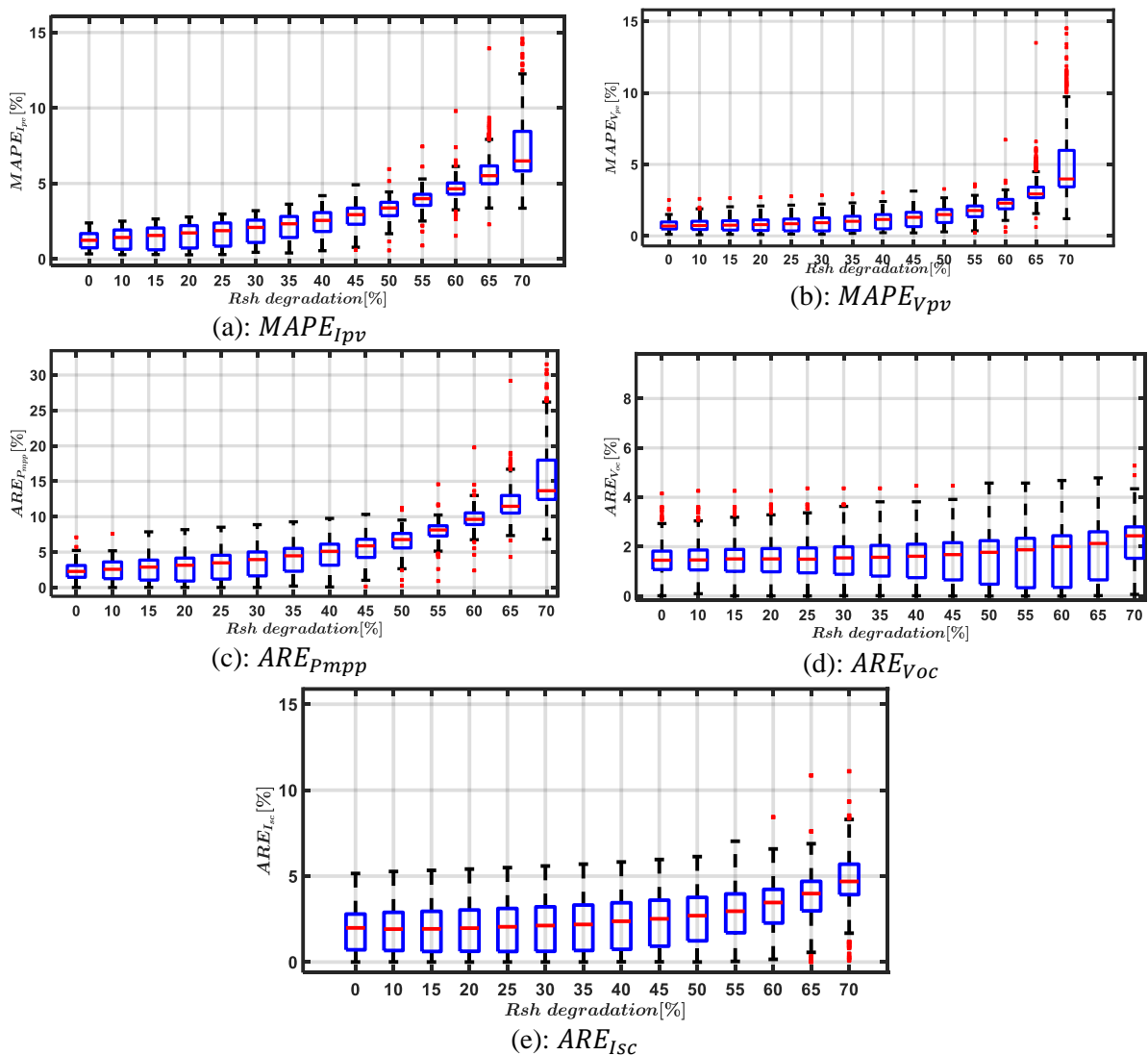


Fig.III.28: Effect of  $R_{sh}$  degradation on the characteristics of the I-V curve



Table.III. 13: Effect of  $R_{sh}$  degradation on I-V curve characteristics

Fault level	$f_1$	$f_2$	$f_3$	$f_4$	$f_5$	$f_6$	$f_7$	$f_8$	$f_9$	$f_{10}$	$f_{11}$	$f_{12}$	$f_{13}$
$\Delta\mu MAPE_{I_{pv}}(\%)$	0,13	0,20	0,30	0,43	0,60	0,82	1,09	1,42	1,83	2,35	3,03	3,96	5,35
$\Delta\mu MAPE_{V_{pv}}(\%)$	0,17	0,19	0,23	0,28	0,35	0,47	0,63	0,87	1,21	1,70	2,49	4,01	7,20
$\Delta\mu ARE_{P_{mpp}}(\%)$	<b>0,19</b>	<b>0,25</b>	<b>0,34</b>	<b>0,48</b>	<b>0,68</b>	<b>0,96</b>	<b>1,30</b>	<b>1,72</b>	<b>2,24</b>	<b>2,91</b>	<b>3,79</b>	<b>5,00</b>	<b>6,82</b>
$\Delta\mu ARE_{V_{oc}}(\%)$	0,19	0,19	0,20	0,20	0,20	0,20	0,21	0,20	0,21	0,22	0,27	0,43	0,76
$\Delta\mu ARE_{I_{sc}}(\%)$	0,01	0,02	0,03	0,05	0,08	0,12	0,18	0,26	0,37	0,53	0,75	1,05	1,50

### III.4.2.2. Experimental data in case of $R_{sh}$ degradation

#### III.4.2.2.1. Evaluation of method M1 with experimental data

For the experiment, three resistances are considered,  $R_{sh\_add1}$ ,  $R_{sh\_add2}$ , and  $R_{sh\_add3}$  corresponding to three fault levels. They are connected in parallel with the PV panel to emulate  $R_{sh}$  degradation. Table.III. 14 summarizes the environmental conditions, and the fault cases.

Table.III. 14: Data for  $R_{sh}$  degradation

Data acquisition in case of $R_{sh}$ degradation				
	Date of acquisition	Weather	Number of I-V curves $G_{poa} \geq 600 W/m^2$	$R_{sh\_add}$
1	13/04/2021	Partly cloudy	82	60 $\Omega$
2	05/04/2021	Partly cloudy	61	50 $\Omega$
3	03/04/2021	Partly cloudy	39	39 $\Omega$

From the histograms displayed in Fig.III.29 and Fig.III.30, we can draw the following conclusions :

- due to variations of the environmental conditions (irradiance and temperature), the shunt resistance in the healthy case,  $R_{sh} \in [54, 71]\Omega$  varies slightly,
- in faulty conditions, the shunt resistances are significantly different from the healthy case,
- the mean values of the residuals are consistent with the calculated variations  $\Delta R_{sh} = R_{sh,mean,h} - R_{sh,f} [\Omega]$  displayed in Table.III. 15.

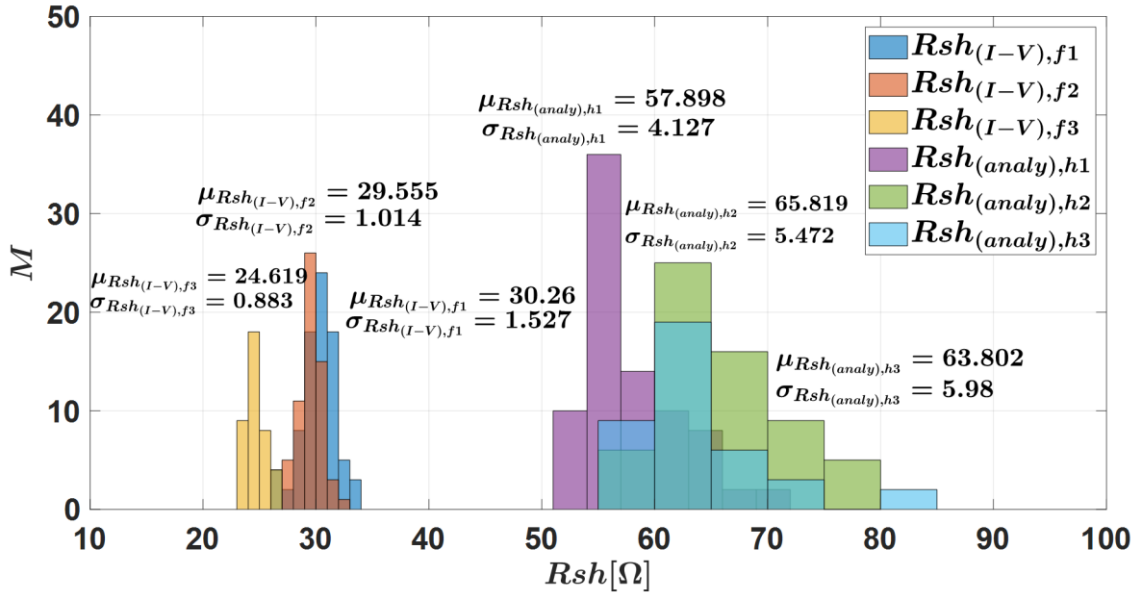
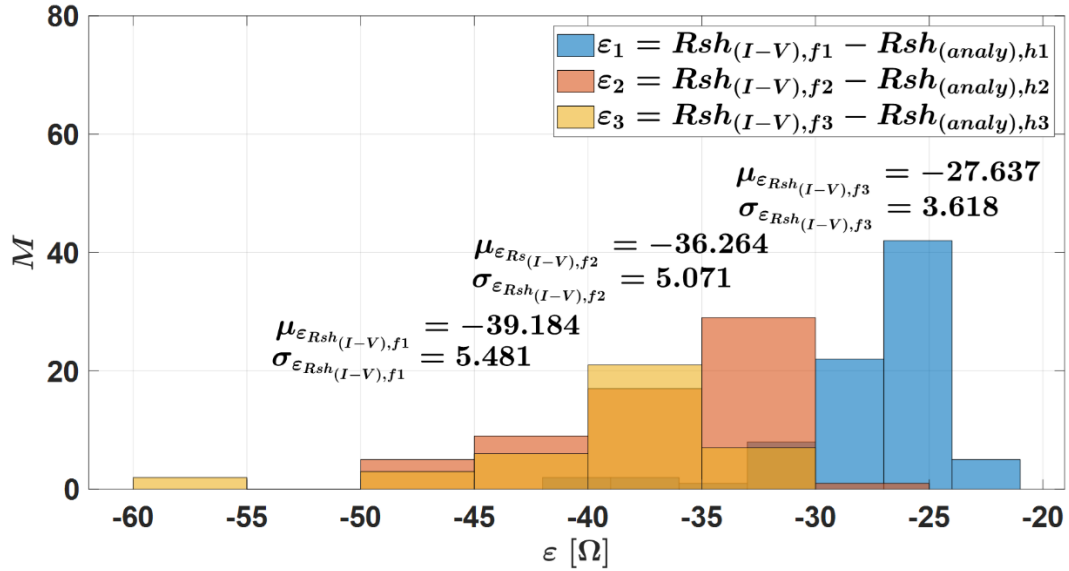

 Fig.III.29: Histograms of  $R_{sh}$  resistance

 Fig.III.30: Histograms of residuals for  $R_{sh}$ 

 Table.III. 15: Three levels of severity for  $R_{sh}$  degradation

Fault level	$Rsh_{add}$ [ $\Omega$ ]	$Rsh_{mean,h}$ [ $\Omega$ ] (Analytical model)	$Rsh_{mean,h}/Rsh_{add}$	$\Delta Rsh$ [ $\Omega$ ]
1	60	57.89	29.46	28.42
2	50	65.81	28.41	37.39
3	39	63.8	24.20	39.59

The cumulative density functions of a normal distribution and the residual in healthy conditions are displayed in Fig.III.30. We also evaluate successfully the normality of the distribution through the Kolmogorov-Smirnov's test. Therefore, we can set the threshold at

$Th_{Rsh} = \mu_{\epsilon_{Rsh}} + 3 * \sigma_{\epsilon_{Rsh}} = 4.512\Omega$ . The fault can be detected for each case as  $\Delta R_{sh} > Th_{Rsh}$ .

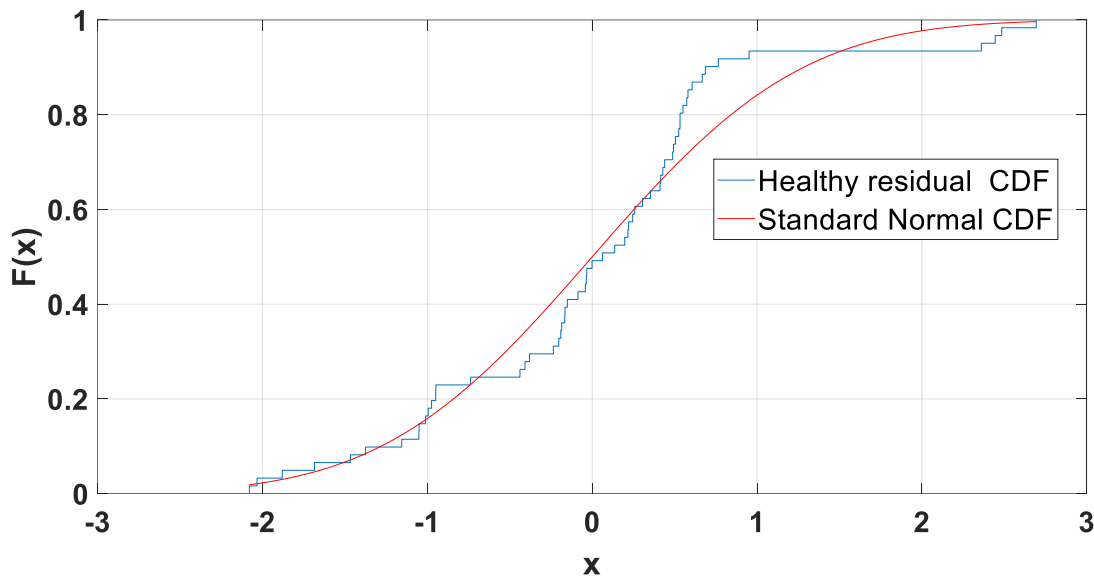


Fig.III.31: Cumulative Distribution Functions

The fault effect on the other parameters plotted in Fig.III.32 shows that there is no significant variation.

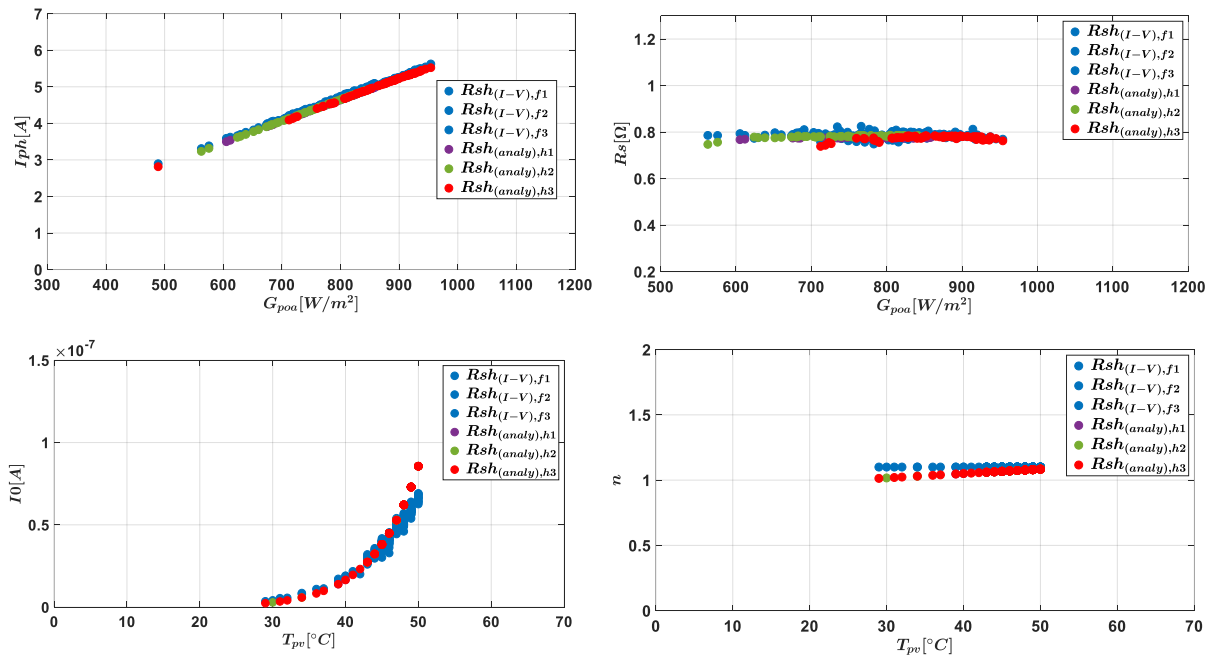


Fig.III.32: Effect of  $R_{sh}$  degradation on the other parameters

## III.4.2.2.2. Evaluation of method M2 method with experimental data

The effects of  $R_{sh}$  degradation on the I-V curve characteristics are shown in Fig.III.33.

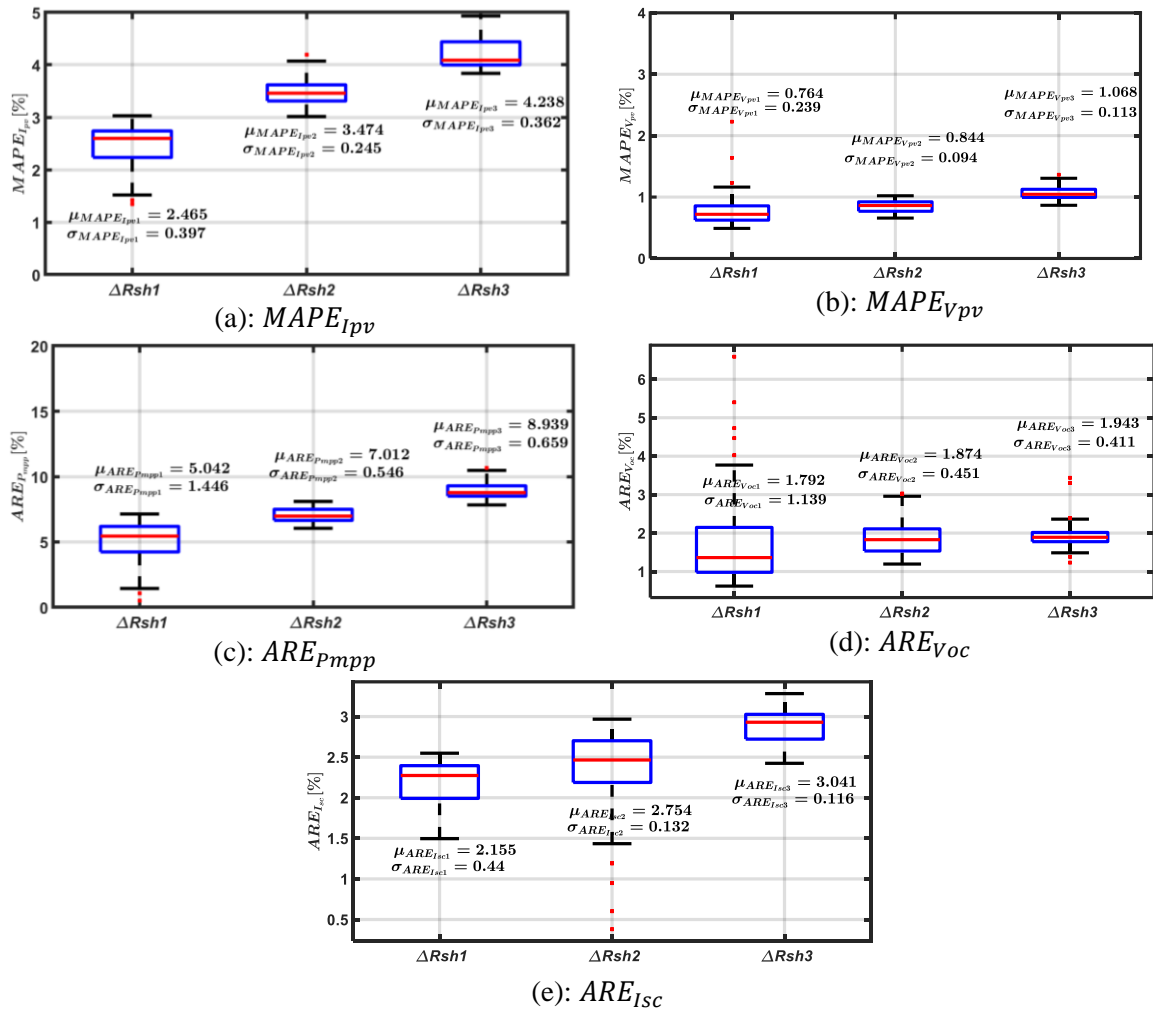


Fig.III.33: Effect of  $R_{sh}$  degradation on the I-V curve characteristics

The relative variations of the mean values (compared to the healthy case) for the five characteristics are presented in *source region* of the I-V curve.

Table.III. 16. From these results, it can be deduced, as with the simulation data, that the maximum power point is the most sensitive feature to the degradation of the shunt resistance. The current of the PV module is more significantly affected than the voltage. The open-circuit voltage and short-circuit current are slightly affected. These results are consistent because the shunt resistance mainly affects the current-source region of the I-V curve.

Table.III. 16: Fault effect on the I-V curve characteristics

Fault level	$f1$	$f2$	$f3$
$\Delta\mu MAPE_{I_{pv}}$ (%)	1.11	1.98	2.64
$\Delta\mu MAPE_{V_{pv}}$ (%)	0.19	0.31	0.66
$\Delta\mu ARE_{P_{mpp}}$ (%)	<b>1.48</b>	<b>2.44</b>	<b>3.39</b>
$\Delta\mu ARE_{V_{oc}}$ (%)	0.45	0.51	0.57
$\Delta\mu ARE_{I_{sc}}$ (%)	0.14	0.46	0.61

III.4.3. Partial shading

Partial Shading (PS) is a natural phenomenon of non-homogeneous irradiance on PV cells/modules due to environmental causes (cloud passage, dust, snow, leaves, ...), building shadows, or soiling. If the bypass diode is activated, several peaks appear in the P-V curve, making it difficult to track the maximum power. Moreover, PS can induce hotspots reducing the output power, efficiency, and reliability.

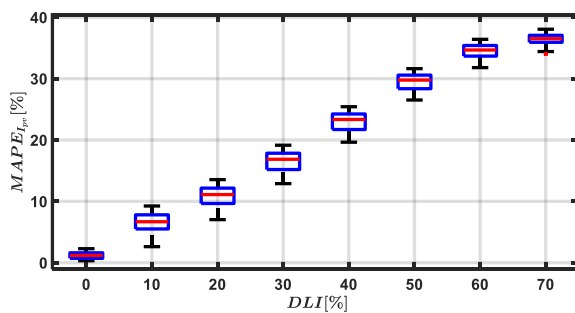
In case of partial shading, the parameters of the Singe Diode Model (SDM) cannot be identified due to the I-V curve. Therefore, method M1 is not applicable. So, only the method M2 method will be evaluated in this section.

III.4.3.1. Evaluation of method M2 with simulation data

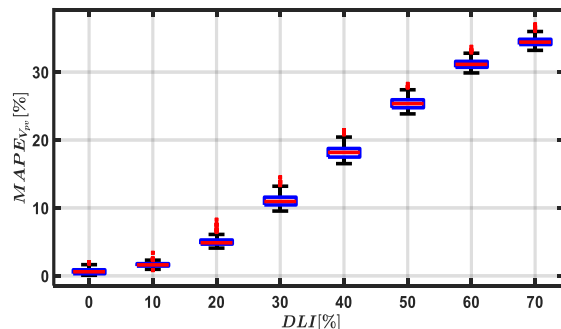
The PV single diode model M3.String developed in [43] is used to simulate the PV module, which is composed of two strings of 18 cells and two bypass diodes. The environmental data  $(T_{pv}, G_{poa})_{testing}$  consist of 343 samples. The first group of 18 cells receives an irradiation  $G_1 = G_{poa}$  while the second group receives an irradiation  $G_2 = G_1(1 - DLI)$ . To simulate the partial shading conditions, different levels of irradiance (DLI) are used, as displayed in [Table.III.17](#).

Table.III. 17: Configuration of the partial shading

No	Different levels of irradiance (DLI) between $G_1$ and $G_2$ in percentage [%]	$G_2$
1	0	$G_2 = G_1 - (DLI \times G_1)$
2	20	
3	30	
4	40	
5	50	
6	60	
7	70	



(a):  $MAPE_{I_{pv}}$



(b):  $MAPE_{V_{pv}}$

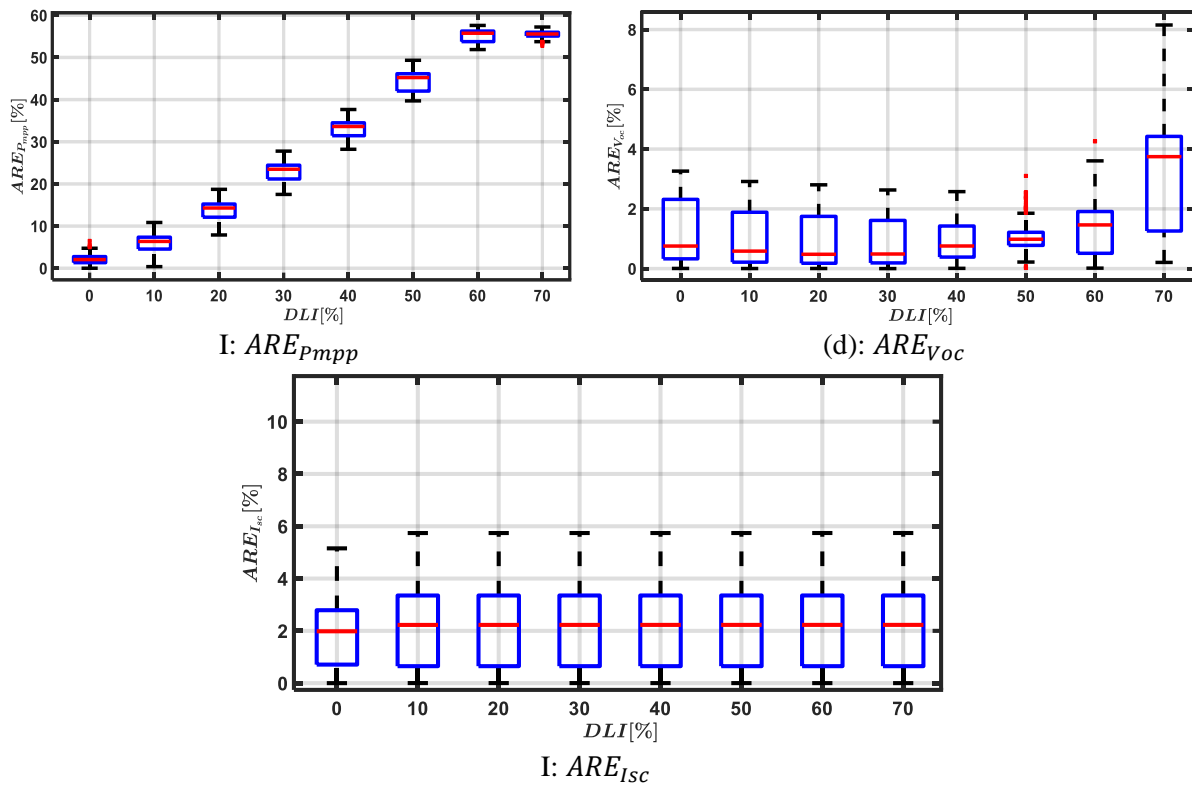
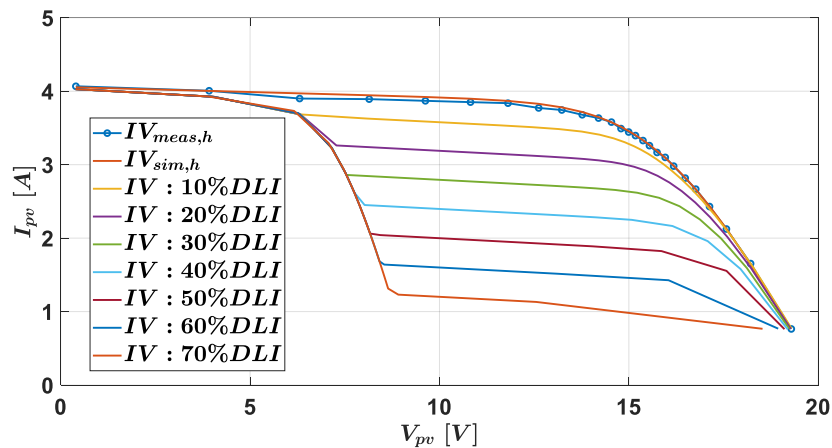


Fig.III.34: Effect of partial shading on I-V curve characteristics

Fig.III.34 shows the impact of partial shading on the I-V curve characteristics in faulty and healthy cases. We can observe that the PV current, voltage, and maximum power point are highly sensitive features. When the partial shading is severe (70%), the mean value of the  $ARE_{V_{oc}}$  significantly increases because the LDP algorithm can no longer distribute the points in the area close to the open-voltage value.



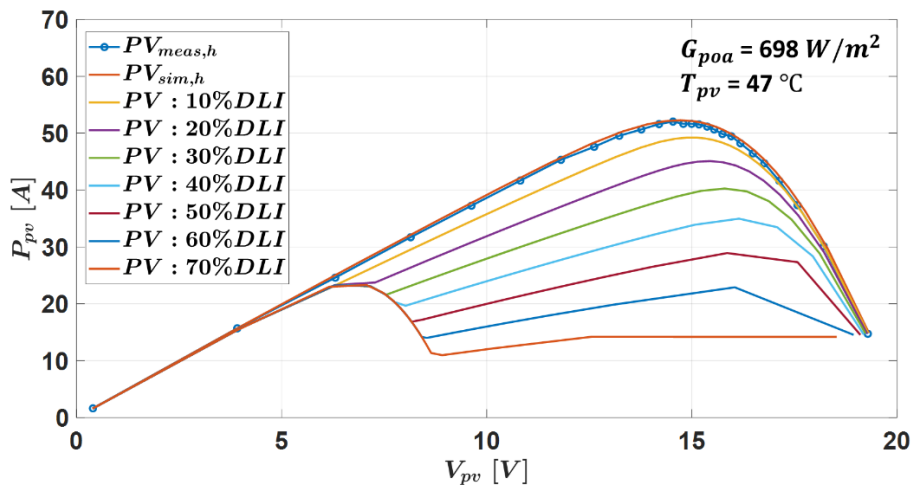


Fig.III.35: Effect of partial shading on I-V and P-V curves

Fig.III.35 shows the I-V and P-V curves under the healthy and different shading levels. We can observe that as the fault severity increases, the output power decreases, and the deformation of the I-V curve is accentuated.

#### III.4.3.2. Evaluation of method M2 with experimental data

The PV panels are installed on the roof of the building, as shown in Fig.III.36. In autumn, every day at around 5 PM, the PV module is affected by partial shading due to the air conditioning installation.

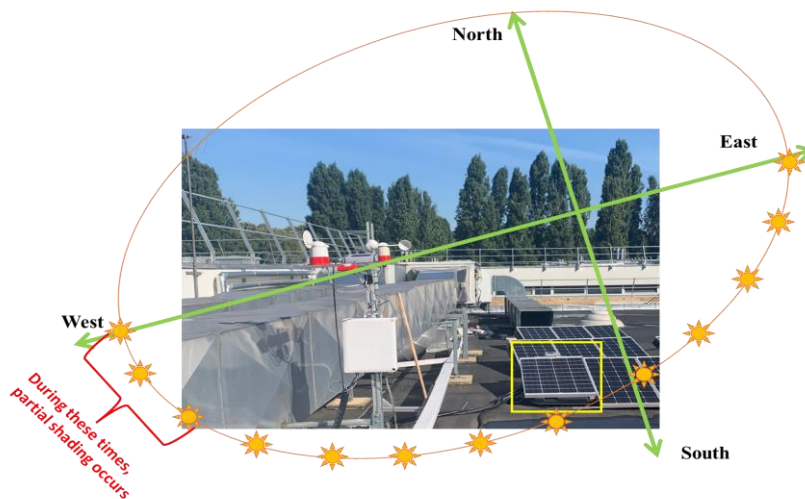


Fig.III.36: PV panel installation site

The data collection periods, weather information, and number of I-V curves are displayed in Table.III. 18.

Table.III. 18: Data acquisition in case of partial shading

Date of acquisition		Weather	Number of I-V curves $G_{poa} \geq 400 \text{ W/m}^2$
1	03/09/2021	Partly cloudy	2
2	08/09/2021	Partly cloudy	2
3	10/09/2021	Partly cloudy	2
4	12/09/2021	Partly cloudy	2
5	19/09/2021	Partly cloudy	2
6	20/10/2021	Partly cloudy	2

Fig.III.37 shows the healthy I-V curves obtained from the simulation of the hybrid model, and the faulty ones measured under partial shading conditions. They will be used for the fault detection.

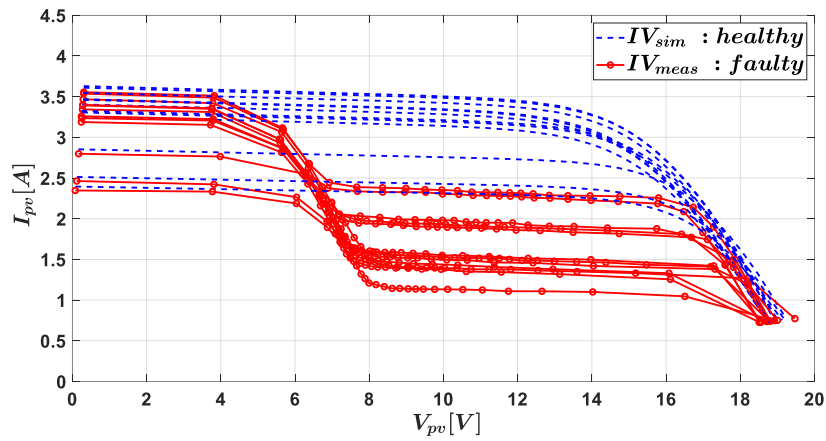
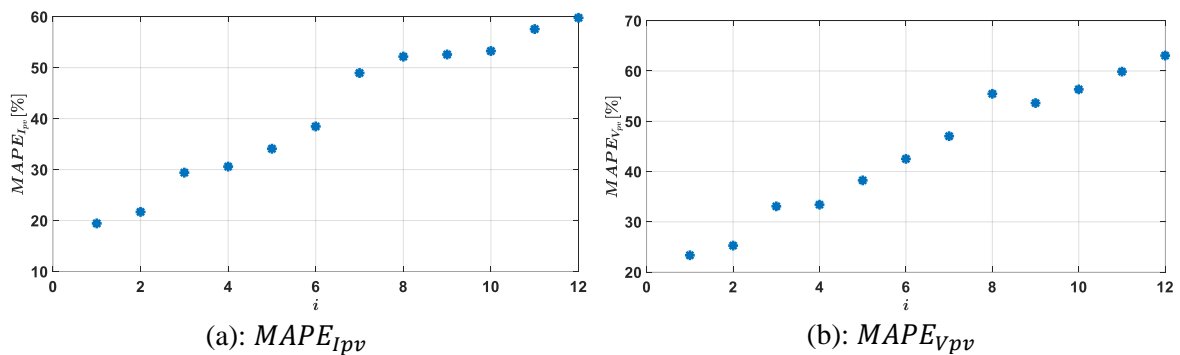


Fig.III.37: I-V curves under healthy and partial shading conditions

The results illustrated in Fig.III.38 show that the PV current, voltage, and maximum power point are highly sensitive features to partial shading. The open-circuit voltage and short-circuit current are not affected.





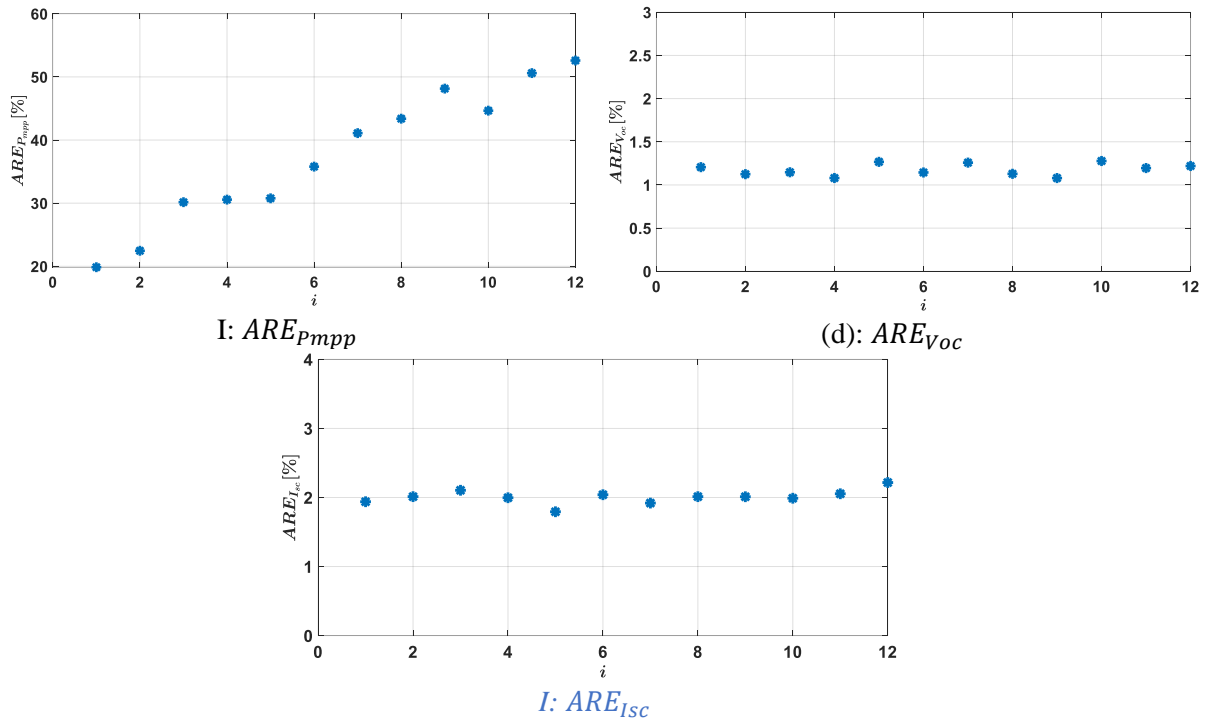


Fig.III.38: Effect of Partial shading on the I-V curve characteristics

### III.5. Conclusion

This chapter first provided a short overview of the most common faults in PV systems, their frequency of occurrence, and their impacts on power losses and safety. Based on the literature review, we classified the fault diagnosis approaches into two categories: visual inspection and automatic analysis based on features analysis.

The automatic analysis is considered for our study because the objective is to propose a low-cost and efficient solution that can be deployed for large-scale PV plants. Two methods (denoted M1 and M2) for fault detection and diagnosis (FDD) for PV systems are developed and evaluated with simulated and experimental data. Method M1, based on analytical models, uses as fault features the five parameters ( $I_{ph}, R_s, R_{sh}, I_0$  and  $n$ ) of the single diode model, while method M2, based on a hybrid model, which is a combination of the analytical models and a numerical model of the PV cells, uses five characteristics ( $I_{pv}, V_{pv}, P_{mpp}, V_{oc}$ , and  $I_{sc}$ ) of the I-V curves. The residuals are calculated between features extracted from experimental measurements and features extracted from the simulated models. Three fault cases are studied: series resistance  $R_s$  degradation, shunt resistance  $R_{sh}$  degradation, and partial shading.

In case of  $R_s$  and  $R_{sh}$  degradation, the results with method M1 have shown that the fault can be accurately detected and its level estimated. The results have also shown that the other parameters are not affected by the fault occurrence. The results with method M2 in both fault

cases show that the maximum power point is the most sensitive feature. In the case of partial shading, the results with method M2 have shown that the PV current and voltage, and the maximum power point have almost the same sensitivity level. The results have also shown that the fault had no impact on  $I_{sc}$  or  $V_{oc}$ . The performance of the methods is summarized in *Table.III. 19*.

*Table.III. 19: Summary of FDD performance*

X: No detection    1: No effect    2: Low    3: High

FDD Method	Fault types					
	$R_s$ degradation		$R_{sh}$ degradation		Partial shading	
M1	$I_{ph}$	1	$I_{ph}$	1	$I_{ph}$	X
	$R_s$	High	$R_s$	1	$R_s$	X
	$R_{sh}$	1	$R_{sh}$	High	$R_{sh}$	X
	$I_0$	1	$I_0$	1	$I_0$	X
	$n$	1	$n$	1	$n$	X
M2	$I_{pv}$	Low	$I_{pv}$	Low	$I_{pv}$	<b>High</b>
	$V_{pv}$	Low	$V_{pv}$	Low	$V_{pv}$	<b>High</b>
	$P_{mpp}$	<b>High</b>	$P_{mpp}$	<b>High</b>	$P_{mpp}$	<b>High</b>
	$V_{oc}$	Low	$V_{oc}$	Low	$V_{oc}$	1
	$I_{sc}$	Low	$I_{sc}$	Low	$I_{sc}$	1

### Reference of chapter III

- [1] Baojie Lie, “electrical measurements Health monitoring of photovoltaic modules using electrical measurements”, PhD thesis , University of Paris Saclay, 2021.
- [2] M. Koentges, S. Kurtz, C. E. Packard, U. Jahn, K. A. Berger, K. Kato, T. Friesen, H. Liu, M. Van Iseghem, and J. Wohlgemuth, “T13-01:2014 Review of failures of photovoltaic modules,” Technical Report, IEA International Energy Agency, 2014. [Online]. Available: [http://iea-pvps.org/index.php?id=275&eID=dam\\_frontend\\_push&docID=2064](http://iea-pvps.org/index.php?id=275&eID=dam_frontend_push&docID=2064) .
- [3] A. Y. Appiah, X. Zhang, B. B. K. Ayawli, and F. Kyeremeh, “Review and performance evaluation of photovoltaic array fault detection and diagnosis techniques,” *Int. J. Photoenergy*, vol. 2019, 2019.
- [4] D. S. Pillai and N. Rajasekar, “Metaheuristic algorithms for PV parameter identification : A comprehensive review with an application to threshold setting for fault detection in PV systems,” *Renew. Sustain. Energy Rev.*, vol. 82, no. November 2017, pp. 3503–3525, 2018.
- [5] K. Abdulmawjood, S. S. Refaat, and W. G. Morsi, “Detection and prediction of faults in photovoltaic arrays: A review,” 2018 IEEE 12<sup>th</sup> International Conference on Compatibility, Power Electronics and Power Engineering (CPE-POWERENG 2018), 10-12 April, Doha, Qatar, pp.1-8, 2018.
- [6] A. Triki-lahiani, A. B. Abdelghani, and I. Slama-belkhdja, “Fault detection and monitoring systems for photovoltaic installations : A review,” *Renew. Sustain. Energy Rev* ,vol. 82, no. September 2017, pp. 2680–2692, 2018.
- [7] A. Mellit, G. M. Tina, and S. A. Kalogirou, “Fault detection and diagnosis methods for photovoltaic systems: A review,” *Renew. Sustain. Energy Rev.*, vol. 91, no. March, pp. 1–17, 2018.
- [8] M. Köntges, G. Oreski, U. Jahn, M. Herz, P. Hacke, K.-A. Weiss, G. Razongles, M. Paggi, D. Parlevliet, T. Tanahashi, and R. French, “Assessment of photovoltaic module failures in the field,” Technique report, 2017. [Online]. Available: [http://www.iea-pvps.org/index.php?id=92&eID=dam\\_frontend\\_push&docID=4059](http://www.iea-pvps.org/index.php?id=92&eID=dam_frontend_push&docID=4059). [9] J. A. Tsanakas, L. Ha, and C. Buerhop, “Faults and infrared thermographic diagnosis in operating c-Si photovoltaic modules: A review of research and future challenges,” *Renew. Sustain. Energy Rev.*, vol. 62, pp. 695–709, 2016.
- [10] M. A. Munoz, M. C. Alonso-García, N. Vela, and F. Chenlo, “Early degradation of silicon PV modules and guaranty conditions,” *Sol. Energy*, vol. 85, no. 9, pp. 2264–2274, 2011.
- [11] M. Aghaei ,A. Fairbrother, A Gok,A Ahmad, S. Kazim, K. Lobato, G.Oreski, A.Reinders, J.Schmitz, M.Theelen, P.Yilmaz, J. Kettle., “Review of degradation and failure phenomena in photovoltaic modules,” *Renew. Sustain. Energy Rev.*, vol. 159, no. July 2021, p. 112160, 2022.
- [12] C. R. Osterwald, A. Anderberg, S. Rummel, and L. Ottoson, “Degradation analysis of weathered crystalline-silicon PV modules,” *Conference Record of the Twenty-Ninth IEEE Photovoltaic Specialists Conference*, 19-24 May, New Orleans, LA, USA., pp. 1392–1395, 2002.
- [13] M.A. Quintana, D.L. King, F.M. Hosking, J.A. Kratochvil, R.W. Johnson, B.R. Hansen, N.G. Dhere, M.B. Pandit., “Diagnostic analysis of silicon photovoltaic modules after 20-year field exposure,” *Conference Record of the Twenty-Eighth IEEE Photovoltaic Specialists Conference*, 15-22 September, Anchorage, AK, USA, vol. 2000, pp. 1420–1423, 2000.
- [14] R. L. Achey, “A Review of the Degradation of Photovoltaic Modules for Life Expectancy,” *J. Palliat. Med.*, vol. 19, no. 4, p. 468, 2016.
- [15] M. A. Quintana, D. L. King, T. J. McMahon, and C. R. Osterwald, “Commonly observed

- degradation in field-aged photovoltaic modules,” Conference Record of the Twenty-Ninth IEEE Photovoltaic Specialists Conference, 19-24 May, New Orleans, LA, USA., pp. 1436–1439, 2002.
- [16] N. C. Park, J. S. Jeong, B. J. Kang, and D. H. Kim, “The effect of encapsulant discoloration and delamination on the electrical characteristics of photovoltaic module,” *Microelectron. Reliab.*, vol. 53, no. 9–11, pp. 1818–1822, 2013.
- [17] G. Jorgensen, K. Terwilliger, S. Glick, J. Pern, and T. McMahon, “Materials testing for PV module encapsulation,” *Natl. Cent. Photovoltaics Sol. Progr. Rev. Meet. Denver, Color. March*, no. May, pp. 24–26, 2003.
- [18] L. Cristaldi, M. Faifer, M. Lazzaroni, M. M. A. F. Khalil, M. Catelani, and L. Ciani, “Diagnostic architecture: A procedure based on the analysis of the failure causes applied to photovoltaic plants,” *Meas. J. Int. Meas. Confed.*, vol. 67, pp. 99–107, 2015.
- [19] M. D. Kempe, “Modeling of rates of moisture ingress into photovoltaic modules,” *Sol. Energy Mater. Sol. Cells*, vol. 90, no. 16, pp. 2720–2738, 2006.
- [20] S. Djordjevic, D. Parlevliet, and P. Jennings, “Detectable faults on recently installed solar modules in Western Australia,” *Renew. Energy*, vol. 67, pp. 215–221, 2014.
- [21] I. Elettronica, V. S. Marta, and I.- Firenze, “Examination of Solar Cells and Encapsulations of Small Experimental Photovoltaic Modules,” no. 1, pp. 137–141, 2002.
- [22] F. NOVOA, “Adhesion and Reliability of Solar Module Materials,” PhD Thesis, Stanford University,” 2015.
- [23] F. Jiang, H. Liu, and X. Zou, “Test and Analysis of Potential Induced Degradation in Crystalline Silicon PV Modules,” Chinese Control And Decision Conference (CCDC), 09-11 June, Shenyang, China, pp. 4993–4996, 2018.
- [24] J. Lindroos and H. Savin, “Review of light-induced degradation in crystalline silicon solar cells,” *Sol. Energy Mater. Sol. Cells*, vol. 147, pp. 115–126, 2016.
- [25] Meydbray, J.; Dross, F. PV Module Reliability Scorecard Report; DNV GL: Oslo, Norway, 2016.
- [26] J. Solórzano and M. A. Egado, “Automatic fault diagnosis in PV systems with distributed MPPT,” *Energy Convers. Manag.*, vol. 76, pp. 925–934, 2013.
- [27] E. Molenbroek, D. W. Waddington, and K. A. Emery, “Hot spot susceptibility and testing of PV modules,” Conference Record of the Twenty-second IEEE Photovoltaic Specialists Conference, 07-11 October 1991, Las Vegas, NV, USA, pp. 547–552, 1992.
- [28] M. Chang, C. Chen, C. H. Hsueh, W. J. Hsieh, Eva Yen, K. L. Ho, H. P. Chuang, C. Y. Lee, Haomin Chen, “The reliability investigation of PV junction box based on 1GW worldwide field database,” 2015 42<sup>nd</sup> Photovoltaic Specialist Conference (PVSC), 14-19 June, New Orleans, LA, USA, pp. 1–4, 2015.
- [29] D. A. R. Barkhouse, O. Gunawan, T. Gokmen, T. K. Todorov, and D. B. Mitzi, “Photovoltaic failure and degradation modes,” *Prog. Photovoltaics Res. Appl.*, vol. 20, no. 1, pp. 318–326, 2017.
- [30] S. R. Madeti and S. N. Singh, “A comprehensive study on different types of faults and detection techniques for solar photovoltaic system,” *Sol. Energy*, vol. 158, no. October, pp. 161–185, 2017.
- [31] Long BUN, “Détection et Localisation de Défauts pour un Système PV”, PhD thesis Electrical Engineering, University of Grenoble, 2011.
- [32] C. Delpha and D. Diallo, “Kullback-Leibler divergence for incipient fault diagnosis,” in *Signal Processing for Fault Detection and Diagnosis in Electric Machines and Systems*, Institution of Engineering and Technology, 2021, pp. 85–118.

- [33] S. Mohanty, B. Subudhi, and P. K. Ray, "A Grey Wolf-Assisted Perturb & Observe MPPT Algorithm for a PV System," *IEEE Trans. Energy Convers.*, vol. 32, no. 1, pp. 340–347, 2017.
- [34] B. Yang, T. Yu, X. Zhang, H. Li, H. Shu, Y. Sang, L. Jiang., "Dynamic leader based collective intelligence for maximum power point tracking of PV systems affected by partial shading condition," *Energy Convers. Manag.*, vol. 179, no. September 2018, pp. 286–303, 2019.
- [35] Y. Chaibi, M. Malvoni, A. Chouder, M. Boussetta, and M. Salhi, "Simple and efficient approach to detect and diagnose electrical faults and partial shading in photovoltaic systems," *Energy Convers. Manag.*, vol. 196, pp. 330–343, 2019.
- [36] ISO\_25178-2:2012, "IEC 61724. Photovoltaic system performance monitoring – guidelines for measurement, data exchange and analysis," 1998.
- [37] A. Chouder and S. Silvestre, "Automatic supervision and fault detection of PV systems based on power losses analysis," *Energy Convers. Manag.*, vol. 51, no. 10, pp. 1929–1937, 2010.
- [38] S. K. Firth, K. J. Lomas, and S. J. Rees, "A simple model of PV system performance and its use in fault detection," *Sol. Energy*, vol. 84, no. 4, pp. 624–635, 2010.
- [39] J. M. Huang, R. J. Wai, and W. Gao, "Newly-designed fault diagnostic method for solar photovoltaic generation system based on IV-Curve measurement," *IEEE Access*, vol. 7, pp. 70919–70932, 2019.
- [40] B. Li, C. Delpha, A. Migan-Dubois, and D. Diallo, "Fault diagnosis of photovoltaic panels using full I–V characteristics and machine learning techniques," *Energy Convers. Manag.*, vol. 248, p. 114785, 2021.
- [41] M. H. Ali, A. Rabhi, A. El Hajjaji, and G. M. Tina, "Real Time Fault Detection in Photovoltaic Systems," *Energy Procedia*, vol. 111, no. September 2016, pp. 914–923, 2017.
- [42] S. Fadhel, C. Delpha, D. Diallo, I. Bahri, A. Migan, M. Trabelsi, M. F. Mimouni., "PV shading fault detection and classification based on I-V curve using principal component analysis: Application to isolated PV system," *Sol. Energy*, vol. 179, no. June 2018, pp. 1–10, 2019.
- [43] V. Kongphet, A. Migan-dubois, C. Delpha, and D. Diallo, "Photovoltaic Fault Detection and Diagnosos : Which level of Granularity for PV Modeling?," 2020 Prognostics and Health Management Conference (PHM-Besancon), 04-07 May 2020, Besancon, France, pp 1-7, 2020

List of figures of chapter III

Fig. III.1: Structure of standard crystalline silicon and thin-film PV module [11] .....	124
Fig.III.2: Encapsulation failure[20].....[20].....	124
Fig. III.3: PV module with broken glass and cell burn [14].....	125
Fig. III.4: Backsheet/encapsulation fault [22] .....	126
Fig. III.5: Bubbles in a PV module [14].....	126
Fig.III.6: Aging mechanisms leading to PV module degradation [25] .....	127
Fig.III.7: PV module with hot spot [14].....	127
Fig.III.8: Different cases of shading and soiling fault [26] .....	128
Fig.III.9: Junction box failure [14].....	128
Fig. III.10: Occurrence distribution of failures over the years of the PV system operation [8], (a1) and (a2): Total failure occurrence of all detected failures; (b1) and (b2): Occurrence of failures that cause measurable power losses .....	130
Fig. III.11: Pareto chart of the most signification modes: (a) All years, (b) System installed in the last ten years. The bars are color-coded by severity [29].....	132
Fig.III.12: Some examples of fault isolation with thermal camera [31].....	133
Fig.III.13: Comparison of I-V characteristics in healthy and faulty cases .....	134
Fig.III.14: Flowchart of the FDD .....	136
Fig.III.15: Boxplot of the residual for $R_s$ degradation .....	138
Fig.III.16: Effect of $R_s$ degradation on the other parameters of the SDM .....	139
Fig.III.17: Effect of $R_s$ degradation on I-V and P-V curves .....	139
Fig.III.18: Effect of $R_s$ degradation on I-V curve characteristics .....	140
Fig.III.19: Histograms of the series resistance $R_s$ .....	142
Fig.III.20: Histograms of the residuals for the three fault severities .....	142
Fig.III.21: Cumulative Distribution functions in case of $R_s$ .....	143
Fig.III.22: Effect of $R_s$ degradation on the other parameters of the SDM .....	144
Fig.III.23: Effect of $R_s$ on the I-V curve characteristics .....	145
Fig.III.24 : Boxplot of residuals for $R_{sh}$ .....	146
Fig.III.25 : Effect of $R_{sh}$ degradation on the other parameters .....	147
Fig.III.26: Effect of $R_{sh}$ degradation on I-V and P-V curves .....	147
Fig.III.27: Effect of $R_{sh}$ degradation on the characteristics of the I-V curve .....	148
Fig.III.28: Histograms of $R_{sh}$ resistance.....	150
Fig.III.29: Histograms of residuals for $R_{sh}$ .....	150
Fig.III.30: Cumulative Distribution Functions .....	151
Fig.III.31: Effect of $R_{sh}$ degradation on the other parameters.....	151
Fig.III.32: Effect of $R_{sh}$ degradation on the I-V curve characteristics .....	152
Fig.III.33: Effect of partial shading on I-V curve characteristics.....	154

Fig.III.34: Effect of partial shading on I-V and P-V curves..... 155

Fig.III.35: PV panel installation site ..... 155

Fig.III.36: I-V curves under healthy and partial shading conditions..... 156

Fig.III.37: Effect of Partial shading on the I-V curve characteristics..... 157

List of tables of chapter III

Table III.1: Fault Classification in PV systems.....	122
Table.III.2: Severity rating of the different degradation modes [29] .....	131
Table.III.3 :Summary of degradation modes with their severity ranking [29].....	131
Table.III.4: List of detectable PV module faults using visual inspection[1] .....	133
Table.III.5: Fault levels for $R_s$ degradation.....	137
Table.III.6: Residuals for $R_s$ degradation.....	138
Table.III.7: Mean values of the residuals .....	141
Table.III.8: Data acquisition in case of $R_s$ degradation .....	141
Table.III.9: Accuracy of fault level estimation in case of $R_s$ degradation .....	143
Table.III.10: Mean value relative variation of the residuals.....	145
Table.III.11: Shunt resistance fault levels used in the PV hybrid model .....	145
Table.III.12 : Residuals for $R_{sh}$ .....	146
Table.III.13 : Effect of $R_{sh}$ degradation on I-V curve characteristics .....	149
Table.III.14: Data for $R_{sh}$ degradation.....	149
Table.III.15: Three levels of severity for $R_{sh}$ degradation .....	150
Table.III.16: Fault effect on the I-V curve characteristics .....	152
Table.III.17: Configuration of the partial shading.....	153
Table.III.18 : Data acquisition in case of partial shading.....	156
Table.III.19: Summary of FDD performance.....	158



## General Conclusion

The efficiency and reliability of PV panels can be seriously compromised by accelerated aging or transportation/installation (intrinsic fault) or shading and soiling (extrinsic faults). These faults can occur at any time. Therefore, they should be detected and diagnosed at their earliest stage to engage in an efficient maintenance policy. Health monitoring is one of the main components of condition-based maintenance. Fault Detection and Diagnosis (FDD) methods have been developed to address the health monitoring of PV panels. Among the different methods, physics-based ones are widely recognized as being efficient if the model is accurate enough. This model requires environmental data (irradiance in the plane of the array and module temperature). The current-voltage curve, known as the I-V curve, is also recognized as a valuable source of information on the PV module's health status. Therefore, in our application, we studied the FDD of PV panels using the analytical Single Diode Model (SDM) to obtain simulated I-V curves from which the fault features are extracted. The objectives of this work were to develop a low-cost and accurate I-V tracer, design a hybrid PV model combining analytical and numerical models, and develop FDD methods in which fault features are extracted from the I-V curve.

In chapter I, we developed the experimental test bench based on a low-cost I-V tracer, a DC-DC converter, and current and voltage sensors. It also comprises an electronic board that emulates the degradation of shunt and series resistances. The number of points (samples) and their distribution of the I-V curve have been set to minimize the measurement duration (disconnection duration), i.e., and the resolution. The logarithmic distribution of points (LDP) was found to perform better than the usual uniform distribution of points (UDP). Indeed, its absolute relative error (ARE) was lower. The I-V tracer was then validated/calibrated using a high-efficiency E4360A Modular Solar Array Simulator (MSAS): we obtained a relative error of 1.33 % in the healthy case. We also show that the proposed low-cost I-V tracer could measure the I-V characteristics of PV modules under faulty conditions (i.e., partial shading,  $R_s$  degradation, and  $R_{sh}$  degradation). We also evaluated its rapidity and reliability. During the development of the test bench, we collected abnormal I-V curves due to over-illumination of the PV module. Thanks to a linear interpolation technique, the abnormal curves were eliminated to avoid any misinterpretation during the process of FDD.

Chapter II presented the model of the PV module, the identification of its parameters, and the validation. A four-step methodology was developed to extract the parameters of the

single diode model. The first two steps are devoted to the training, while the last two are for validation. The analytical models were still valid despite the dispersion observed when identifying the five parameters. Indeed, the combination of the five parameters is crucial, and it was found that for each combination, the model was able to provide a simulated I-V curve close to the measured one with a relative error of less than 3%. We concluded that the PV model was accurate for fault detection and diagnosis.

In Chapter III, based on the literature review, we first provided a rapid overview of the main faults and their frequency of occurrence that affect PV modules. The fault effects on the output power and safety were also presented. We developed two FDD methods (denoted M1 and M2) based on the automatic analysis of fault features instead of visual inspection because our objective was to propose a solution that can be deployed on large-scale PV plants. The method M1 uses the five parameters ( $I_{ph}$ ,  $R_s$ ,  $R_{sh}$ ,  $I_0$  and  $n$ ) of the single diode model as fault features, while M2 uses the five characteristics ( $I_{pv}$ ,  $V_{pv}$ ,  $P_{mpp}$ ,  $V_{oc}$ , and  $I_{sc}$ ) of the I-V curves. M1 is based on the analytical models of the parameters, and M2 exploits a hybrid model, which is a combination of the analytical models and a numerical model of the PV cells. The measured features are compared to their healthy counterparts (obtained from the simulation) to generate residuals.

Three fault cases are studied: series resistance  $R_s$  degradation, shunt resistance  $R_{sh}$  degradation, and partial shading. The experimental and simulation results showed that with M1, the degradation of the resistances could be accurately detected and the fault level estimated. The results also showed that the other parameters of the model were not affected. The results with M2 showed that for all the fault cases (degradation and partial shading), the maximum power point was the most sensitive fault feature. In partial shading, the results with demonstrated that the current, voltage, and maximum power point have almost the same sensitivity level.

## Perspectives

Several studies could be conducted in the future :

The developed I-V tracer should be evaluated on a large-scale PV plant to assess its effectiveness and performance in more realistic conditions. This could be done on the test bench in Laos, whose development was stopped due to the Covid pandemic. It would also be an opportunity to improve the measurement near the open-circuit voltage. The acquisition time

could be optimized according to the position of the sun. It would also be interesting to evaluate the I-V tracer with other technologies of PV cells.

The scope of the fault emulator could be enlarged with more fault severity levels, particularly incipient faults whose detection, even if more tedious, helps improve condition-based maintenance.

Building a database including measurements from the two sites (France and Laos) would also be relevant. It will evaluate the accuracy and robustness of fault detection and diagnosis methods.

Under partial shading conditions, the I-V curve is very distorted. It should be interesting to develop an efficient and robust technique to extract the parameters of the single diode model. In that case, method M1 could be an alternative.

We only evaluated the threshold-based technique to analyze the residuals in this work. With a higher number of faults and fault cases, it would be interesting to evaluate machine learning techniques, especially if other environmental data were measured.

Finally, we have only dealt with faults on the DC side. It would be interesting to tackle the faults that can occur on the AC side when the PV plant is connected to an AC power grid.

## Appendix: Hybrid PV model based on the single diode with $R_s$ and $R_{sh}$ model

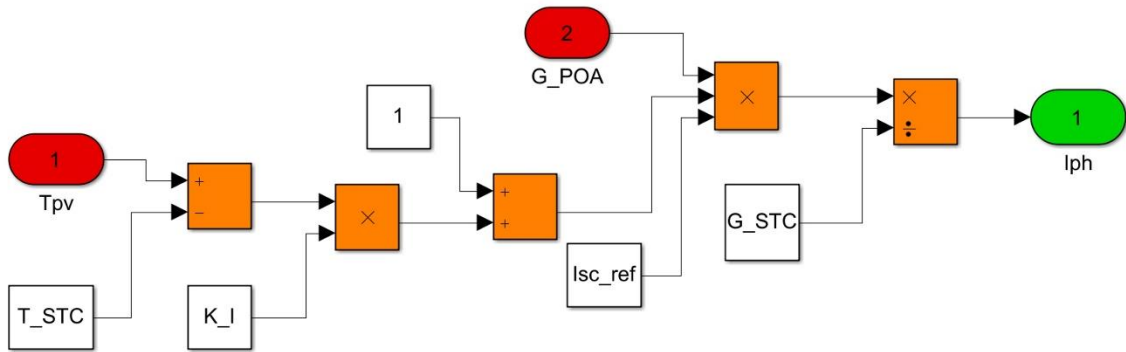
Summary of the eight reference values estimated from the analytical model of parameters

The single diode of PV model with five electrical parameters and eight reference values									
$I_{pv} = I_{ph} - I_0 \left[ \exp\left(\frac{q(V_{pv} + I_{pv}R_sN_s)}{nN_sKT}\right) - 1 \right] - \left(\frac{V_{pv} + I_{pv}R_sN_s}{R_{sh}N_s}\right)$									
Five electrical parameters	Analytical model	The eight reference values							
		$I_{sc.ref}$ [A]	$K_{I.ref}$ [%/°C]	$V_{oc.ref}$ [V]	$K_{V.ref}$ [%/°C]	$R_{s.ref}$ [mΩ]	$\beta_{ref}$ [-]	$R_{sh.ref}$ [Ω]	$n_{ref}$ [-]
$I_{ph}$	$I_{ph} = I_{sc.ref}[1 + K_{I.ref}(T_{pv} - T_{STC})] \frac{G_{POA}}{G_{STC}}$	5.79	0.061	-	-	-	-	-	-
$I_0$	$I_0 = \frac{I_{sc.ref} + K_{I.ref}(T_{pv} - T_{STC})}{\exp\left(\frac{qV_{oc.ref}[1 + K_{V.ref}(T_{pv} - T_{STC})]}{nKN_sT}\right) - 1}$	5.79	0.061	20.68	-0.519	-	-	-	-
$R_s$	$R_s = R_{s.ref} \left[ \frac{T}{T_n} (1 - \beta_{ref} \ln\left(\frac{G_{POA}}{G_{STC}}\right)) \right]$	-	-	-	-	709	0.036	-	-
$R_{sh}$	$R_{sh} = R_{sh.ref} \frac{G_{STC}}{G_{POA}}$	-	-	-	-	-	-	49.85	-
$n$	$n = n_{ref} \frac{T}{T_n}$	-	-	-	-	-	-	-	1.01

The analytical model of parameters and their reference value in the table are used to implement the physical PV module model called the hybrid PV model, this model is established under the MATLAB Simulink environment.

### 1. Photo generated current ( $I_{ph}$ ) implementation

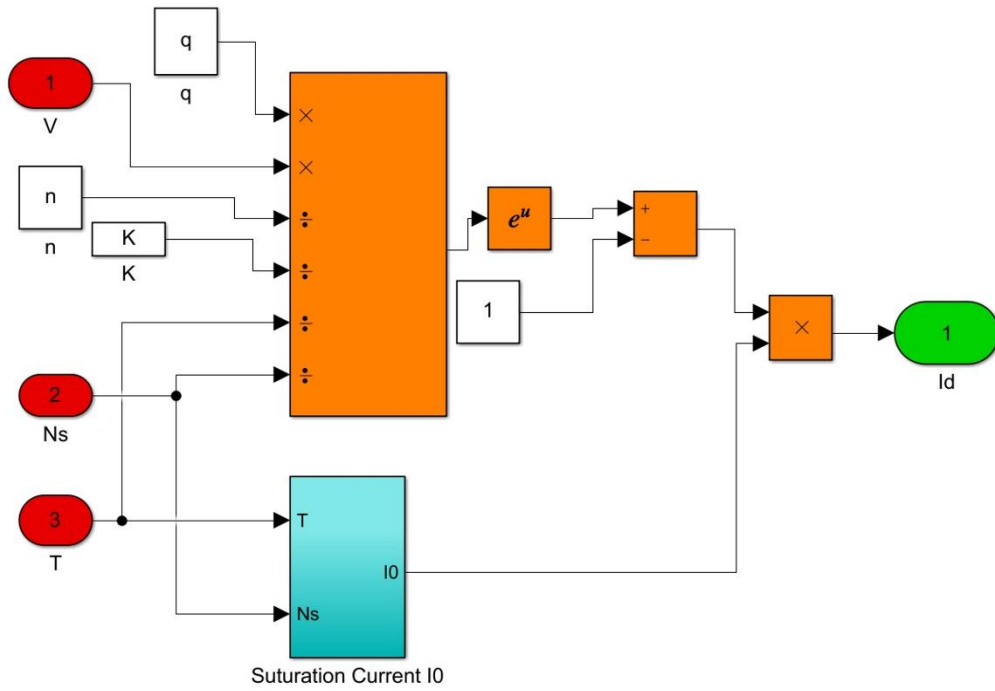
$$I_{ph} = I_{sc.ref} [1 + K_{I.ref}(T_{pv} - T_{STC})] \frac{G_{POA}}{G_{STC}}$$



Detailed of  $I_{ph}$  implementation

### 2. Diode current ( $I_d$ ) implementation

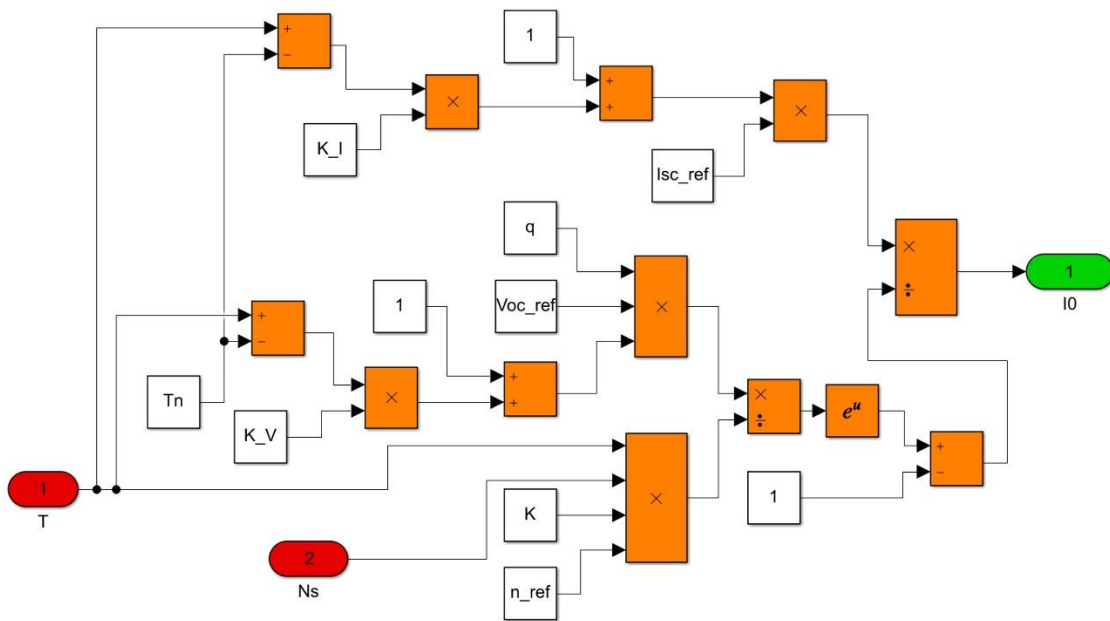
$$I_d = I_0 \left[ \exp\left(\frac{q(V_{pv} + I_{pv}R_sN_s)}{nN_sKT}\right) - 1 \right] , \text{ where } V = V_{pv} + I_{pv}R_sN_s$$



*Detailed of Id implementation*

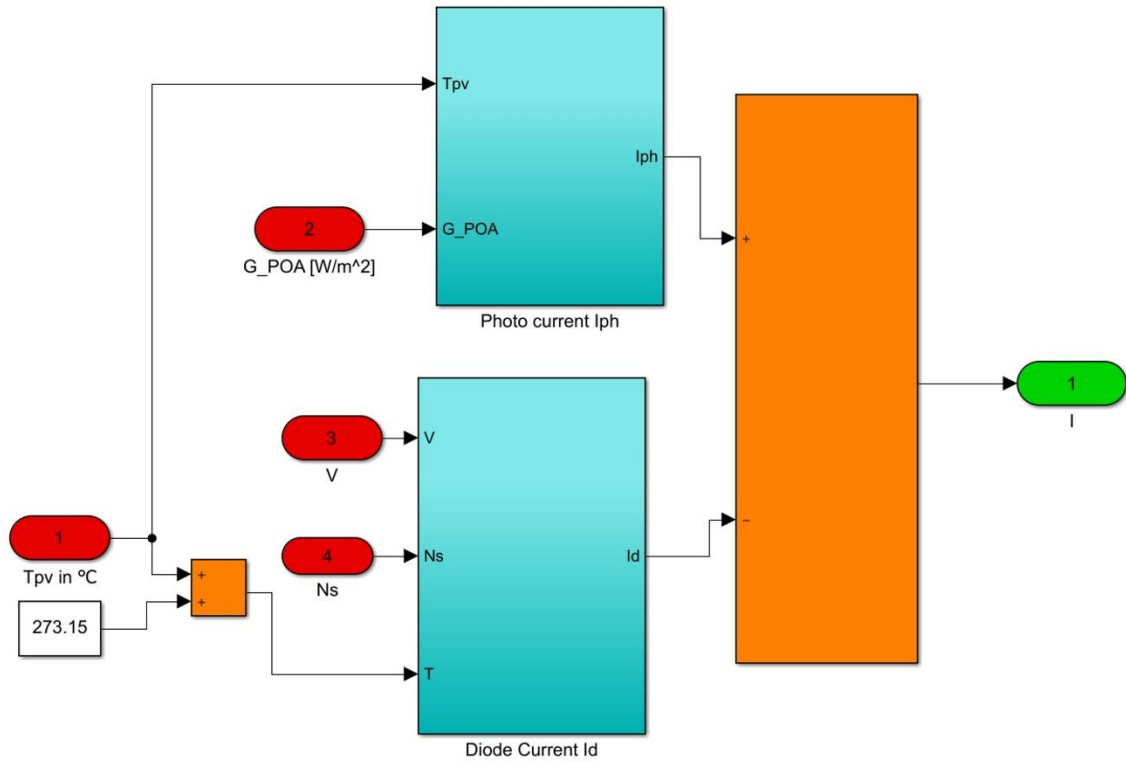
3. Diode saturation current ( $I_0$ ) implementation

$$I_0 = \frac{I_{sc\_ref} + K_{I\_ref}(T_{pv} - T_{STC})}{\exp\left(\frac{qV_{oc\_ref}[1 + K_{V\_ref}(T_{pv} - T_{STC})]}{nKN_sT}\right) - 1}$$



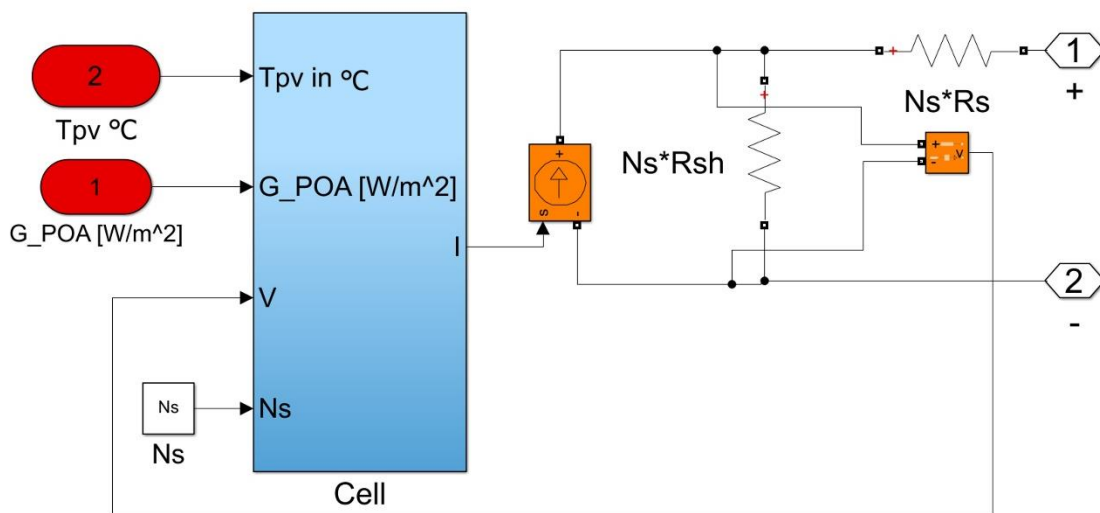
*Detailed of I0 implementation*

4. Combination of  $I_{ph}$ ,  $I_d$  and  $I_0$



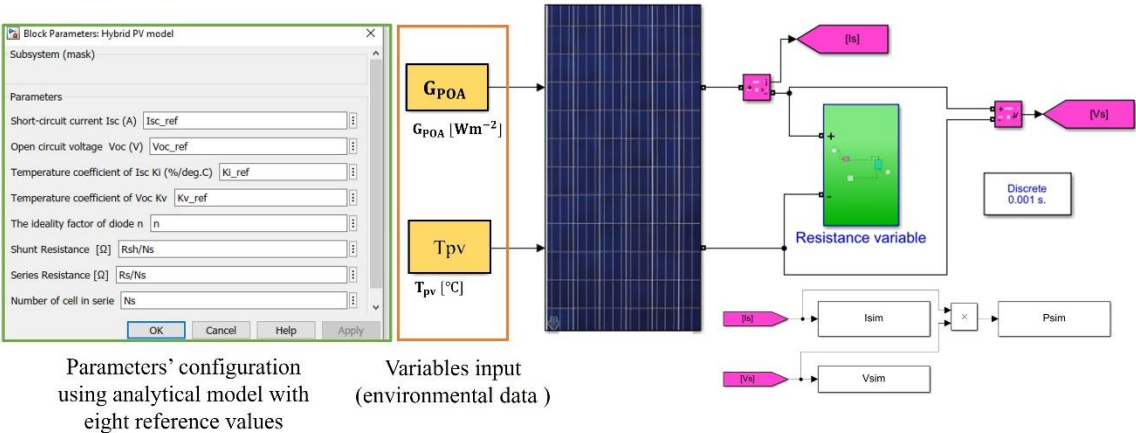
*Detailed of  $I_p, I_d$  and  $I_0$  combination*

5. PV electrical model with  $R_s$  and  $R_{sh}$  depending on  $N_s$



*PV electrical model depending on  $N_s$*

6. Whole PV model



Presentation of the whole hybrid PV model

**Titre : Contribution à la détection de défauts dans les modules PV en utilisant les courbes I-V**

**Mots clés :** Photovoltaïque, Traceur I-V, Modèle photovoltaïque, courbe I-V, Détection et Diagnostic de défaut

**Résumé :**

La surveillance continue de l'état de santé des modules PV est obligatoire pour maintenir un rendement élevé et minimiser les pertes de puissance dues aux défauts ou aux pannes.

Dans ce travail, un traceur embarqué à faible coût est développé et optimisé pour mesurer la courbe I-V en moins de 0,2 s afin de minimiser la durée de l'interruption de la production électrique. Le traceur proposé et validé avec un analyseur du commerce.

Les données expérimentales sont utilisées pour valider le modèle analytique du module PV. Ce modèle s'appuie sur les cinq paramètres ( $I_{ph}$ ,  $R_s$ ,  $R_{sh}$ ,  $I_0$  and  $n$ ) du circuit électrique à une diode. Il est combiné au modèle numérique de Matlab-Simulink pour mettre en place le modèle hybride qui sera utilisé comme référence pour le diagnostic. Ce modèle est validé avec une erreur relative inférieure à 3% pour plusieurs données environnementales (éclairage et température).

Les données mesurées sont utilisées pour extraire les cinq paramètres du modèle électrique équivalent ainsi que les principales caractéristiques de la courbe I-V (courant, tension,  $V_{oc}$ ,  $I_{sc}$  et  $P_{mpp}$ )

Les courbes I-V mesurées sont aussi utilisées pour évaluer les deux méthodes de diagnostic des défauts (notées M1 et M2).

M1 s'appuie sur le modèle analytique des cinq paramètres ( $I_{ph}$ ,  $R_s$ ,  $R_{sh}$ ,  $I_0$  and  $n$ ) alors que M2 utilise les cinq caractéristiques ( $I_{pv}$ ,  $V_{pv}$ ,  $P_{mpp}$ ,  $V_{oc}$ , and  $I_{sc}$ ) et le modèle hybride pour générer les courbes I-V de référence.

Les résidus sont calculés entre les indicateurs des défauts extraits des mesures expérimentales et ceux issues des courbes de référence. Trois cas de défaut ont été étudiés : dégradation de la résistance série  $R_s$ , dégradation de la résistance shunt  $R_{sh}$  et l'ombrage partiel. Les résultats basés sur des données expérimentales obtenues sous différentes températures et éclairagements ont montré que la dégradation des résistances série et shunt et l'ombrage partiel étaient mieux détectés par les caractéristiques qu'avec les paramètres.

**Title : Contribution to fault detection of PV modules using I-V curves**

**Keywords :** Solar photovoltaic, I-V tracer, PV model, I-V characteristic, Fault detection and diagnosis.

**Abstract :**

Continuous monitoring of the health status of PV modules is mandatory to maintain high efficiency and minimise power losses due to faults or failures.

In this work, a low-cost embedded tracer is developed and optimised to measure the I-V curve in less than 0.2 s to minimise the duration of power generation interruption. The proposed tracer is validated with a commercial analyser.

The experimental data is used to validate the analytical model of the PV module. This model is based on the single diode electrical circuit's five parameters ( $I_{ph}$ ,  $R_s$ ,  $R_{sh}$ ,  $I_0$  and  $n$ ). It is combined with the Matlab-Simulink numerical model to set up the hybrid model that

The measured I-V curves are also used to evaluate two fault diagnosis methods (denoted M1 and M2). The method M1 uses the analytical models of the five parameters ( $I_{ph}$ ,  $R_s$ ,  $R_{sh}$ ,  $I_0$  and  $n$ ) while M2 uses the five characteristics ( $I_{pv}$ ,  $V_{pv}$ ,  $P_{mpp}$ ,  $V_{oc}$ , and  $I_{sc}$ ) of the I-V curves as fault features, and the hybrid model to generate the I-V reference curves.

The residuals are calculated between the fault indicators extracted from the experimental measurements and those from the reference curves. Three fault cases were studied: degradation of the series resistance, degradation of the shunt resistance, and partial shading. The results based on experimental data, obtained under different temperatures and illuminations, showed that the I-V



will be used as a reference for the diagnosis. This model is validated with a relative error of less than 3% for several environmental data (irradiance and temperature).

The measured data are used to extract the five parameters of the equivalent electrical model and the main characteristics of the I-V curve (current, voltage, Voc, Isc and Pmpp)

curves' characteristics are more sensitive to series and shunt resistance degradation and partial shading than the parameters.